SYNTHESIS, CHARACTERIZATION AND HOST-GUEST COMPLEXES OF SUPRAMOLECULAR ASSEMBLIES BASED ON CALIXARENES AND CUCURBITURILS

BY

BAA EBENEZER

A THESIS SUBMITTED IN FULFILMENT OF THE REQUIREMENTS FOR THE DEGREE OF

DOCTOR OF PHILOSOPHY

DEPARTMENT OF CHEMISTRY
FACULTY OF SCIENCE
RHODES UNIVERSITY
MAKHANDA
SOUTH AFRICA

February 2022

ABSTRACT

The field of supramolecular chemistry has grown large and wide in both deepness of understanding, range of topics covered and scope and applications. Supramolecular self-assemblies are facilitated by a wide range of non-covalent intra and inter molecular interactions that range from hydrogen bonding to π-interaction and van der Waals. Macrocyclic compounds such as cucurbiturils and calixarenes have emerged as important classes of compounds with excellent potential of forming supramolecular assemblies. The porous nature of these compounds enables them to form host-guest supramolecular complexes stabilized by diverse range of non-covalent interactions. Furthermore, these compounds contain donor atoms capable of forming bonds with metal ions to yield metal complexes with interesting porous characteristics that deviate from their traditional hydrophobic cavity. The versatile nature of the resulting pores imply that they can accommodate diverse types of guests.

This work explores the synthesis and characterization of a host of calixarenes and cucurbiturils. Self-assembly of these macrocycles with various metal ions results to the formation of porous metal organic framework (MOF) complexes. Four new calixarene typed compounds obtained from aromatic aldehydes and twenty-six cucurbituril metal complexes are reported. These macrocylces and their metal complexes also form supramolecular complexes with DMSO, methanol, isoniazid hydrochloride and ciprofloxacin hydrochlorides through either self-assembly, mechanochemistry and exposure to solvent vapors. The bulk materials have been characterized using nuclear magnetic resonance spectroscopy (NMR), Fourier transformed infrared spectroscopy (FTIR), powder and single crystal diffraction techniques and thermal studies thermogravimetric analysis (TGA) and differential thermal calorimetry (DSC). Data obtained from this study reveals that calixarenes can form supramolecular complexes with a frequently used laboratory solvents with BN22 showing appreciable selectivity for DMSO sorption from a solvent mixture. These compounds also form supramolecular complexes with drug molecules such as isoniazid and ciprofloxacin. Furthermore, the data reveals that choice of synthetic route of supramolecular ensembles dictates if the guest drug molecule will occupy the intrinsic or extrinsic pores of cucurbituril complexes. Biological studies on the obtained complexes reveal that the cucurbituril complexes are non-cytotoxic while the calixarenes show antibacterial activity against *Escherichia coli* and *Staphylococcus aureus*.

Additionally, the study showed that ciprofloxacin can be successfully released from a calixarene host in a simulated body fluid although the host was also found to cross the dialysis membrane.

The results of this study are important in that;

- they can be exploited and developed in the selective sorption of certain guests and
- that they can be used in the development of drug delivery systems that play a dual role of delivery and therapeutic activity.

DECLARATION

I, **Baa Ebenezer** hereby declare that the work contained in this thesis is my own original work and that all other sources used or quoted have been fully acknowledged and referenced. The work has not been submitted before for the award of any other degree at any other university.

Signature: …… 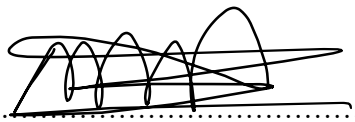 ……. Date: 9th June, 2022

DEDICATION

This thesis is dedicated to my lovely wife, Ojong Baa,
for her unconditional love and tireless support throughout my studies,
my sons Ngwang and Nsah for making it seem like fun even when all was not always and
accepting to see me put in so much focus on my work even at their young age

and

my mom Nicoline Mbuli for constant encouragement and believe in me.

ACKNOWLEDGEMENTS

Special thanks go to my team of supervisors, Professors GM Watkins, RMW Krause, DN Tantoh and Dr VJ Smith, for affording me this opportunity to further my studies. Your invaluable advice, guidance, comments, and encouragement throughout this journey have undeniably contributed to completing this research. The invaluable discussions and advice greatly improved my knowledge across a broad spectrum of topics in chemistry.

Many thanks to the HOD of the Chemistry Department for providing a financial lifeline during the very last stages of my studies. The department's support staff, from Mrs Tarr, Mr Chindeka, Mr Dondashe, Mr Monde, to name a few, played a vital role in seeing me through this challenging journey; a million thanks. Special thanks also go to Dr Jonathan Britton, Mr Chindeka and Mrs Gail Cobus for assistance with PXRD, elemental analysis and powder XRD. Unreserved gratitude is also expressed to Dr Eric Hosten of Nelson Mandela University for unwavering support in collecting and solving single crystal data. Your timeous efforts in assisting me are appreciated. Many thanks also go to Michelle Isaacs of the Marine Natural Products laboratory of Rhodes University for carrying out the biological analysis of my compounds. I also want to thank Dr Jarmo Kalinski for assisting with the mass spectrometry data collection.

I would also like to thank my laboratory mate Mr Siya Hulushe of F12 with whom I had several interesting discussions, which contributed to the many successes in this work. Laboratory mates of F2 and F22 also provided valuable suggestions and assistance towards the successful completion of this work, for which I say thank you all.

I would also like to extend sincere gratitude to my mom Nicoline Mbuli for the continual support and encouragement throughout my studies; I owe you every progress I have made thus far. My parent-in-law Mr. Enokenwa Ben and Mrs Enokenwa Comfort also provided invaluable support throughout my studies. Mr. and Mrs. Nkwate also afforded profound assistance while my wife and I struggled to forge ahead with our studies; for that, I am immensely grateful. To my brother Kongnyu Cyprian (late) and wife, I lack words for your interventions and belief in me. I could hardly thank you enough. The Grahamstown Baptist Church family was also a strong pillar of support; you supported me wholeheartedly and showed me, unreserved love. Your kind words, prayers and gifts brought much-needed tranquility during my studies.

To my dearly loved wife, you are indeed priceless, and your support can never be measured. You brought hope in the hopeless moments, light in the darkest nights, courage in the stormy gale. You saw the end and made sure I did not get my eyes off it. Against all odds, you believed I could make it and made sure your presence provided an aura for this thesis to see the light of day: a million thanks. For my two sons Ngwang and Nsah, what an incredible joy it had you beside me. You relieved the tense moments and inspired me to keep moving irrespective of the hardship of the moment: thanks for being there.

TABLE OF CONTENTS

LIST OF FIGURES

LIST OF TABLES

LIST OF SCHEMES

LIST OF ABBREVIATIONS

MOFs metal organic frameworks
CB cucurbituril
Pg pyrogallol
NMR nuclear magnetic resonance
FTIR Fourier transformed infrared
TGA thermogravimetric analysis
DSC differential scanning calorimetry
(P/S)XRD (powder/single) X-ray diffraction
UV ultraviolet
INH(Cl) isoniazid(hydrochloride)
CIP ciprofloxacin
Hhdb p-hydroxybenzoic acid
OMCB octamethylsubstituted cucurbituril
DMSO dimethyl sulfoxide
MeOH methanol

EtOH	ethanol
MLCT	metal-to-ligand-charge-transfer
BTBH	4,4',4"-benzene-1,3,5-tribenzoic acid
HMTA	hexamethylene tetraamine
TFA	trifluoroacetic acid
DBO	2,3-diazabicclo[2,2,2]oct-2-ene
DBH	2,3-diazabicclo[2,2,2]hept-2-ene
DDS	drug delivery system
ZIF-8	zeolitic imidazole framework
VER	verampil hydrochloride
DOX	doxorubicin
MDR	multidrug resistant
PBS	phosphate buffer saline
THF	tetrahydrofuran
PTX	paclitaxel
DNA	deoxyribonucleic acid
BioMOF	biological MOF
OxA	oxalic acid
MalA	malonic acid
SucA	succinic acid
GluA	glutaric acid

1 CHAPTER ONE

1.1 INTRODUCTION

Macrocyclic compounds such cucurbiturils, calixarenes, crown ethers, cyclodextrins and phthalocyanines, have been extensively exploited in the fields of pharmacy, medicine, and nutrition, for improving the solubility of the active ingredient of drugs and their stability and bioavailability for the sensing of proteins and nucleic acids [1]. The basis of these applications is often the formation of host-guest complexes with molecules of interest. Beyond the biological sphere, these compounds have also inspired research in fields such as catalysis, guest capture and storage, water purification, and sensing, among others [2–6]. While these organic macrocycles have found success in various applications, there has also been a surge in metalating them to obtain supramolecular metal-organic frameworks (MOFs) which, for most cases, are porous solid, incorporating, the usually-porous covalent organic macrocyclic precursor possess interesting structural diversity and porosity [7–15]. In the early days of MOFs development, the employment of macrocyclic molecules as ligands was not common, however, due to their success in applications including drug delivery, catalysis, sensing, and guest capture, these macrocyclic compounds have been and are increasingly being used as ligands for porous MOF complexes. The advantage these macrocycles have over non-macrocyclic ligands is that they form MOFs that possess two types pores; one (the intrinsic) arising from the macrocyclic ligand (usually hydrophobic) and the other (the extrinsic) from the complex (due to the MOF structure). The advantage of such structures lies in the fact that they can tolerate both hydrophobic and hydrophilic guests thus increasing the spectrum of possible guest. It has also been shown that constructing MOF structures from such macrocycles increases dimensionality and flexibility [12,15]. Such MOFs are therefore attractive, either as drugs themselves or as delivery vehicles and warrant further investigation.

Regarding the chemistry behind the applications of these macrocyclic materials (particularly calixarenes and cucurbiturils) and the resulting MOFs, proper understanding of factors such as inter- and intramolecular interactions involving these materials and their guests are fundamental to understanding the host-guest chemistry involved. In the sections that follows, these two classes of macrocycles are examined, considering their synthesis, inter and intramolecular interactions, MOF materials from these macrocycles and their host guest chemistry and applications.

1.2 Calixarenes

Calixarenes are a class of macrocyclic porous compounds with hydrophobic cavities capable of forming interactions with non-polar hosts [15]. They have been subject of considerable research in recent times because of their interesting host-guest chemistry and the ease of construction, usually by reacting aldehydes or alcohols with phenolic arenes in either acidic or basic media. Although the term calixarenes is usually used to refer to macrocycles obtained from phenol and its derivatives, in a more restricted terminology, calixarene refer to compounds obtained from phenol [16,17]. Resorcinol-based based compounds are referred to as resorcinarenes while pyrogallol based compounds are referred to as pyrogallolarenes etc (***Figure 1.1***). Phloroglucinol based macrocycles are less common because the reaction between aldehydes and phloroglucinol leads to insoluble polymers and not the desired phloroglucinarene [18]. Except where specified, the term calixarene will be used in its broadest sense in this work to refer to compounds obtained from different phenol derivatives.

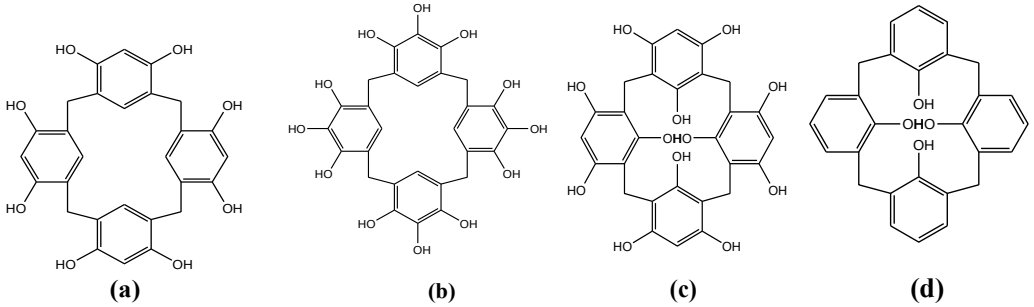

Figure 1.1: Different calixarenes obtained from phenolic derivatives (a) resorcinarene (b) pyrogallolarene (c) phloroglucinarene (d) simple calixarene

The number of aromatic rings in the parent structure can vary from 4 to 20, although calixarenes with 4, 5, 6, 7, and 8 are known to be the most common [1]. Generally, they are named as calix[*n*]arene, resorcin[*n*]arene, pyrogallol[*n*]arene where "*n*" represents the number of monomer units. Calixarenes are amoeboid in character and tend to adopt any of four conformations, as indicated in ***Figure 1.2***. With reference to the cone structure (a), the lower end of the cone containing the -OH groups is usually referred to as lower rim and the end containing the -R groups is usually known as the upper rim.

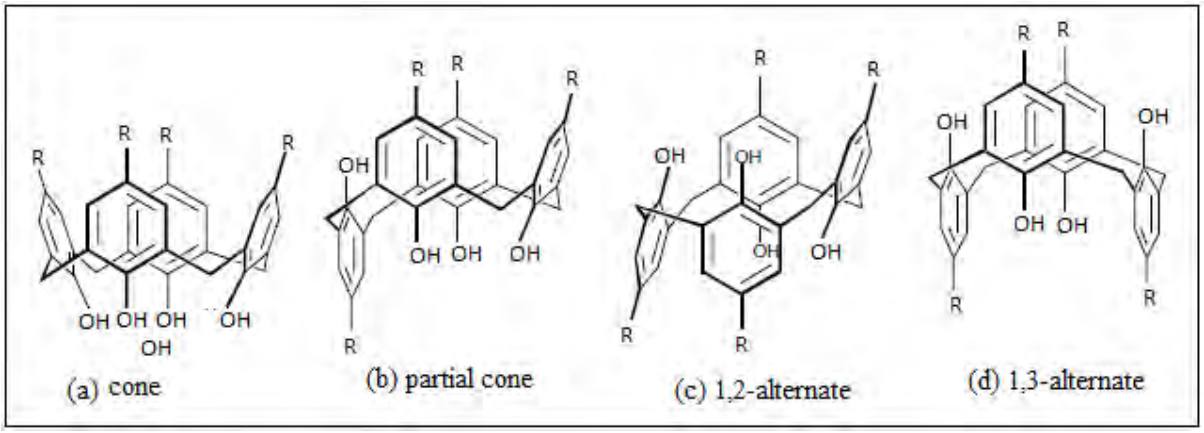

Figure 1.2: Conformations of calixarenes [1]

The conformational interconvertibility is made possible by rotation of the aromatic rings around the methylene carbon atoms. This behavior can be investigated through either NMR or single-crystal diffraction studies. Studies have shown that introducing an aromatic ring at the methylene carbon leads to other conformations in which some of the aromatic rings of the backbone are not aligned to the vertical but rather the horizontal axis [19,20]. In the case of methylene bridges, conformational freezing can be achieved by attaching moieties to the phenolic oxygen atoms. Knowledge guided embroidery has been used not only to freeze the conformation, but also to attach recognition moieties for protein binding [21] as depicted in ***Figure 1.3***, lectin binding, and inhibition [22] amongst several other applications. The spike in interest of calixarenes can be attributed to the significant host-guest recognition of toxicological molecules, the ease of synthesis, the variable reactive sites, functionalizability, toxicity against microbes, porosity, and pore size control, amongst other factors [1].

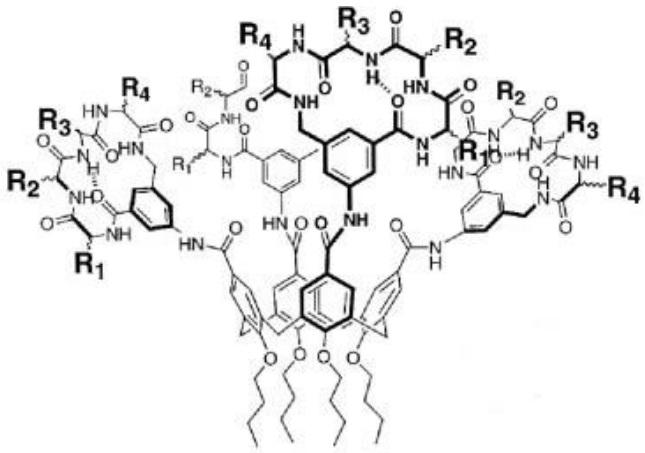

Figure 1.3: A functionalized calixarene that inhibits binding of vascular endothelial growth factor to its receptor [adapted [23]]

Native as well as functionalized calixarenes have been reported to form interesting host-guest inclusion complexes with a host of molecules including anthelmintics, antibacterial drugs, proteins, and pesticides in addition to reported antiviral, antithrombotic, antibacterial, antituberculosis, and anticancer activities [21,24–29]. The variety of aldehydes with varied functionalities that can be used to synthesize these calixarenes means that calixarenes with diverse functionalities can be obtained. Judicious choice of starting materials can, therefore, yield calixarenes that not only display porosity but may possess excellent potential to serve as secondary building blocks of other materials such as metal-organic frameworks.

1.3 Calixarene metal-organic frameworks

Owing to the -OH groups and the π-electron-rich aromatic system, calixarenes can interact with metallic ions in one of several ways, as depicted in ***Figure 1.4***. Interactions (c) to (f) have to do with ion recognition while (a) and (b) involve some anion complexation and generally lead to the formation of coordination complexes [23]. For this study, this section will focus on interactions involving either (a) or (b).

Native and functionalized calixarenes, resorcinarenes, and pyrogallolarenes have been reportedly used as MOFs building units. In such native species, coordination to the metal ion is usually through the phenolic oxygens but also through groups attached to the aromatic rings. Self-assembly of calixarenes and metal ions has led to the obtention of structures varying from simple 3D to cages and capsules. Structure and pore dexterity make these materials interesting candidates for variety of applications.

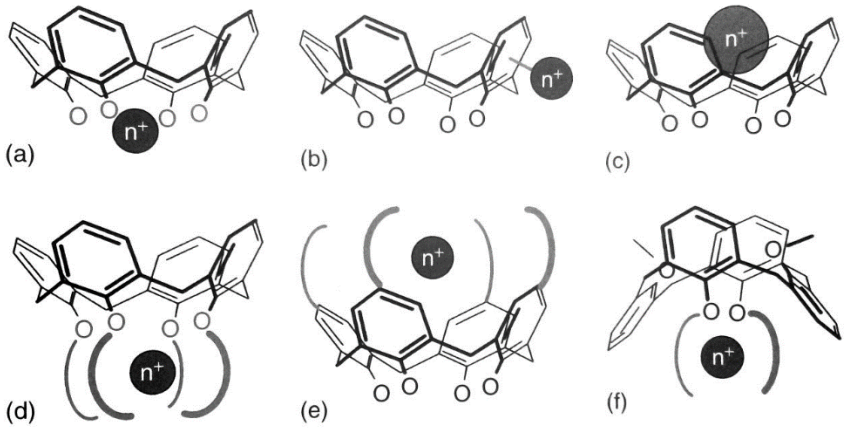

Figure 1.4: Interaction of metallic ion with calixarene [Adapted [23] pp 871]

By synthesizing carboxylate calix[4]arene and calix[5]arene uranyl MOFs Pasquale et al. [30]

demonstrated that calix[4]arene promote hexameric self-assembly while calix[5]arene on the other hand promotes icosahedral assembly depicted in ***Figure 1.5 a*** and ***b***. Single-crystal XRD of the nanoscale cage-like uranyl complex constructed from carboxylate functionalized calix[4]arene revealed a non-interpenetrating cage with each containing six subunits calixarene units and eight uranyl subunits. Due to the negative charge subunit, the cage acquired a negative charge and thus could host a polycationic counterion such as 1,4,7,10-tetraazacyclododecane. This occupied the cavity with a balanced charge while the empty space was occupied by unlocalized pyridine cations. The uranyl oxygen atoms are arranged perpendicular to the calixarene oxygens so that they define an octahedral environment around the metal atom. The anionic MOF exhibited ligand economy and possessed photoluminescence and photocatalytic activity. A similar carboxylate functionalized zirconium MOF with a six-fold-connected node of C_{3i} symmetry with a fourfold-connected calixarene linker C_2 symmetry has been reported by Schulz et al. [13]. The structure of the intertwined rod networks possesses accessible pores through each pore system with a maximum pore diameter of 5 Å. Gou et al. [31] reported a series of calix[4]resorcinarene cobalt-based MOFs containing an elegant nanosized Co_{16} coordination cage pillared by isophthalic acid derivatives (***Figure 1.5d***). The cages were found to have internal dimensions of 2.3 nm and 2.7 nm, respectively.

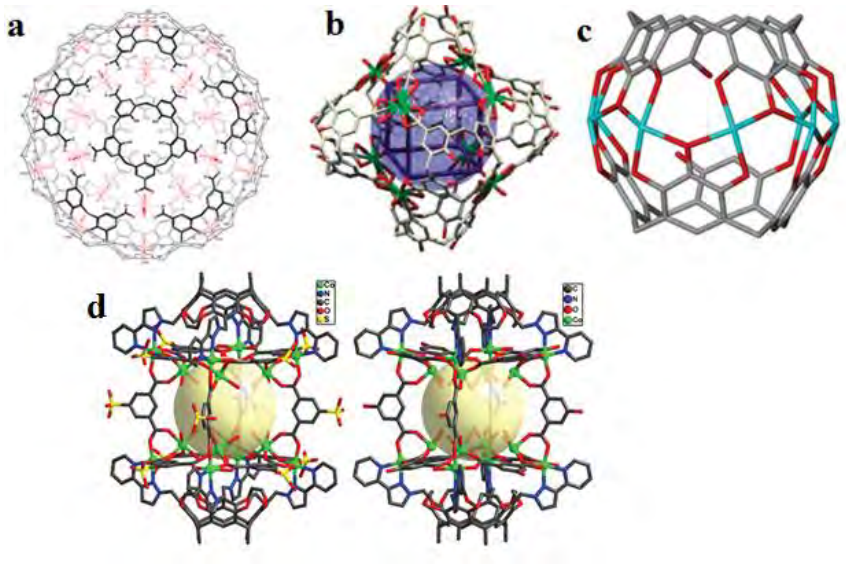

Figure 1.5: (a) Cage structure of uranyl MOF (b) cage structure of (a) with 1,4,7, 10-tetraazacyclododecane guest [30] and (c) hexameric pyrogallol/resorcinol Zn MOF [32] (d) Coordination cages with isophthalic acid derivatives as pillars [31].

Atwood et al. [32] obtained similar hexameric $M_{18}L_6$ zinc MOF nanocapsule using a pyrogallol[3]resorcin[1]arene mixed macrocycle (***Figure 1.5c***). The authors postulated that by introducing defects through replacing a pyrogallol with the resorcinol ring, it is possible to control the number of metal ions and the overall geometry and consequently, their properties. The idea of mixed macrocycles is motivated by the fact that most resorcinol moieties are unfavorable for coordination leading to metal-organic nanocapsules. The introduction of such defects in macrocycles involving pyrogallolarene and subsequent metal coordination has been reported by the group [32–39]. Similar work by Su et al. [40] has reported a pyrogallol[4]arene titanium monomeric bowl-like complex $T_{12}PgC_3$ with height and diameter being 1.5 nm and 2.2 nm, respectively. This complex showed the highest nuclearity for the calixarene family and could effectively catalyze methylene blue photodegradation. Theury et al. [41] prepared alternate stacking sodium and cesium-calixarene metal complexes in basic media. The sodium salt formed a 1:1 dimeric complex in which two metal ions bridged by the solvent molecules are sandwich between two monoanionic calixarene molecules. The cesium salt forms a polymeric structure in which the metal ions and the calixarene ligands are alternating. The coordination of the cesium ion to the calixarene is endo due to the absence of bulky substituents on the calixarene ring.

1.4 Cucurbiturils and cucurbituril based metal complexes

Cucurbiturils usually written as cucurbit[*n*]uril and abbreviated (CB[*n*]) [where "*n"* represents the number of monomer units] is a family of macrocyclic compounds constructed by assembling "*n*" number of glycoluril units with "*2n*" number of formaldehyde units, via condensation reaction of glycoluril and formaldehyde in acidic medium. Despite initial report on synthesis in the early 1900s, the structure of cucurbituril remained unsolved until seven decades later when Mock et al., [42,43] used NMR and X-rays techniques to characterize and determine the cyclic hexamer. By the 2000s Kimoon et al. [42] discovered that in addition to the cyclic hexamer, it is possible to obtain cucurbiturils with ring sizes varying from five to ten. This discovery broadened the scope and applications of these compounds prompting an increase in research focused on these materials. The name cucurbituril for this group of compounds was coined by Mock having determined the structure and found that it was akin to a "pumpkin-shape" depicted in ***Figure 1.6*** (which belongs to the botanical family Cucurbitaceae). The rigid and chemically robust skeletal structure of these

compounds is characterized by a hydrophobic interior cavity with carbonyl oxygen on both ends of the portals which render them electronegative.

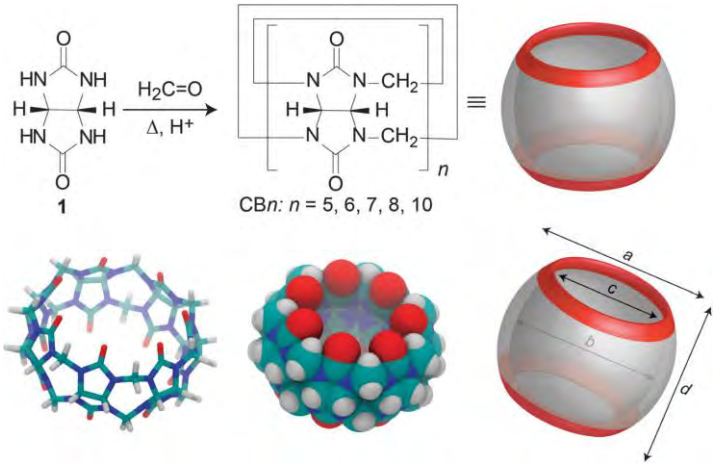

Figure 1.6: (Top)Synthesis of CB(*n*) homologues by condensation of glycoluril (1) and formaldehyde under acidic conditions. (Bottom) Different representations of the CB7 structure [44]

Table 1:1: Dimension of CB(*n)* homologues [44]

		CB5	CB6	CB7	CB8
Outer diameter	a	13.1	14.4	16.0	17.5
Cavity	b	4.4	5.8	7.3	8.8
	c	2.4	3.9	5.4	6.9
Height	d	9.1	9.1	9.1	9.1

1.5 Intermolecular interactions in calixarenes, calixarene based MOFs, cucurbiturils and cucurbituril based MOFs

Supramolecular chemists always desire to design and control the formation of intermolecular interactions to obtain materials with new structures and properties. These interactions are generally noncovalent and encompass a range of attractive and repulsive effects. A supramolecular system can, therefore, not be regarded as being the effect of a single interaction but rather an interplay of all these interactions and effects relating to both host and guest as well as their surroundings. In complex molecules, there are usually many types of interactions such as hydrogen bonds, π-interactions, van der Waals and hydrophobic interaction, which give rise to the observed structure and behavior. This section will review inter and intra interactions involving the calixarenes, calixarenes MOFs and cucurbiturils with or without guests. Even though we discuss these

interactions separately, it is worth reemphasizing that the overall supramolecular assembly is the consequence of the synergistic effect of all rather than individual interactions.

1.5.1 Hydrogen bond interactions

A hydrogen bond reflects the dipole-dipole interactions wherein a hydrogen atom covalently attached to an electronegative atom or electron-withdrawing group is attracted by the neighboring dipole on an adjacent molecule or functional group. It is conventionally written as "D-H···A" where D is the electronegative donor atom, and A is a similar acceptor moeity. It has been described as the "masterkey" interaction in supramolecular chemistry because of its relative strength [45]. Normal hydrogen bond energies are usually in the range of 4-60 kJ/mol and proportional to distance between interacting atoms in neutral molecules. The strength also depends on the angle between interacting atoms with the strongest interaction formed when interacting atoms are at an angle of 180^{o} and weakest at 90^{o} [19,45].

Due to the presence of phenolic groups, intermolecular hydrogen bonding in calixarenes can give rise to simple dimers or polymeric porous complexes. These interactions can be mediated by small molecules such as water, as in C-methylcalix[4]resorcinarene reported by Oliver et al. [46]. Two unique hexameric resorcinarene assemblies linked by water molecules into a heterodimeric, supramolecular assembly involving thirty-eight components held together by one hundred and twenty-nine intra and intermolecular hydrogen bonds were isolated in the same crystal structure (***Figure 1.7***). The structures each contained seven and eight water molecules per assembly with the former described as being partially collapsed. Similar cases involving hydrogen bonding interactions involving the hydroxy group have been reported by [47,48]. In the case of Cave et al. obtained a nanocapsule stabilized by distorted intermolecular hydrogen bond involving both the calixarene and the carbonyl function of the enclosed ethyl guest. The calixarene reported by Gerkensmeier et al. arrange in a head-to-head and tail-to-tail fashion in a structure stabilized by a combine total of 72 O-H····O hydrogen bonds involving the OH groups of the calixarene. The authors also found the presence of 16 acetonitrile solvent molecules in eacH unit cell which also take part in O-H····N hydrogen bonding of the acetonitrile and the calixarene.

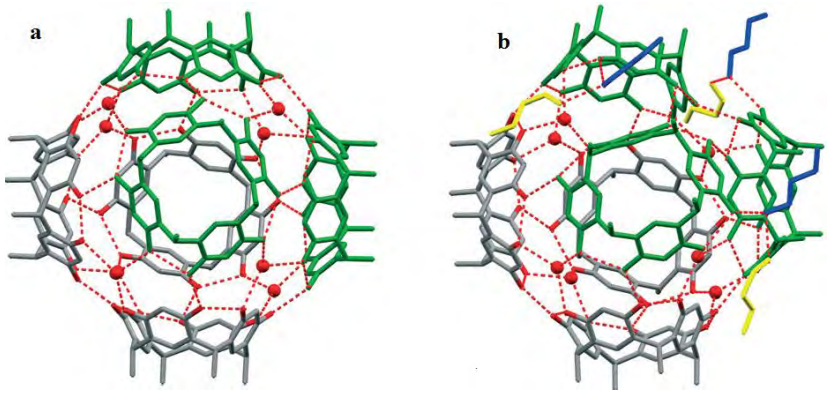

Figure 1.7: Hexameric (a) regular (b) irregular assembly with associated butanol guest [46]

Zafrani and Cohen [49] reported on Calix[4, 5]tetrolarenes macrocycles shown in ***Figure 1.8*** both adopting a pinched cone conformation with OH groups of the tetramer at the pinched end of the macrocycle and enhancing the hydrogen bond interactions. As opposed to the tetraoligomer, the pentaoligomer shows a more distorted structure wherein four of the five OH groups are tightly bound by a zigzag-like hydrogen-bond chain and the fifth OH group rather forming a hydrogen bond with the neighboring methoxy group. In the tetraoligomer however, all four OH groups are tightly bound by intramolecular hydrogen bonding which locks the structure as opposed to the free pentamer. The distorted hydrogen-bonding pattern in the pentamer gives rise to a less sterically hindered structure as opposed to the hindered tetramer

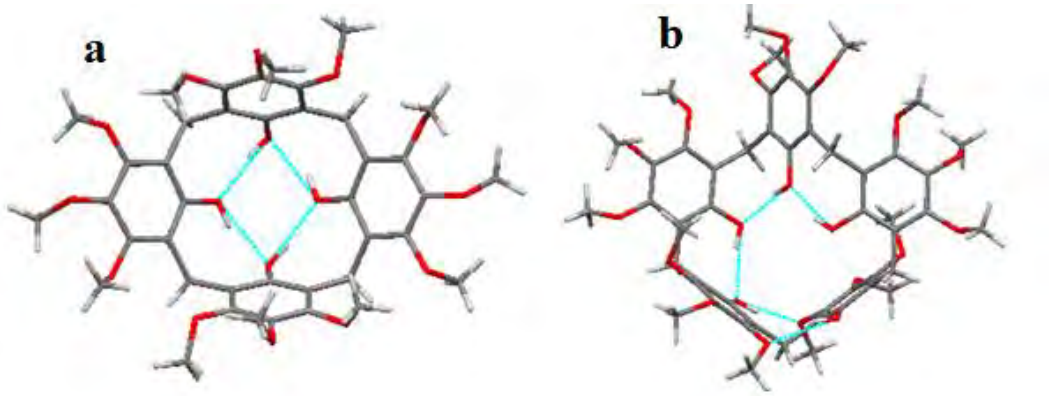

Figure 1.8: Top view of the (a) tetrameric and (b) pentameric structures with the hydrogen bonds indicated in sky-blue [49]

Atwood and coworkers [34] obtained a cobalt-seamed hexameric nanocapsule, [Co_{24}(*C*-pentylpyrogallol[4]arene)$_6$], wherein 48 of the 72 phenolic groups are deprotonated to form metal-coordination bonds, while the remaining 24 upper-rim phenolic groups hold the supramolecular assembly together via hydrogen-bonding. This bonding pattern revealed a structure comprising of

96 metal-oxygen coordination bonds and 24 intramolecular hydrogen bonding interactions of the O-H…O- type. It has also been shown that the presence of a host plays an important role in the formation host capsule. Previous work by the same group [38] reported a gallium pyrogallolarene with hydrogen bonding facilitated by metal coordinated water molecules. The metal-bound water molecules form hydrogen bonds with acetone guests within the asymmetric unit as well as with other water molecules but not with free water molecules. Similarly, Guo et al. [31] reported the existence of hydrogen bonding between guest sulfonic acid -OH and water molecules present in the open channels. The presence of water molecules in the channels supports the hypothesis that the presence of guest facilitates the formation of hydrogen bonds. Dawn et al. [25] reported on a resorcinarene gatifloxacin complex stabilized by multiple interactions of hydrogen bonding, π-alkyl, acid/base, and charge-transfer interactions. The perfect interplay of these interactions stabilized the complex in both the solid and solution phase. Alkyl-π interactions and hydrogen bonding led to the respective downfield shift of the methyl protons in the gatifloxacin and broadening of the resorcinarene hydroxyl peaks in the H-NMR.

In the case of CBs, their electrostatic potential map shows high electron density at the carbonyl oxygens illustrating their ability to bind to cation [44,50]. Their inner cavity, on the other hand does not have either electron pairs or functional groups directed towards the inside. This renders impossible the formation of hydrogen bonding between CB molecules. Most hydrogen bonding interactions in CBs involve the presence of guest molecules. With portals being electronegative and the cavity being hydrophobic, most interactions in cucurbiturils, especially involving guests are those that involve a positively charge species [50]. Generally, CBs will form stable inclusion complexes stabilized by a combination of interactions including ion-dipole, hydrogen-bonding, and hydrophobic interactions [51]. The electronegative carbonyl oxygen atoms serve as a good acceptor for a hydrogen bond interaction. Cong et al. [51] investigated a host-guest complex involving isoniazid (INH) with CB6 and CB7 and found that, when INH interacts with CB6, the pyridyl moiety lies on the outside as opposed to inclusion in the cavity of CB7. These complexes are stabilized by hydrogen bonding interactions involving the portal oxygen atoms and the hydrazide hydrogens of the INH as indicated by the molecular models. The optimized structure of the CB6-INH has four sites for hydrogen bonding and CB7-INH has two sites for hydrogen bonding; this multisite interaction was proposed as the reason for the extra stability of the CB6-

INH complex when compared to CB7-INH despite the host residing on the outside. Kim et al. [52] have observed strong C-H···O hydrogen bonding interactions between the portal carbonyl groups and CH or CH_2 groups of CB6 molecules is responsible for the distorted square geometry of the obtained crystals. Shen et al. [53] reported OMCB6-M-Hydb (OMCB = octamethyl-substituted cucurbituril; M = Na, Cs; Hydb = *p*-hydroxybenzoic acid) complexes. The Hydb coordinated through the OH group such that the carboxylate end is left free for eventual hydrogen bonding as depicted in ***Figure 1.9***. The resulting supramolecular system involved an interplay of hydrogen bonding and ion-dipole interactions wherein the carboxyl groups of the coordinated Hyb molecules interact with neighboring coordinated water molecules and coordinated Hyb molecules through hydrogen bonding to form a supramolecular chain.

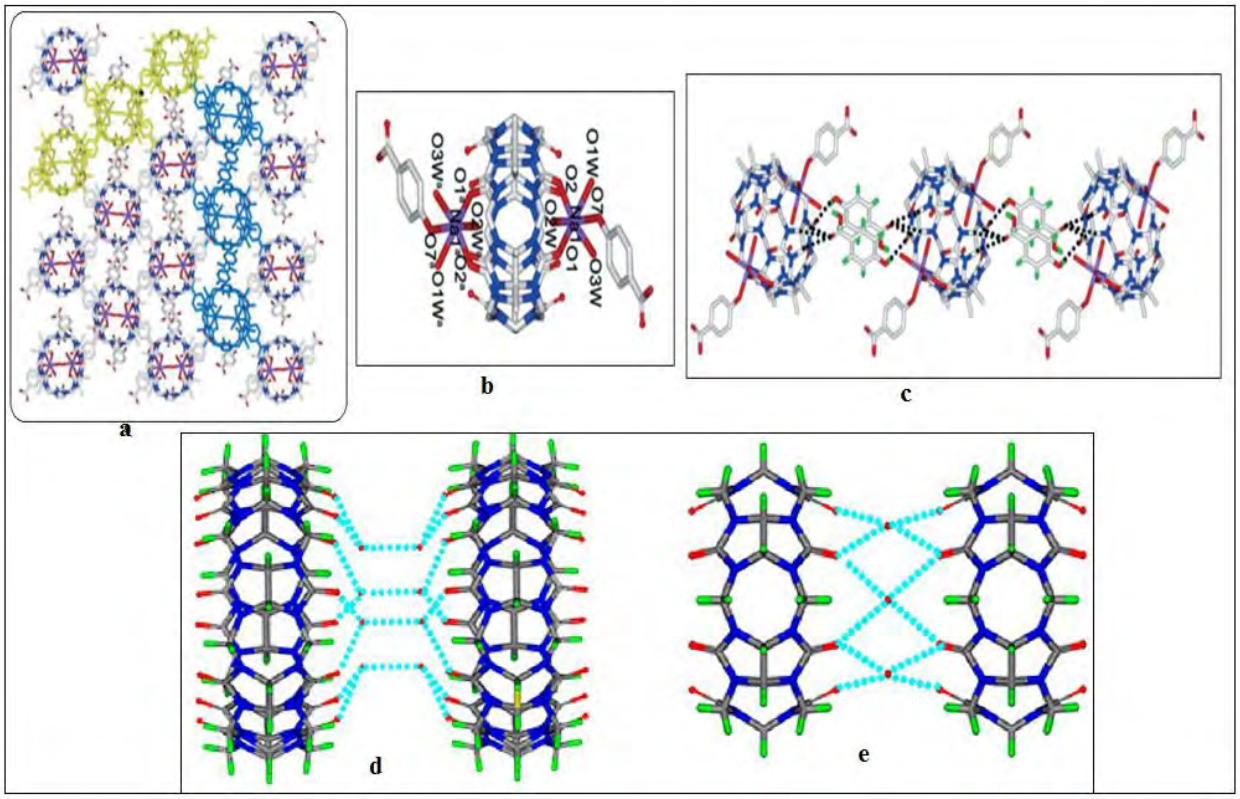

Figure 1.9: (a) Overall view of the OMCB6-M-Hydb supramolecular assembly (b) OMCB6-Na-Hydb showing the Na and Hydb (c) OMCB6-Na-Hydb complex showing the hydrogen bonding interactions [54], unusual hydrogen bonding in (d) CB8 and (e) CB6 [55]

Bardelang et al. [56] investigated outer-surface interactions between cucurbiturils and inorganic anions and the ensuing supramolecular assemblies and observed that nitrate or chloride favor the formation of 1D nanotubes stabilized by an unusual hydrogen bonding across CB6 and CB8

(shown in ***Figure 1.9d*** and ***e***) involving the anion and methylene groups. Ni et al furthered the investigation using inorganic anions of transitions some metals and found that in addition to the unusual hydrogen bonding, outer surface interaction is also driven by ion-dipole interactions involving the satellite anions and the portal carbonyl oxygen atoms.

1.5.2 Π-interactions

Interactions involving π systems are common in many compounds and play an important role in supramolecular chemistry. The π electrons of aromatic systems usually can form one of four types of interactions:

- π-π interactions equally known as π - π stacking interactions
- π- alkyl interactions
- π- cation interactions and
- π- anion interactions.

When an electron-rich aromatic ring interacts with a relatively electron-deficient aromatic ring it gives rise to π-π stacking interactions. These π-π stacking interactions in supramolecular structures can be characterized by strong binding energy from delocalized collective charge fluctuations in contrast to complexes where other types of bonding are present [57]. Such interactions may be classed based on the orientation and angles of approach of the aromatic rings. A face-to-face interaction occurs when the interacting rings lie parallel to each other while an edge to face interaction occurs when the rings are at right angles. Intermediate angular arrangements are also known to result in similar interactions.

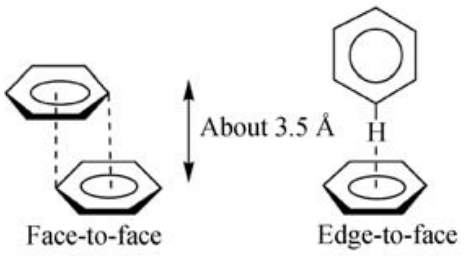

Figure 1.10: Different types of π-π interactions [45]

Face-to-face stacking is said to responsible for the slippery feel of graphite and the stabilization of DNA double helix [45]. It is worth mentioning here that despite referring to π-π interactions as face-to-face stacking, the interacting the rings are usually displaced (ash shown in ***Figure 1.10***) not as usually incorrectly assumed. Additionally, they are also known to play important roles in protein folding, molecular recognition, template-directed synthesis and assembly of variety van der Waals supramolecular architectures in both biological and artificial systems [57]. The presence

of aromatic moieties in calixarenes means that π- interactions are common. A typical example of face-to-face or centroid to centroid π - π stacking has been demonstrated by Gou et al. [31] where centroid-to-centroid and centroid to-plane distances are 3.68 and 3.37 A° based on the pyridine moieties leads to π - π interactions of adjacent [Co_{16}] coordination cages and result to the formation of the supramolecular layered structure shown in ***Figure 1.11***. A similar kind of π - π stacking system has been reported by Zheng et al. [58] who prepared NH_3-Ag^+-NH_3 calixarene complexes where the cation is trapped as guest. Each calix[4]arene interacts with two neighbors through aromatic π stacking giving centroid/centroid distance of 3.901 A°. N-H··· π interactions were also observed between the hydrogen of the silver complex and π systems of the aromatic ring.

Park et al. [59] obtained Pt^{2+} metallogel of tetra terpyridine functionalized calixarene prepared in DMSO/H_2O mixture. The proposed gel formation which depends on amount of water used occurs through a self-assembled network structure by intermolecular interactions such as π-π stacking and MLCT resulting in aggregation. Solvent formulations of H_2O/DMSO (7:3 v/v) gave the strongest π-π stacking and MLCT interactions as indicated by longer luminescence lifetimes. These π-π stacking interactions were also found to be stronger in the self -assembled solid than the gel due to the presence of solvent molecules between the gelator molecules. This suggests that such interactions can be enhanced by the presence of secondary molecules which affect the strength of the interactions.

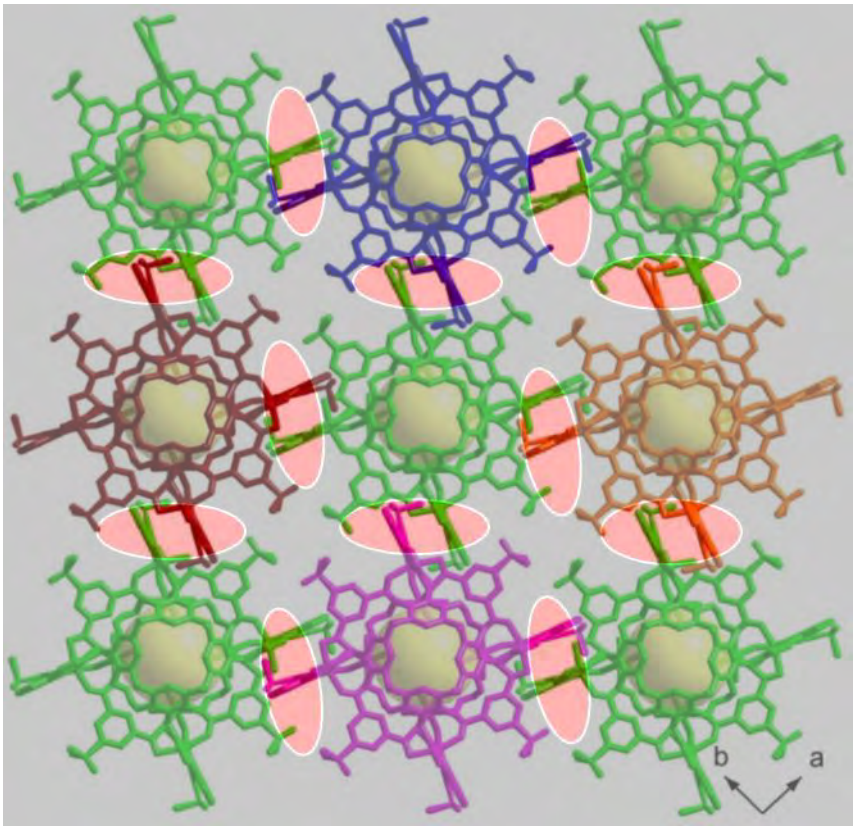

Figure 1.11: Π - π stacking in supramolecular assembly. The stacking sites are indicated in red ovals in the background[SI of [31]]

Π–π stacking interactions have also been observed in cucurbiturils. Chen et al. [60] reported on CB6 based supramolecular assemblies for applications in radioactive cesium capture. The polyaromatic compound 4,4',4"-benzene-1,3,5-tribenzoic acid (BTBH) was employed as a directing agent to obtain supramolecular assemblies based on both CB6 and CB7. A mixture of the CB, BTBH and NH_3 resulted to a π-π stacking and C-H·····π supramolecular assembly where the CB units are sandwiched between two BTB- units. The NH_4^+ ion resulting from the deprotonation of the acid and NH_3 forms cation dipole interaction and hydrogen bonding with the portal carbonyl oxygen atoms of the CB. Similar type of π-π stacking has also been reported by Ni et al. [55] who explored self-assemblies based on outer surface interactions of CB(*n*)s. The account which details outer-surface interactions involving CB(*n*)s with a series of species indicates that the carbonyl oxygen of the glycoluril unit in the CB will always form π-π stacking and C-H·····π bonding when there is π system within the supramolecular assembly. The authors demonstrated this by obtaining supramolecular assemblies of CB(*n*) and 4-sulfocalix[4]arene, hydroquinone, and p-hydroxybenzoic acid.

Despite less common, another type of interaction is π – alkyl which originates from the interaction of an aromatic ring with an alkyl group. This kind of interaction arises from a difference in electron density between an alkyl group and an aromatic ring. As seen in ***Figure 1.12***(d) there is a π – alkyl interaction between the resorcinarene aromatic ring and the methyl substituent on the host.

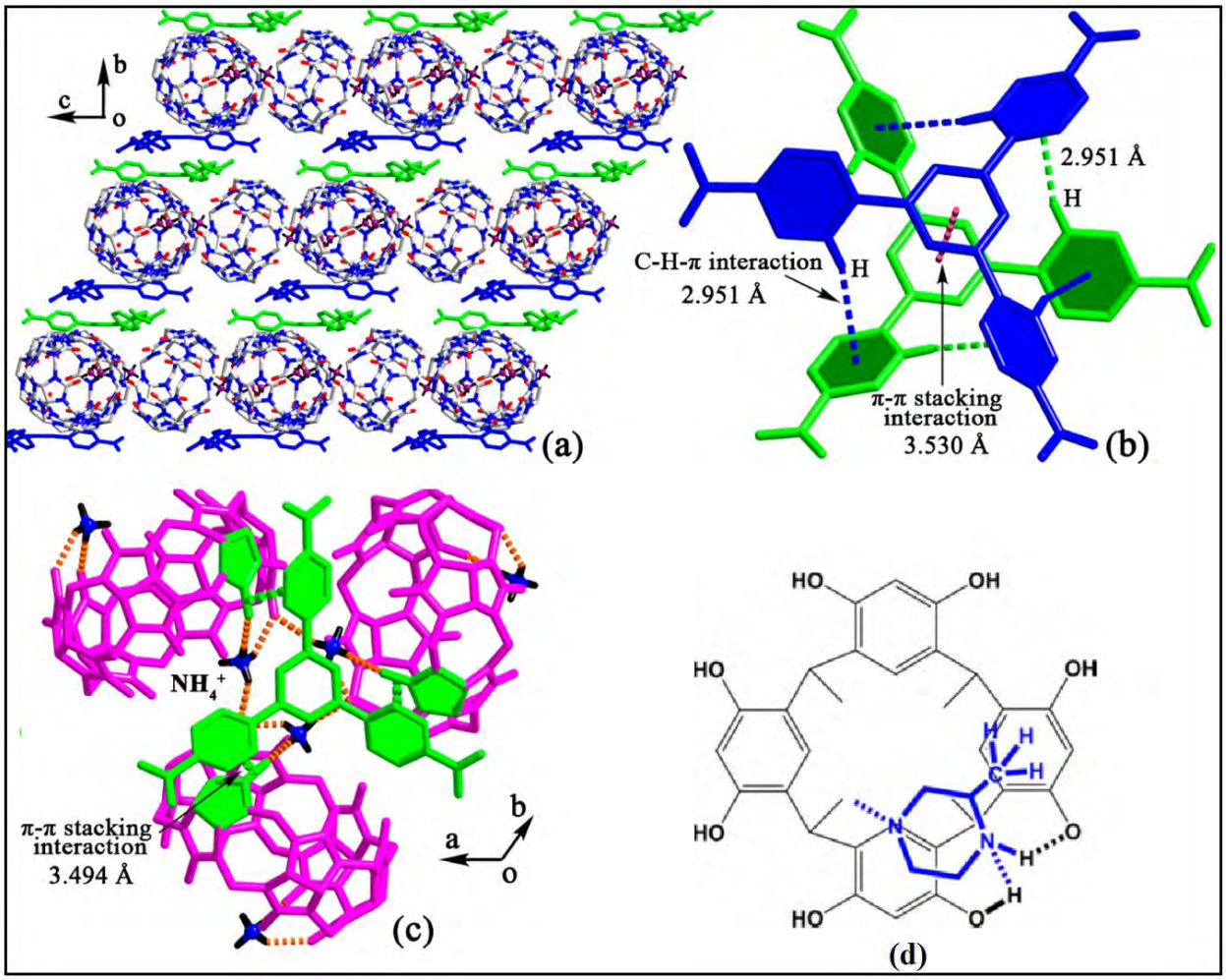

Figure 1.12: (a) Overall structure of CB-BTBH assembly (b) Assembly of CB-BTBH showing π–π stacking and C-H····· π intermolecular interactions (c) Assembly of CB-BTBH showing π–π stacking and NH_4^+ CB interactions [60] (d) C-H····· π intermolecular interactions involving a calixarene/host complex [25]

A similar kind of interaction has been observed between the methyl group of the acetonitrile guest trapped in the cavity of pyrogallolarene with CH···aromatic centroid distances of 2.562 and 2.974 A°[61]. By encapsulating 3-methylpyridine, they demonstrated the presence of π-alkyl interaction between the methyl group of the pyridine and aromatic ring of the host zinc-seamed pyrogallol[4]arene molecular capsules.

Another type of interaction is the π-cation which results from the interaction of aromatic π electrons with a cation for example ferrocene [$Fe_2(C_5H_5)_2$]. The partial donation of π electrons into the empty orbitals of the cations such as transitions metals somewhat disqualifies such interactions from being considered as non-covalent. It is worth noting however, that these interactions do not only involve metallic cations but also involve non-metallic inorganic and organic cations such as NH_4^+ and RNH_3^+ respectively. Such π-cation interactions are common in calixarene based supramolecular assemblies. As a proof of concept, [62] synthesized gallium-pyrogallolarene seamed porous structure and trapped thallium, Tl ions within. The entrapment of the Tl^+ ions occurs via Tl-π interactions facilitated by such factors as ionic radius and shorter cation-π (centroid of pyrogallol) interaction distances. These interactions were found to be sufficiently strong to maintain the Tl ions within the structure in both solution and solid - state to such extent that even titration with Zn ions did not lead to the release of the Tl ions, as indicated by NMR data. Parallel studies by Thuery et al. [41] have indicated the presence of cesium-π bonding by a calixarene with the cation complexed in endo fashion and the interaction facilitated by absence of bulky para substituents on the calixarene.

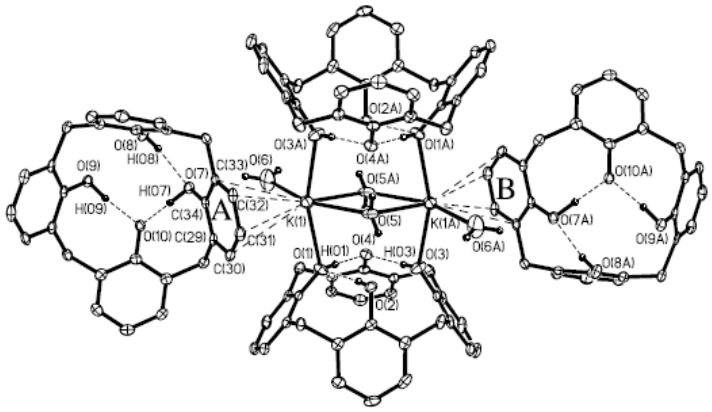

Figure 1.13: Cation – π interaction between K and the aromatic ring indicated in doted lines) [adapted from ref [63]]

Figure 1.13 shows another case where cation-π interactions are observed [63]. The bridging K^+ ions are coordinated to the calixarene through the phenolic oxygen and to each other through bridging water molecules. Opposite metallic ions then interact with aromatic rings of neighboring calixarenes. Cation-π interaction is evident in the work of Orda-Zgadzaj et al. [64], who synthesized a series of calixarenes and introduced various organic cations as guests (***Figure 1.14***). The interaction of the cations with the π electrons led to the formation of a charge-transfer complex due to the transfer of charge from the π system to the cations indicated by color change in the

aryltropylium salt. They found that the guest molecule can interact with the cationic end either being in or outside of the cavity. However, having the cationic end of the guest inside the pore of the host leads to more stable guest complex indicating the stronger interactions that occur between the positive end and the π system of the calixarene.

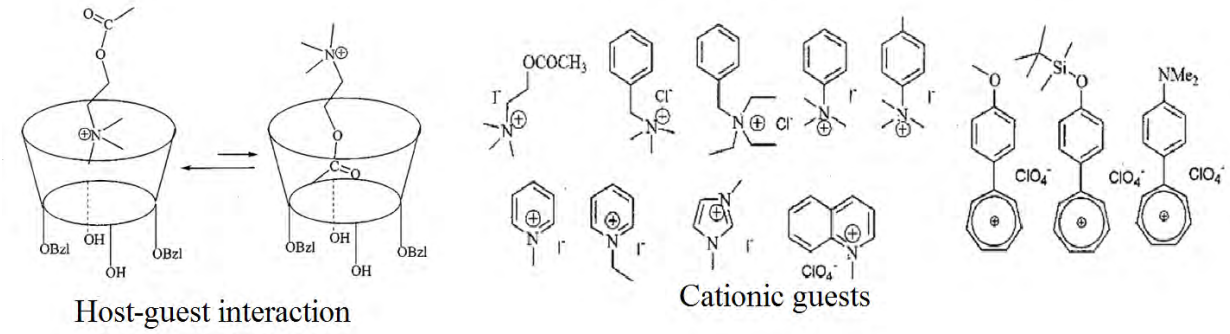

Figure 1.14: Host-Guest interaction and the different cationic guests [64]

Similar work has also be carried out by Imonigie and Macartney [65] who investigated the inclusion of (Ferrocenylmethyl)trimethylammonium complexes in para-sulfonated anionic calixarenes. As in the case of the work carried out by Orda-Zgadzaj et al. the host-guest complex here is also stabilized by the charge transfer from the π system to the cations, in a lock-and-key kind of interaction.

The rich electron cavity of calixarenes implies that while they can conveniently host cations and neutral molecules, anion are not suitable guests. If the calixarene is, however, π-metallated on the outside of the macrocycle or modified with some electron-withdrawing group, conditions are created for endo-inclusion of anions [23]. It has been shown that η-metallation leads to an increase in the size of the cavity and thus, the possibility of inclusion of larger guest [66]. Not only can this approach be used to encapsulate larger guest for a given macrocycle, but it can also potentially be used as molecular switch through switching η-metallation. Rosokha et al. have noted evidence which suggest that anion-π interactions can be used to design and exploit artificial receptors for anions. Additionally, although it is generally thought that the interaction of an aromatic ring with an anion should be repulsive, an overall charge difference between the centroid of a neutral aromatic ring and an anion usually leads to an attractive interaction. They further stressed that, this charge difference can lead to potential charge transfer and consequent formation of charged complexes which are generally characterized by color changes especially when transition metals

are involved [67]. Wang and Wang [68] investigated non-covalent interactions involving electron deficient tetraoxacalix[2]arene[2]triazine and a range of anions including NO_3^-, BF_4^-, PF^-_6, and SCN^-. These anions form complexes with the tetraoxacalix[2]arene[2]triazine with the stability constants increasing in the order $NO_3^- > BF_4^- > PF^-_6 > SCN^-$ (***Figure 1.15***). The complexes are stabilized by a synergic combination of anion-π and lone pair electron-π interactions between halide and triazine centroid and between the oxygen of water and the centroid of the triazine [68].

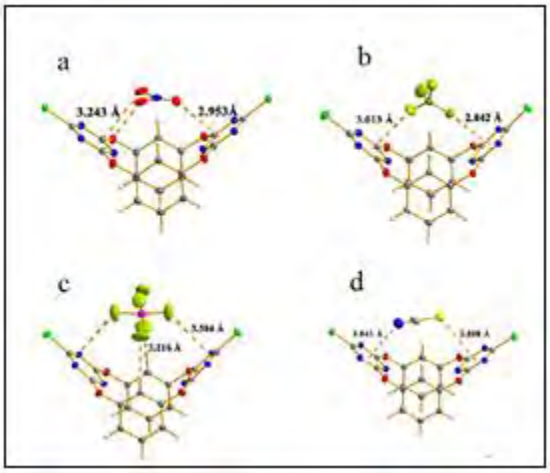

Figure 1.15:tetraoxacalix[2]arene[2]triazine complex of (a) NO_3^- (b) BF_4^- (c) PF^-_6 and (d) SCN^- [68]

The concept of obtaining exterior π–metallated complexes and subsequent inclusion of anion was exploited by the Steed group [69] who obtained endo inclusion complexes of anions and cations in π–metallated cyclotriveratrylenes which are similar compounds to calixarenes. The inclusion of anionic species such as BF_4^-, ReO_4^-, $CF_3SO_3^-$ and $CF_3CO_2^-$, within host cavity was achieved by having two transition metal ions on the outside of the cavity bound to the π electrons and reducing the electron repulsion within between the anion and these electrons. The resulting anion-π interaction yielded host-guest complexes. Similar follow- up research by the same group [70] on calix[4]arene revealed similar kind of interaction within the cavity with a higher binding constant of the anion within the cavity compared to that in the cyclotriveratrylene ascribed to the size match. Fairchild and Hayes [66] reported a cryptophane-anion complex whose exterior is that η-metallated with Ru (***Figure 1.16***). Size and anion-π interactions proved pivotal in stabilizing the structure as too small or too large anions are less tightly bound (***Figure 1.16b*** and ***c***). Fochi et al. [71] reported on a series of cavitand based coordination cages wherein the cavitands were complexed with Pd or Pt ions. The self-assembling compounds crystalized with an anion and in

some cases solvent molecules enclosed in the pore. In the case of triflate anions, weak interactions resulted in triflate-resorcinarene distances in the range of 2 - 3 Å.

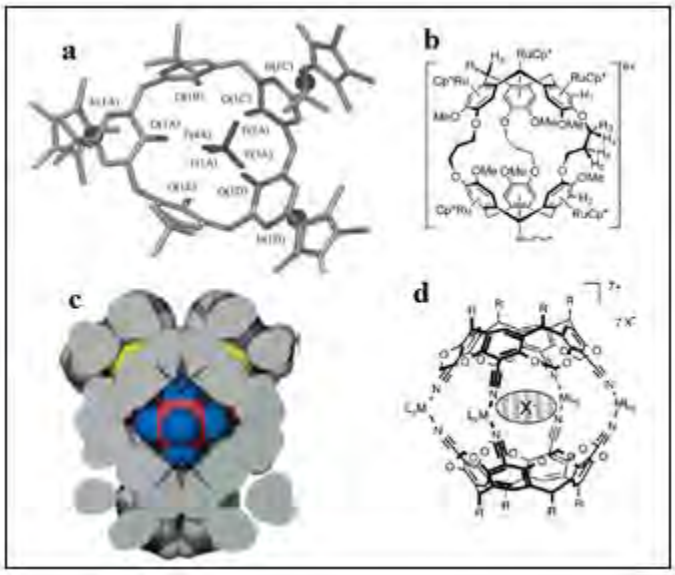

Figure 1.16: (a) SXRD structure of trimetallic p-tert-butycalix[4]calixarene complex showing tetrafluoroborate guest [70] (b) Cp-Ru-calixarene complex XRD structure (b) Vertically sliced view of the capsule in (b) with SbF6 as guest; dashed blue lines indicate closed contacts [(b) and (c) [66] (d) inclusion of anionic guest in resorcinarene based metallo-cavitand [70]

1.5.3 Van der Waals interactions

These are electrostatic attractive interactions resulting from polarization of an electron cloud around a molecule or atom by the nearness of an adjacent nucleus [45]. Unlike hydrogen bonds, the van der Waals force is non-directional. Two main determinants of van der Waals interactions are nearness and polarizability. Two very close and easily polarized molecules are more likely to experience some van der Waals interactions. The strength of these interactions is directly proportional to surface area and decreases as a function of distance to the negative 6^{th} power and is additive with every bond in the molecule contributing to the overall interaction energy [19,45]. These interactions come to light in supramolecular chemistry when the inclusion of small non-polar molecules is concerned. Van der Waals interactions however do not occur in isolation but synergy with other interactions and play an important part in directing self-assembly of supramolecular structures. The molecular structure of calixarenes presents a hydrophobic nano environment constructed from van der Waals interaction. This causes them to display well-defined and near constant shape and size which makes it possible to form inclusion complexes with small

organic molecules [72]. Although van der Waals interactions are generally weaker compared to other noncovalent interactions such as hydrogen bonds, they are interesting because they are capable of collectively potentially creating relative stabilities in many structures to enable guest exchange and chemical transformations inside the cavities of porous materials [72]. As a proof of concept of the stabilizing effect of such interactions, Ananchenko et al. [72] investigated the van der Waals nanocapsular complexes of amphiphlic calixarenes containing alkanoyl chains with tetrahydrofuran as guest. The calixarene arranges in a tail-to-tail fashion with the tetrahydrofuran trapped within and the layers held together by hydrogen bonds when the alkanyol chains are shorter as represented in ***Figure 1.17***. However, if the alkanoyl chains on the calixarene host are longer than required to encapsulate a single guest molecule but just long enough to encapsulate two tetrahydrofuran guests, hydrogen bonds become disrupted. When this happens the main stabilizing intermolecular interaction becomes the van der Waals which binds the two calixarene layers and enables complex formation. They also found that when the alkanyol chain becomes too long - $C_{10}OH$, van der Waals interactions are so strong that the guest cannot compete, and the addition of hydrogen bond is required to stabilize the calixarenes.

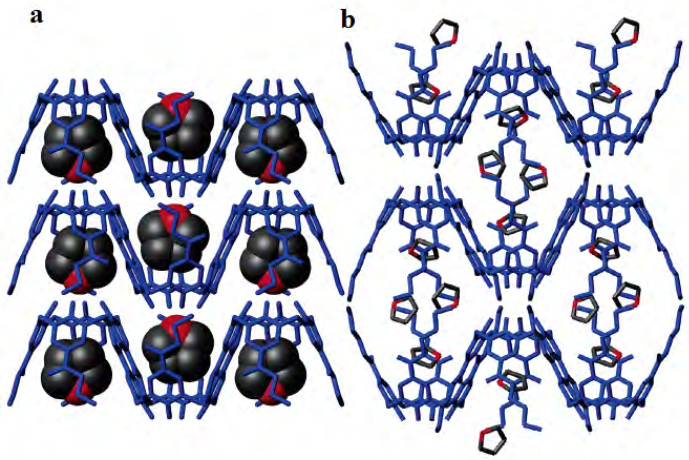

Figure 1.17: (a) No calixarene capsule due to the short chains; only one guest molecule is present (b) Calixarene capsule stabilized by van der Waals interactions with two guest per molecule [72]

In a similar development, Thompson et al. [73] investigated the adsorption of butanol on silica-supported calixarene with similarly appended alkyl chains as found in the case by Ananchenko et al. With the calixarene anchored to the silica through the hydroxyl groups leaving the alkyl substituent exposed Thompson et al. found that starting from H-calix[4]arene-SiO_2 and replacing

the H with alkyl rings leads to an increase in adsorption of butanol with the amount of butanol adsorbed directly proportional to the length of the alkyl chain. This increase in the amount of butanol adsorbed was ascribed to the increase in mainly van der Waals strength resulting from increase in alkyl chain length. The possibility of other interactions such as OH-π and CH-π was however, not overruled given the fact that with the H-calix[4]arene-SiO_2 some adsorption was still noticed. Van der Waals interactions are generally not very common in metal complexes of calixarenes; however, if these calixarenes contain alkyl groups, these interactions can occur. This has been typified in the Cs complexes reported by the Atwood group who observed that the "lower rim" C-hexyl chains of pyrogallol[4]arenes generally interdigitate to make the most of van der Waals interactions in bilayer arrangements of O-alkylcalix[4]arenes, resorcin[4]arenes, or pyrogallol[4]arenes [61].

As with calixarenes, van der Waals interactions can also be found in cucurbituril supramolecular systems and are common in host-guest inclusion systems in which they can act as driving force for complexation [74,75]. A theoretical investigation of host-guest complex formation between C_{60} fullerene and CB[9] cucurbituril has highlighted van der Waals interactions as the main stabilizing force [76]. Hoe et al. [77] obtained a honeycomb cucurbituril MOF with extended hexagonal channels and stabilized by a combination of van der Waals interactions between the coordination polymer chains arising from curvature and hydrogen bonds facilitated by water molecules in the channels.

1.6 Synthetic approaches to calixarenes and calixarene based MOFs

1.6.1 Calixarenes: synthesis and embroidery

Calixarenes are generally obtained by the condensation of either phenol, resorcinol, pyrogallol, or phloroglucinol or their derivatives with an aldehyde in the presence of either an acid such as HCl or a base such as NaOH or transition metal as catalyst [16,17,78,79] as shown in ***Scheme 1.1.*** The reaction can be carried out either by refluxing the reagents or by mechanical grinding although the former is most common. Over the years, the synthesis has gone beyond native calixarenes to embroidery of these compounds to afford them with desired characteristics. This section will preview some the embroidery of calixarenes.

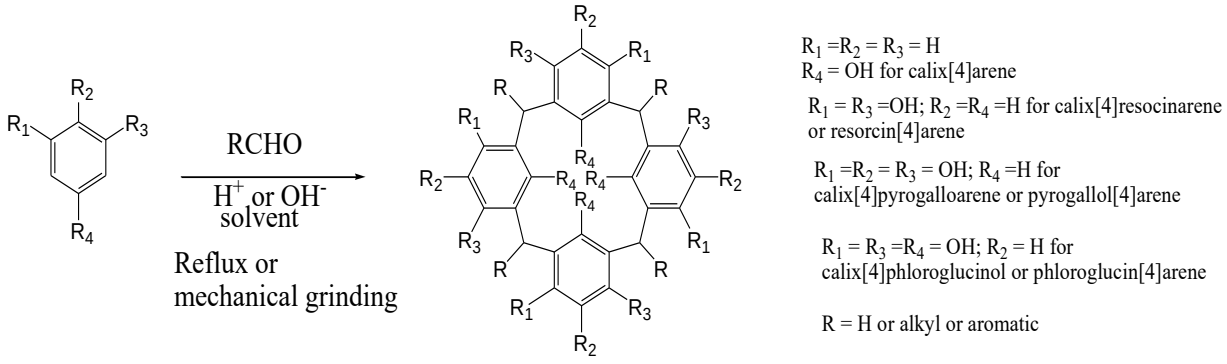

Scheme 1.1: Synthesis of calixarenes

As stated earlier, calixarenes can have ring sizes ranging from 4-20 with the tetramer being the most common and easily synthesized. One step condensation with phenol derivatives and aldehydes gives good yields and purity of calixarenes with even- numbered rings (n = 4, 6, 8); odd number (n = 5, 7, 9) rings can also be obtained by this method, though in low yields [45]. Otherwise, the best approach to obtaining ring sizes other than n = 4 is by a stepwise approach. The identity of R can vary from hydrogen to either aromatic or other alkyl substituents; this has been varied in different synthetic approaches to alter the properties of the resulting calixarene.

Calixarenes analogues have been obtained from other aromatic hydroxy derivatives like bisphenols, diphenylphenol, 2-methoxyazulene, naphthol (amongst others) as can be depicted on the ***Figure 1.18***.

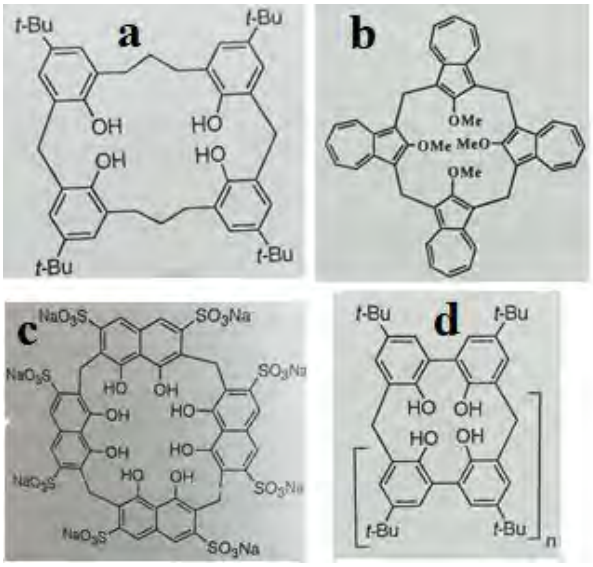

Figure 1.18: Other calixarene analogues synthesized from diverse starting materials [16]

The host-guest complexes of many calixarenes are usually so unstable that modifications are necessary. Because native calixarenes may not always posses the desired characteristics, different

approaches have been used to modify them to achieve these characteristics. These approaches include synthesis of calixarenes capsules including cacerands and cravitands, and post-synthetic modifications.

The regidification of resorcinarenes by inserting alkyl, silyl, oxo, phosphoryl [23,78], aromatic [80] bridges between the oxygen atoms at the lower rim leads to cup-like shaped structures with deep cavities exceeding 4 $\mathring{A}$. Such ether structures are known as cavitands (**Scheme1.2**). The synthesis of these structures usually proceeds via heating the resorcinarene and respective reagent in the presence of an appropriate base and solvent. Although the term cavitand was initially coined for resorcinarenes and their derivatives, the scope has since expanded to include calixarenes with enforced cavities large enough to accommodate guest molecules [23]. Cavitands possess permanent intramolecular cavities and give rise to host-guest complexes which exist both in solution and solid-state.

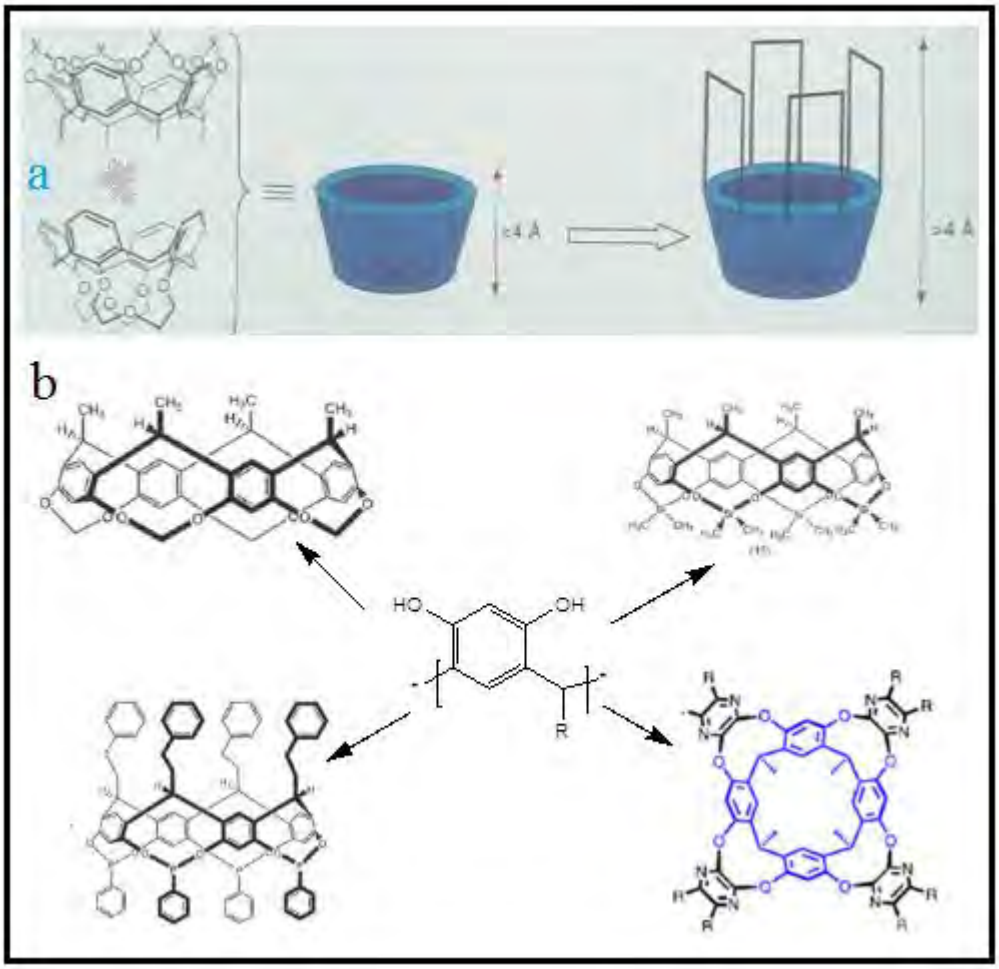

Scheme 1.2 (a) Increasing pore depth in calixarene to obtain a cavitand [23] (b) synthetic scheme for cavitands [45]

Following the success of his work on cavitands, Cram an coworkers sought to obtain a new and diverse class of molecules, a process that lasted until six years until the first report on this new class of molecules known as carcerands [78]. Carcerands (***Figure 1.1***) contain two pyrogallolarene or resrocinarene with a covalent bridge either through carbon or sulfur atoms. Unlike cavitands these molecules permanently imprison their guest and release thereof can only happen if the structure is ruptured [78].

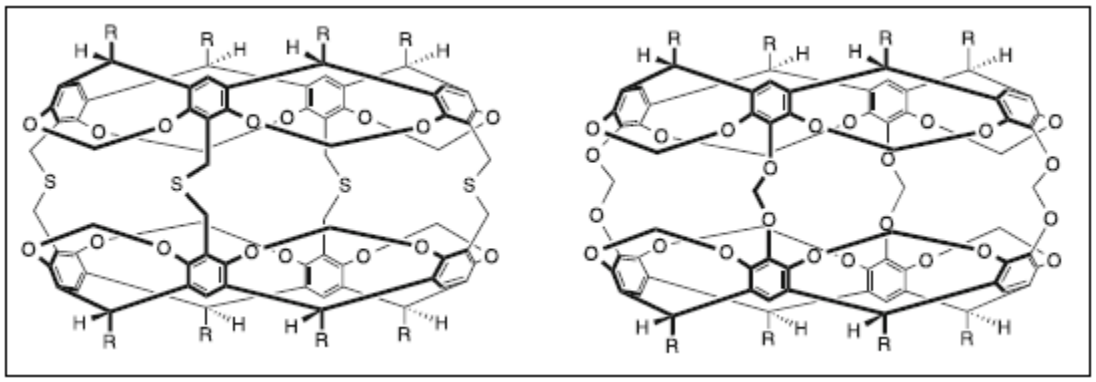

Figure 1.19: Sulfur and oxygen bridged carcerand [78]

Just like their cavitand counterpart, carcerands are synthesized using dihalogenoalkane such as bromochloromethane or dichloromethane or sulfur-containing group such as CH_2SH [78]. Other than bridging the lower rim oxygens, ethers and esters have also been prepared by adding various reagents to react with the lower rim phenolic groups. An interesting carcerand-like compound has been reported by Fochi et al. [71] in which the cavitand moieties are rather bridged by metal ions. The metal ions attach to the cavitand through the nitrogen atom of a nitrile group attached to the second position of the resorcinol ring of the calixarene. The nanocages formed via self-assembly through the slow evaporation of dichloromethane at room temperature, affirming the assertion by Avram and Cohen [81] that chlorinated solvent seems to facilitate the process of self-assembly. Schultz et al. [13] and Park et al. [59] reported a functionalization strategy where the phenolic groups were etherified with ethyl bromoacetate and a series of subsequent steps afforded desired ligands.

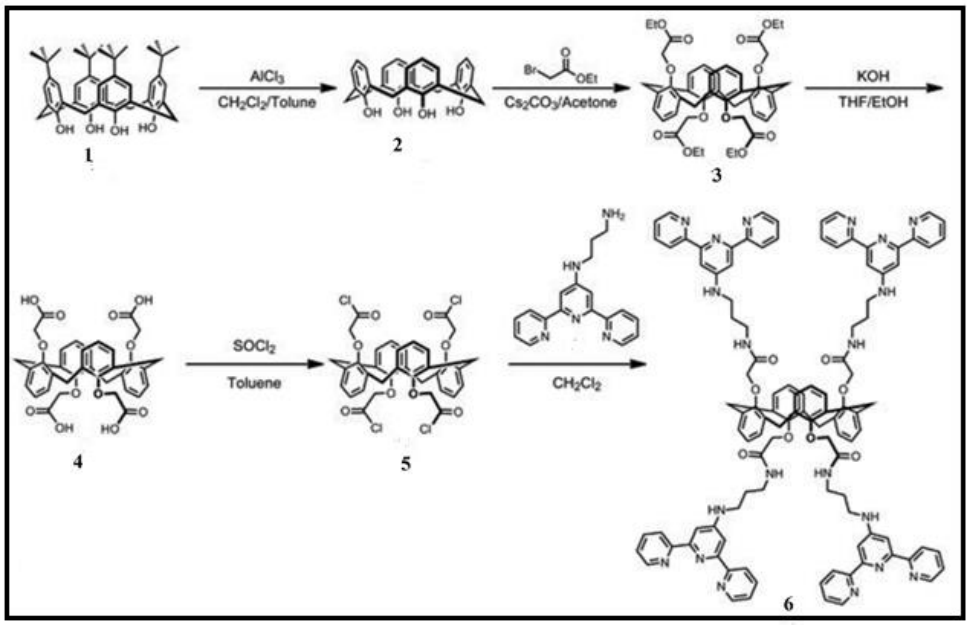

Scheme 1.3: Synthetic procedure for calixarene derivatives [59]

While Schultz et al. [13] exploited **4** (shown in **Scheme 1.3**) as ligand for Zr MOF for selective detection of NO_2. The group further modified **4** to **6** as a precursor for Pt -gels. A more detailed exploration into lower rim etherification and esterification has been treated by Gutsche [16,17].

Another post-synthetic approach that has been extensively exploited is the appending groups on the upper rim of the calixarene ring. Modification at the upper rim may proceed through one of the following well-known reactions, including electrophilic substitution, dealkylation of *p*-alkylcalixarenes, *para*-Claisen rearrangement, *para*-quinone methide. The focus in the current section stands however, not to deal with these elaborately but rather to give examples where functionalization at the upper rim has been carried out (the reader is once again referred to Gutsche for reviews and details). When using calixarenes as MOFs ligands, chemists are always on the lookout on strategies to introduce extra functionalities and groups such as carboxylates capable of binding to metal ions in addition to the OH groups. This is a result of the consequent dexterity of the resulting MOFs containing such additional metal-binding groups. Pasquale et al. [30] have used a two-step procedure (**Scheme 1.4**) that involves formylation with hexamethylene tetraamine (HMTA) and trifluoroacetic acid (TFA) and subsequent reduction with a mixture of $NaClO_2$ and NaH_2PO_4 to obtain carboxylate functionalized calixarene ligand for MOF synthesis.

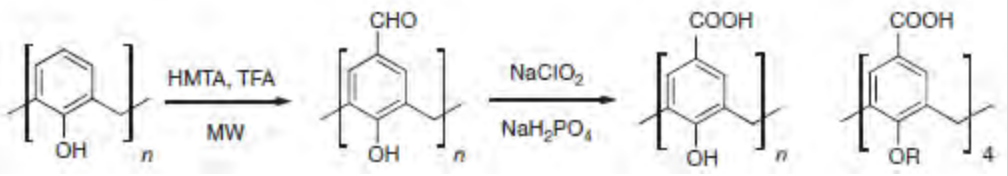

Scheme1.4: Upper rim carboxylate functionalization of calixarene

In a rather different approach, Liu et al. [82] obtained dialdehyde upper rim calixarene by first attaching alkyl functions to two of the lower rim oxygen atoms (**Scheme 1.5**). Treatment of this etherified calixarene with $CHCl_2OCH_3$ and $SnCl_4$ as catalyst yielded formyl functions adjacent to those containing the alky groups on the lower rim. Subsequent reaction of this formylated calixarene with 1,10-phenanthroline-5,6-dione resulted in an extended structure that was further modified by complexing with ruthenium and the resultant complex was used for colorimetric sensing of acetate and fluoride sensing.

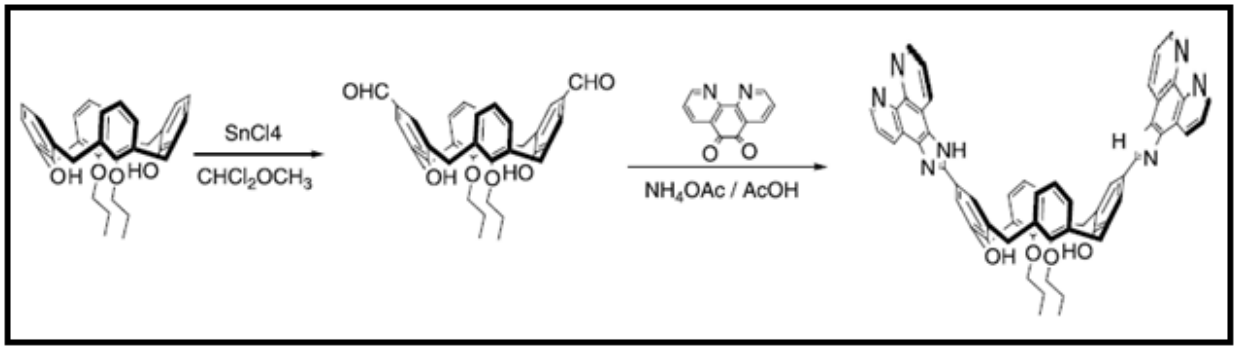

Scheme 1.5: Upper rim functionalization of calixarene

Like other aromatic rings, nitration, sulfonation, and halogenation is possible with calixarene rings using standard reagents with yields reaching 87 % reported for nitration [83–86]. However, reaction conditions in some cases have to be milder, especially when such harsh nitrating or sulfonation conditions can cause breakdown of the calixarene [87]. Sulfonation has usually been employed not just to introduce functionality but also increase water solubility due to the charge on the sulfate group. This reaction proceeds through either direct sulfonation, ipso-sulfonation, or chloro-sulfonation (**Scheme 1.5**) In addition to improving water solubility, the sulfonyl group has also been introduced to impart catalytic activity, selective binding and biological activity [86], and to act as a coordination point amongst others [85,88]. Sulfonation and subsequent etherification to give alkyl chains at the lower rim has been used to obtain molecules with surfactant (amphiphiles) properties that are able to self-assemble to form distinct nanostructures in aqueous media [89]. The

interesting aspect of such amphiphiles is the fact that they have a guest binding site that can be explored for producing important soft materials.

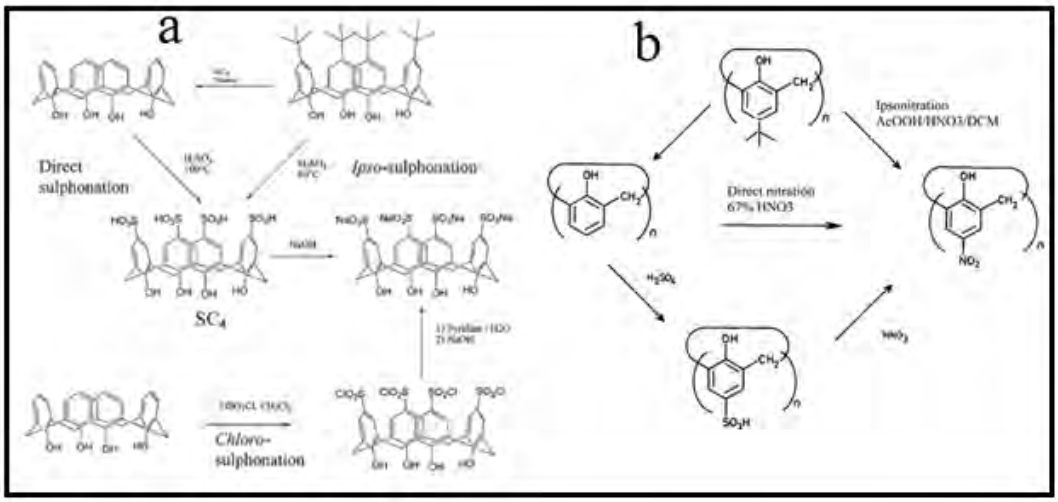

Scheme 1.6: Different (av)sulfonation and (b) nitration routes

Like sulfonation, nitration is also known to proceed through direct nitration, sulfonation followed by nitration and ipsonitration [83,87,90,91]. Due to the possibility of reduction, these nitro calixarenes are potentially good intermediate for the synthesis of precursors for other reactions.

1.6.2 Self-assembly in calixarenes

Calixarenes can self-assemble into porous and stable structures stabilized by intermolecular forces which exist in both solid and solution phase. Self-assembly in calixarenes has been reported to form globular dimeric or hexameric capsules that can be used as hosts for several molecules [62]. Worth noting is that such globular dimeric or hexameric structures have so far only been reported in cases where the calixarene bridges are methylene or where one of the methylene hydrogen atoms is replaced by an aliphatic chain. Substituting one of the hydrogen atoms at the methylene bridge with aromatic ring is known to yield structures that deviate from the cup shape which favors such globular structures. Self-assembly of pyrogollolarenes and resorcinarenes as hydrogen-bonded capsules, tubes, and bilayers are common with the nature of solvent and alkyl groups playing a vital role in the assembly [62]. Understanding the processes involved in self-assembly in both solid and solution phases and the parameters that allow control over the supramolecular assembly are critical to supramolecular chemists.

It has been found that the presence of water in pyrogallolarene facilitates self-assembly through hydrogen bonding [92]. As illustrated in the ***Figure 1.17*** (page 20), Ananchenko et al. [72] have demonstrated that the nature of the R-group on the alkyl carbon also plays an essential role in determining the kind of structure obtained. Long alkyl chains can, because of van der Waals interactions lead to interactions between two molecules and produce dimeric structures, whereas shorter chains do not favor such interactions. Besides the nature of the alky chains, other factors that affect the self-assembly of calixarenes are the nature of solvents and guests given that such arrangements are usually held by intermolecular forces that do not preclude the host of solvent [58]. Cave et al. [48] obtained a self-assembled capsule (by slow evaporation from ethyl acetate) containing six resorcin[4]arene molecules and eight water molecules forming a system stabilized by sixty hydrogen bonds; thirty-six of which are intermolecular with the polar water molecules playing a significant role in the hydrogen bonding (***Figure 1.20b***). Upon crystallization, ethyl acetate solvent molecules were trapped both in the intrinsic and extrinsic pores and participate in hydrogen bonding through their carbonyl functionalities. A previously reported pyrogallolarene aggregate was obtained from acetonitrile wherein the presence of hydrogen bonds was responsible for the pyrogallolarene arranged in the build-up of double layers aggregation of the molecules [47]. The supramolecular structure is stabilized by a total of seventy-two hydrogen bonds with the solvent molecules trapped in the pores and participating in the hydrogen bonding, in a structure with a head-to-head and tail-to-tail orientation where polar molecules are separated by interacting lipophilic chains. Dalgarno et al. [92–94] subsequently simultaneously carried out self-assembly of pyrogallolarene and encapsulation of various molecules in ***Figure 1.20a***. In agreement with results obtained by Gerkensmeier et al. [47] and Cave et al. [48] structures reported by Dalgarno et al. are held together by extensive intermolecular hydrogen bonding involving not only the calixarene molecules but as well the encapsulated guest and solvent molecules. There has also been similar work reported with resorcin[4]arene hexameric capsules self-assembly wherein water and butanol molecules are involved in hydrogen bonding that stabilizes the structure [46].

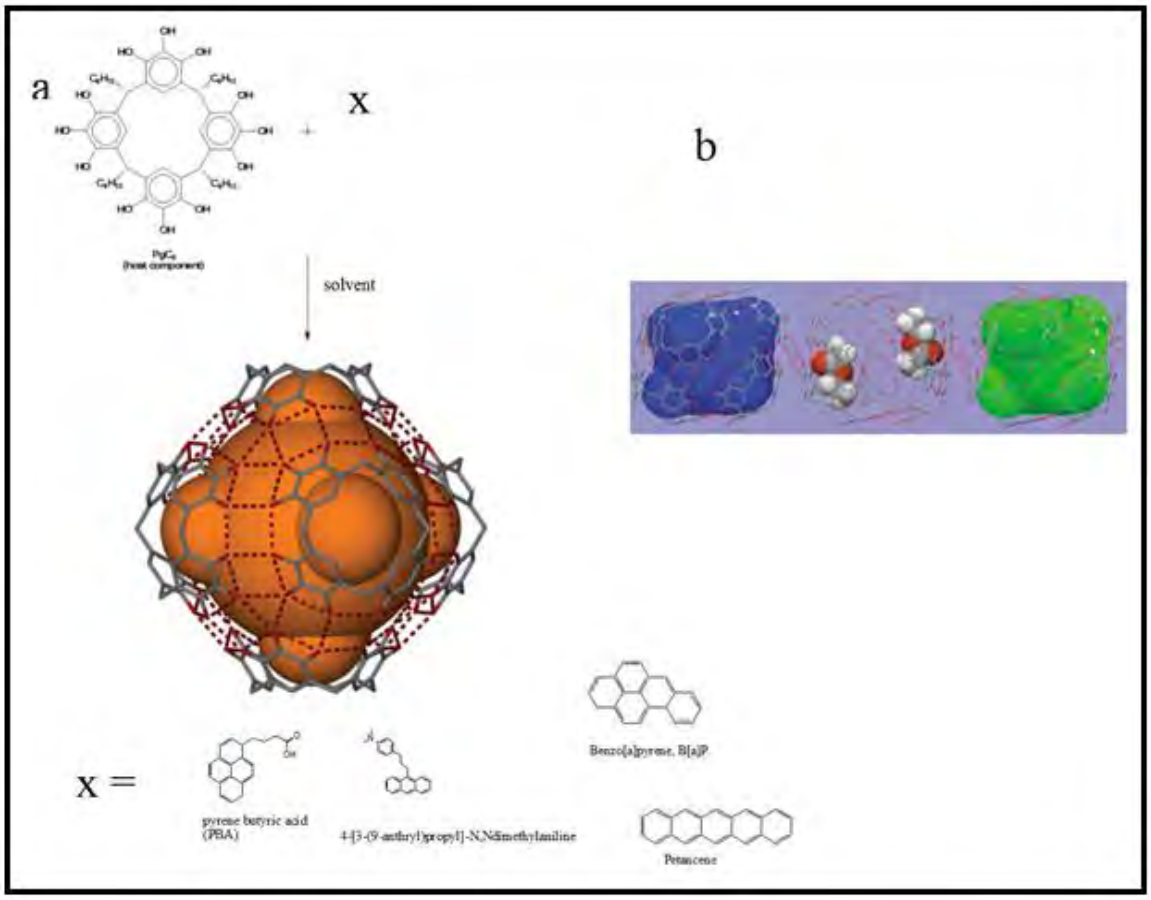

Figure 1.20: (a)Simultaneous self-assembly of pyrogallol[4]arene with guest (b) Encapsulation of ethyl acetate in the pores of pyrogallol[4]arene [92,93], [48]

1.6.3 Synthesis of calixarene based MOFs

Since the pioneering work of Yaghi et al. [95,96] Kitagawa et al. [97] and Ferey et al. [98] on MOFs, research on the subject has exponentially grown in scope and application. Several synthetic methods, including solvo/ hydrothermal, microemulsion, ultrasonic irradiation/ sonochemical, mechanochemical, and microwave-assisted synthesis, have been developed over time as researchers seek to obtain MOFs materials for different applications and on different scales (***Figure1.21***). MOFs may be obtained on different scales ranging from macro to micro to nanoscale. The latter scale is, however, more desirable because of the exciting properties associated with materials at the nanoscale. Generally, to obtain nanoscale MOFs, two main synthetic approaches are employed:

a) Confining the supramolecular assembly; a process that generally leads to MOF formation at nanoscopic locations through methods like emulsions or template synthesis, and
b) Favoring nucleation against crystal growth, using such methods as fast precipitation or by using microwave and ultrasound synthesis. [99]

The choice of a synthetic approach is usually determined by the end goal of the MOF and may yield amorphous or crystalline material depending on the ability to control nucleation and growth kinetics of the nanoparticles.

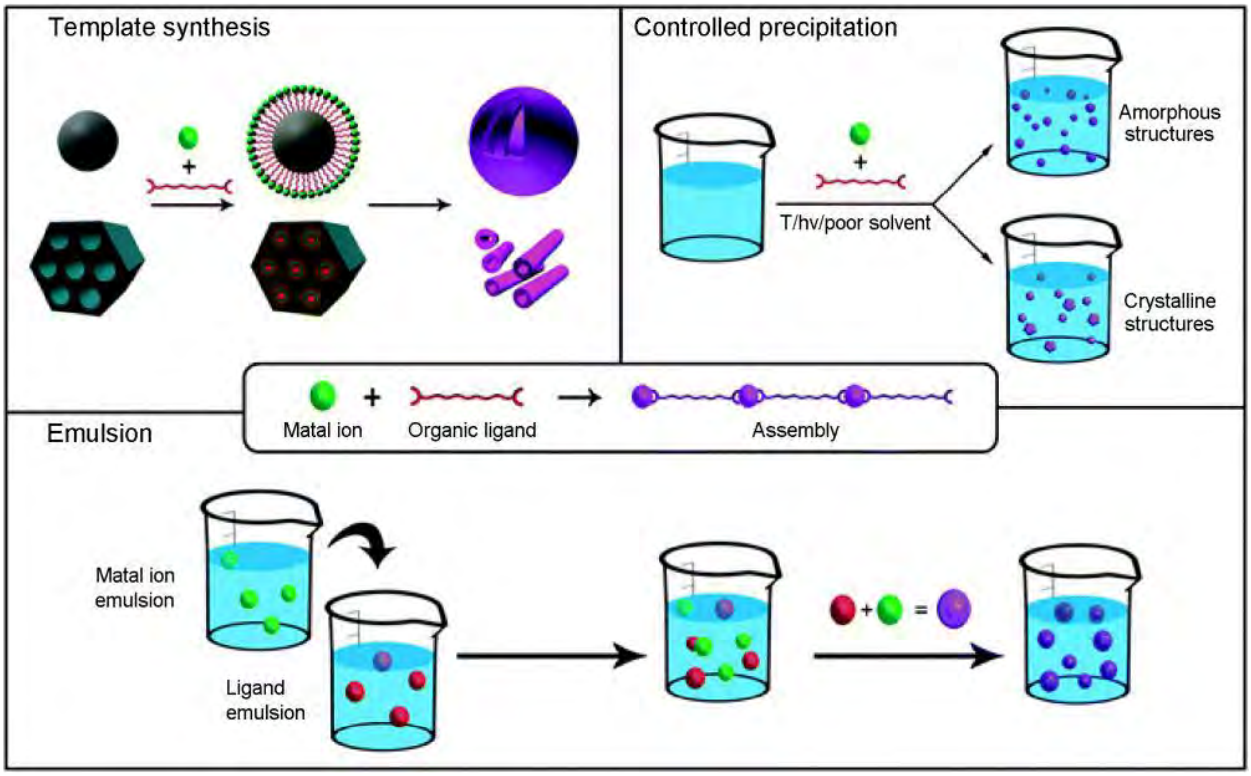

Figure1.21: Representation of synthetic approaches for preparing nanoscale MOFs [99]

Focus here will not be to discuss all the methods and approaches to obtaining MOFs [the reader may consult Baa et al. [99] for details on the methods] but rather to look at the various methods that have been used to obtain MOFs based on calixarene macrocycles. Despite the plethora of synthetic methods to calixarene based MOFs, a review of literature on this topic indicates that slow solvent evaporation and diffusion from/into mother liquors and solvothermal are the most exploited methods. These methods favor metal directed self-assembly and are therefore attractive in cases where structural elucidation through single-crystal X-ray diffraction is envisaged. The sheer lack in the reported literature of any reason suggesting why other methods such as emulsion, mechanochemistry, spray drying amongst others have not been used suggests that such absence of reports is not due to difficulty with calixarene macrocycle but rather insufficient research in that light.

Single crystals of the uranyl cage depicted in Figure *1.5**a*** and ***b*** (see page 5) were obtained at room

temperature by slow diffusion of acetonitrile on DMF solution of the reactions and pyridine as a base to deprotonate the ligand [30]. Solvothermal synthesis of the same material was reported to only yield decomposition by-products of the cage [30], suggesting the unsuitability of the solvothermal method to the synthesis of the material. Similar room temperature metal directed self-assembly complexes of pyrogallolarene and resorcinarene MOFs have been reported with cesium chloride by the Atwood group [61]. Cesium MOF crystals of the ligands were easily grown in water-acetonitrile mixture, with both solvents coordinating to the metal centers. The same group obtained coordination polymer chains of dimeric pyrogallol[4]arene capsules by first reacting pyrogallol[4]arene with the metal salt in hot DMSO [100]. Subsequent reaction of these capsules with 4,4'-bipyridine hot DMSO solution led to the crosslinking of the capsules as the DMSO ligands are displaced to produce structures indicated in ***Figure 1.22***.

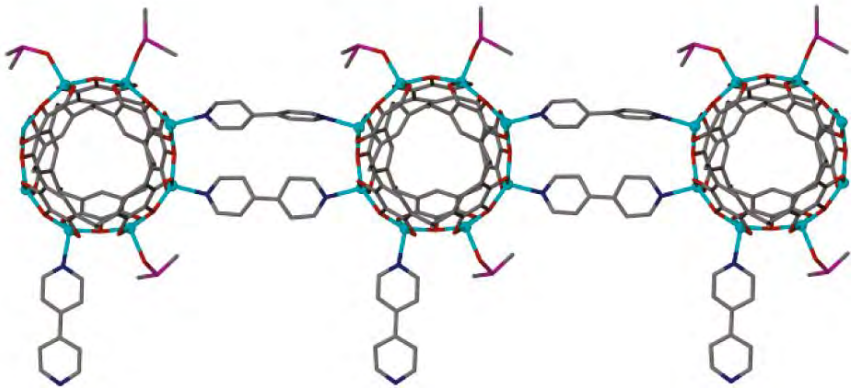

Figure 1.22: Crystal structures of self-assembled MOFs [100]

Nevertheless, most calixarene based MOFs have been synthesized through a solvothermal approaches [13,30,31,40,57,71,78] using either a single solvent or a mixture of solvent given the fact that this approach offers the ability to control the self-assembly using metal ions which possess weak coordination ability to calixarenes into thermodynamically stable complexes [101].

1.7 Synthetic approaches to cucurbiturils and cucurbiturils based MOFs

1.7.1 Cucurbiturils and analogues

The synthesis of these compounds involves refluxing glycoluril and formaldehyde in a concentrated acid medium either HCl or H_2SO_4. When temperatures are maintained at greater than 110 ^oC, the product is significantly CB6. However, when temperatures are lowered to between 70-90 ^oC, a mixture of analogues is formed containing mainly CB5, 10-15%, CB6 50-60%, CB7 20-

25% and CB8 10-15% [42]. These homologues can then be separated by means of fractional crystallization and dissolution. The possibility of obtaining analogues of different ring sizes, has greatly increased the scope of application of these materials especially in cases where pore size is particularly important. ***Figure1.23*** shows the variability of cucurbituril homologues. Over the years, research has explored beyond synthesis of the traditional cucurbituril to a variety of derivatives such as inverted cucurbiturils, hemicucurbiturils, bambusurils amongst others that have been reported [44,102].

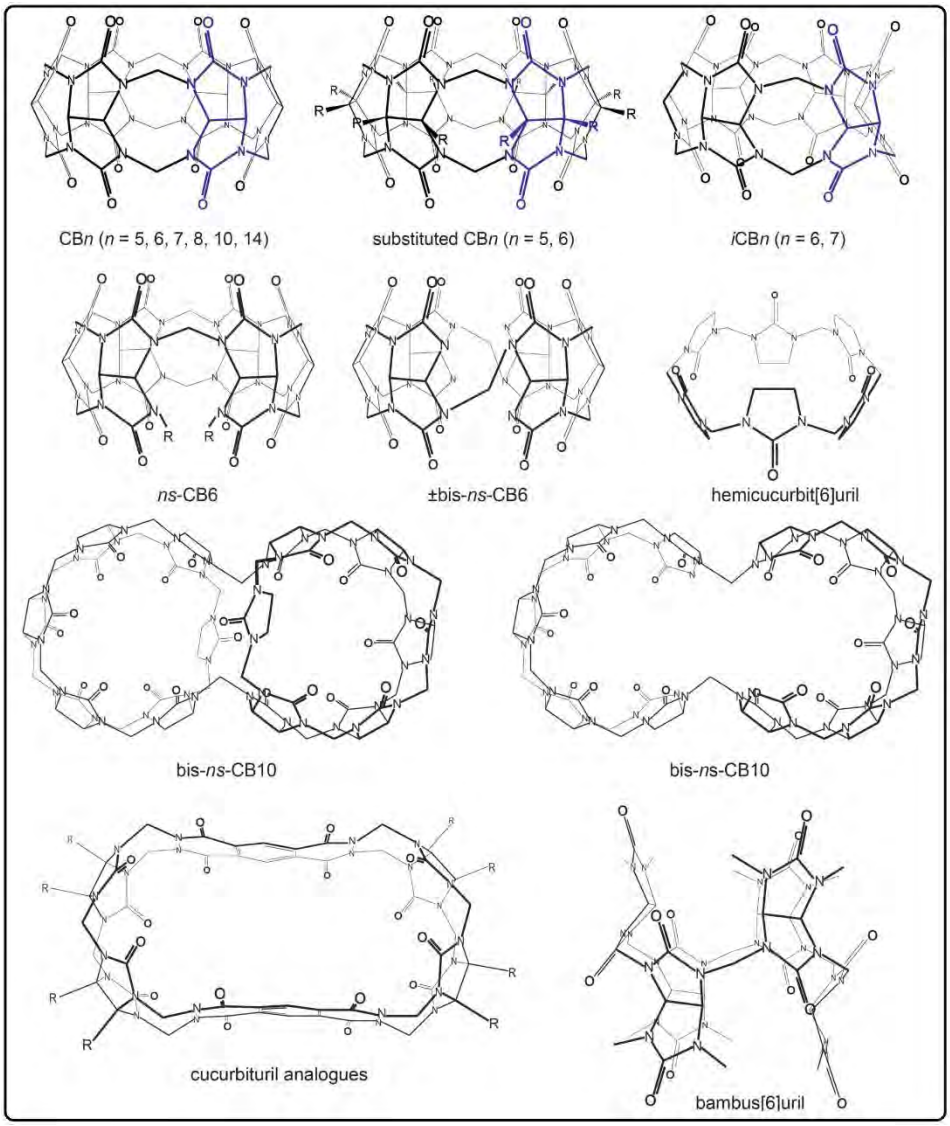

Figure1.23: Cucurbiturils and their Derivatives [44,102]

Cucurbiturils as secondary building blocks for MOFs are also beginning to emerge premised on the fact that they possess electron pair donor atoms like nitrogen and oxygen which can form

coordinate bonds. Cucurbiturils easily form metal complexes with various metal ions although the different homologues tend to show varied abilities to coordinate and as well varied selectivity for different metal ions [42,54]. Furthermore, it has been observed that several other factors including coordination geometry and radius of metal ions, temperature, counter-anions, solvent, metal-to-ligand ratio, and pH amongst other things also affect the formation of the supramolecular assembly [54].

Upon complexation with metal ions cucurbiturils (especially the five and five member homologues) form simple complexes including molecular bowls, molecular capsules coordination polymers and supramolecular assemblies. Unlike the higher homologues, the four- and five-member ring cucurbiturils can form complexes wherein the metal ion covers the portal completely. Higher homologues (n > 5) form metal complexes wherein only some of the portal oxygen atoms are coordinated or involve two or more complexing metal ions. ***Figure 1.24*** depicts the coordination of metal ions across the different cucurbiturils homologues.

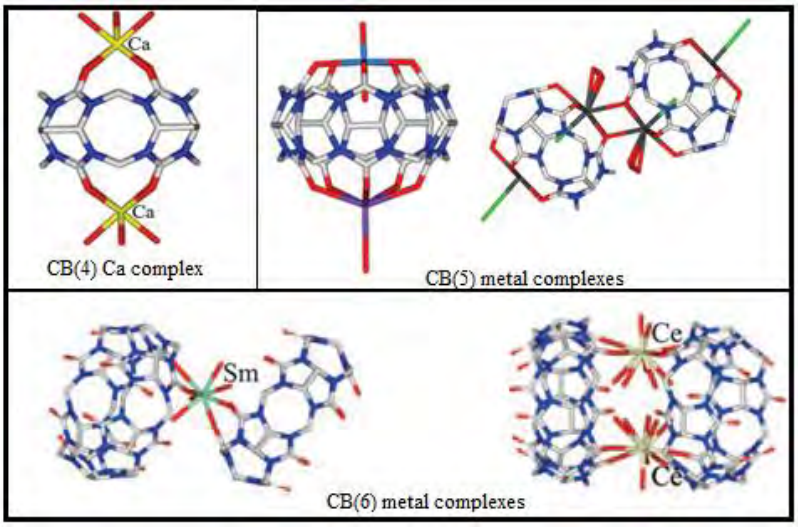

Figure 1.24: Representation of coordination modes of cucurbituril homologues [103]

Because cucurbiturils have donor atoms at two opposite ends, they can form polymeric network structures that extend as one to three dimensional structures (***Figure 1.25***). Linear self-assembly coordination complexes of cucurbiturils with metal ions usually with anionic directing units on the exterior of the cucurbituril cavity is known to result to honeycomb structures shown in ***Figure 1.25a*** [77,103,104]. Although such assembly is not uncommon for the other homologues, it is more

commonly found in five-member homologue in which the metals can occupy the portal completely.

The Kim group has demonstrated this by complexing CB6 with alkali metals Na, K, Cs and Rb complexes of the CB6 wherein coordination occurs through the C=O oxygens. In the case of the Rb, the complex forms a 1D structure with Rb ions bridging the CB units through O-Rb-O linkages resulting to a honeycomb polymeric coordination chain containing linear hexagonal channels. Similar results were obtained with Rb replaced by K. Crystals of CB6-Na revealed that the Na ions together with water molecules act like a lid on the barrels of the CB6 covering the portals with either water or THF molecules enclosed in the cavity. The door-like lids could be removed by adding trifluoroacetic acid, the structure can then be opened to release the guest.

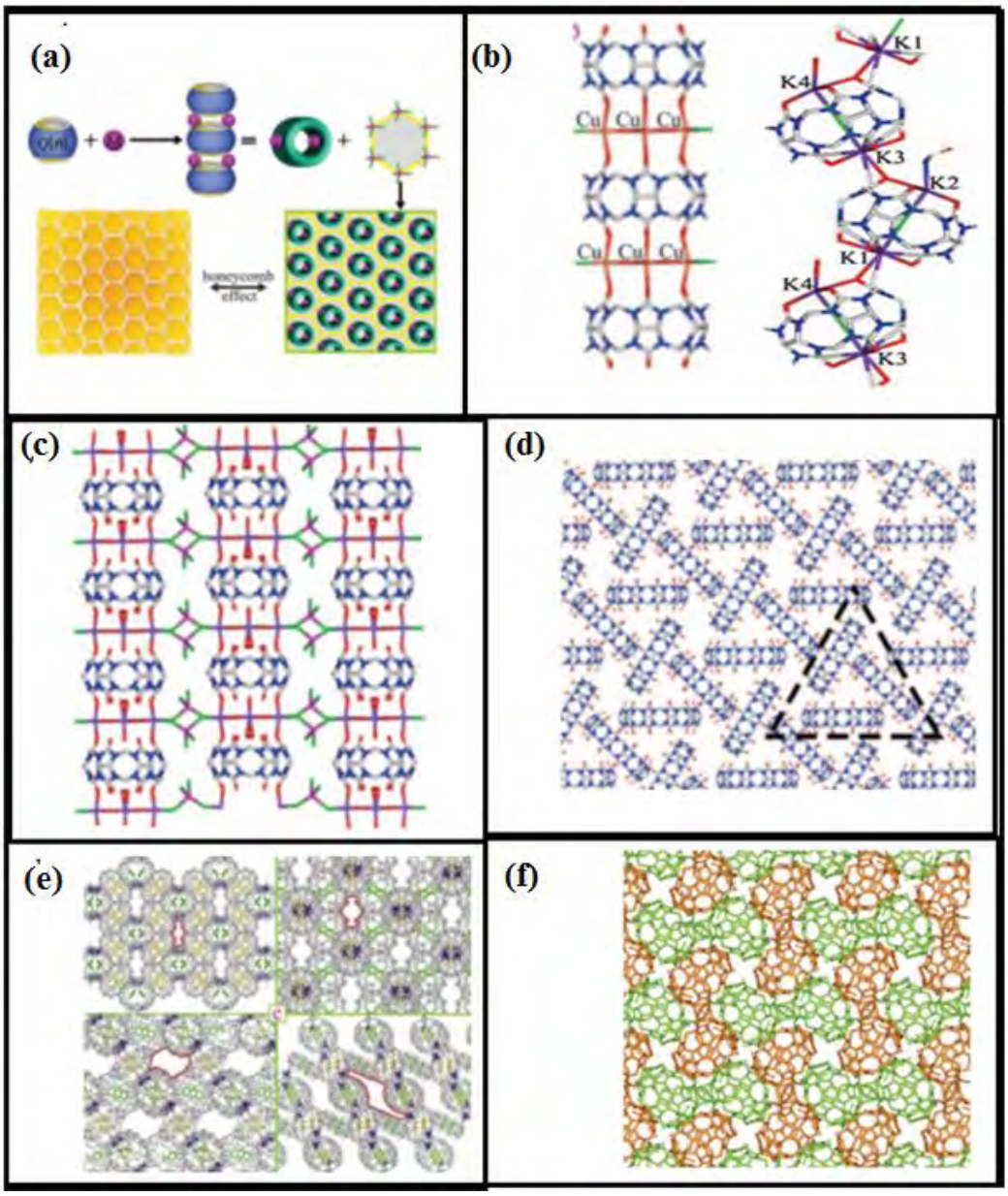

Figure 1.25: Some examples of CB-metal complexes. (a) Schematic for the formation of the honeycomb structure (b) 1D straight and zigzag CB metal complexes (c-d) 2D CB metal complexes and (e-f) 3D metal complexes showing the channels [abstracted from [103]]

Similar lid-like type complexes were also obtained with Cs [77,105–107]. Similar type of complexes were also prepared by Shen et al [53] using octamethyl-substituted cucurbituril alkali metals in the presence of polychloride cadmium anions. The interaction between the polychloride cadmium anions and the cucurbituril involves ion-dipole and the electrostatically positive outer surface of the cucurbituril. In the presence of the polychloride cadmium ions, Na and Rb did not form any complexes whereas K and Cs form coordinate bonds through the portal carbonyl oxygen

atoms. Parallel studies by the Nau group [108] have examined the chemoselective transformation of included guests promoted by transition-metal ions coordinated to the cucurbituril rim. The weak metal-ligand bonding interactions influences the photodeazetation of the bicyclic azoalkanes 2,3-diazabicylo[2.2.2]oct-2-ene (DBO) and 2,3-diazabicylo[2.2.1]hept-2-ene (DBH) in the presence of CB7. Another investigation found that the presence of $[CdCl_4]^{2-}$ in a CB7-La complex resulted to the formation of the honeycomb structure with the complex cation occupying the extrinsic pores of the cucurbituril metal complex. Single crystal x-ray analysis revealed that the complex anion acts as a structure directing agent to the resulting honeycomb supramolecular structure stabilized by hydrogen bonding, C−H···Cl, and ion-dipole interactions to obtain hollow tubular structures [103].

Although CB7 is not known to easily coordinate to metal ions, the Tao group successfully obtained hydroquinone-CB7-rubidium metal complexes wherein the hydroquinone serves to facilitate complex formation [109,110]. The single crystal data for the complex revealed that each portal of the CB7 is covered by a pair of rubidium ions which coordinate through the portal carbonyl oxygen atoms. The hydroquinone was found to be in the intrinsic cavity of the CB7 where is interacts through direct coordination of its OH group to the metal ions at the portal of the CB7 and intermolecular boding with the CB7 host. The authors credited the formation of the complex to the presence of the hydroquinone guest. Another 3D CB8 cesium metal complex studied by the same group involved the use of p-hydroxybenzoic acid as a co-ligand [111]. The crystals structure of the complex revealed that two different inclusion complexes of the co-ligand and the CB8 in a four-molecule unit are formed. Within a single CB8 unit, the co-ligands are arranged in a head to tail fashion and the two complexes can be distinguished by the orientation of the co-ligand: vertical in one and slightly horizontal in the other. Once again as in the case of hydroquinone, the coordination of the OH group of the p-hydroxybenzoic acid molecules induces further coordination of the cesium ions to the carbonyl oxygen of the CB8 molecule. The overall supramolecular assembly is a 3D structure with 3D channel system as shown above in Figure 1.25e. In all the cases reported here, the coligand is enclosed in the cavity of either the CB7 or CB8. It is however anticipated that the use of dicarboxylic acid ligands like malonic or terephthalic acid will result to metal complexes where the coligand acts as a pillar and not enclosed in the cavity of the cucurbituril.

While research on MOFs obtained from macrocycles such as calixarenes, cucurbiturils, cyclodextrins is active and still emerging, it is perhaps understandable that much interest is currently geared at obtaining the MOFs at different scales rather than investigating the influence of synthetic approach influences the nature of the macromolecular cages obtained. One should bear in mind that since synthetic routes equally have a direct bearing on the outcome of the MOF in terms of morphology and scale, investigating different approaches is, therefore, not of any less importance as the synthesis itself. An advantage associated with MOFs obtained from such macrocycles lies in the fact that they are excellent candidates for diverse applications because they usually have at least two types of pores with one set arising from the ligand itself (intrinsic pores) and the other from MOF structure (extrinsic pores). Consequently, this kind of structure offers possibility of hosting more than one type of guests especially in drug related applications.

1.8 Drug delivery

Advancement in pharmaceutical science during the past century has led to better healthcare systems as professionals now have at their disposal drugs and machines capable of treating diseases that were once fatal or near fatal [19]. This has led to a decrease in mortality and increased life expectancy. Undermining the tremendous developments particularly in drug science, have been issues related to pharmacokinetics, metabolic properties, dosage, toxicity, systemic circulation, solubility, etc. [112]. For instance, cancer chemotherapy is plagued by severe side effects, while certain drugs, despite their outstanding activities, are poorly solubilized. Consequently, drug delivery vehicles are necessitated, especially in cases where a drug suffers issues such as large undesirable dosage, poor solubility, bioavailability, and stability [99]. A drug delivery system (DDS) is a formulation or a device that can introduce a therapeutic substance in the body and improves its efficacy and safety by controlling the rate, time, and place of release of drugs in the body [113]. At present, DDSs enjoy extensive clinical application, and substantial commercial successes are mostly sustained release systems whose main objective is to provide constant blood levels of a drug over an extended period [114]. Drug delivery systems are essential because they offer; -

- improved therapy
- increased patient compliance through reduced dosing frequency, convenient routes of administration and improved targeting for a specific site to reduce unwanted side effects and

- a sustained or prolonged release using many natural, semi-synthetic, or synthetic polymers that are coated on the surface of a drug to provide the release for longer duration [115].

Ideally, a DDS transports an active compound to a specific site, releases the active compound, and is either eliminated or undergoes degradation. To qualify as an efficient DDS, the delivery vehicle must meet specific requirements, including controlled release of the active compound while avoiding "burst effect" (a situation whereby the drug is released from the DDS prematurely) [99,116]. Several drug delivery systems, including liposomes, micelles, emulsions, and polymeric nanoparticles have shown great promise in controlled and targeted delivery of drug molecules [115]. While each of the carriers has its advantages, none is ideal in application. Due to their wide range of useful properties, porous materials including silica, MOFs, cyclodextrins, cucurbiturils, aluminosilicates, have either been used or are currently being researched for various purposes, including the development of drug delivery system, sustained drug delivery system and improvement in the solubility of poorly soluble drugs. Generally, once in the system, it is expected that liquid will penetrate and subsequently flow through the pores of the porous carrier to provoke release of guest. This is a process that depends on both the geometry and surface properties of the material. Properties of the porous materials which make them suitable for applications in delivery systems include stable uniform porous structure, high surface area, and tunable pore size with narrow distribution and readily adaptable for thermolabile drugs [115]. Additionally, as with other carriers, it is expected that for a material to be used as a carrier, it meets the following general requirements:

- Structural control over size and shape of drug or imaging-agent cargo-space.
- Biocompatible, nontoxic.
- Precise, nanoscale-container and/or scaffolding properties with high drug or imaging-agent capacity features.
- Well-defined scaffolding and/or surface modifiable functionality that can be finetuned for specific targets.
- Lack of immunogenicity.
- Appropriate cellular bond, endocytosis, and intracellular trafficking to allow therapeutic delivery or imaging in the cytoplasm or nucleus.
- Acceptable bioelimination or biodegradation profiles.

- Controlled or triggerable drug release.
- Molecular-level isolation and protection of the drug against inactivation during transit to target cells.
- Minimal nonspecific cellular and blood-protein binding properties.
- Ease of consistent, reproducible, clinical-grade synthesis [113].

A porous solid may present one or more types of pores; the roughness of the surface may give rise to bottle-like (blind) or cylindrical shaped pores, transport pores (channels), and closed pores shown in ***Figure1.26***. While closed pores are usually not connected to other pores and are somewhat described as being isolated, the rest are connected to the others so that material can possibly flow from one to the other. Open pores are connected to the external surface of a solid and allow the passage of an adsorbate through the solid. Closed pores are void within the solid, which is not connected to the external surface. Transport pores are connected parts of the external surface of the solid to the inner microporosity. Blind pores are connected to the transport pores but do not lead to any other pore or surface.

Figure1.26: Physical picture of a porous solid material A – surface roughness, B – bottle-like (blind) pores, C – closed pores, D – transport pores (pores through the solid) and E – cylindrical blind pores

1.8.1 Methods of drug loading

When drugs are loaded unto nonporous materials, the drug molecules are usually confined to the outer surface of the carrier, which, for the most part, has a small surface area implying a low drug loading capacity. In contrast, using porous carriers with a higher surface area presents a possibility of higher loading percentage suitability for controlled release [117]. This potential justifies the

extent to which research has veered in the use of porous materials as carriers. Several methods have been developed to load drug molecules into porous carriers and are discussed below. The discussed methods are based on the reviews [115] and [117].

1.8.2 Simple mixing

In this method, the adsorbent is placed in the drug solution and stirred over a magnetic stirrer so that the drug penetrates the pores. The solution is then allowed to stand for a given time, separated, and dried over 24 h at 60 ºC. This method has been used for a variety of drugs like ibuprofen, dexamethasone, griseofulvin, ranitidine, and furosemide. Most research on the use of MOFs and COFs as DDS follow this approach with a few modifications. Various MOFs have been studied for their abilities to load and release of many drugs, including indomethacin [118], doxorubicin [119], ibuprofen [120], 5-fluorouracil [121] amongst several other drugs. Because MOFs are still in their early developmental stage in this field, the method is widely used for its simplicity.

A closely related method is to simple mixing is solvent evaporation. This method differs from simple mixing in that the adsorbent is usually sieved in the range of 250–350 μm to nullify the effect due to variation in particle size. The porous host is added to the drug solution, and the solvent evaporated at ambient temperature [[121]].

1.8.3 Loading under high pressure

In this method, the drug-carrier mixture in the required ratio is put into the high-pressure adsorption equipment for a period over 24 h after which the resultant mix is washed with water to remove the unadsorbed drug (**Scheme 1.7**). Prior to mixing the carrier and the drug, activation, which in many cases involves the thermal or pressure removal of solvent molecules is performed. This process usually creates a capillary pressure at the liquid–vapor interface of the solvent (surface tension) which subsequently forces the pores to collapse and an eventual collapse of the framework porosity [121]. To overcome this challenge, a drying procedure that uses supercritical carbon dioxide ($scCO_2$)-assisted drying, and impregnation procedures may be an effective method for obtaining a high load of drug in the pores of a porous material. In a modified procedure, Matsuyama et al. [121] loaded ibuprofen into a MOF by mixing the carrier and the drug in a high-pressure cell, and CO_2 was pumped into the high-pressure cell through a pre-heater at a pressure and temperature of 20 MPa and 333 K. After stirring on a magnetic stirrer for 6 h, the unincorporated drug was removed at 80 ºC.

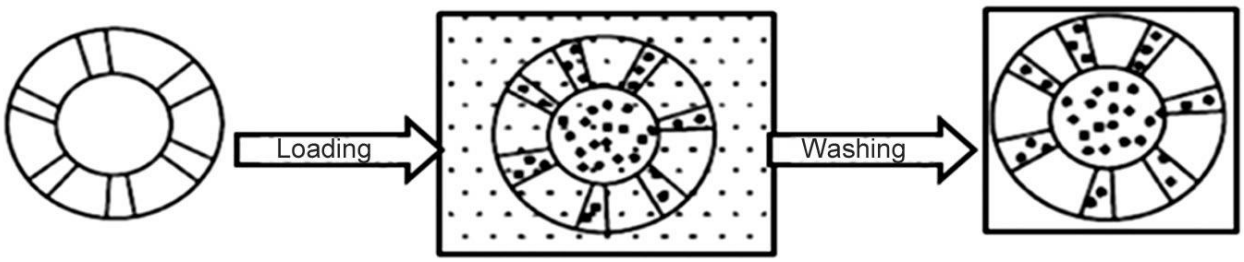

Scheme 1.7: Diagrammatic representation of the drug loading in porous material under high pressure [121]

1.8.4 Layer-by-layer adsorption

The technique is applied for drugs such as polypeptide and proteins, which have low thermal stability and usually performed at room temperature. A layer-by-layer assembly of two oppositely charged polyelectrolytes at solid surfaces is developed as alternating layers of these polyelectrolytes on a charged substrate due to their electrostatic attraction and the complex formation resulting in the defined macromolecular layer on the surfaces. The process usually involves the successive deposition of the drug microcrystals on the porous material and covering with polyelectrolyte multilayer walls [122]. While this method has been widely used for loading drugs such as ibuprofen, indomethacin, dexamethasone [122], its application in MOF drug loading appears not to have been reported in literature.

1.8.5 Vacuum process

This approach involves adding the adsorbent to a solution of the drug and evacuating the mixer for an appropriate time. The drug carrier mixtures can then be allowed to stand for a while, and the solid filtered out and dried [121].

1.9 Drug release mechanisms

Drug release from porous carriers can either be through desorption of the adsorbed entity or release of an entity not adsorbed but rather chemically attached to the carrier through some modifications process (***Figure 1.27***). Cucurbituril and calixarene-based controlled drug-delivery systems can be designed in various forms, including inclusion complexes, amphiphilic self-assembled micelles, hydrogels, vesicles and liposomes, and supramolecular nanovalves on mesoporous silica nanomaterials [123]. Attention here is, however, on inclusion complexes of cucurbiturils, calixarenes and those of their porous metal complexes. The action or release of the drug from the pores could be triggered using different stimuli. In the following description of mechanisms, examples will be drawn from calixarenes, cucurbiturils, and related MOFs, and non-calixarene MOFs to illustrate work that has been published on the different mechanisms proposed. There is a

plethora of release mechanisms, however just a few are presented here as may be relevant to proper understanding of this study.

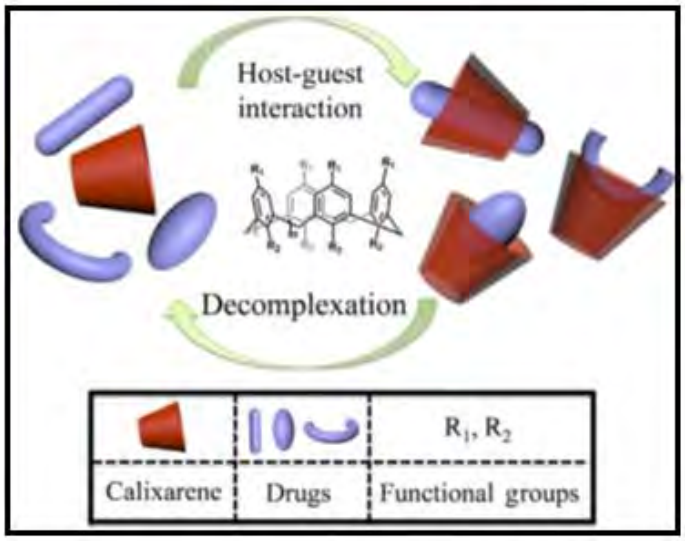

Figure 1.27: Host-guest complexation and decomplexation [123]

1.9.1 Solution equilibrium and drug release

For a given carrier-drug complex where the drug is adsorbed on the portal or cavity or a combination of both, there will exist an equilibrium between the free drug in solution and the encapsulated or adsorbed form. Any given condition may favor the free drug or adsorbed drug, and this can be described using association (binding) constant, which indicates which of the two states of the drug is favored. For an efficient carrier, it is expected that an adsorbed drug is sufficiently protected, that is, a relatively high binding constant but however not too tightly bound to make release difficult. Binding constants (1.1 to 1.8) × 10^4 M^{-1} have been reported for doxorubicin interactions with Fe(III)-trimesate MOF nanoparticles with a drug-carrier stoichiometry of 1:1 [124]. Similarly, a study of 1:1 complexation of nedaplatin, (an antineoplastic drug), and *p*-4-sulfocalix[4]arene, (a macromolecule possessing a bipolar amphiphilic structure with excellent biocompatibility and relatively low hemolytic toxicity) for potential use as a drug delivery system was reported with a stability constant in the range 3.6 x 10^4 M^{-1} and 2.1 x 10^4 M^{-1} which corresponds to -6.2 and -5.9 kcal mol^{-1}, respectively for the free energy of complexation [125]. As a third example, a cancer drug delivery vehicle was prepared based on *p*-sulphonatocalix[4]arene (SC[4]A) and dinuclear platinum compound by side-on binding of the two parts. The 4,4'-dipyrazolylmethane ligand of the Pt complex was located within the *s*-CX[4] cavity of the calixarene with binding further stabilized by ion–ion interactions and hydrogen

bonding between the metal complex amine groups and the s-CX[4] sulfate groups. Release profile studies revealed that the system releases dinuclear platinum complex upon in vivo administration due to the high content of blood serum existing in the body [126]. A parallel type of release using a large octahedral coordination cage based on Co_4-p-tert-butylsulfonylcalix[4]arene (Co4-(SC4A-SO2)) subunits and 4,4',4''-(benzene-1,3,5-triyl-tris(benzene4,1-diyl))tribenzoate (BBB) has been observed by Du et al. [127] for the release of anti-inflammatory ibuprofen.

1.9.2 pH controlled release

The release of a drug from a porous carrier can be pH triggered if the cage is stabilized by the influence of some electronegative portals [23]. Such portals present more effective electrostatic guest binding but also easily release the guest upon acidification [128]. Under such circumstances, the drug/cage complex is stable at a given pH; slight changes from this will lead to the desorption of the drug. Site-specific illnesses such as cancer and tuberculosis are interesting candidates for such kind of release triggers since affected cells usually have pH values that are different from the normal physiological pH of 7 – 7.5, due to waste produced by the microbes [99]. A pH-dependent drug/cage complex that is stable under such physiological conditions of pH will most likely undergo some changes under pH condition of diseased cells that may lead to the desorption of the drug. This is the basis of most drug delivery studies from porous materials in cancer and tuberculosis therapy. Zhang et al. [129] showed proof of this concept using rationally designed pH responsive MOF nanocarriers ZIF-8 for the simultaneous delivery of doxorubicin hydrochloride DOX/verapamil hydrochloride VER, for multi-drug resistance MDR cancer therapy. The polyethylene glycol folate PEG-FA showed high drug loadings (8.9% and 32% for DOX and VER, respectively), good stability, biocompatibility as well as high cytotoxic activity toward B16F10 and multidrug-resistant MCF-7 (MCF-7/A) cells. After intravenous injection, accumulation of the drug in cancer cells was observed. The authors demonstrated that during a 24h period at lower pH (pH =5, the pH for endosome in tumor cell) the amount of drug released is higher [(27.37 ± 0.92) % of DOX and (76.48 ± 0.68) % of VER] compared to [(9.68 ± 1.25) % of DOX and (18.18 ± 0.74)% of VER] at higher physiological pH of 7.4. These findings are salient since they indicate that the successful application of MOFs in the delivery of cancer therapy could lead to a reduction in systemic toxicity common with conventional administration routes.

Yang et al. [130]exploited a cationic porous drug carrier ZJU-101 synthesized by the solvothermal method for the loading and delivery studies diclofenac sodium, an anionic drug. The drug delivery in the inflamed tissues (pH=5.4) demonstrated a more effective release compared to that in the healthy tissues (pH=7.4), indicating a physiological pH responsive drug release. This discriminatory drug release process is controlled by anion exchange between anions in phosphate buttered saline (PBS) and coordinated/free diclofenac anions. [131,132] also demonstrate the pH-dependent release of paclitaxel (PTX) conjugated with folic acid and doxorubicin. The pH responsiveness of cucurbiturils has also been demonstrated by Sindelar et al. [133] who constructed a molecular switch that could be used to control the position of CB7 wheel on a dicationic pseudorotaxane carboxylic acid axle by varying the pH of the system. They showed by H-NMR spectroscopy that when the terminal carboxylic acid are deprotonated by raising the pH, the CB7 moves from the edge of the axle to the center, over the dipyridinium rings. Reducing the pH leads to a return of the CB7 to the ends of the axle containing the carboxylic acids. The increase in release amount with decreasing pH once more demonstrate the role pH plays in release profiles. Pennakalathil et al. [134] reported the synthesis of nanoparticles based on a conjugated oligomer obtained by coupling divinylfluorene and dibromobenzothiodiazole monomers. The water stable camptothecin carrying nanoparticle was further capped with CB7 to decrease cytotoxicity and increase the stability.

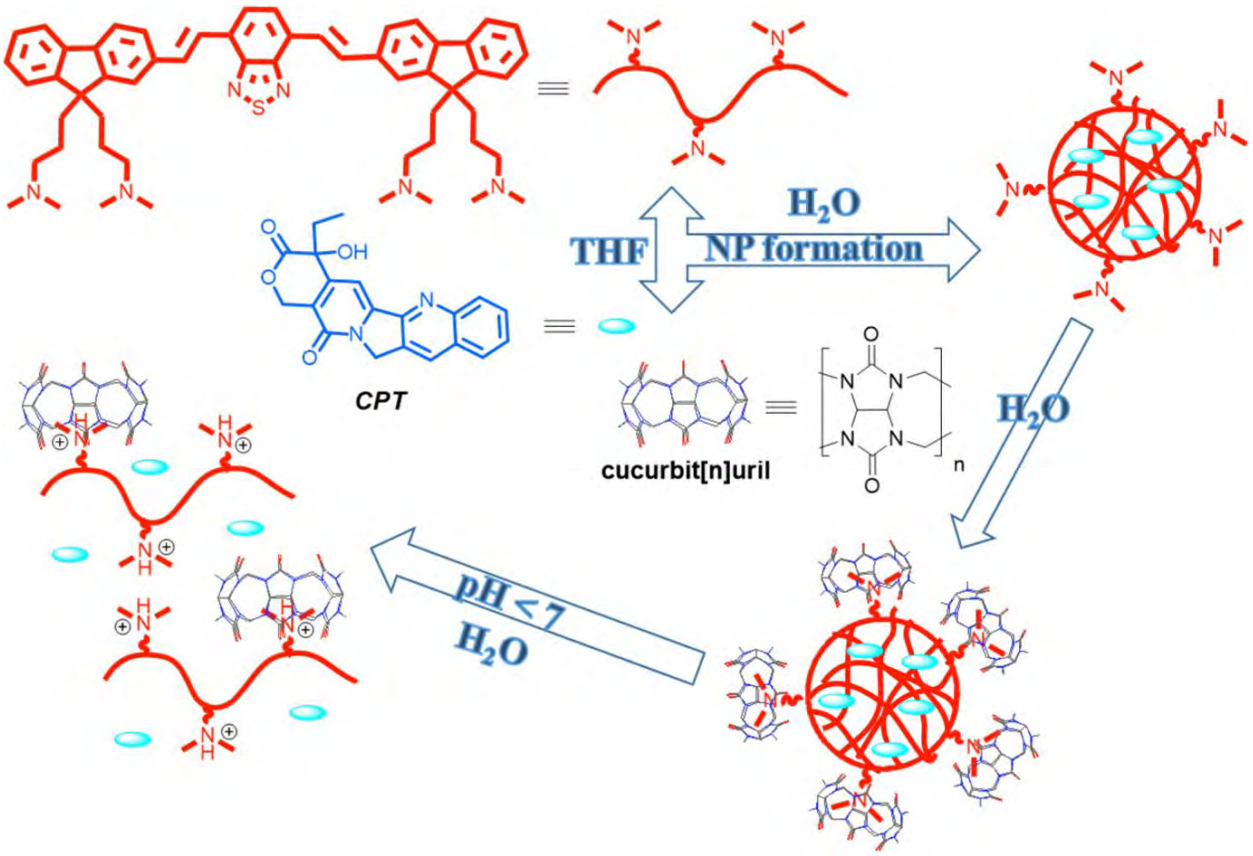

Scheme 1.8: Preparation of CB-capped drug-drug loaded nanoparticle and pH triggered release mechanism [134]

The camptothecin release study revealed a faster release at low pH (at 5.0) compared to physiological pH (7.4) confirming the pH-responsive nature of the nanoparticles. On the other hand, CB7-capped drug-loaded nanoparticles was equally found to regulate the release rate by providing slower release at pH 7.4 than the nanoparticles in the absence of CB7s (**Scheme 1.8**).

1.9.3 Degradative release

Another approach to controlled drug release is by means of degradative release, a situation in which the drug gets released as the carrier breaks down. Because porous materials especially MOFs easily breakdown under acidic conditions as a result of the breakdown of the coordination bonds by the acidic protons, this method is attractive for the delivery of a drug with MOFs in acidic environments such as cancerous tissues [135]. In addition to the drug performing its function, the porous carrier can be designed so that upon breakdown, biologically active species are generated. In this regard, MOFs containing biologically active metals like calcium, iron, zinc can be envisioned. Song et al. [135] used a Zn based MOF as a delivery vehicle for 5-FU using simulated body fluids with different pH.

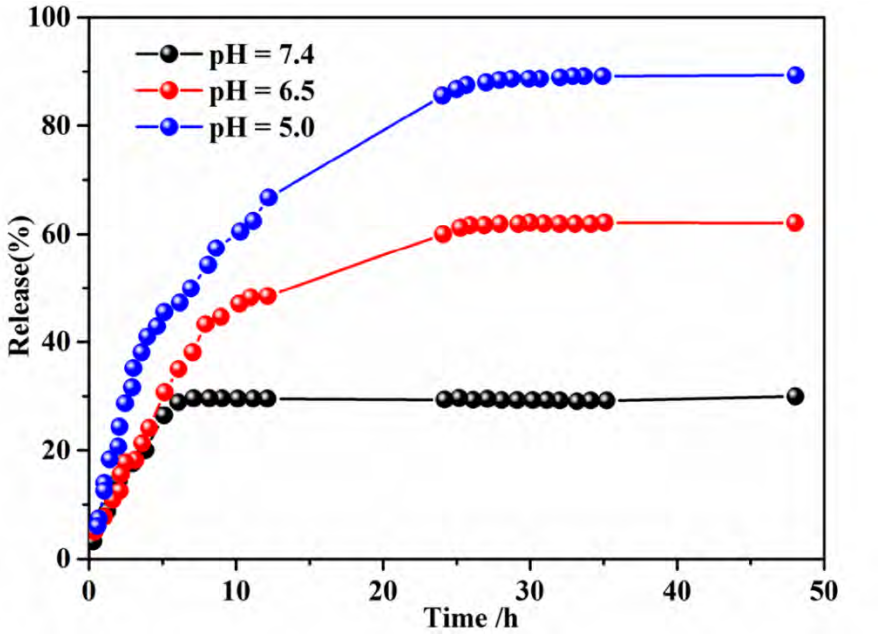

Figure 1.28: Release of 5-FU at different pH [135]

While the drug release is pH-dependent and increases with increasing acidity (**Figure1.28**), the authors also found that the breakdown of the MOF triggers this release. Another example of breakdown prompted release has been reported by Cunha et al. [136], who studied the release of caffeine using a series of different MOFs. Fast release (lasting up to 6 hrs) of caffeine from the MOFs was attributed to the breakdown of the unstable MOFs in the release medium. In cases where the MOFs were stable, drug release was found to proceed through slow diffusion through the slightly amphiphilic 1D pores lasting up to 72 hrs. One other approach to degradative release is using the drug molecule as a spacer or active metal nodes (**Scheme 1.9**). The advantage of this approach lies in the fact that it could reduce toxicity concerns and the possibility of higher drug content [137]. While permanent porosity is not a requirement, such MOFs could be particularly useful in combination therapy. Serre et al. [138] demonstrated this approach by obtaining MOF based on nicotinic acid (which has pellagra-curative, vasodilating, and antilipemic properties) and Fe(III). Subsequent ibuprofen loading indicated that the amount thereof is less than the amount of nicotinic acid present in the MOF structure. Release profiles indicated that both drugs are released upon the gradual breakdown of the MOF.

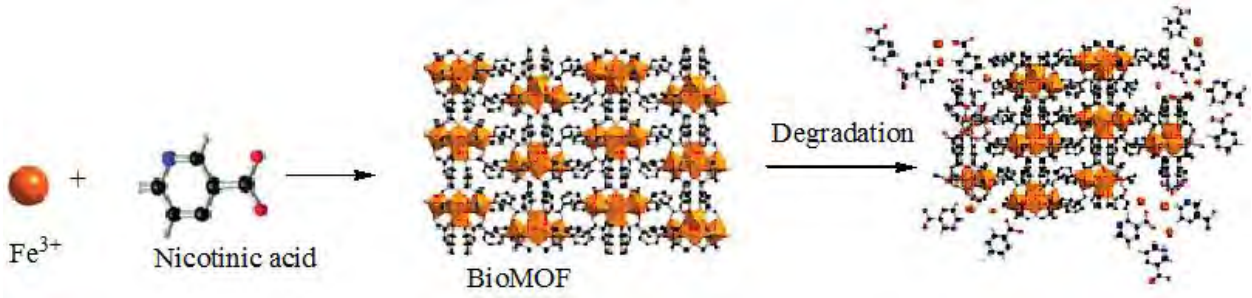

Scheme 1.9: Release profile of drug through degradation of the BioMOF [137]

1.9.4 Drug action without release

The possibility of functionalizing calixarenes offers the possibility of imparting biological activities. This widens the scope of applications of these materials beyond acting as carrier molecules or ligand for complexation. A wide array of biological applications ranging from protein recognition, inhibition, and detection to antimicrobial, lectin binding and inhibition, DNA binding, and cell transfection, antitumor activities is possible depending on the appended moieties. Noruzi et al. [139] reported on the synthesis, characterization, and biological studies thiosemicarbazide-functionalized calix[4]arene ligand with transition metal complexes. The complexes showed significant antibacterial activities against *E. coli* bacteria and considerable in vitro anticancer activity against Saos-2 bone cancer cell lines. The authors also found that the compounds show high blood compatibility. ***Figure 1.29*** shows some functionalized calixarenes; **5** was exploited as ligand for the mutated p53 protein (p53-R337H) and Kv1.2 potassium channel which are biologically two tetrameric proteins considered to be medically relevant. **6** shows a calixarene that has appended sugar units which mimics the cholera toxin that attacks cells and thereby prevent cells from damage [23]. Compound **7** is capable of disrupting VEGF binding to its receptor selectively inhibiting VEGF-dependent signaling and suppressing angiogenesis and tumorigenesis [21]. Compound **8** was evaluated against five tested methicillin-resistant strains of *Staphylococcus aureus* (MRSA)] and a considerable increase in antibacterial activity in three of five strains with respect to the starting material was observed [140].

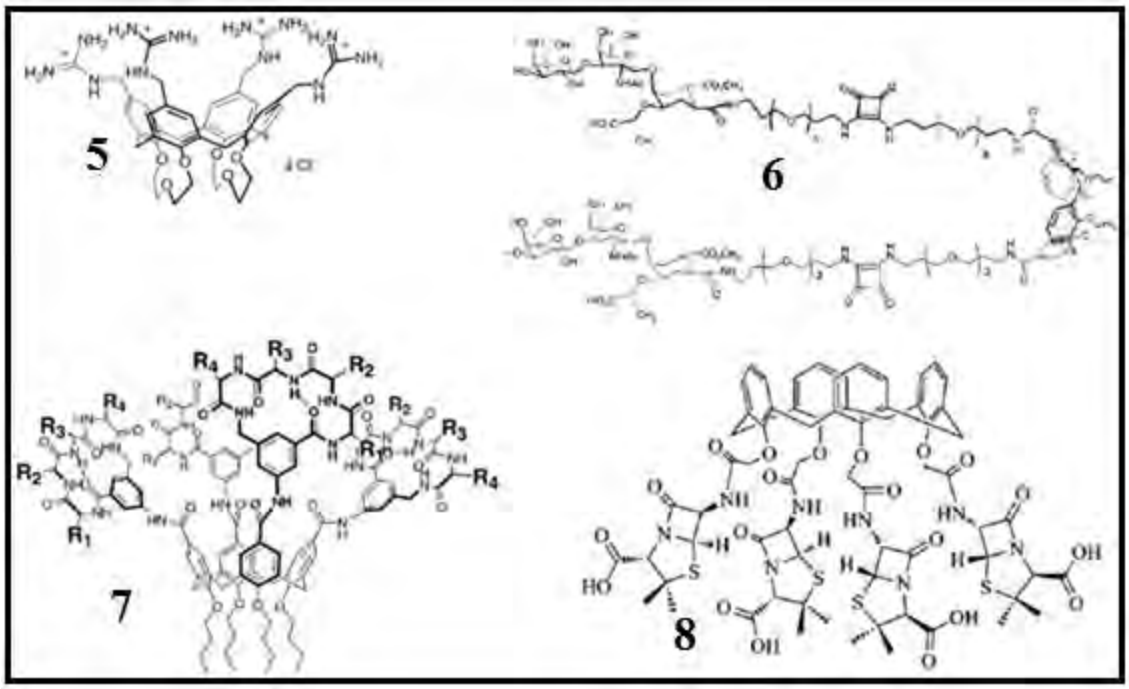

Figure 1.29: Some biologically active functionalized calixarenes

1.9.5 Diffusion

Diffusion has also been proposed as one of the mechanisms by which a drug is released from carriers. Drug release through diffusion is usually prompted by a concentration gradient. Ibuprofen release from a Co_4- *p*-tert-butylsulfonylcalix[4]arene subunits and 4,4',4''-(benzene-1,3,5-triyl-tris(benzene- 4,1-diyl))tribenzoate coordination cage has been studied under pH. The ibuprofen molecules diffuse into the calixarenes cavities, and internal voids of the coordination cage and the subsequent two-step release is due to slow diffusion through the cage apertures [127]. A similar two-step slow diffusion release mechanism has been observed for the release of mercaptopurine from a fluorescent zinc-calixarene-based dimeric capsule. As in the case of ibuprofen release above, slow-release here is due to the slow diffusion rate of mercaptopurine from the windows of the cavities owing to the strong interaction of S-π and the π-π interactions between mercaptopurine and the aromatic skeleton [141] .

1.10 Objectives

Site-specific diseases such as cancer and tuberculosis have remained a significant health concern not necessarily because of lack of chemotherapeutic agents but mainly because of issues related to bioavailability, dosage, and systemic circulation. It is on this premise that drug delivery to such sites becomes essential and has attracted enormous research attention.

The design and fabrication of carrier systems capable of delivering drugs precisely to such sites and in a controlled manner is particularly impressive. Macrocyclic compounds such as calixarene, cyclodextrins cucurbiturils, among others, have shown proof of the ability to form supramolecular host guest complexes which can be used to deliver cargoes in a controlled manner. Scientists have thus built on the potential of MOFs to explore the applications of MOFs built from such macrocycles for drug delivery. Whereas strictly organic materials are generally characterized by relatively good biocompatibility, appreciable loading capacities, and lack of proper control delivery profile, inorganic materials, on the other hand, are characterized by reduced loading capacity, poor compatibility, and better release control profiles. MOFs take advantage of their organic and inorganic components, drawing the advantages of both that they present as good candidates for DDSs. We hypothesize that a MOF constructed from calixarene or cucurbituril will possess two types of pores: one set arising from the calixarenes and the other from the MOF structures. While the pores of both classes of macrocyclic compounds are hydrophobic, the MOF pores are hydrophilic and should, in principle, be able to load hydrophobic and charged drug into the calixarene or cucurbituril and MOF pores respectively. Drawing on these properties, the main aim of this work is to synthesize and characterize calixarenes from aromatic aldehydes and cucurbiturils and their MOFs. The host-guest chemistry of the synthesized compounds shall be investigated using selected laboratory solvents and drug molecules (isoniazid and ciprofloxacin).

1.11 Specific Objectives

1) Synthesize and characterize a range of cucurbiturils, resorcin[4]arenes and pyrogallol[4] arenes
2) Synthesize and characterize MOFs based on the ligands in (1).
3) Evaluate the host-guest complexes of the ligands in (1) and their MOFs based on selected laboratory solvents and drug molecules including isoniazid, and ciprofloxacin.
4) Evaluate as a proof of concept the release profiles of the drugs from the different carriers.

2 CHAPTER TWO

This chapter presents an instrumentation and an overview of the experimental approaches used in this work. General synthetic procedures, starting materials, solvents, operating principles of instruments and implications of the obtained results in the understanding of structure and function of the synthesized compounds are presented.

2.1 Experimental section

This chapter outlines a general overview of synthetic approaches used in this work. Background of the instrumentation and nature of results obtained from the various techniques employed are also examined although not in details.

2.2 Materials

All chemicals were purchased from Sigma Aldrich or Merck and used without any further purification. The following organic chemicals were used as precursors for the synthesis of the calix[4]arene and pyrogallol[4]arene ligands; resorcinol, pyrogallol, 3,4-dihydroxybenzaldehyde, *p*-chlorobenzaldehyde. The following were used for the synthesis of the cucurbiturils; urea, glyoxal solution and formaldehyde.

The following metal salts were used in the synthesis of metal complexes, manganese (II) chloride, iron(II) chloride, cobalt(II) chloride, nickel(II) chloride, copper(II) chloride and zinc(II) chloride, manganese(II) acetate cobalt(II) acetate, nickel(II) acetate and zinc(II). In the synthesis of cucurbituril metal complexes we used the following bridging dicarboxylic acids: oxalic, malonic, succinic and glutaric acid.

The solvents used in this work include dimethyl formamide (DMF), dimethyl sulfoxide (DMSO), Millipore water dispensed by MilliQ systems, ethanol, methanol, acetonitrile, hydrochloric and sulfuric acid.

2.3 General synthetic procedures

All compounds synthesized in this research were obtained via solvothermal or slow evaporation techniques following reports from literatures. In the synthesis of the ligands, resorcinol or pyrogallol was dissolved in ethanol or methanol of mixture of both and hydrochloric acid added. The mixture was stirred for a few minutes and the desired aldehyde added and then refluxed at between 70-90 ^{o}C for up to 36 hours. The precipitated product was filtered, and the solvent left for eventual crystal growth.

In the typical synthesis of a cucurbituril, glycoluril was first synthesized by reacting glyoxal with urea in the ratio 1:2 respectively in water HCl mixture. The obtained white powder was then

reacted with the formaldehyde in the ratio 1:2 in concentrated acid at temperatures greater than 120 ºC for 36 hours. After cooling, the resultant powder was filtered and washed with either methanol-water mixture of ethanol water mixture then dried at 50 ºC in an oven.

The MOFs were synthesized by either solvothermal or slow evaporation methods using various systems of solvents and modifications were made where necessary. Detailed synthetic procedures are discussed in the relevant chapters.

Drug loading experiment were mainly carried out mainly through mechanochemistry, solution chemistry and/or one-pot synthetic approach. The obtained host-guest complexes were then analyzed to determine any interaction and as well the amount of drug contained in the host.

To determine if a drug was released from complex system, the complex was suspended in Millipore water and filtered at given times and the filtrate used for bioassay.

2.4 X-Ray diffraction

2.4.1 Powder X-ray diffraction (PXRD)

PXRD was used both as a characterization technique and for the determination of structural changes and/or determination of guest sample. This technique is used determine if a material is crystalline, phases, sample purity, crystallite size, and, in some cases, morphology. This technique also draws on the fact that when X-rays interact with materials, they produce a diffraction pattern that is a fingerprint of that material [142,143]. Data collection was carried out by Dr J Britton (Rhodes University) using a Bruker D8 Discover diffractometer equipped with LynxEye detector under a Cu-Ka radiation with l = 1.5405 Å. The samples were ground and loaded unto the sample holder and the data collected in the 2θ range 10-80º at 0.010º per minute. Specific details are presented in the relevant chapters.

2.4.2 Single crystal X-ray diffraction

In cases where crystals were obtained, these were collected and sent for single crystal diffraction. Since most porous materials may collapse once the solvent is removed through drying, the crystals were allowed in the mother liquor and sent as such for analysis. The data collection was carried out by Dr E Hosten (Nelson Mandela University), Dr V Smith (Rhodes University) at Stellenbosch University. Structure solution and refinement was done by the Dr V Smith and Dr E Hosten using SAINT and/ X-Seed. Non-hydrogen atoms were refined with anisotropic thermal parameters and

the hydrogen atoms were introduced to positions which were calculated. Hydrogen atoms of hydroxyl groups were allowed to rotate around the C-O bond until the best fit was obtained. Relevant crystallographic data is presented in the appropriate chapters.

2.5 Elemental Analysis

Carbon, hydrogen, and nitrogen analysis was carried out by Mr. Francis Chinedeka (Rhodes University) on an Elementar Vario Micro cube possessing a thermal conductivity detector (TCD), with temperatures of 1150 ºC in the combustion tube and 850 ºC in the reduction tube. The technique works on the principle that by subjecting compounds to high temperatures in the presence of oxygen they decompose to form respective oxides of carbon, hydrogen and nitrogen that can be quantified, and data used to determine empirical formular [144].

Metal content was determined using atomic absorption spectroscopy. For this technique, a calibration curve was obtained using the calibration standard and the metal complexes were digested in in concentrated sulfuric acid and diluted to the to 25 mL using water and then analyzed [145,146]. By combining the carbon, hydrogen and nitrogen elemental analysis and the flame atomic absorption spectroscopy data, it is possible to determine the empirical and molecular formular of the metal complexes.

2.6 Thermal analysis

Thermal analytical techniques including TGA and DSC are routinely used in studying thermal behavior such as structural changes and decomposition profiles of compounds [147]. This technique involves subjecting a sample to increasing temperature at a given rate or maintaining at a given temperature under nitrogen or helium as an inert atmosphere since most samples can undergo oxidative or reductive processes under non-inert conditions [148]. Different parameters are then measured to give information about the structure and composition of the compound.

2.6.1 Thermogravimetric analysis (TGA)

TGA technique involves following the mass of a sample as it is being heated under controlled atmosphere and at a given rate [147,148]. By analyzing the mass loss, both qualitative and quantitative information about the thermal behavior of the sample can be obtained [148]. For this research use was made of a top loader PerkinElmer TGA 4000 equipped with a PerkinElmer TGA-FTIR interface, TL 8000, for evolved gas analysis. The apparatus requires mass of sample to be in

the range 2.5-5 mg and temperatures ranging from ambient up to 900ºC can be attained. From the decomposition profile of a sample, the mass losses could be quantified. In some cases, the evolved gases were analyzed with the FTIR for further elucidation of the compound.

2.6.2 Differential Scanning Calorimetry (DSC)

Unlike the TGA which monitors mass changes as a function of temperature, the DSC monitors energy changes as a function of temperature. These energy changes enables the characterization of the material through measurement and determination of transitions (such as glass transitions and melting) that occur in a sample, at what temperature they occur [147,148]. This research made use of the Perkin Elmer DSC 6000 which can measure temperatures from ambient up to 445 ºC. This technique measures the heat absorbed by the sample contained in an aluminum pan and compares with a similar empty pan as a reference. Data from the DSC allows for the identification of phase changes, solvent and/or guest evolution, melting as well as decomposition.

2.7 Fourier transform infrared spectroscopy (FTIR)

FTIR is a fast and easy and non-destructive technique for analysis of compounds especially with those containing known functional groups. Because interaction between host and guest often lead to shifts in vibrational wavelength of the interacting sites, this technique was routinely used to characterize host guest complexes [149]. Additionally, coordination of metal ions to ligands also results to shifts in bands in the ligand which also justifies the use of this technique in characterization. FTIR was therefore used as a first tool to check if a reaction had taken place be it for the ligand or metal complex synthesis. In the case of ligand synthesis, the IR spectra was usually compared with results from literature and the starting material to ascertain if any reaction had taken place. In cases where a reaction had occurred, further characterization was carried out to further ascertain the formation of a new entity. For this work we used a PerkinElmer Spectrum 100 FT-IR spectrometer to scan samples between 4000-600 cm^{-1} and a PerkinElmer Spectrum 400 FT-IR/FT-FIR spectrometer to scan in the range 700-200 cm^{-1} to check metal ligand bond formation. In the case of FIR, the samples were prepared by grinding in a mortar and mixing with liquid paraffin after which it was evenly spread between KBr discs and the IR recorded. Further details of the Technique are presented in the relevant chapters.

2.8 Nuclear magnetic resonance spectroscopy (NMR)

NMR is also another non-destructive information rich analytical technique which can give information about molecular structure as well as dynamic processes occurring within a sample [150]. It can both be used qualitatively and quantitatively for analysis of samples even at very low concentrations [151]. It is generally used to determine the environment around given atoms usually hydrogen, carbon, fluorine, nitrogen, and phosphorus although it is also possible to use several other elements. Both 1D and 2D NMR were extensively used to characterize the ligands and the synthesized host-guest complexes using deuterated solvent *viz*; methanol, acetone, DMSO, and deuterium oxide. Additionally, NMR titrations were also used to determine stoichiometry of the obtained host-guest complexes. NMR data for this study was done using Bruker NMR 400 and 600 for the analysis. In the presentation of NMR spectra data, 'd' is used to indicate a doublet, 's' is used for a singlet and 't' for a triplet. The specific details of the experiment are discussed in the concerned chapters.

2.9 Ultraviolet (UV) spectroscopy

In this work, UV spectroscopy has been used mainly to analyze host-guest interactions and the presence of characteristic band of guest released from the host in solution. The technique works on the principle that specific compounds will absorb energy at a given wavelength. By using the Beer-Lambert's law it is possible to determine quantitively the amount of sample present in solution. Perkin Elmer Lambda 25 UV/VIS Spectrometer was used for this study.

3 CHAPTER THREE

This chapter presents the synthesis of *tetra*-(*p*-chlorobenzyl)resorcin[4]arene and *tetra*-(p-chlorobenzyl)pyrogallol[4]arene and their interactions with vapors of methanol, water and DMSO. The ensuing structural changes resulting from the interaction of these compounds with guest have also been investigated.

3.1 Synthesis of *tetra*-(*p*-chlorophenyl)resorcin[4]arene and *tetra*-(*p*-chlorophenyl) pyrogallol[4]arene, host-guest complexes and vapor-phase induced structural changes.

The two compounds described here were synthesized following a literature report[152] with slight modifications and characterized using NMR, FTIR, DSC, and single crystal XRD. These compounds were then used as host to selectively adsorb DMSO from a mixture of solvents. The subsequent structural changes undergone by these compounds after the interactions were also investigated.

3.2 Synthesis of tetra-(*p*-chlorophenyl)resorcin[4]arene (BN22)

A mixture of resorcinol (1.00 g, 9 mmol), *p*-chlorobenzaldehyde (1.27 g, 9 mmol) and about 5 mL of dilute HCl (50 %) was refluxed at 70 – 80 ºC in 50 mL of ethanol for 36 hours. The precipitate formed was filtered out and washed three times with 5 mL of ethanol and the filtrate left for eventual crystal growth. After drying the precipitate in an oven at 50 ºC for 36 hours, the obtained pale-yellow powder weighed 0.97 g, 46 % yield (based on *p*-chlorobenzaldehyde). Upon exposure to air the appearance of the tetra-(*p*-chlorophenyl)resorcin[4]arene powder turned from pale yellow to russet. Pale yellow crystals suitable for single crystal analysis were obtained by recrystallization from either DMF, DMSO or methanol by means of slow evaporation. Crystals were also obtained by slow evaporation of the filtrate from the synthesis.

To investigate if the solvent used has any effect on the conformation of the obtained product, resorcinol (1.00 g, 9 mmol), *p*-chlorobenzaldehyde (1.27 g, 9 mmol) and about 5 mL of HCl was refluxed at 70 – 80 ºC in 50 mL of using methanol for 36 hours (**Scheme 3.1**). After heating under reflux for 36 hours under same conditions as with ethanol, a cream precipitate was obtained. The precipitate was filtered and washed 3 times with 5 mL of methanol then dried. After exposure to air and light, the color of the powder changed color from cream to grey.

The compounds are hereafter referred to as BN22M for the compound synthesized in methanol and BN22E for the compound synthesized in ethanol. In cases where a characterization technique gave results with insignificant differences for BN22M and BN22E, no distinction is made between BN22E and BN22M and the compound is simply referred to as BN22.

3.3 Synthesis of *tetra-(p*-chlorophenyl)pyrogallol[4]arene (*p*-ClBP)

A mixture of pyrogallol (1.00 g, 7.9 mmol), *p*-chlorobenzaldehyde (1.21 g, 7.9 mmol) and about 5 mL of dilute HCl was refluxed at 70 – 90 ºC in 50 mL of ethanol for 36 hours. The precipitate formed was filtered, washed three times with 5 mL ethanol and the filtrate left for crystal growth. After drying in an oven at 50 ºC for 24 hours, the obtained cream powder weighed 0.85 g, 43.4 % yield. This compound did not show any color change upon exposure to moisture or light suggesting that it is stable to stable to moisture and light. Crystals suitable for single crystals were obtained by recrystallization from either DMF, or DMSO through slow evaporation.

To investigate if the solvent used has any effect on the conformation of the obtained product, a mixture of pyrogallol (1.00 g, 7.9 mmol), *p*-chlorobenzaldehyde (1.21 g, 7.9 mmol) and about 5 mL of HCl was refluxed at 70 – 90 ºC in 50 mL of methanol for 36 hours (**Scheme 3.1**). The precipitate formed gave a cream powder upon drying. This powder is also relatively air and light stable as the case of ethanol. The compounds are hereafter referred to as *p*-ClBPE and *p*-ClBPM for the samples obtained using ethanol and methanol respectively. In cases where a characterization technique gave same result for both *p*-ClBPM and *p*-ClBPE, the compound is simply referred to as *p*-ClBP.

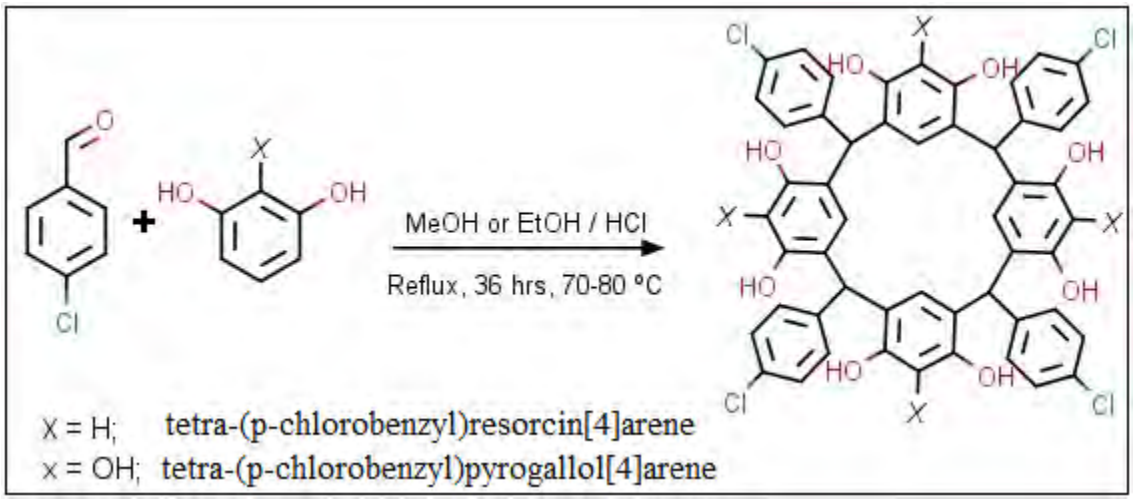

Scheme 3.1: Synthetic scheme for tetra-(p-chlorobenzyl)resorcin[4]arene (BN22) and tetra-(p-chlorobenzyl) pyrogallol[4]arene (*p*-ClBP)

3.4 Results and discussions

The obtained powders were characterized using FTIR, NMR, DSC, and single crystal XRD. The FTIR spectra of the obtained compounds depicted in ***Figure 3.1*** compare quite well with other calixarenes that have been reported in literature especially in the finger print region where calixarenes are reported to look quite similar[16,17]. The υOH band both BN22 and pClBP both appear 3100-3400 as expected for calixarenes [16]. The υOH stretch for BN22 is broader than the pyrogallol counterpart *p*-ClBP indicating that the strength of intermolecular hydrogen bonding in BN22 is greater than in *p*-ClBP. The O-H in-plane bending occurs between 1400-1300 cm^{-1} for both compounds and broader for BN22 due to the strong hydrogen bonding. In fact, the O-H in-plane bending vibration appears at 1323 cm^{-1} whereas for *p*-ClBP the same vibration occurs at 1368 cm^{-1}. The C-Cl vibrational band occurs at 718 cm^{-1} and 707 cm^{-1} for BN22 and *p*-ClBP respectively. The FTIR spectra of the BN22M and BN22E showed minimal differences just like that of *p*-ClBPM and *p*-ClBPE. This suggests, and was later confirmed by other analyses, that the only difference between the compounds is that they can adopt different conformations. It is likely that rapid conformational interconversion and hence averaging effect is account for the similarity in the spectra. In conformity with literature reports [16,17], the FTIR spectra of the resorcinarene and pyrogallolarene share significant similarities between 1000 cm^{-1} and 1300 cm^{-1}.

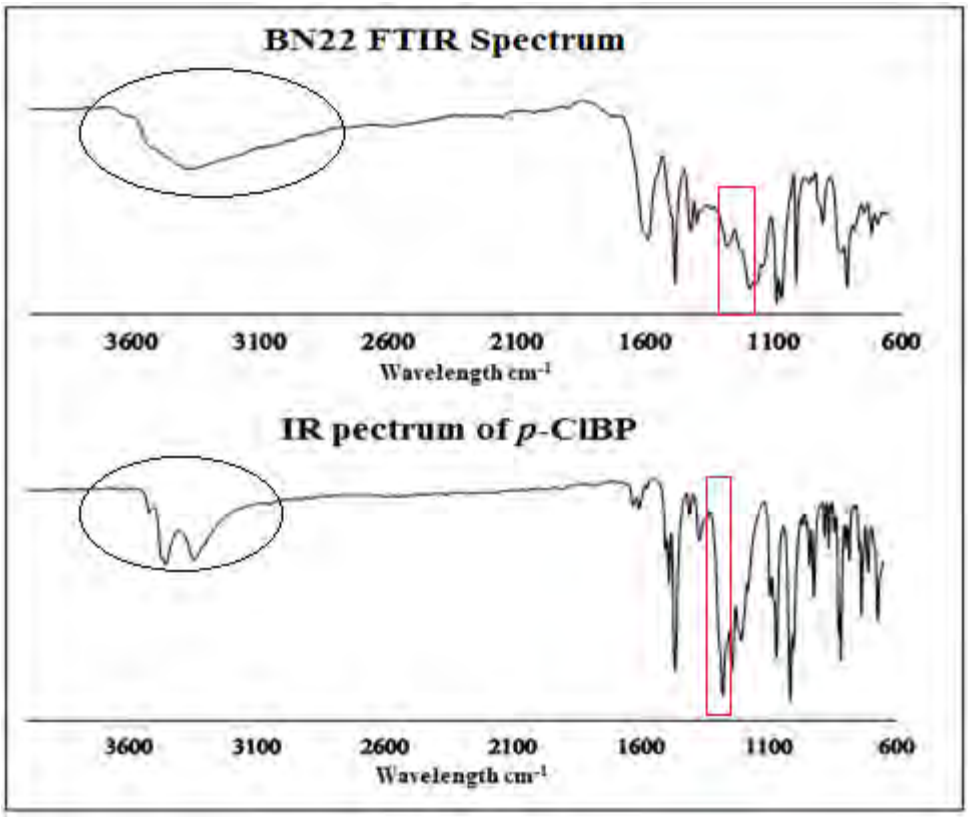

Figure 3.1: FTIR spectra of (top) BN22E (bottom) *p*-ClBP

From the NMR spectra of BN22M and E shown in ***Figure 3.2*** and ***Figure 3.3*** it is apparent that the samples are reasonably pure irrespective of the solvent used and despite the low yields. The H-NMR spectra for BN22E@DMSO-d_6 shows signals at 5,34 ppm (s, 2H), 5,49 ppm (s, 4H), 6,15 ppm (s, 2H), 6,23 ppm (s, 2H), 6,34 ppm (s, 2H), 6,57 ppm (d, 8H), 6,97 ppm (d, 8H), 8,74 ppm (s, 4H) and 8,83 ppm (s, 4H). On the other hand, BN22M@acetone-d_6 shows signals at 5.67 ppm (s, 4H), 6.03 ppm (s, 4H), 6.18 ppm (s, 4H), 6.66 ppm (d, 8H) and 6.96 ppm (d, 8H). The H-NMR spectrum of BN22M @DMSO-d_6 shows signals at 5.62 ppm (s, 4H), 6.19 ppm (broad, 3H), 6.39 ppm (broad, 3H), 6.63 ppm (d, 8H), 7.05 ppm (d, 8H) and 8.73 ppm (s,8H) while the ^{13}C-NMR spectrum of BN22E@DMSO-d_6 shows a total of ten signals. The spectrum of BN22M@DMSO-d_6 shows a total of eight signals. In the ^{13}C-NMR spectrum of BN22E, there are two pairs of signals at 120.75 ppm, 120.82 ppm and 153.20 ppm and 153.35 ppm which in the case of BN22M give rise to a single signal each at 120.60 ppm and 153.38 ppm respectively. Despite these differences (in chemical shifts), the rest of the signals in BN22E can be matched with those in BN22M.

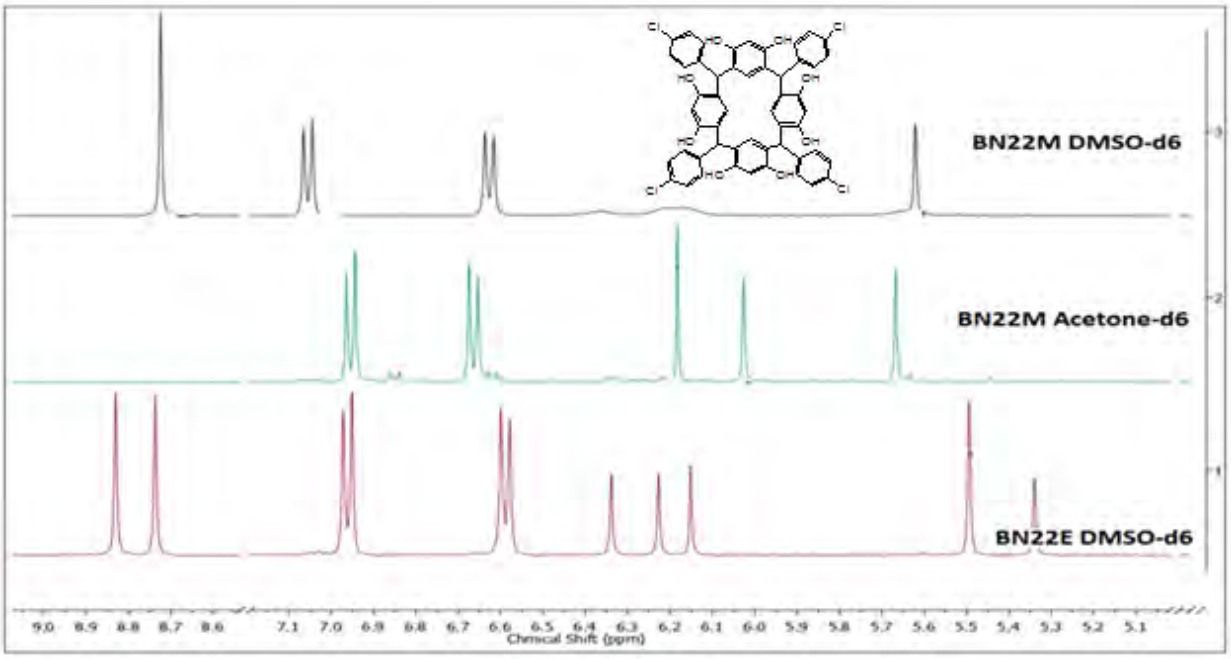

Figure 3.2: HNMR of (top) BN22M and (bottom) BN22E

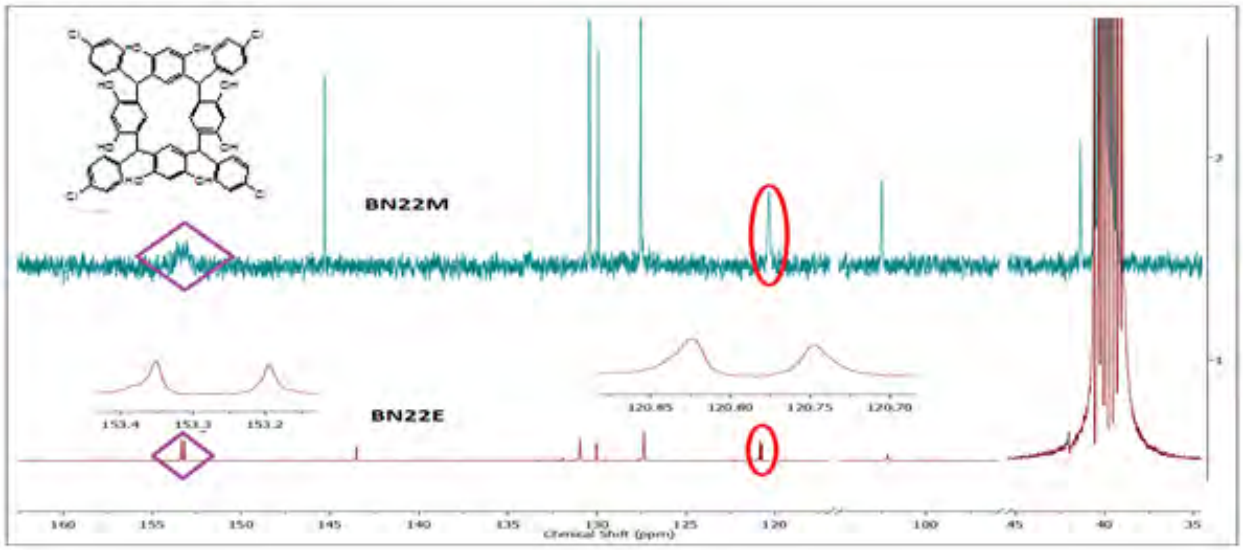

Figure 3.3: ^{13}C-NMR spectra of (top) BN22M and (bottom) BN22E [the NMR was performed in a sumber of solvent to check solvent effects. The H-NMR of BN22E is performed in DMSO- d_6 while that for BN22M is performed in acetone- d_6. The ^{13}C-NMR was performed in DMSO-d_6]

At first glance the H-NMR for all compounds are not very clear especially for the samples where ethanol was used as solvent. Even in the absence of impurities that would complicate the elucidation. The disparities in NMR signals for the BN22M&E samples when obtained in different solvents, indicates that the solvents, used in synthesis influences the obtained conformation. This

is evident from the differences in number of signals and chemical shifts of the resorcinol protons when the solvent of synthesis is changed from ethanol to methanol. In the H-NMR of the BN22M@DMSO-d_6, the OH proton signal appears as a single peak whereas in the H-NMR of BN22E@DMSO-d_6, the OH signal appears as two peaks. This suggest that in BN22M, the OH protons are in the same chemical environment whereas in BN22E, the OH groups are found in different chemical environment. The OH proton signal is however not observed inBN22M@acetone-d_6.

The signals at 8.74 and 8.83 ppm in BN22E@DMSO-d_6 are ascribed to the OH protons. The corresponding signal in BN22M@DMSO-d_6 appears as a singlet at 8.73 ppm. The *p*-chlorobenzyl rings protons appear as doublets while the methine proton appears as a singlet near 5 ppm. In BN22E@DMSO-d_6, the resorcinol protons appear as four singlet signals whereas in BN22M@acetone-d_6 they appear as two signals. This suggest that obtaining the compound from different solvent can yield different conformations. The differences observed between BN22M@acetone-d_6 and BN22M@DMSO-d_6, suggest that in solution, there is also significant solvent interaction with the compound which result to structural transformations if they are obtained using aromatic aldehydes. When using aromatic aldehydes and ethanol as solvent, conformers that deviate from the "*cone configuration*" [16,17] are obtained.

The single crystal structure of BN22E shown in ***Figure 3.4*** was essential to understanding the H-NMR of the compound. This data indicates that the resorcinol rings adopt a 1,3-alternate-like configuration, (with one set of opposite rings lying flat on the equatorial position and the other vertically oriented). The chlorine bearing benzene rings are on the other side of the molecule with one ring being disordered. Corresponding resorcinolic protons on adjacent rings are therefore in different environments while those on opposite rings are in same chemical environment and thus a splitting of the signals occurs. The methine protons and the *p*-chlorobenzyl proton signals are in the same environment and do not experience any splitting. Comparing the H-NMR spectrum of BN22E@DMSO-d_6 with that of BN22M@acetone-d_6 (see ***Figure 3.2*****)**, it is observed that no splitting of the methine protons occurs as with BN22E@DMSO-d_6. The H-NMR of BN22M@acetone-d_6 is in fact two singlet less compared to BN22E. The integration of the signals indicates that all singlets signals have the same number of protons. This suggests that

corresponding resorcinolic protons are in the same chemical environment in BN22M. This observation indicates that the conformation of the compound with respect to the resorcinol rings is u,u,u,u. Furthermore, unlike the BN22E case where the OH protons are clearly visible, the OH protons are not visible in the case of BN22M@acetone-d_6 as in DMSO-d_6. With the resorcinolic rings all pointing in the same direction, there is a ring of intramolecular hydrogen bonding that forms across the eight OH groups which distorts the electron cloud around the OH protons thus making it signals broaden and not detectable in the H-NMR spectrum.

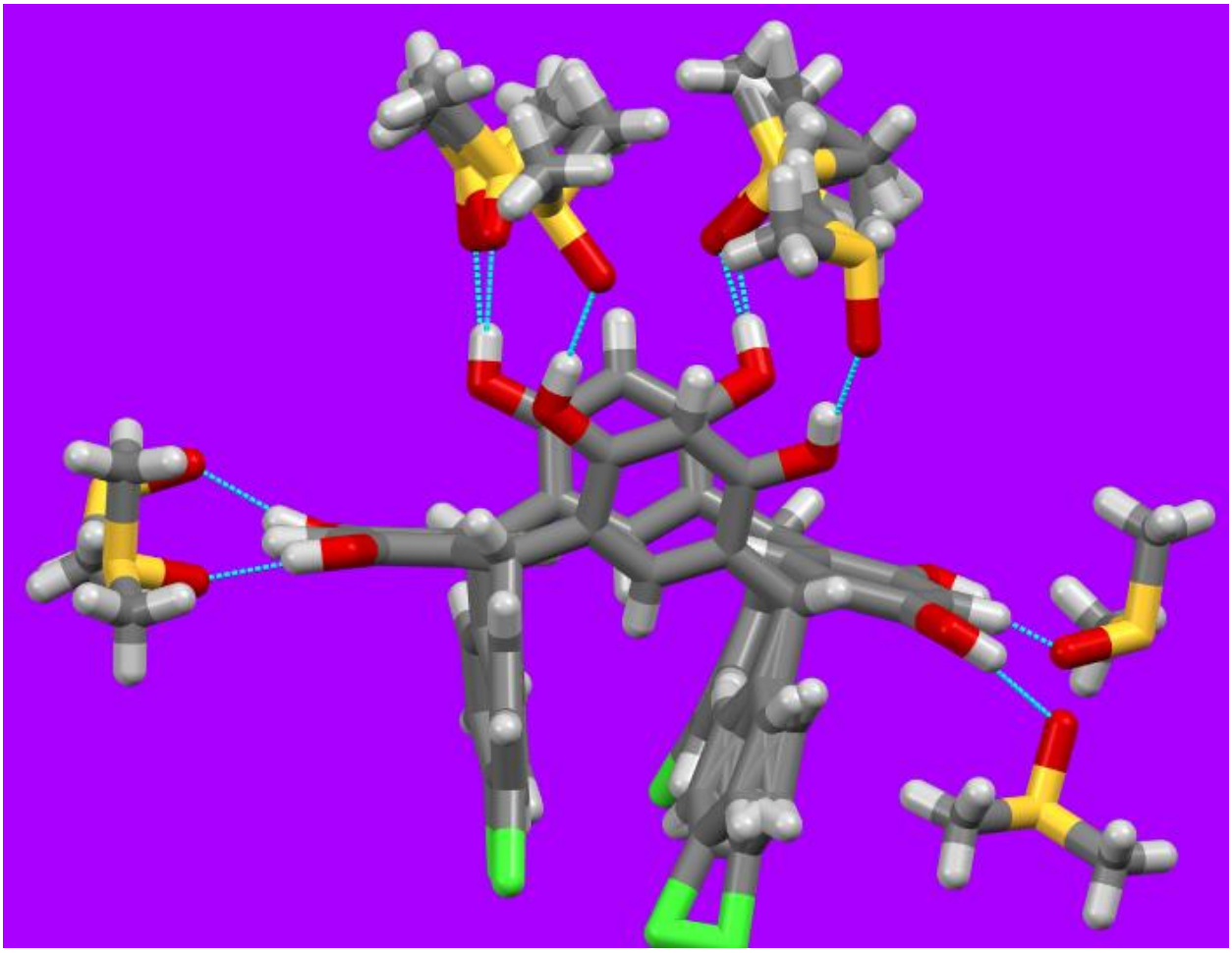

Figure 3.4: BN22E crystal structure grown in DMSO showing the orientation of the rings

The H-NMR data of the single crystals obtained from the filtrate (see **Appendix C4**) of BN22M reveal that the conformation of the crystals is same as that of BN22E. This suggests that synthesizing in methanol yields a mixture of two conformations with the cone conformation

obtained as powder and the 1,3-alternate remaining in solution and crystallizing out upon slow evaporation of the solvent.

Comparing the ^{13}C-NMR spectrum of the BN22E@DMSO-d_6 and BN22M@DMSO-d_6 (***Figure 3.3*****;** *page* ***61*****)**, we find that BN22M has two signals less than BN22E. The signals in BN22M appear shifted compared to those of BN22E. The signals at 120.75 ppm and 120.83 ppm in BN22E, combine to give a signal at 120.36 ppm in BN22M while the signals at 153.20 ppm and 153.35 ppm in BN22E combine to give a signal at 153.39 ppm in BN22M. A closer look indicates that only the signals due to the carbon atoms and protons on the resorcinol ring and the methine show considerable changes. The signals arising from the chlorine bearing rings (whether carbon or proton) do not show significant change in chemical shifts. This indicates that in both BN22E and BN22M, the environment of the chlorine bearing rings remains practically unchanged.

To further investigate solvent interaction involving BN22M, the H-NMR spectroscopy of the sample was carried out in different deuterated solvents and the result is shown in ***Figure 3.5***. The H-NMR spectra of sample in deuterated methanol, acetone, tetrahydrofuran, and acetonitrile appear very similar suggesting that the nature of the interaction of the sample with the solvent is similar for these solvents. The H-NMR spectra of the sample in DMSO has been discussed above. In the case of pyridine however, it is observed that the spectrum is markedly different for the others. The remarkable difference observed between the H-NMR spectrum of the compound in pyridine and in the other solvents likely arises from the fact pyridine deprotonates the compound thereby distorting the electronic environment around the compound.

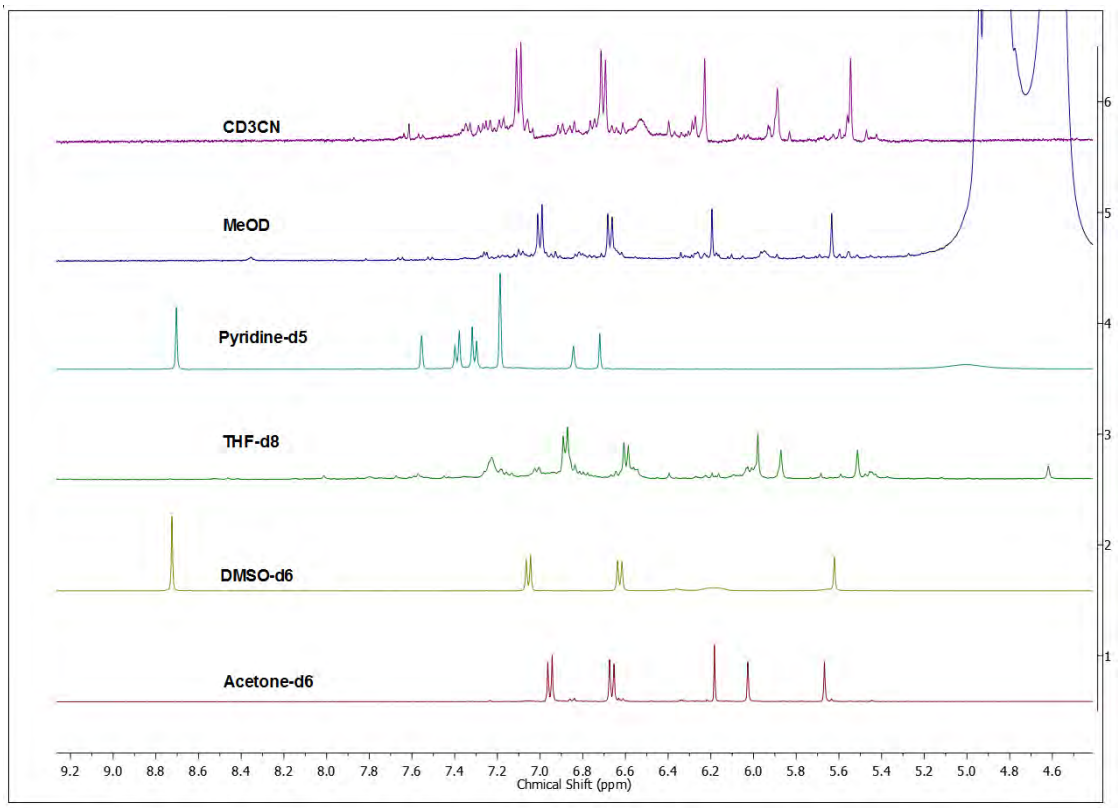

Figure 3.5: H-NMR spectra of BN22M in different solvents

DSC analysis (details will be discussed in the section 3.8 pg 78) of the BN22E powder represented in ***Figure 3.16*** (page ***79***) shows an exothermic event at 251 °C and an endothermic event at 407 °C in addition to the solvent ascribed event occurring between 50 and 80 °C. While the peak at 407 °C is associated with melting, TGA thermogram showed no mass loss at 251 °C, suggesting that the DSC peak at this temperature is due to a structural change. The narrowness of the melting peak in the DSC suggests that the compound is obtained in appreciably high purity. BN22M also shows an exothermic structure change at 247 °C before subsequently melting at 425 °C compared to than BN22E which melts at 407 °C.

The H-NMR spectrum of *p*-ClBPE@DMSO-d_6 represented in in ***Figure 3.6a(i)*** show signals at 4.98 ppm (s, 2H), 5.65 ppm (s, 4H), 5.91 ppm (s,2H), 6.61 ppm (d, 8H), 6.98 ppm (d, 8H), 7.68 ppm (s, 4H), 7,76 ppm (s, 4H), 7.81 ppm (s, 2H), and 7.98 ppm (s, 2H). The H-NMR spectra of *p*-ClBPM@DMSO-d_6 (***Figure 3.6*** **a(ii)**) shows similar signals and splitting. The four signals at between 7.68 ppm to 7.98 ppm are assigned to the OH protons based on their integration and the fact that they disappear on addition of few drops of deuterium oxide. The assignment of the pair of doublets was unambiguous while the singlet at 5.65 ppm was assigned to the methine proton

labelled “a”. The lone pyrogallol aromatic proton gives rise to two signals at 4.98 ppm and 5.91 ppm due to adjacent pyrogallol rings having different orientation. The integration and later single crystal data for the compound was used to confirm this assertion. The ^{13}C-NMR spectra of *p*-ClBPE@DMSO-d$_6$ (***Figure 3.6b***) gives the same results as that of *p*-ClBPM@DMSO-d$_6$. The signal at around 42 ppm is assigned to the methine carbon while the aromatic protons are clearly seen between 120 -150 ppm. The splitting pattern observed in these compounds is similar to reports by Gutsche [153] and Hogberg [154].

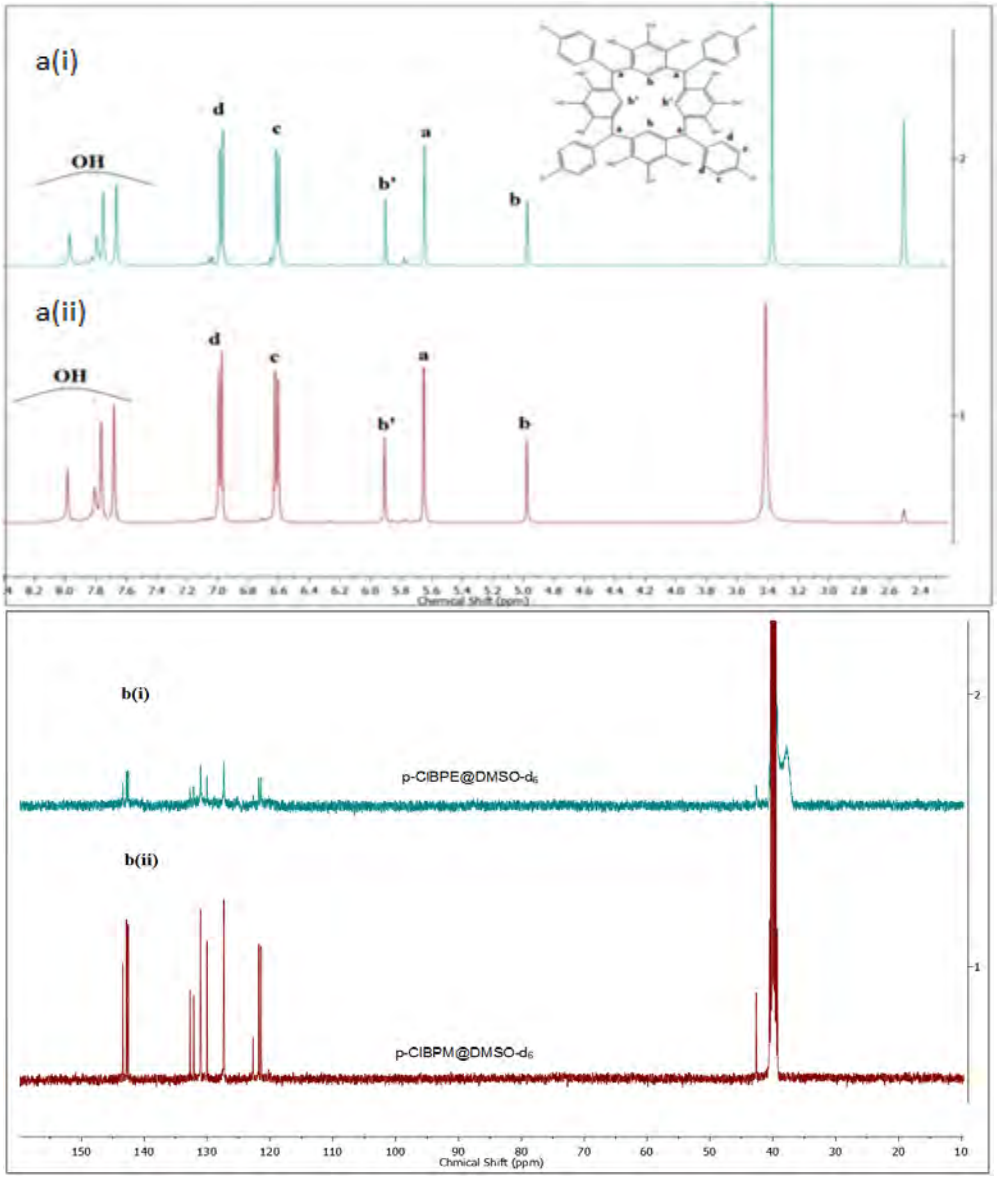

Figure 3.6: (a): H-NMR spectra of a(i) p-ClBPE@DMSO-d6 and a(ii) pClBPM@DMSO-d6 **(b)** ^{13}C-NMR spectra of p-ClBPE

Pale yellow hexagonal block single crystals of BN22E suitable for analysis were grown by slow evaporation from concentrated solution of DMSO. The compound crystallizes in the space groups *P-1* with eight molecules of DMSO (***Figure 3.4*** see page ***63***) in the unit cell. Two of the DMSO molecules and one of the chlorine bearing rings are disordered between two positions. The resorcinol backbone rings adopt a 1,3-alternate-like configuration (with a pair of opposite resorcinol rings lying flat in the equatorial position and the other pair vertically oriented) while the chlorine bearing rings are on the other side of the molecule.

Table 3.1: Selected crystallographic data and bond lengths (Å) and angles (º) for BN22 and *p*-ClBP

Compound	BN22	p-ClBP
Weight (g/mol)	928.12	994.64
Color	Light orange	Arsh
System	Triclinic	Triclinic
Space group	P-1	P-1
Temperature (k)	200	200
a(Å)	13.011(5)	10.925(11)
b(Å)	13.964(5)	13.729(12)
c(Å)	20.922(7)	14.701(13)
α(Å)	83.235(1)	90.038(7)
β(Å)	79.213(1)	106.329(8)
γ(Å)	70.647(1)	105.715(8)
V(Å)	3769.74	2029.97
GOOF	1.099	1.001
Z	1	1
R-factor	0.0742	0.0645
F(000)	928	935

BN22

Atom 1	Atom 2	Bond length
CL00	C01S	1.7379
Cl1	C023	1.7505
CL3	C021	1.7459
CL1A	CL1B	1.2578
O00G	H27	0.8455
O00H	H26	0.8543
O00I	H17	0.8582
O00J	H28	0.8202
O00K	H29	0.8424
O00D	H18	0.7777
O00E	H30	0.7607
O00F	H25	0.8051

p-ClBP

Atom 1	Atom 2	Bond length
CL1	CL2	1.739
CL2	C25	1.739
CL1	C12	1.739
O1	H1A	0.819
O4	H4	0.820
O5	H5	0.820
O6	H6	0.821
O9	H9	0.820
07	H7	0.822

The hydroxyl groups on the resorcinol rings each connect to a DMSO molecule through a single hydrogen bond as depicted in ***Figure 3.4*** (page ***63***). The four chlorine atoms in the molecule do not take part in hydrogen bonding. The overall supramolecular assembly when viewed along the *a*-axis portrays rectangular channels (***Figure 3.7d*)** along which the eight DMSO molecules are located. The packing diagram of BN22E reveals that the DMSO molecules are not found inside the cavity of the compound but rather along channels formed by the supramolecular assembly (***Figure 3.7d*).**

Light-orange single crystals of *p*-ClBP suitable for single crystal analysis were obtained from DMF. Like the BN22E, the compound crystallizes in the space group *P-1* with each tetra-(*p*-chlorophenyl)pyrogallol[4]arene molecule connected to a DMF molecules via hydrogen bonding. Each unit cell contains two molecules of *p*-ClBP and two molecules of DMF. As in the case with BN22E, the chlorine atoms do not take part in hydrogen bonding. The space filling packing diagram of the compound (probe radius of 1.2 Å and grid spacing of 0.7 Å) reveals a porous 3D channel system (Figure 3.7***b*** and ***c***) with an accessible volume of 12.6 % of the unit cell volume derived using the mercury CCDC software. The overall supramolecular assembly presents a layered structure in which the DMF molecules occupy the interlayer channels when viewed down the *a* axis (Figure 3.7***c*** and ***d***).

Unlike in BN22E where all the OH groups take part in hydrogen binding, in *p*-ClBPE, only one of the OH groups are involved in hydrogen bonding. This observation confirms the deductions from the FTIR spectra with regards to hydrogen bonding.

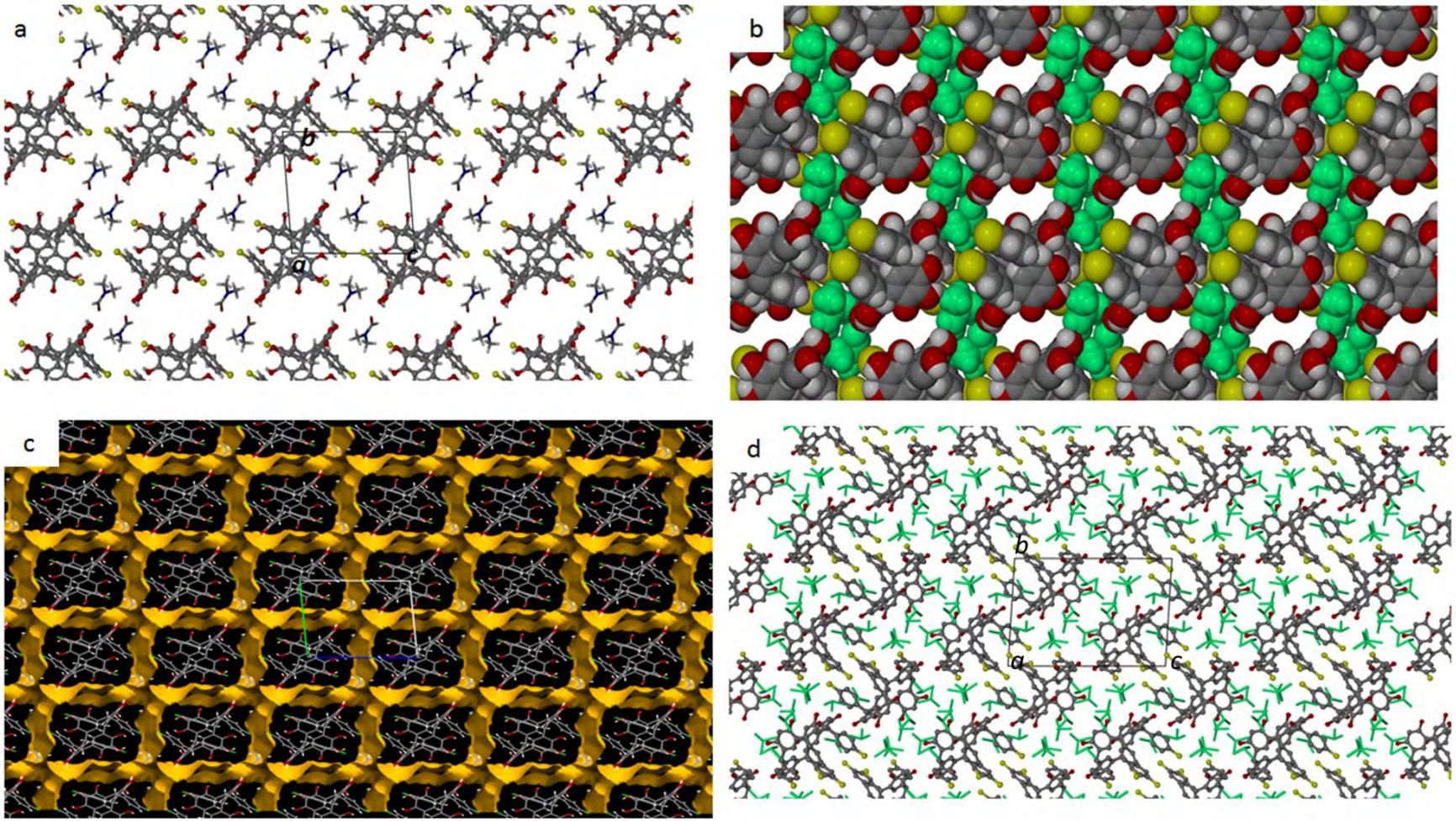

Figure 3.7: (a) Packing of *p*-ClBP along *a*-axis (b) Space filling model of *p*-ClBP showing the solvent (green) and unoccupied channels white (c) packing of *p*-ClBP showing 3D (Mercury derived [155]) available channels along *a*-axis (d) packing of BN22 showing the solvent molecules (green) down *a* axis [additional images of the pore system of p-ClBP are shown in appendix H]

3.5 Vapor sorption studies and host-guest complexes

The ability of any compound to selectively adsorb certain organic compounds, be it in the vapor or liquid state, is of paramount importance to the industry since many industrial processes require the separation and recovery of some organic components from mixtures and solutions. In this regard, there have been reports of calixarene films for separation and recovery of various organic and inorganic species [156]. The porous nature and π-electron rich cavity of calixarenes provide the basis of interactions with the host and consequent sorption properties.

For the vapor sorption studies reported in this work, the capacity of the desolvated powders to adsorb solvent vapors when suspended above a solution was investigated. For this study, only the ethanol obtained samples were used. ***Figure 3.8*** shows a cartoon diagram of the experimental setup for the solvent studies. Two separate systems were investigated; a mixture of two high boiling liquids DMSO and H_2O and a mixture of a high boiling liquid and a low boiling liquids DMSO and MeOH were investigated. While separation of the latter is expected to be considerably easy by means of fractional distillation, the former, despite the significant difference in boiling points of the components is energy-intensive, necessitating other separation alternatives.

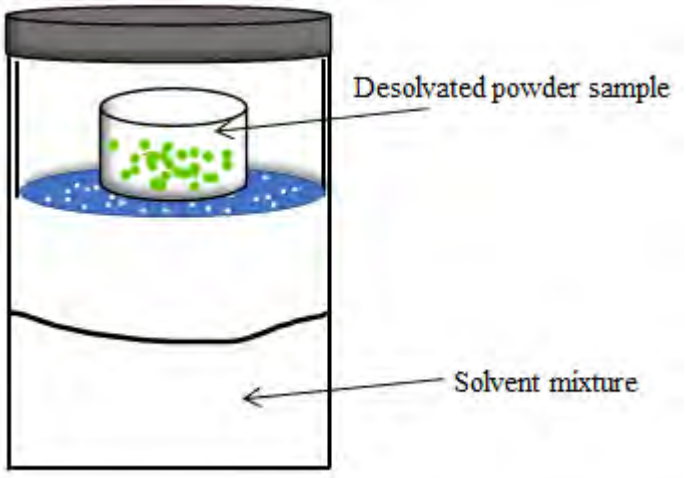

Figure 3.8: Cartoon representation of the experimental setup for solvent sorption studies

Prior to the sorption studies, the host powders were heated to and maintained for ten minutes at 200 °C for complete desolvation and thereafter suspended over the vapor of the liquid mixtures in a sealed vial for 72 hours. Ten millilitres of the liquid mixtures were typically used and prepared by mixing the respective liquids in the following ratios 0:10, 1:9, ……, 9:1, 10:0. After the incubation period, the samples were analyzed by means of FTIR, H-NMR, TGA-IR, DSC, and

PXRD. In cases involving methanol as guest, the analysis was run as soon as the sample was removed from the vial to minimize any potential loss of methanol.

3.6 Results and discussions for sorption studies involving BN22E

For this section, presentation of and discussion of results will focus on the solution systems DMSO 10:0, DMSO/MeOH 5:5, DMSO/MeOH 0:10, DMSO/H_2O 5:5, and DMSO/H_2O 0:10. The other results not included here are indicated in the appendix D and E.

The FTIR spectra of the samples in both the methanol/DMSO and water/DMSO systems as shown in ***Figure 3.9*****,** reveal a shift of the υOH band of BN22E from 3500 cm^{-1} to about 3100 cm^{-1} which does not occur in the case compound exposed to pure water. This red shift to lower frequency indicates a stretching of the OH bond of BN22E due to an increase in H-bond strength because of the adsorption of the DMSO. The δC-O-H in-plane vibrational band at 1267 cm^{-1} in the desolvated sample also shifts to lower frequency confirming an increase in strength of hydrogen bonding in the host-guest complexes [149]. The characteristic band of the DMSO is indicated with the orange band in ***Figure 3.9***.

When the sample is exposed to absolute methanol, the υOH stretch shows very slightly to lower frequency but also broadens. This suggests the formation of hydrogen bonds as well between the calixarene and the methanol guest. The in-plane OH bending vibrational band (δC-O-H) also witnesses a shift to lower frequency confirming the strengthening of the hydrogen bonds. However, when the position of the OH band in the DMSO/MeOH system is compared for different solvent mixtures, it is observed that the change in wave number is greater when DMSO is adsorbed than methanol indicating that stronger interactions are formed between the host and DMSO than with methanol as guest.

In the case of DMSO/H_2O system, the FTIR spectra for all samples (except for absolute water) show a similar pattern. The presence of adsorbed DMSO is indicated by the very intense characteristic band near 1000 cm^{-1} (shaded in green) [149,157]. The υOH band in the case of the DMSO/MeOH shifts to lower wave number indicating the strengthening of the hydrogen bonds. When exposed to absolute water, the FTIR spectra of the sample shows no difference compared to the dehydrated sample suggesting that water is not adsorbed by the desolvated BN22E.

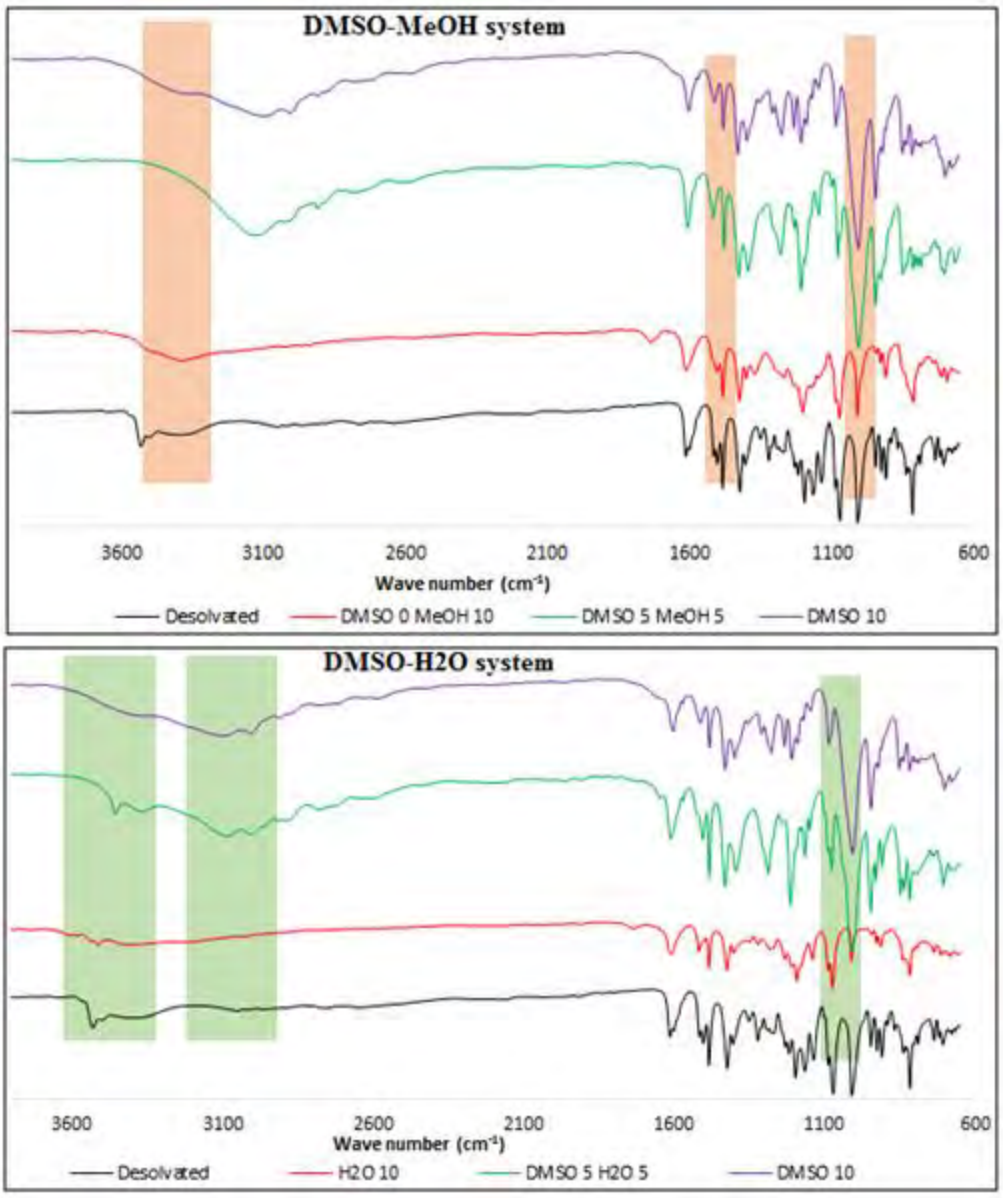

Figure 3.9: Infrared spectra of the samples of BN22E obtained from different vapor systems

Thermal analysis of the desolvated and resolvated samples was also used to ascertain and quantify the amount of adsorbed guest. Data from both DSC and TGA shown in ***Figure 3.10*** indicate the release of adsorbed DMSO occurs in a series of steps and is dependent on the amount of DMSO in solution mixture. The intermolecular interactions of the DMSO with the host is strong such that temperatures exceeding 200 ^{o}C is required to completely remove all DMSO guest molecules. These strong interactions explain why DMSO is adsorbed at the expense of either water or methanol even though both water and methanol are capable of also forming hydrogen bonds.

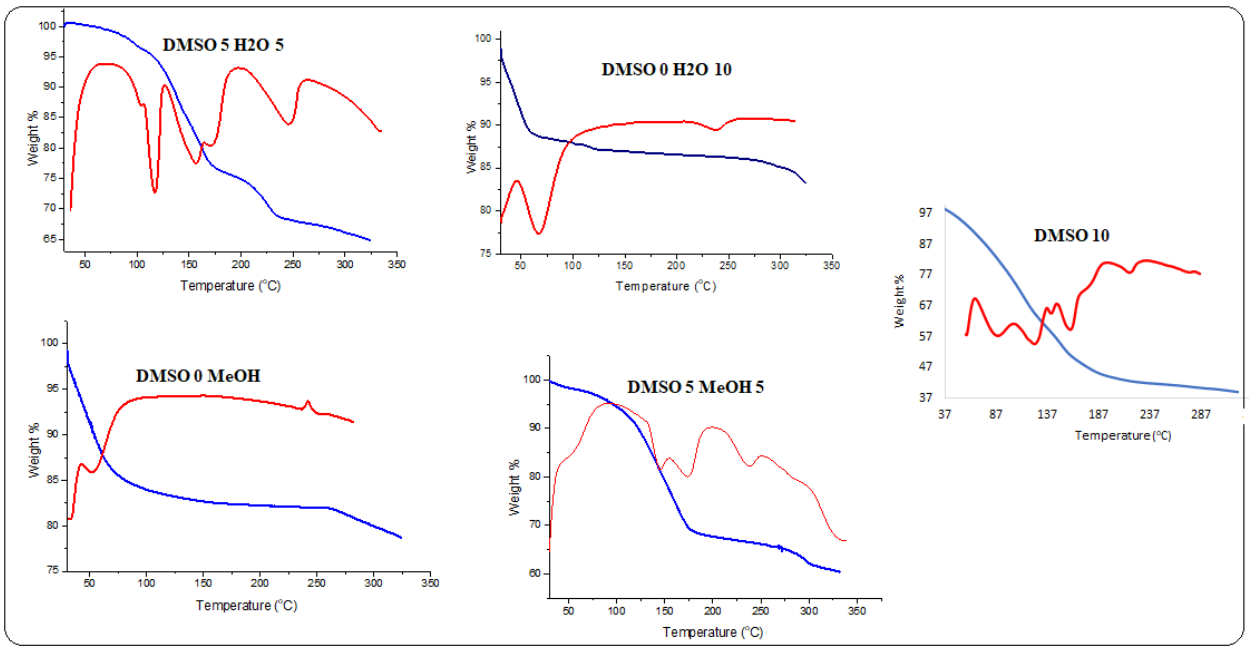

Figure 3.10: DSC and TGA graphs of the powders suspended over different solvents systems [the DSC curves are indicated in red]

Looking at the DSC data of both DMSO/MeOH and DMSO/H_2O systems, (***Figure 3.10***), when the calixarene is suspended over pure DMSO, the evolution of surface bound DMSO guest molecules occurs at about 60 ºC. However, for the mixed solvent systems (see **Appendix E2** and **E3**), no thermal events are observed in the regions near 60 ºC suggesting that surface adsorption of neither DMSO, water or methanol occurs. This supports the suggestion that competing guest vapors reduces DMSO sorption. In absolute methanol or water, however, there is some surface adsorption although the interaction is very weak, such that they are easily evolved at temperatures from 40-60 ºC. The presence of an endothermic peak at 138 ºC (when the sample is exposed to absolute water) is assigned to a structural change as there is no corresponding observed mass loss at this temperature on the TGA thermogram. This supports evidence form the PXRD studies. In the presence of absolute methanol, the host compound undergoes an exothermic structural change at 262 ºC. These changes are confirmed by the absence of mass loss on the TGA curves at the respective temperatures for which peaks were observed in the DSC.

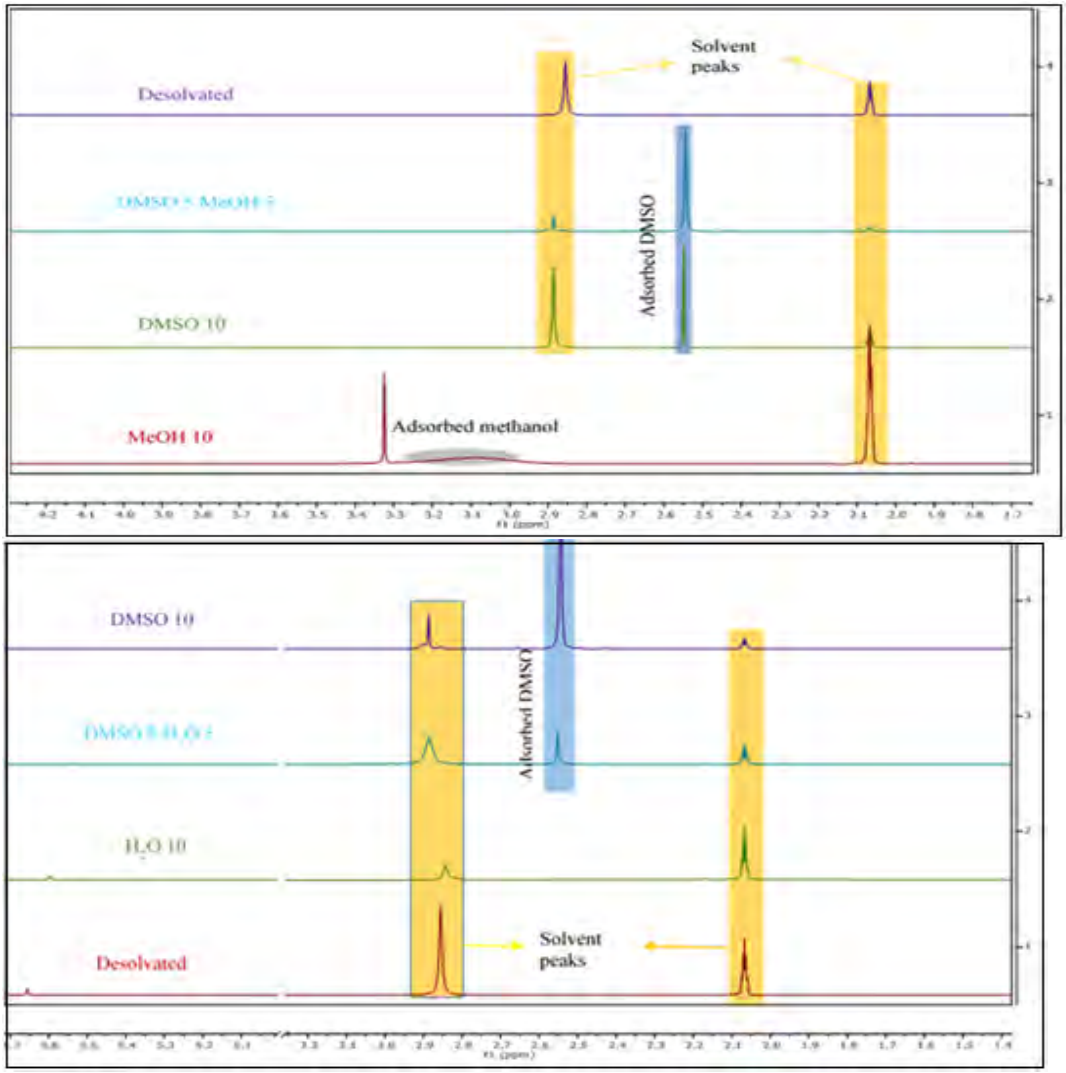

Figure 3.11: Section of the HNMR spectra of samples obtained from (top) methanol/DMSO and (bottom) water/DMSO system [the other section of the spectra is discussed in the section regarding structural changes]

Proton NMR spectroscopy was also used to characterize the host-guest complexes. ***Figure 3.11*** shows part of the spectra from 1 to 5 ppm, the aromatic region of the spectra is discussed in the section on structural changes (section 3.8 pp. 80). The NMR studies were carried in deuterated acetone. In the case of DMSO/MeOH system, the signal of the DMSO appeared at 2.55 ppm, a shift of 0.05 ppm when compared to pure DMSO. When exposed to absolute methanol, the H-NMR spectrum shows a broad signal between 3.0-3.2 ppm and a singlet at 3.35 ppm (respectively assigned to OH and CH_3 of methanol) suggests that methanol had been adsorbed. Similarly, in the case of DMSO/H_2O system, the DMSO signal is observed at 2.27 ppm a shift of 0.07 ppm, which indicates the adsorption of DMSO. In the case of absolute water, the H-NMR of the sample after

the incubation period remains largely unchanged. However, given that the H-NMR was carried out in deuterated methanol, it is inconclusive from these results is water is adsorbed given the fact that proton exchange is possible in methanol-d_4.

Room temperature PXRD was also used to characterize selected powders after incubation with the vapors (See **Appendix F1** for complete PXRD). Prior to the PXRD studies, the crystalline powder was desolvated and preserved in a desicator. PXRD of the vapor exposed samples were performed and compared to the pattern of the desolvated sample to verify structural transformations due to adsorbed vapors. The PXRD pattern reveal that the host material is crystalline. The diffractogram (***Figure 3.12***) indicates changes when the host interacts with both water and DMSO although the changes are more pronounced in the case where DMSO is adsorbed. The interaction of the sample with DMSO leads to a reduction in the number of diffraction peaks indicating an increase in amorphous character of the sample[158,159]. On the other hand, an increase in the number of peaks when the sample is exposed to absolute water suggests that there is the formation of a new phase. This suggest that there is an interaction between the desolvated BN22E sample and water possibly leading to a host-guest complex.

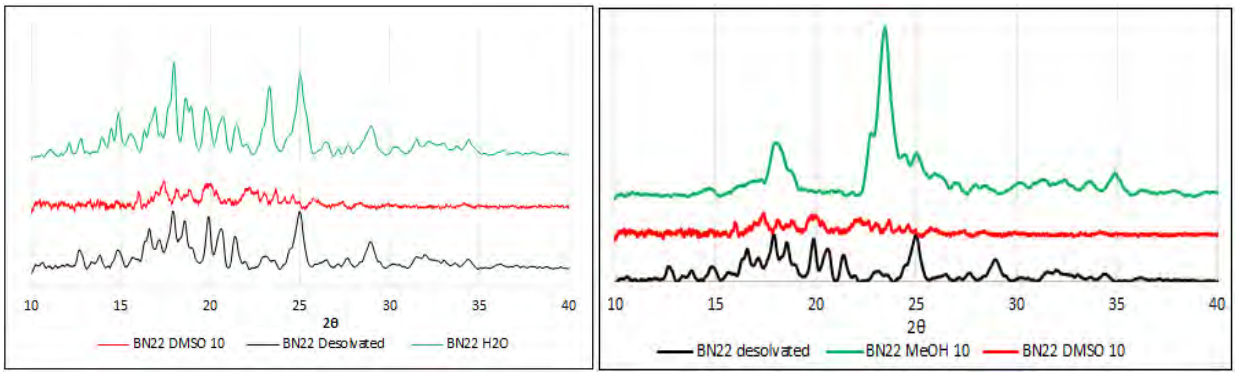

Figure 3.12: PXRD pattern for BN22E exposed to water and DMSO

In all cases, the data from both IR, TGA, DSC, and PXRD indicate the presence of DMSO in the powder indicating that there is preferential vapor adsorption. Despite water and methanol capable of forming stronger intermolecular hydrogen bonds than DMSO, we postulate that the selective adsorption of DMSO by BN22E should be due to its size. Even though DMSO is not found inside the cavity of the host, it appears the size of the rectangular channels shown in ***Figure 3.7*** (*page **69***) will fit DMSO molecules better than water or methanol. The host-guest size complementarity should, therefore, favor the selective adsorption of DMSO over methanol and water.

Despite methanol having a higher vapor pressure than DMSO, at higher mole fractions of methanol, DMSO is still adsorbed indicating that the vapor pressure at least for methanol does not influence the preferential adsorption of DMSO. Methanol and water are only adsorbed in cases where there is no competing solvent. Furthermore, the amount of adsorbed DMSO is generally, directly proportional to the amount in solution (***Figure 3.13***); reasonably because of increase in the amount of DMSO in the vapor phase.

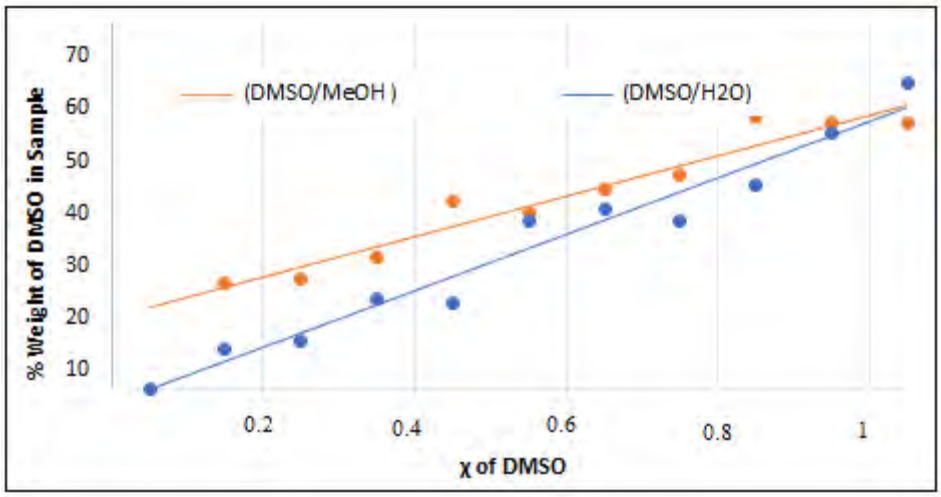

Figure 3.13: Percentage weight of DMSO adsorbed by BN22E versus mole fraction in solution for the DMSO/H_2O and DMSO/MeOH systems

To explain the decrease in amount of adsorbed DMSO as the amount or either water or methanol is increased, we suggest that the presence of either methanol or water vapor causes the opening of channels and together with hydrogen bond competition some of the DMSO molecules go through the structure unadsorbed. Again, the adsorbed DMSO does not get released in one step as revealed by the TGA and DSC data in (***Figure 3.10*** *page* ***73***) but in a series of steps that range from three to five depending on the composition of the mixture. At lower mole fraction of DMSO, the adsorbed molecules are generally released in three steps while at higher mole fractions, the release occurs in five to six steps, depending on the composition of the liquid phase.

3.7 Sorption studies involving pClBP

A similar approach followed above for BN22E was applied here to pClBP powders.

In both the methanol/DMSO and water/DMSO systems, characteristic infrared symmetric S=O stretching bands of DMSO were observed near 1000 cm^{-1} and the asymmetric stretch near 1500 cm^{-1}. The shifts in the bands of the host confirm that there is an interaction between the host and the guest DMSO as shown in the FTIR spectra in ***Figure 3.14***. It is also observed that as the DMSO

is adsorbed by the host, the symmetric S=O stretching band near 1000 cm^{-1} become more intense. The FTIR spectra of the sample shown in ***Figure 3.14*** reveals that when the sample is exposed to pure methanol or water adsorption does not occur.

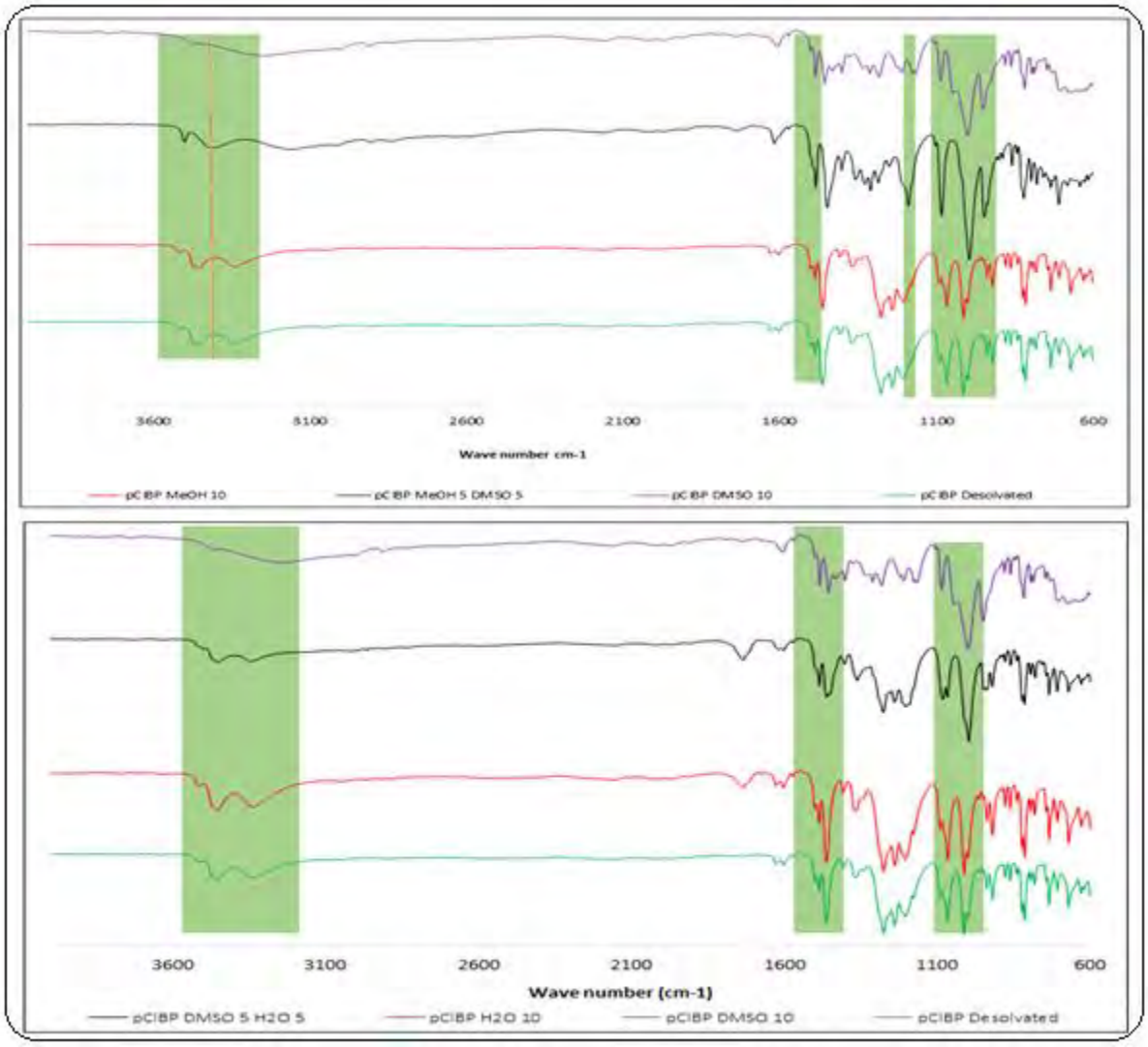

Figure 3.14: FTIR spectra of *p*-ClBP exposed to (top) DMSO-methanol mixtures (bottom) DMSO-H_2O mixtures

The adsorption of guest DMSO was also confirmed by means of evolved gas analysis (Appendix D2). Both TGA and DSC analysis suggest that neither water nor methanol is adsorbed by pClBP. As in the case of BN22E, the amount of DMSO adsorbed increases with increased mole fraction in solution although less DMSO is adsorbed compared to the BN22E. The adsorption of DMSO in the DMSO/MeOH follows a linear relation whereas that on DMSO/H_2O appears to follow an exponential relation (***Figure 3.15***). The amount of DMSO adsorbed adsorbed at mole fraction of 0.9 DMSO differ very little. The higher adsorption in DMSO/MeOH suggests that the adsorption

is proportional to the strength of intermolecular interactions. With *p*-ClBP having four more oxygen atoms than BN22E, it is expected that the molecule is more sterically hindered compared to BN22E explaining the reduced amount of adsorbed DMSO.

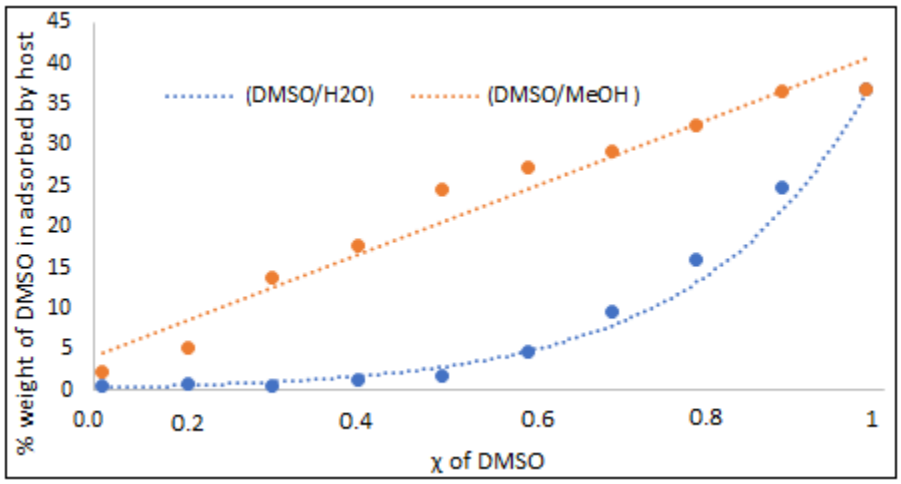

Figure 3.15: Percentage weight of DMSO adsorbed by *p*-ClBP versus mole fraction in solution for the DMSO/H_2O and DMSO/MeOH systems

The TGA data (***Figure 3.16***) also reveals that for the same mole fraction of DMSO in solution, there is more adsorption in the DMSO-methanol system compared to the DMSO-water system. This should arise from the fact that the interaction in solution between water and DMSO is much stronger than methanol and DMSO [160].

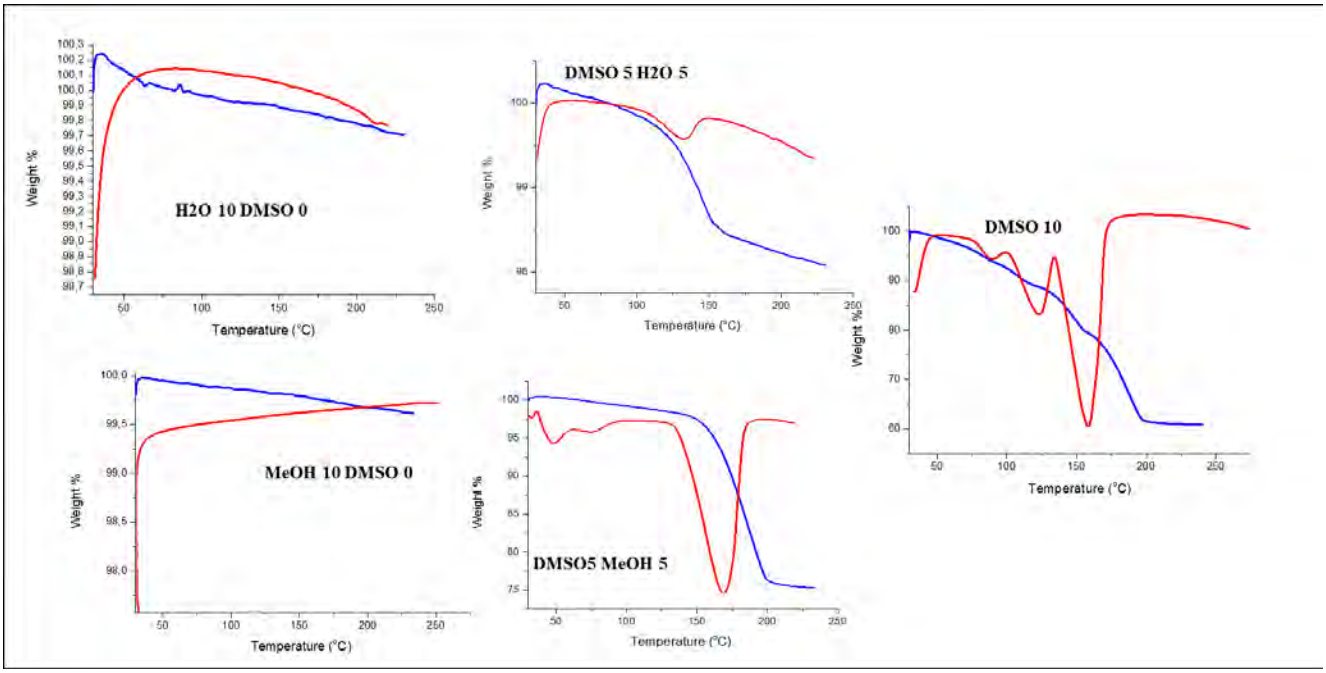

Figure 3.16: TGA (blue) and DSC (red) thermograms of *p*-ClBPE exposed to different mole fractions of solvent vapors

It is observed from both the FTIR and thermal investigation that significant differences are only observed in the product when the amount of DMSO in solution exceeds 20 percent. In the case of BN22E; however, it is observed that the host can adsorb DMSO at 10 % DMSO in solution (see **Appendix E**). This shows that the (*p*-tetrachlorophenyl)resorcin[4]arene (BN22E) is more sensitive to DMSO than the (*p*-tetrachlorophenyl)pyrogallol[4]arene.

The PXRD patterns for the samples after exposure to different solvents vapors are shown in ***Figure 3.17.*** Although exposure to absolute methanol or water does not appear to lead to any adsorption, the PXRD of the powder after exposure to water or methanol appear the same but different from water. In the case of BN22E, the PXRD patterns for the sample exposed to absolute DMSO shows more amorphous character compared to all other cases investigated confirming the adsorption of DMSO.

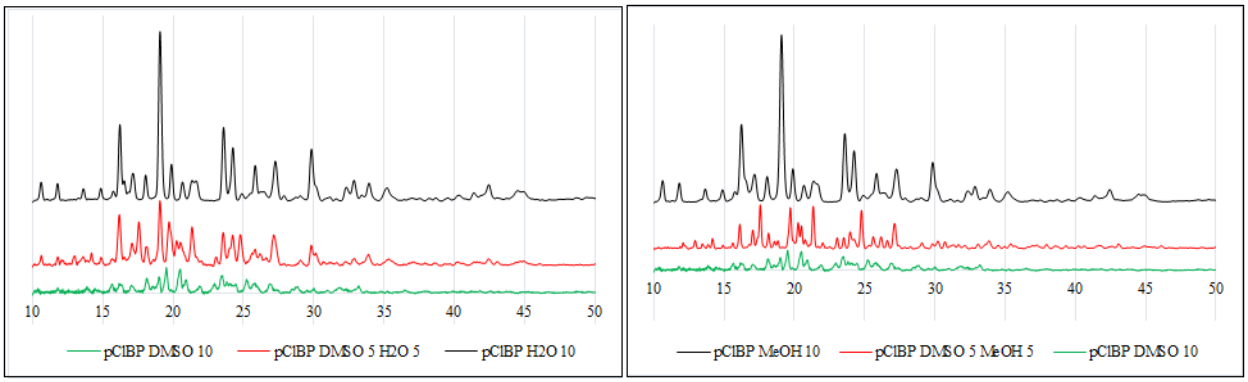

Figure 3.17: PXRD patterns for *p*-ClBPE exposed to different solvent systems and solvent mixtures

3.8 Structural changes involving BN22E

Having confirmed the presence of adsorbed DMSO in both DMSO/H_2O and DMSO/MeOH systems through various techniques, an unusual splitting in the HNMR signals prompted further investigation (***Figure 3.2*** *page* ***61***). **Scheme 3.2** illustrate the investigation that were carried out to understand the structural transformations. We observed that once DMSO is adsorbed by the calixarene, not only do the peaks shift, as expected due to the interaction, and altered magnetic moments, but - there is also a doubling and, in some cases, tripling of some of the proton resonances. This occurs almost exclusively in the aromatic region of the calixarene spectra. The appearance of these new signals suggests that there is formation of a new conformation(s), which possibly results from the flipping of the resorcinolic or *p*-chlorophenyl rings. When the dry sample is exposed to absolute methanol vapor, the resorcinolic signals "H_a" and "$H_{a'}$" and "H_b and $H_{b'}$" coalesce to give two signals whose intensity is comparable to the methine signal. Integration of these signals indicates a 1:1 ratio with the methine signal.

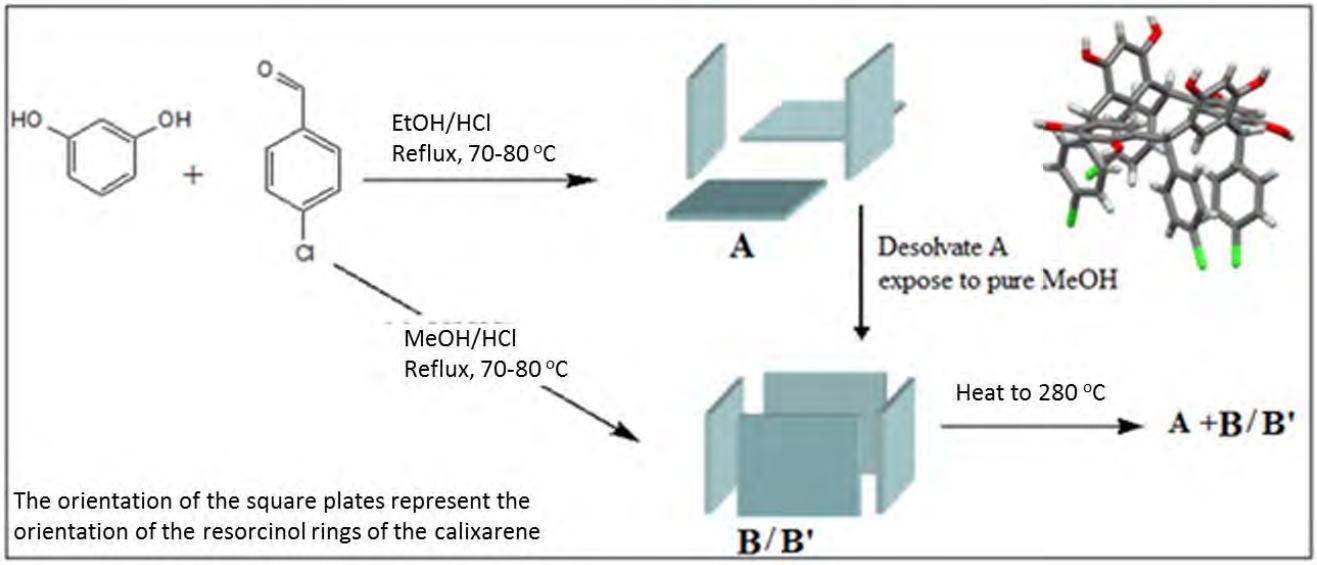

Scheme 3.2: Schematic representation of conformation change when BN22E is exposed to pure methanol and the single crystal XRD of BN22 before exposure. [B and B' have similar but not exact conformations with respect to the resorcinol rings. The schematic representation here is with respect to the resorcinol rings only, the chlorine bearing rings are not shown in the scheme]

The coalescence of the some of the proton signals demonstrate that when the dry powder is exposed to methanol vapor, the equatorial resorcinol rings can adopt different arrangement such that the calixarene adopts a cone or "u, u, u, u" conformation in which the $H_a/H_{a'}$ and $H_b/H_{b'}$ protons are in the same chemical environment. In this case, we also observe the disappearance OH resonances. This is attributed to the fact that when the resorcinol rings are in the vertical arrangement there is a ring of H-bonded OH groups that is possible, running through the eight OHs that could distort the electron density on the OH and consequently causes the signal to broaden to the point that it is not detectable.

On the other hand, when either DMSO or water is adsorbed, $H_a/H_{a'}$ and $H_b/H_{b'}$ do not coalesce. Rather, there is a doubling of resonance signals (when sample is exposed to pure water) particularly for the aromatic protons on the chlorine bearing rings. The intensity of the new peaks and the parent peaks are in the ratio 1:5 respectively suggesting that approximately 20% of the sample gets converted to a new conformation. Although characterization of the powder exposed to absolute water with NMR spectroscopy does not reveal as expected any broad signal to suggest that water is adsorbed, H-NMR spectra does indicate that there is indeed and interaction of the sample with water which subsequently leads to some structural changes.

When the desolvated BN22E sample is exposed to pure DMSO, the signals due to the protons on the chlorine bearing rings triple in an intensity ratio of 7:5:3. This suggests that there are two additional conformations formed. Similar observations of additional signals are made for the other signals.

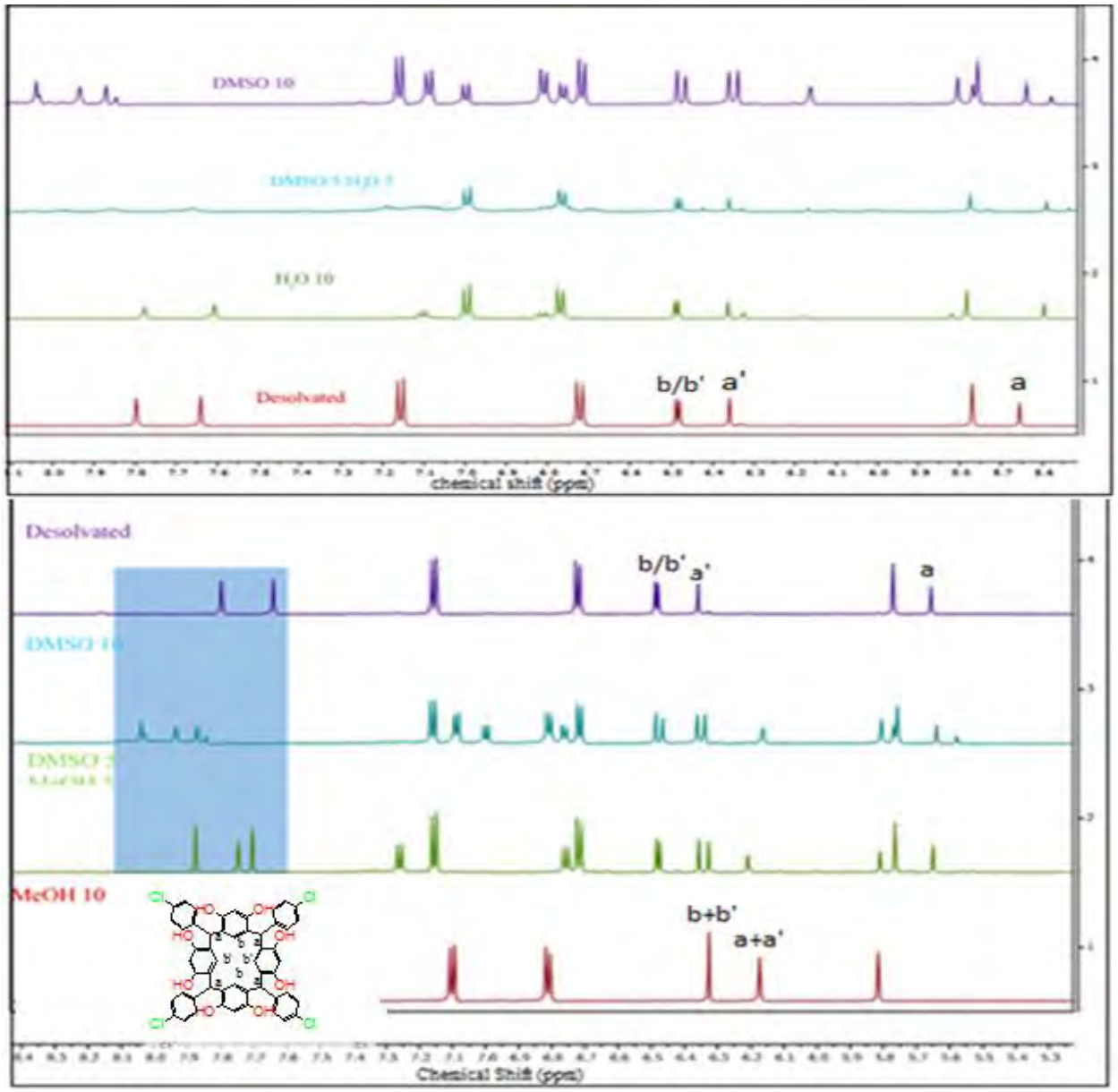

Figure 3.18: H-NMR Spectra of spectra exposed to (top) DMSO/H_2O system (bottom) DMSO/MeOH system

When the sample is exposed to absolute methanol, the new phase formed becomes thermally stabilized by strong hydrogen bonding requiring temperatures exceeding 200 ºC for any structural change as depicted in ***Figure 3.18***. Another observation from the sample exposed to absolute

methanol is the significant interaction between the calixarene and the NMR solvent (acetone-d6) which results in a downfield shift in the signal of the acetone. The acetone most likely takes part in either hydrogen bonding or other intermolecular interactions which results in the shift of the signal.

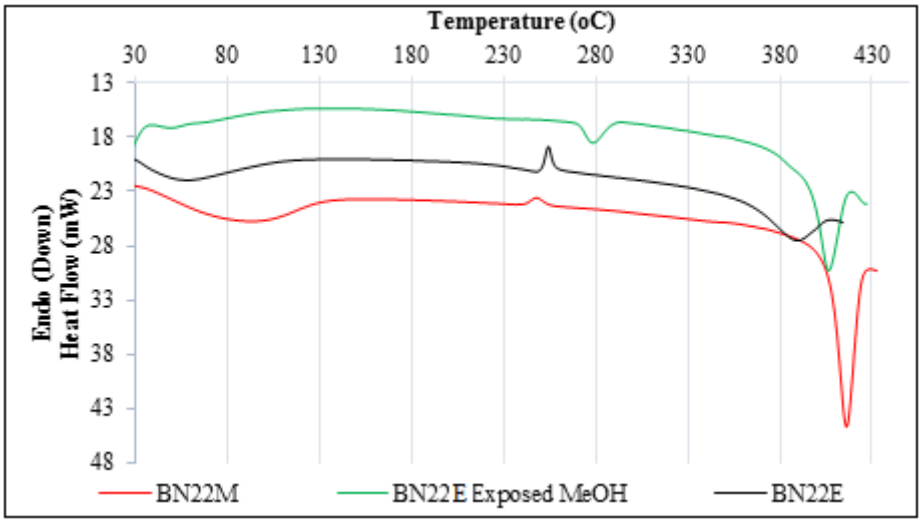

Figure 3.19: DSC thermograms of BN22 as-synthesized and exposed to methanol.

The structural differences the BN22M, BN22E and "BN22E exposed MeOH", are also echoed by the DSC thermograms (***Figure 3.19***). The ethanol synthesized sample has a lower melting point (407 ºC) compared to the same compound obtained by exposing the dried ethanol synthesized powder to absolute methanol (417 ºC) which is different from the methanol synthesized compound (425 ºC). The higher meting points of BN22M and BN22E exposed methanol is likely due to the strong intramolecular hydrogen bonds which form across the OH groups. Furthermore, while the methanol synthesized and the "BN22E exposed MeOH" samples undergo an exothermic structural change near 251 ºC, the ethanol synthesized, sample undergoes an endothermic structure change at 279 ºC. The difference in melting point between two seemingly the same conformations (BN22M and BN22E exposed MeOH) suggests that despite having same conformation with respect to the orientation of the resorcinol rings, these compounds may differ in conformation with regards to the orientation of the chlorinated rings.

Having confirmed that the ethanol synthesized conformation can be converted to methanol synthesized conformation at least with respect to resorcinol ring orientation, we investigated if heating the sample to just beyond the 280 ºC and cooling will lead to initial chair conformation of BN22E. To this end, the BN22E sample was desolvated and exposed to absolute methanol to

achieve the vertical flipping of the equatorial resorcinol rings. Once we had confirmed this vertical flipping from the H-NMR, the sample was then heated to 300 ºC and allowed to cool to room temperature under nitrogen atmosphere after which the H-NMR of the sample was recorded. The H-NMR results depicted in Figure 3.20 indicate that there is a partial conversion of the cone "u,u,u,u" conformation to possibly the chair conformation as evidenced by appearance of the OH proton signals, doubling of the aromatic proton signals on the chlorinated ring and the appearance of multiple signals for the resoncinol proton signals. The obtained product is therefore a mixture of cone conformation and the chair conformation.

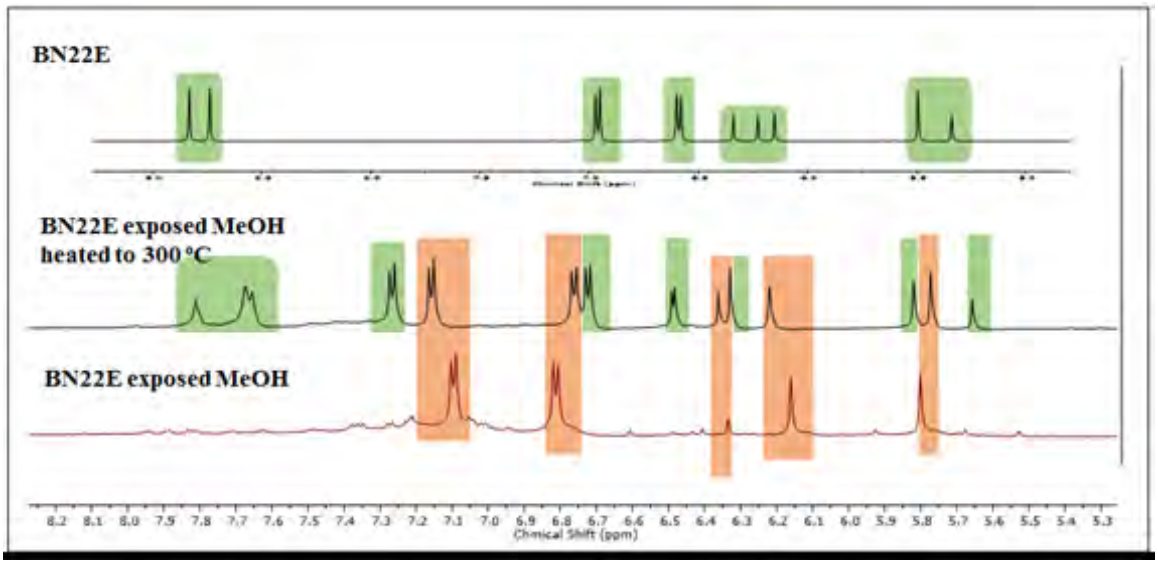

Figure 3.20: HNMR showing structural transformation when BN22 (in DMSO-d6) is exposed to methanol then heated.

The orange shades indicate peaks of sample BN22E exposed to MeOH and the green indicate signals arising from BN22E. The spectra in the middle appears to be a mixture, the top and bottom spectra, despite the upfield shift of the OH protons which possibly results from interactions between the components of the mixture, which are absent in pure BN22E. It will therefore appears that once the equatorial resorcinol rings have been vertically flipped, the process cannot be fully reversed thermally. H-NMR kinetics studies on the "BN22E exposed MeOH" sample was also carried out to determine if the conformation would change in solution. The NMR was recorded in deuterated acetone from 292-314 K and the result is shown in ***Figure 3.21.*** The results indicate that there is almost no change in the signals. This confirms that once vertically flipped, the rings become locked through very strong intramolecular hydrogen bonding interactions which require very high temperatures for any noticeable structural transformation.

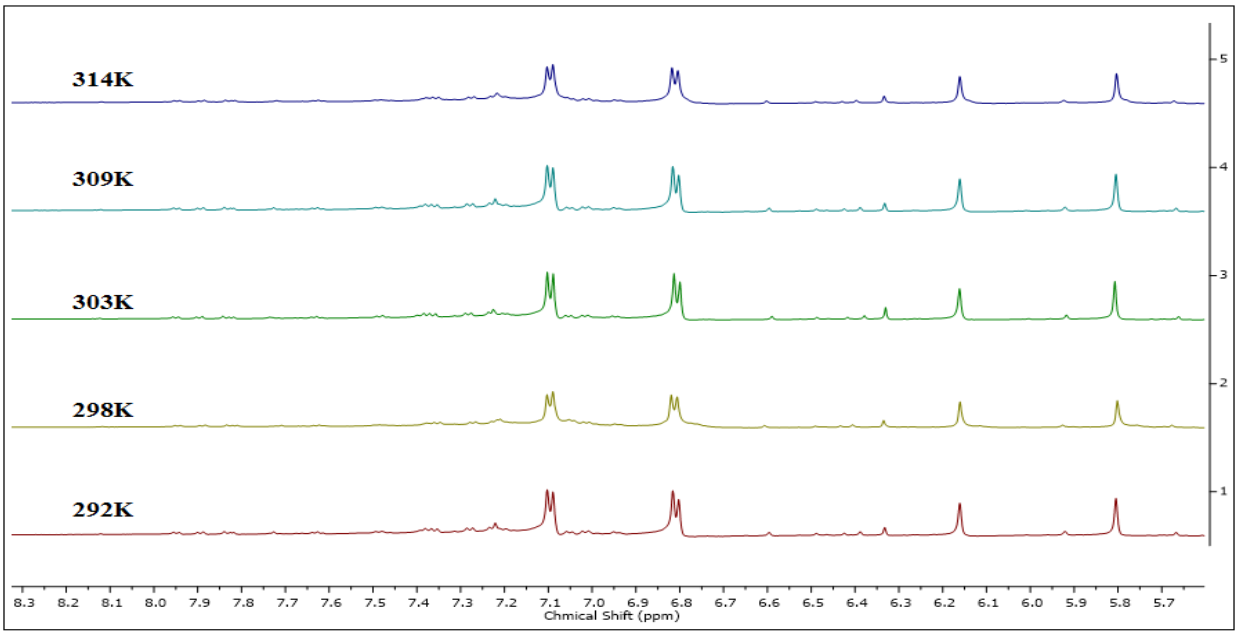

Figure 3.21: Kinetics HNMR for BN22E exposed MeOH

3.9 Conclusions

Two calixarenes were successfully synthesized and characterized based on different techniques. Results indicate that the solvent used has an effect on the conformation of the product in the case of *tetra*-(*p*-chlorobenzyl)resocin[4]arene (BN22). Synthesizing in ethanol favors the 1,3-alternate conformation while using methanol favors the cone conformation. The cone conformation can be obtained by exposing the 1,3-alternate conformation to methanol. Conformational reversibility in the solid state is however not fully possible. The BN22M sample is so stable that temperatures exceeding 200 degrees are required to achieve any meaningful structural change. *tetra*-(*p*-chlorobenzyl)pyrogallol[4]arene (*p*-ClBP) on the other hand appears to show no conformational preference across solvents. The same conformation is obtained irrespective of the solvent used for synthesis. Both compounds (BN22 and *p*-ClBP) can selectively adsorbed DMSO vapors from a mixture of common solvents. BN22 shows a higher sensitivity to DMSO than *p*-ClBP

4 CHAPTER FOUR

This chapter explores the synthesis of cucurbituril metal complexes using four dicarboxylic acids as bridging ligands. Supramolecular one-pot synthesis and mechanochemistry of these complexes and a cationic drug guest is also investigated.

4.1 Synthesis of glycoluril

Urea (1.2 g, 0.02 mol) was dissolved in 40 mL deionized water, and 10 mL of 36 % HCl was added. A thirty per cent glyoxal solution (2 g, 0.01 mmol) was added, and the solution was stirred on a hot plate maintained at 70 ºC for 45 minutes (**Scheme 4.1**). Midway through the 45 minutes, a white precipitate started forming. After cooling, the white precipitate was filtered and washed with water-ethanol solution (1:1) and the powder dried at 50 ºC in an oven. This product was used in the synthesis of cucurbiturils without any further purification.

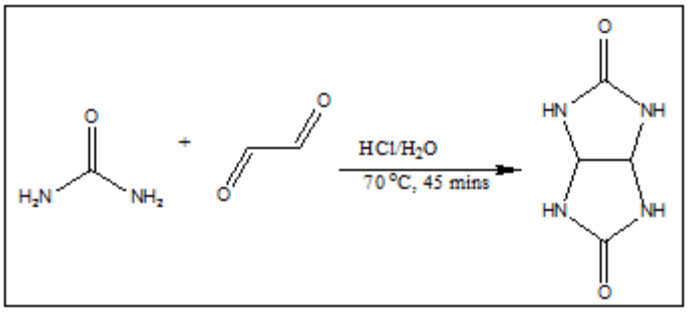

Scheme 4.1: Synthesis of glycoluril

4.2 Synthesis of cucurbituril

To date, the synthesis of cucurbiturils still follows the procedure used by Behrend and colleagues in 1905 [44]. In a typical synthetic procedure, 2 g (0.014 mol) of glycoluril were stirred in a concentrated acid solution (H_2SO_4) until complete dissolution. While still at room temperature, 2.00 mL (0.029 mol) of 40 % formaldehyde solution was added slowly. The temperature of the mixture was raised to 115-120 ºC and maintained as such for 24 hours (**Scheme 4.2**). After cooling to room temperature, the pale-yellow solution was diluted with a 50:50 mixture of methanol and acetone to precipitate the cucurbituril. The precipitate was filtered and washed thoroughly with a mixture of water and ethanol (100 mL) and then dried at 50 ºC in an oven. The crude powder was used as-synthesized for preparation of metal complexes.

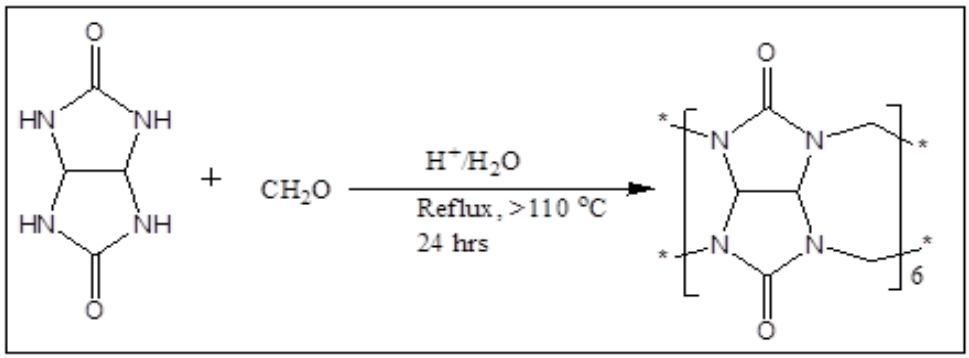

Scheme 4.2: Synthesis of cucurbituril (CB)

4.3 Synthesis of mixed ligand metal complexes

Metal complexes of the cucurbituril were obtained using four dicarboxylate bridging ligands: oxalic acid, malonic acid, succinic acid, and glutaric acid. The following metal salts were used: $MnCl_2 \cdot 4H_2O$, $FeCl_2 \cdot 4H_2O$, $CuCl_2 \cdot 2H_2O$, and $ZnCl_2$.

4.3.1 Synthesis of CB-OxA-Mn complex

Manganese chloride tetrahydrate, 0.120 g; 0.6 mmol; was dissolved in 4 mL of deionized H_2O. The temperature was maintained at 80-90 ºC, and 0.100 g; 0.1 mmol of cucurbituril was added, and the mixture stirred until complete dissolution. Oxalic acid (OxA) (0.036 g; 0.4 mmol) was then added and the solution stirred for a further ten minutes on a hot plate, after which it was allowed to cool. The precipitate formed was filtered out and dried, and the filtrate was left to slowly evaporate in a water bath maintained at 30 ºC in a fume hood. Colorless crystals were obtained within five to seven days (yield ≈ 64 %).

4.3.2 Synthesis of CB-MalA-Mn complex

Manganese chloride tetrahydrate, 0.120 g; 0.6 mmol; was dissolved in 4 mL of deionized H_2O. The temperature was maintained at 80-90 ºC, and 0.100 g; 0.1 mmol of cucurbituril was added, and the mixture stirred until complete dissolution. Malonic acid (MalA) (0.042 g; 0.4 mmol) was then added and the solution stirred for a further ten minutes on a hot plate, after which it was allowed to cool. The solution was then allowed to slowly evaporate in a water bath maintained at 30 ºC in a fume hood. Colorless crystals were formed within five to seven days (yield ≈ 57 %).

4.3.3 Synthesis of CB-SucA-Mn complex

Manganese chloride tetrahydrate, 0.120 g; 0.6 mmol; was dissolved in 4 mL of deionized H_2O. The temperature was maintained at 80-90 ºC, and 0.100 g; 0.1 mmol of cucurbituril was added,

and the mixture stirred until complete dissolution. Succinic acid (SucA) (0.047 g; 0.4 mmol) was then added and the solution stirred for a further ten minutes on a hot plate, after which it was allowed to cool. The solution was then allowed to slowly evaporate in a water bath maintained at 30 ºC in a fume hood. Colorless crystals were formed within five to seven days (yield ≈ 55 %).

4.3.4 Synthesis of CB-GluA-Mn complex

Manganese chloride tetrahydrate, 0.120 g; 0.6 mmol; was dissolved in 4 mL of deionized H_2O. The temperature was maintained at 80-90 ºC, and 0.100 g; 0.1 mmol of cucurbituril was added, and the mixture stirred until complete dissolution. Glutaric acid (GluA) (0.053 g; 0.4 mmol) was then added and the solution stirred for a further ten minutes on a hot plate, after which it was allowed to cool. The solution was then allowed to slowly evaporate in a water bath maintained at 30 ºC in a fume hood. Colorless crystals were formed within five to seven days (yield ≈ 55 %).

4.3.5 Synthesis of CB-OxA-Fe complex

Iron chloride tetrahydrate, 0.120 g; 0.6 mmol; was dissolved in 4 mL of deionized H_2O. The temperature was maintained at 80-90 ºC, and 0.100 g; 0.1 mmol of cucurbituril was added, and the mixture stirred until complete dissolution. Oxalic acid (OxA) (0.036 g; 0.4 mmol) was then added and the solution stirred for a further ten minutes on a hot plate, after which it was allowed to cool. The precipitate formed was filtered out and dried, and the filtrate was left to slowly evaporate in a water bath maintained at 30 ºC in a fume hood. Light brown crystals were formed within five to seven days (yield ≈ 58 %).

4.3.6 Synthesis of CB-MalA-Fe complex

Manganese chloride tetrahydrate, 0.120 g; 0.6 mmol; was dissolved in 4 mL of deionized H_2O. The temperature was maintained at 80-90 ºC, and 0.100 g; 0.1 mmol of cucurbituril was added, and the mixture stirred until complete dissolution. Malonic acid (MalA) (0.042 g; 0.4 mmol) was then added and the solution stirred for a further ten minutes on a hot plate, after which it was allowed to cool. The solution was then allowed to slowly evaporate in a water bath maintained at 30 ºC in a fume hood. Light brown crystals were formed within five to seven days (yield ≈ 50 %).

4.3.7 Synthesis of CB-SucA-Fe complex

Manganese chloride tetrahydrate, 0.120 g; 0.6 mmol; was dissolved in 4 mL of deionized H_2O. The temperature was maintained at 80-90 ºC, and 0.100 g; 0.1 mmol of cucurbituril was added and

the mixture stirred until complete dissolution. Succinic acid (SucA) (0.047 g; 0.4 mmol) was then added and the solution stirred for a further ten minutes on a hot plate, after which it was allowed to cool. The solution was then allowed to slowly evaporate in a water bath maintained at 30 ºC in a fume hood. Light brown crystals were formed within five to seven days (yield ≈ 57 %).

4.3.8 Synthesis of CB-GluA-Fe complex

Manganese chloride tetrahydrate, 0.120 g; 0.6 mmol; was dissolved in 4 mL of deionized H_2O. The temperature was maintained at 80-90 ºC, and 0.100 g; 0.1 mmol of cucurbituril was added, and the mixture stirred until complete dissolution. Glutaric acid (GluA) (0.053 g; 0.4 mmol) was then added and the solution stirred for a further ten minutes on a hot plate, after which it was allowed to cool. The solution was then allowed to slowly evaporate in a water bath maintained at 30 ºC in a fume hood. Light brown crystals were formed within five to seven days (yield ≈ 54 %).

4.3.9 Synthesis of CB-4,4'-OxA-Cu complex

Copper chloride dihydrate, 0.100 g; 0.6 mmol; was dissolved in 3 mL of deionized H_2O. The temperature was maintained at 80-90 ºC, and 0.100 g; 0.1 mmol of cucurbituril was added, and the mixture stirred until complete dissolution. Oxalic acid (OxA) (0.036 g; 0.4 mmol) was then added and the solution stirred for a further ten minutes on a hot plate, after which it was allowed to cool. The sky-blue precipitate formed was filtered out and dried and the filtrate was left to slowly evaporate in a water bath maintained at 30 ºC in a fume hood. Blue cube-shaped crystals were obtained between five to seven days (yield ≈ 61 %).

4.3.10 Synthesis of CB-MalA-Cu complex

Copper chloride dihydrate, 0.100 g; 0.6 mmol; was dissolved in 3 mL of deionized H_2O. The temperature was maintained at 80-90 ºC, and 0.100 g; 0.1 mmol of cucurbituril was added, and the mixture stirred until complete dissolution. Malonic acid (MalA) (0.042 g; 0.4 mmol) was then added and the solution stirred for a further ten minutes on a hot plate, after which it was allowed to cool. The solution was then allowed to slowly evaporate in a water bath maintained at 30 ºC in a fume hood. Blue cube-shaped crystals were obtained between five to seven days (yield ≈ 59 %).

4.3.11 Synthesis of CB-SucA-Cu complex

Copper chloride dihydrate, 0.120 g; 0.6 mmol; was dissolved in 4 mL of deionized H_2O. The temperature was maintained at 80-90 ºC, and 0.100 g; 0.1 mmol of cucurbituril was added, and the

mixture stirred until complete dissolution. Succinic acid (SucA) (0.047 g; 0.4 mmol) was then added and the solution stirred for a further ten minutes on a hot plate, after which it was allowed to cool. The solution was then allowed to slowly evaporate in a water bath maintained at 30 ºC in a fume hood. Blue crystals were formed within five to seven days (yield ≈ 49 %).

4.3.12 Synthesis of CB-GluA-Cu complex

Copper chloride dihydrate, 0.120 g; 0.6 mmol; was dissolved in 4 mL of deionized H_2O. The temperature was maintained at 80-90 ºC, and 0.100 g; 0.1 mmol of cucurbituril was added, and the mixture stirred until complete dissolution. Glutaric acid (GluA) (0.053 g; 0.4 mmol) was then added and the solution stirred for a further ten minutes on a hot plate, after which it was allowed to cool. The solution was then allowed to slowly evaporate in a water bath maintained at 30 ºC in a fume hood. Blue crystals were formed within five to seven days (yield ≈ 55 %).

4.3.13 Synthesis of CB-OxA-Zn complex

Zinc chloride tetrahydrate, 0.080 g; 0.6 mmol; was dissolved in 3 mL of deionized H_2O. The temperature was maintained at 80-90 ºC, and 0.100 g; 0.1 mmol of cucurbituril was added and, the mixture stirred until complete dissolution. Oxalic acid (OxA) (0.036 g; 0.4 mmol) was then added and the solution stirred for a further ten minutes on a hot plate, after which it was allowed to cool. The precipitate formed was filtered out and dried, and the filtrate was left to slowly evaporate in a water bath maintained at 30 ºC in a fume hood. Colorless crystals were obtained after five to seven days (yield ≈ 53 %).

4.3.14 Synthesis of CB-MalA-Zn complex

Zinc chloride tetrahydrate, 0.080 g; 0.6 mmol; was dissolved in 3 mL of deionized H_2O. The temperature was maintained at 80-90 ºC, and 0.100 g; 0.1 mmol of cucurbituril was added, and the mixture stirred until complete dissolution. Malonic acid (MalA) (0.042 g; 0.4 mmol) was then added and the solution stirred for a further ten minutes on a hot plate, after which it was allowed to cool. The precipitate formed was filtered out and dried, and the filtrate was left to slowly evaporate in a water bath maintained at 30 ºC in a fume hood. Colorless crystals were obtained after five to seven days (yield ≈ 57 %).

4.3.15 Synthesis of CB-SucA-Zn complex

Zinc chloride tetrahydrate, 0.080 g; 0.6 mmol; was dissolved in 3 mL of deionized H_2O. The temperature was maintained at 80-90 ^oC, and 0.100 g; 0.1 mmol of cucurbituril was added, and the mixture stirred until complete dissolution. Succinic acid (SucA) (0.047 g; 0.4 mmol) was then added and the solution stirred for a further ten minutes on a hot plate, after which it was allowed to cool. The precipitate formed was filtered out and dried, and the filtrate was left to slowly evaporate in a water bath maintained at 30 ^oC in a fume hood. Colorless crystals were obtained after five to seven days (yield ≈ 54 %).

4.3.16 Synthesis of CB-GluA-Zn complex

Zinc chloride tetrahydrate, 0.080 g; 0.6 mmol; was dissolved in 3 mL of deionized H_2O. The temperature was maintained at 80-90 ^oC, and 0.100 g; 0.1 mmol of cucurbituril was added, and the mixture stirred until complete dissolution. Glutaric acid (GluA) (0.053 g; 0.4 mmol) was then added and the solution stirred for a further ten minutes on a hot plate, after which it was allowed to cool. The solution was filtered, and the filtrate was left to slowly evaporate in a water bath maintained at 30 ^oC in a fume hood. Colorless crystals were obtained after five to seven days (yield ≈ 58 %).

4.3.17 Synthesis of isoniazid Salt

Isoniazid monochloride was prepared following a literature report [161].

4.3.18 Synthesis of isoniazid monochloride (INHCl)

To 20 mL of water, 2.00 g (0.016 mol) of isoniazid was added and stirred until complete dissolution. HCl 1.56 mL of 32 % stock solution (0.016 mol) was added to this solution, followed by 5 mL of deionized water. The solution was stirred at room temperature overnight. The solvent was evaporated and the product dried under vacuum to obtain a pale pink powder. Then, the solvent was evaporated, and the final product was dried under a vacuum (yield ≈ 94 %).

4.4 One-pot synthesis of metal complex-drug supramolecular assembly

4.4.1 Synthesis of CB-Cu-OxA-INHCl

Copper chloride dihydrate, 0.100 g; 0.6 mmol; was dissolved in 3 mL of deionized H_2O. The temperature was maintained at 80-90 ^oC, and 0.100 g; 0.1 mmol of cucurbituril was added, and the mixture stirred until complete dissolution. Oxalic acid (0.036 g; 0.4 mmol) was then added and the

solution stirred for a further ten minutes on a hot plate, after which it was allowed to cool. The sky-blue precipitate formed was filtered out. 0.07 g, 0.4 mmol of isoniazid monochloride INHCl, was added to the filtrate and stirred at room temperature until complete dissolution. The solution was left in a water bath maintained at 30 ^{o}C in a fume hood to evaporate slowly. Blue crystals were obtained between five to seven days (yield ≈ 45 %).

4.4.2 Synthesis of CB-Cu-MalA-INHCl

Copper chloride dihydrate, 0.100 g; 0.6 mmol; was dissolved in 3 mL of deionized H_2O. The temperature was maintained at 80-90 ^{o}C, and 0.100 g; 0.1 mmol of cucurbituril was added, and the mixture stirred until complete dissolution. Malonic acid (MalA) (0.042 g; 0.4 mmol) was then added, and the solution was stirred for a further ten minutes. After cooling to room temperature, 0.07 g, 0.4 mmol, of isoniazid monochloride INHCl, was added to the solution and stirred until complete dissolution. The solution was left to slowly evaporate in a water bath maintained at 30 ^{o}C in a fume hood. Blue crystals were obtained between five to seven days (yield ≈ 44 %).

4.4.3 Synthesis of CB-Cu-SucA-INHCl

Copper chloride dihydrate, 0.120 g; 0.6 mmol; was dissolved in 4 mL of deionized H_2O. The temperature was maintained at 80-90 ^{o}C, and 0.100 g; 0.1 mmol of cucurbituril was added, and the mixture stirred until complete dissolution. Succinic acid (SucA) (0.047 g; 0.4 mmol) was then added, and the solution was stirred for a further ten minutes. After cooling to room temperature, 0.07 g, 0.4 mmol, of isoniazid monochloride INHCl, was added to the solution and stirred until complete dissolution. The solution was left to slowly evaporate in a water bath maintained at 30 ^{o}C in a fume hood. Blue crystals were formed between five to seven days (yield ≈ 49 %).

4.4.4 Synthesis of CB-Cu -GluA-INHCl

Copper chloride dihydrate, 0.120 g; 0.6 mmol; was dissolved in 4 mL of deionized H_2O. The temperature was maintained at 80-90 ^{o}C, and 0.100 g; 0.1 mmol of cucurbituril was added, and the mixture stirred until complete dissolution. Glutaric acid (GluA) (0.053 g; 0.4 mmol) was then added and the solution stirred for a further ten minutes on a hot plate then allowed to cool to room. The solution was then allowed to slowly evaporate in a water bath maintained at 30 ^{o}C in a fume hood. Blue crystals were formed within five to seven days. Isoniazid monochloride INHCl, 0.07 g, 0.4 mmol, was added to the solution and stirred at room temperature until complete dissolution.

The solution was left to slowly evaporate in a water bath maintained at 30 ºC in a fume hood. Blue crystals were formed between five to seven days (yield ≈ 47 %).

4.4.5 Synthesis of CB-Zn-OxA-INHCl

Zinc chloride tetrahydrate, 0.08 g; 0.6 mmol; was dissolved in 3 mL of deionized H_2O. The temperature was maintained at 80-90 ºC, and 0.10 g; 0.1 mmol of cucurbituril was added, and the mixture stirred until complete dissolution. Oxalic acid (OxA) (0.036 g; 0.4 mmol) was then added and the solution stirred for a further ten minutes on a hot plate, after which it was allowed to cool. The precipitate formed was filtered out, and 0.07 g, 0.4 mmol of isoniazid monochloride INHCl, added to the filtrate and stirred at room temperature until complete dissolution. This liquor was left to slowly evaporate in a water bath maintained at 30 ºC in a fume hood. Colorless crystals were obtained after five to seven days in quantitative yield (yield ≈ 43 %).

4.4.6 Synthesis of CB-Zn-MalA-INHCl

Zinc chloride tetrahydrate, 0.08 g; 0.6 mmol; was dissolved in 3 mL of deionized H_2O. The temperature was maintained at 80-90 ºC, and 0.10 g; 0.1 mmol of cucurbituril was added, and the mixture stirred until complete dissolution. Malonic acid (MalA) (0.042 g; 0.4 mmol) was added and the solution stirred for a further ten minutes on a hot plate, after which it was allowed to cool. The solution was filtered, and 0.07 g, 0.4 mmol of isoniazid monochloride INHCl, added to the filtrate and stirred at room temperature until complete dissolution. This liquor was left to slowly evaporate in a water bath maintained at 30 ºC in a fume hood. Colorless crystals were obtained after five to seven days in quantitative yield (yield ≈ 44 %).

4.4.7 Synthesis of CB-Zn-SucA-INHCl

Zinc chloride tetrahydrate, 0.08 g; 0.6 mmol; was dissolved in 3 mL of deionized H_2O. The temperature was maintained at 80-90 ºC, and 0.10 g; 0.1 mmol of cucurbituril was added, and the mixture stirred until complete dissolution. Succinic acid (SucA) (0.047 g; 0.4 mmol) was then added and the solution stirred for a further ten minutes on a hot plate, after which it was allowed to cool. The solution was filtered, and 0.07 g, 0.4 mmol of isoniazid monochloride INHCl, added to the filtrate and stirred at room temperature until complete dissolution. This liquor was left to slowly evaporate in a water bath maintained at 30 ºC in a fume hood. Colorless crystals were obtained after five to seven days in quantitative yield (yield ≈ 44 %).

4.4.8 Synthesis of CB-Zn-GluA-INHCl

Zinc chloride tetrahydrate, 0.080 g; 0.6 mmol; was dissolved in 3 mL of deionized H_2O. The temperature was maintained at 80-90 ºC, and 0.100 g; 0.1 mmol of cucurbituril was added, and the mixture stirred until complete dissolution. Glutaric acid (GluA) (0.053 g; 0.4 mmol) was then added and the solution stirred for a further ten minutes on a hot plate, after which it was allowed to cool. The solution was filtered, and 0.07 g, 0.4 mmol of isoniazid monochloride INHCl, added to the filtrate and stirred at room temperature until complete dissolution. This liquor was left to slowly evaporate in a water bath maintained at 30 ºC in a fume hood. Colorless crystals were obtained after five to seven days in quantitative yield (yield ≈ 47 %).

4.4.9 Mechanochemistry

In a typical synthesis, a given metal complex was airdried for a few hours and then mechanically ground together with INHCl or ciprofloxacin with the addition of few drops of acetone. After that, the sample was airdried and then analyzed

4.5 Results and discussions

4.5.1 Characterization of glycoluril

Glycoluril was obtained as a white water-insoluble powder at 68% yield. The synthesis of glycoluril was confirmed using FTIR, NMR, and thermal analysis. ***Figure 4.1*** displays the FTIR spectrum, DSC and TGA thermogram respectively of the compound. The FTIR spectra is characterized by the strong and intense carbonyl vibrational band at 1675 cm^{-1}. In free amines, the NH stretching vibrations usually occur at 3300-3500 cm^{-1} [162]. However, when the NH group is involved in hydrogen bonding, the band shifts to lower wavenumbers [162–164]. The broadband at 3150 cm^{-1} is ascribed to the NH stretching vibration with strong inter and intramolecular hydrogen bonding. The bands at 3056 cm^{-1} and 2828 cm^{-1} are due to the aliphatic C-H stretching. The bands at 1244 cm^{-1} and 1112 cm^{-1} are respectively assigned to the C-N and C-C- stretching. DSC analysis showed that the compound is thermally stable beyond 250 ^{o}C after which it melts in the range 300 - 343 ^{o}C. The TGA decomposition profile of the compound reveals no mass loss up to 330 ^{o}C when it begins to decompose. This indicate that the compound is thermally stable

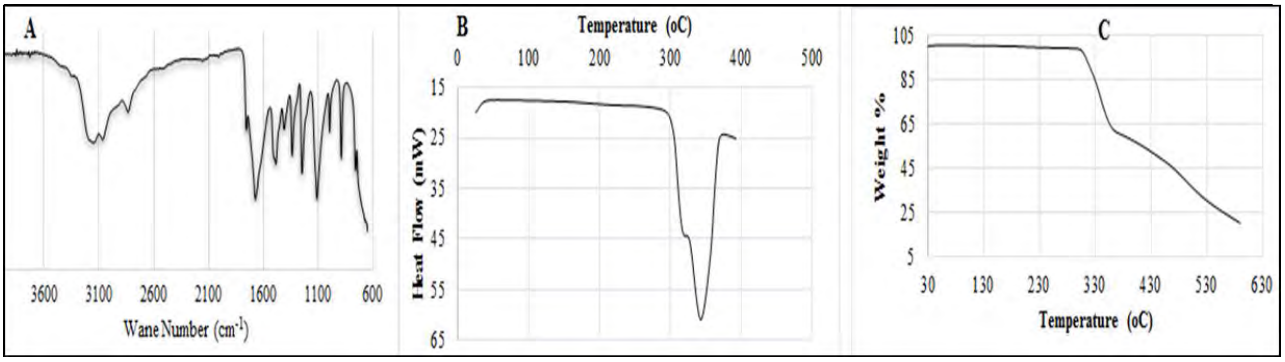

Figure 4.1: FTIR, DSC and TGA spectra of glycoluril

The H-NMR spectra of the obtained glycoluril is consistent with expectation, with the N-H proton appearing at 5.25 ppm and the C-H protons appearing at 7.16 ppm. The signals at 3.42 and 2.50 ppm are respectively assigned to water and deuterated DMSO. With regards to the ^{13}C-NMR spectra, the carbonyl peak appears at 161.89 ppm and the methine carbon signal at 65.07 ppm (***Figure 4.2***).

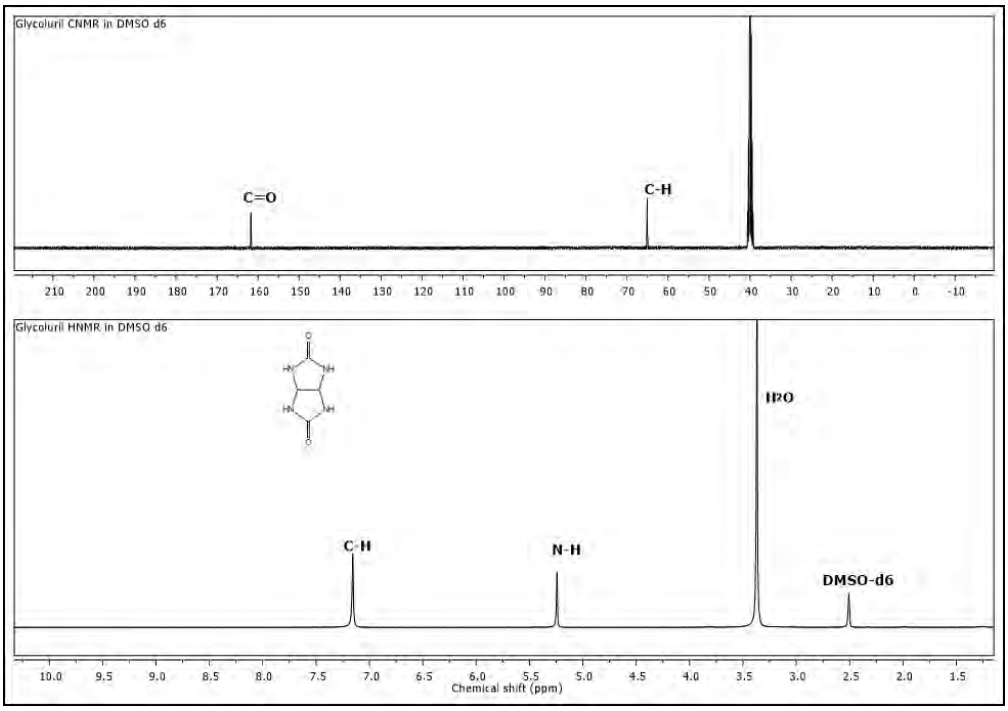

Figure 4.2: ^{13}C-NMR and H-NMR of glycoluril

4.6 Characterization of cucurbituril

After drying the filtered precipitate, the cucurbituril powder weighed 1.51 g (~ 65 % yield with respect to glycoluril). The reaction was carried out in concentrated acid at temperatures exceeding 110 ºC so that the formation of CB6 was favored [165]. The cucurbituril was analyzed using FTIR, TGA and NMR spectroscopy.

The FTIR spectra shown in ***Figure 4.3A*** reveals an intense band at 1713 cm^{-1} is ascribed to the C=O vibration. The aliphatic C-H vibrational bands are observed at 2913 cm^{-1} and 2996 cm^{-1}, while the broadband between 3000 and 3600 cm^{-1} is due to the presence of water adsorbed into either the pore or surface of the cucurbituril. The absence of N-H stretching vibrations suggests that the cucurbituril has been obtained. The C-N and C-C stretching vibrations respectively shift from 1244 cm^{-1} and 1112 cm^{-1} in glycoluril to 1228 cm^{-1} and 1185 cm^{-1} in the cucurbituril.

The TGA thermogram of the cucurbituril shows two thermal events, the first being the evolution of water occurs between room temperature and 150 ºC and the second corresponding to the decomposition which onsets at 309 ºC. The decomposition step occurs in two steps; the first step involves the loss of approximately 60% of the total mass while is a gradual decomposition which involves about 20% of the sample as shown in ***Figure 4.3B***.

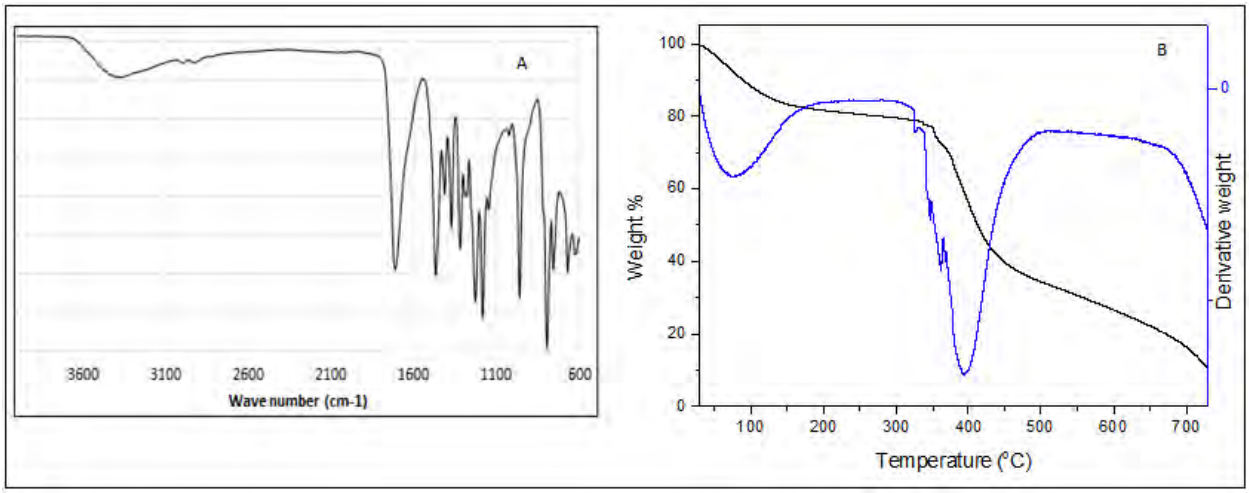

Figure 4.3: A: FTIR spectra B: TGA thermogram of CB6

The carbon-13 and proton NMR spectra shown in ***Figure 4.4*** suggests the successful synthesis of cucurbituril. The H-NMR spectra displays three signals at 4.24 ppm (dd, 12H), 5.51 ppm (s, 12H), 5.64 ppm (d, 12H) while the ^{13}C-NMR showed signals at 50.58 pp, 70.10 ppm and 156.22 pp. The resonance singlet signal at 5.51 ppm is assigned to the methine protons on the glycoluril subunit while the signals at 4.24 ppm and 5.64 ppm are assigned to the methylene protons indicated in red and green. Through space interaction of the proton coded in red with the methine protons on the glycoluril subunits is responsible for the additional splitting of the signal. The Assignment of the ^{13}C-NMR spectra is unambiguous; the signal at 156.22 is assigned to the carbonyl while the signals at 50.58 ppm and 70.10 ppm are respectively assigned to the methylene and methine carbon atoms. These results are consistent with literature [166,167].

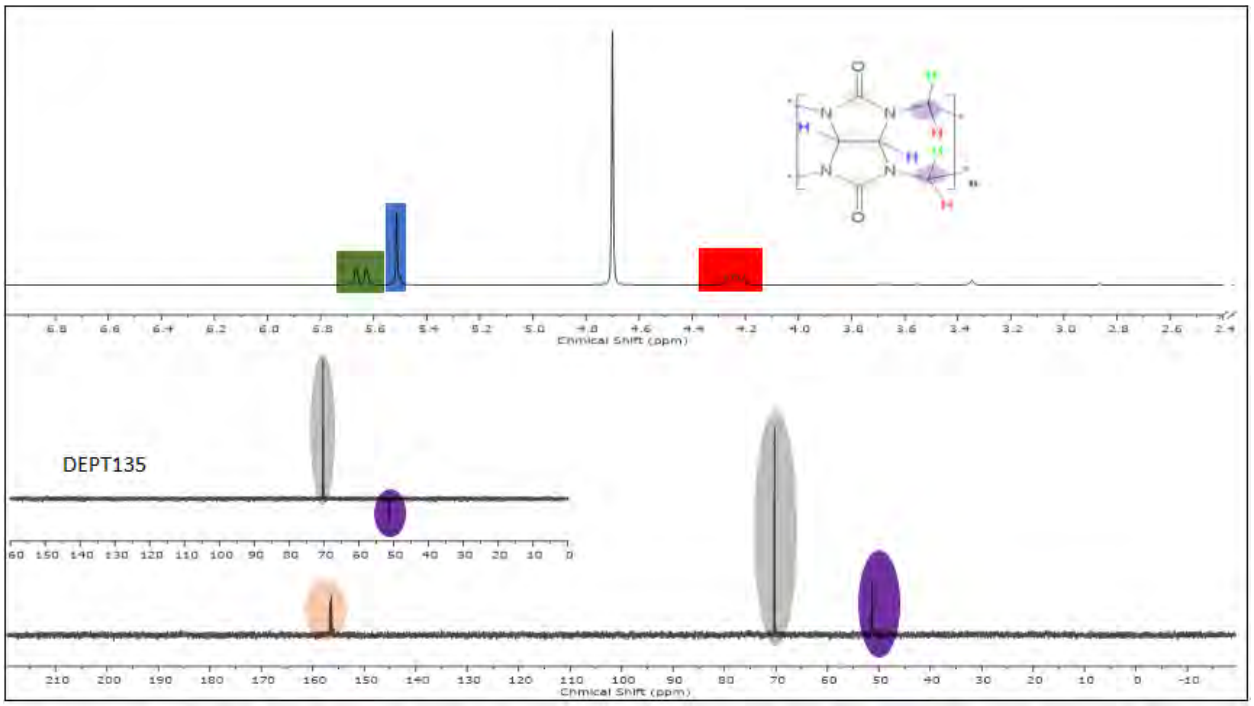

Figure 4.4: NMR spectra of CB6

4.7 Characterization of metal complexes

Metal complexes were obtained in good yields, mostly as crystals by slow evaporation from water. These complexes were analyzed using FTIR, TGA, elemental analysis H-NMR (in the case of Zn complexes), and single-crystal XRD. In the case of oxalic acid, a precipitate was formed after stirring for three to five minutes on a hot. The other acids did not form any precipitate at elevated temperature.

While the main objective here was to obtain complexes where the dicarboxylic acid bridges the two metals to form polymeric structures of the form $^{*}\!\!+\!\!\!-\text{M-CB-M-CA}\!\!+\!\!\!-_{n}{}^{*}$, it is worth mentioning that cucurbituril rotaxanes have often been reported using ligands with functional groups at both ends such as diamines [168]. The ability of diamines to form a spindle around which the cucurbituril rotates results from the presence of a positive charge midway the spindle which gets enclosed in the cucurbituril cavity. Coligands have also been used as structure directing units to obtained metal complexes of cucurbiturils [109,111]. However, it is anticipated that the absence of a positive charge midway the chains of the acids used here preclude their inclusion and favors the formation of the predicted structures.

The FTIR spectra of the ligands and complexes depicted in ***Figure 4.5 -Figure 4.8*** were compared, considering the position and intensity of the different bands to determine if complexation had occurred. A general observation which has also been noted elsewhere [111], is that FTIR spectraof metal complexes obtained from cucurbiturils shows only small shifts in terms of the position of the bands. A similar observation has been made here with the FTIR of the complexes. The FTIR spectra of the complexes show an intense band near 1700 cm^{-1} assigned to the cucurbituril C=O stretching vibration. Across the different complexes, this cucurbituril C=O stretch appears shifted compared to the same band in the uncoordinated cucurbituril. This shift results from the coordination of the C=O carbonyl oxygen to the metal ions, which distorts its electron cloud.

Furthermore, FTIR spectra of the complexes show a shoulder near the cucurbituril carbonyl band assigned to the C=O vibration of the bridging dicarboxylic acid used. These observations are consistent with the results by Chen et al. [111]. The intense bands of the cucurbituril mask the other bands due to the carboxylic acid. ***Table 1:1*** indicates the position of the carbonyl bands both for the cucurbituril and the carboxylic acid.

Table 4:1: C=O IR band values for the C=O of cucurbituril (CB) and carboxylic acid (CA) for the obtained complexes.

		OxA	MalA	SucA	GluA	C=O in free CB
Fe^{2+}	CB	1715	1717	1717	1715	1711
	CA	1662	1638	1651	1657	
Mn^{2+}	CB	1708	1707	1709	--	
	CA	1651	1651	1664	1638	
Cu^{2+}	CB	1727	1697	1707	1692	
	CA	1643	1628	1628	1628	
Zn^{2+}	CB	1715	1715	1716	1717	
	CA	1632	1651	1632	1638	

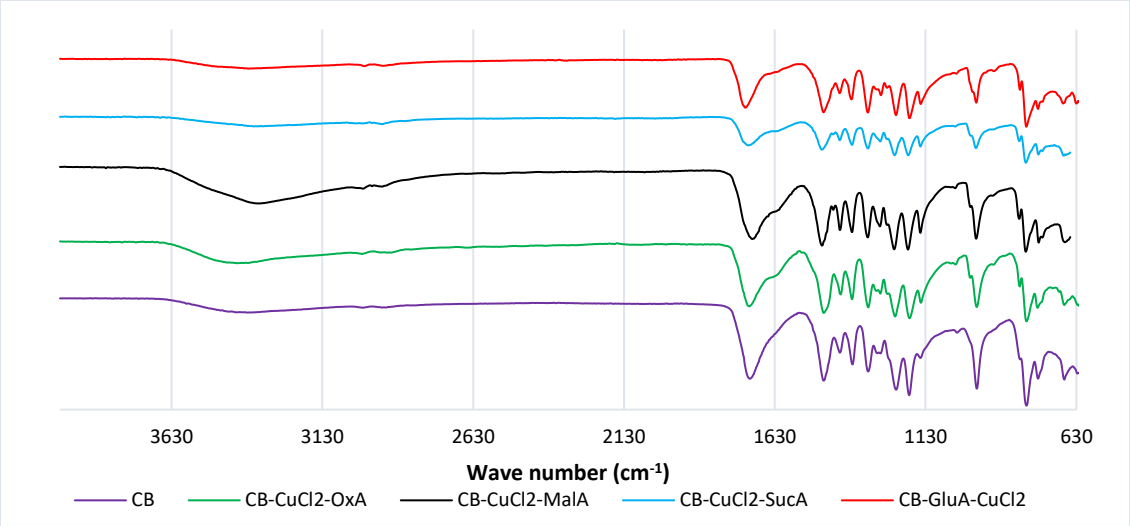

Figure 4.5: FTIR spectra of CB and copper metal complexes

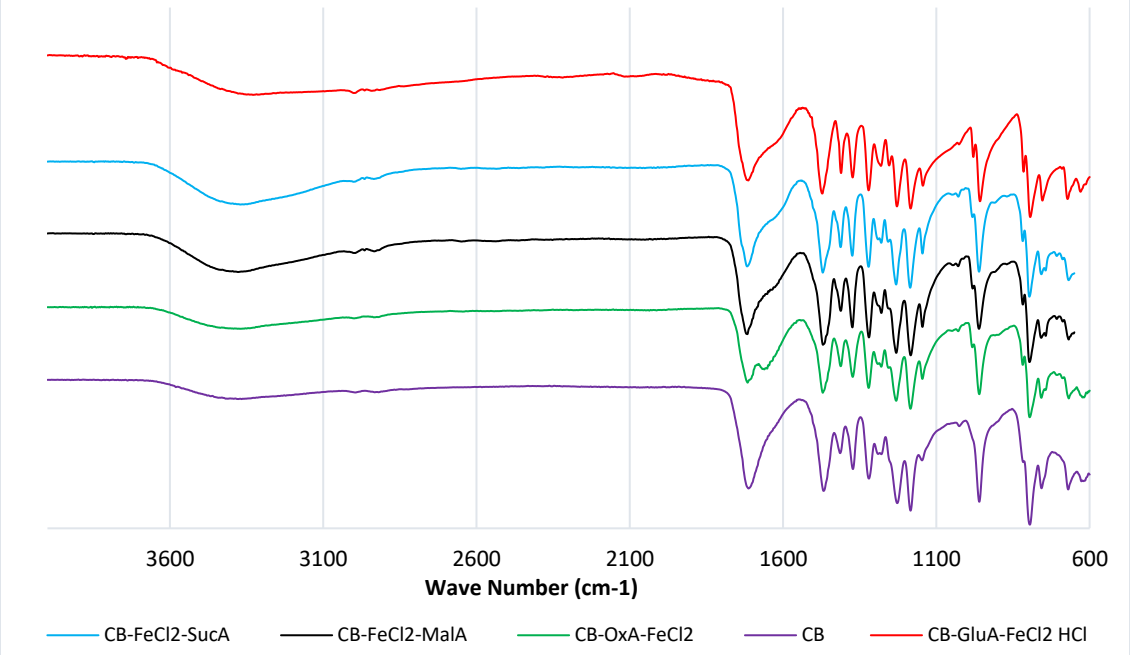

Figure 4.6: FTIR spectra of CB and iron metal complexes

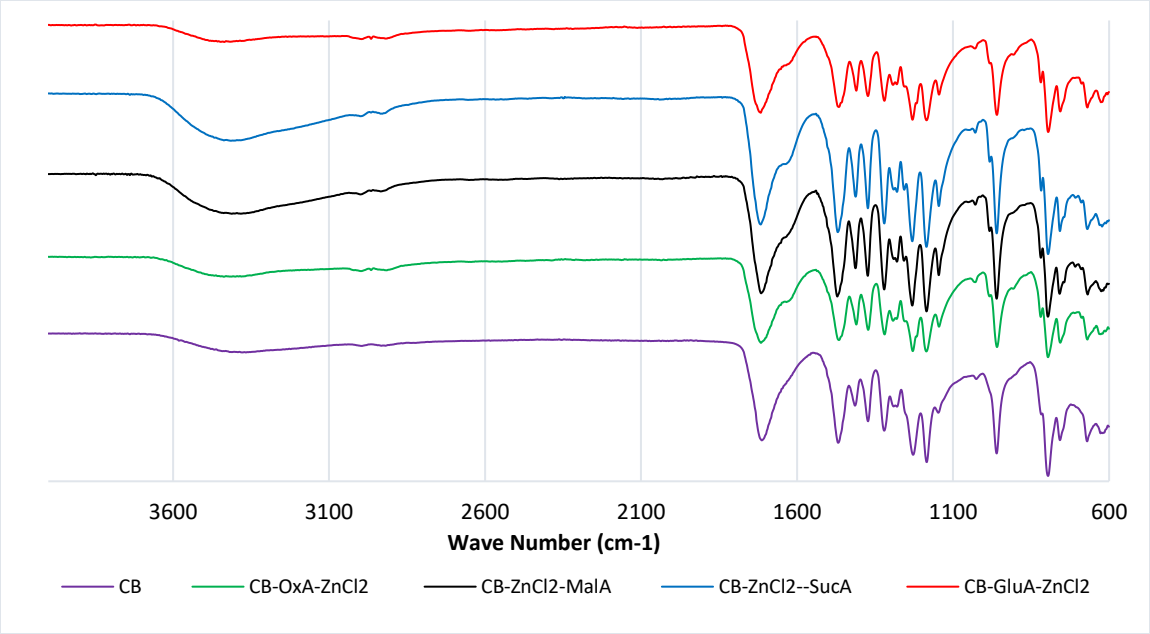

Figure 4.7: FTIR spectra of CB and zinc metal complexes

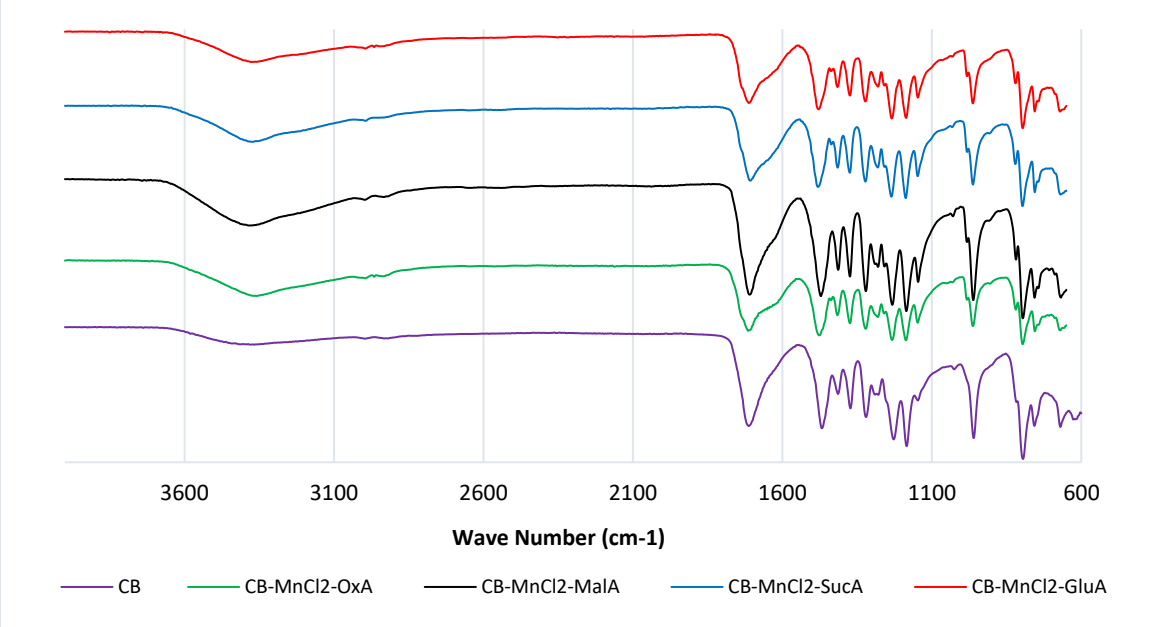

Figure 4.8: FTIR spectra of CB and manganese metal complexes

Table 4:2 shows the elemental analysis data. The amount of metal was determined using atomic absorption spectroscopy. The elemental analysis data suggest that the metal to cucurbituril to acid ratios are 2:1:2 and 2:1:1 for oxalic and glutaric acid complexes, respectively. The manganese-oxalic acid complex shows a high metal content, suggesting more than one metal ion at each portal. The elemental analysis data shows a similar trend for the series malonic, succinic and glutaric,

different from oxalic acid. This disparity for oxalic acid suggests that its coordination mode is different from malonic, succinic and glutaric. At this stage, it is, however, unclear what the coordination network looks like.

Table 4:2: Elemental analysis data for the complexes

Compound	C Found (Calc'd)	H Found (Calc'd)	N Found (Calc'd)	Molecular Formular
CB-Fe-OxA	25.65 (25.79)	3.07 (3.44)	18.33 (18.05)	$Fe_4C_40H_{36}N_{24}O_{20}$ $14H_2O$ Cl_6
CB-Mn-Ox	22.74 (22.72)	3.15 (3.21)	15.22 (15.90)	$Mn_8C_{40}H_{36}N_{24}O_{20}$ $16H_2O$ Cl_6
CB-Mn-MalA	30.31 (30.59)	3.94 (3.79)	21.72 (21.96)	$Mn_2C_{39}H_{38}N_{24}O_{20}$ $12H_2O$ Cl_4
CB-Mn-SucA	29.69 (30.38)	4.24 (4.05)	22.54 (22.27)	$Mn_2C_{40}H_{40}N_{24}O_{20}$ $12H_2O$ Cl_6
CB-Mn-GluA	27.91 (27.99)	4.11 (3.97)	19.98 (19.59)	$Mn_2C_{40}H_{40}N_{24}O_{20}$ $14H_2O$ Cl_5
CB-Cu-OxA	30.26 (30.24)	3.78 (3.84)	21.19 (21.23)	$Cu_2C_{40}H_{36}N_{24}O_{20}$ $12H_2O$ Cl_2
CB-Cu-MalA	25.78 (26.52)	3.90 (4.08)	19.64 (19.01)	$Cu_2C_{39}H_{38}N_{24}O_{16}$ $18H_2O$ Cl_6
CB-Cu-SucA	26.50 (27.25)	3.90 (4.20)	20.28 (19.10)	$Cu_2C_{40}H_{40}N_{24}O_{16}$ $18H_2O$ Cl_6
CB-Cu-GluA	26.58 (27.50)	3.52 (4.14)	19.21 (18.71)	$Cu_2C_{41}H_{42}N_{24}O_{16}$ $16H_2O$ Cl_6
CB-Zn-OxA	28.97 (29.54)	3.68 (3.69)	21.56 (21.68)	$Zn_2C_{40}H_{36}N_{24}O_{20}$ $14H_2O$ Cl_6
CB-Zn-MalA	29.42 (30.23)	4.01 (3.74)	22.13 (21.69)	$Zn_2C_{39}H_{38}N_{24}O_{16}$ $10H_2O$ Cl_4
CB-Zn-SucA	29.48 (30.32)	3.96 (3.79)	22.12 (21.21)	$Zn_2C_{40}H_{40}N_{24}O_{16}$ $10H_2O$ Cl_4
CB-Zn-GluA	28.97 (29.70)	3.69 (4.23)	21.62 (21.28)	$Zn_2C_{41}H_{42}N_{24}O_{16}$ $14H_2O$ Cl_5

The H-NMR data of the CB-zinc-carboxylic acid complexes were collected, and the spectra indicated in ***Figure 4.9-Figure 4***.*11* (*page* ***104-105***). These spectra were compared with that of cucurbituril and the carboxylic acid to determine if both entities were present in the obtained complex. In all cases, the signals due to the carboxylic acid and the cucurbituril could be identified. By comparing the signals of the pure starting materials and the corresponding product, a shift in the signals both of the cucurbituril and the carboxylic acid was observed, suggesting that both entities were present and coordinating. The H-NMR spectra of CB-$ZnCl_2$-SucA shows two signals for the CH_2 protons suggesting that the carboxylic acid molecules may be found in different environments within the complex. This may be due to coordination along different axes, which results in the observed spectrum.

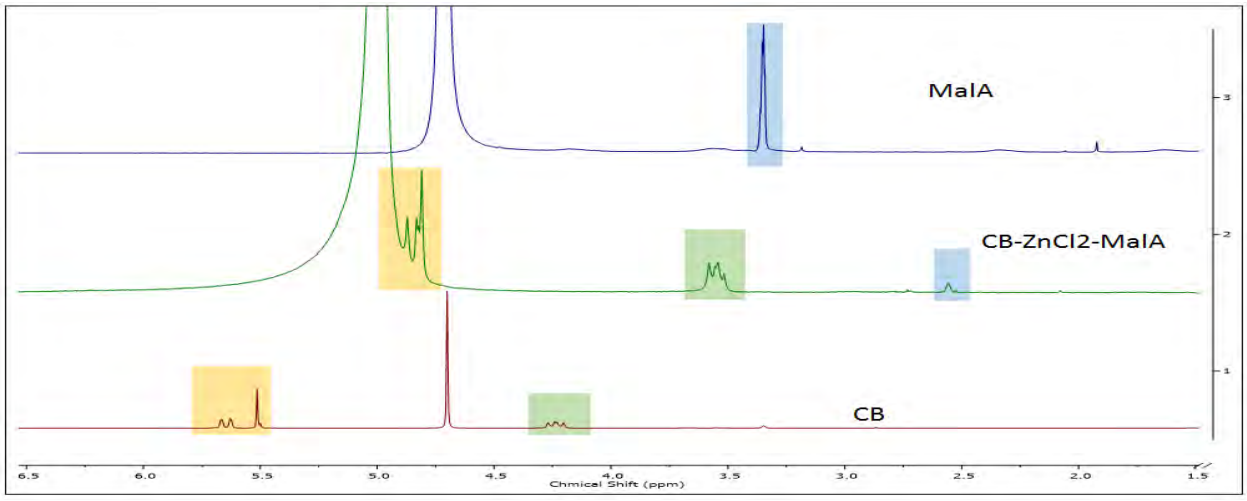

Figure 4.9: HNMR of CB-ZnCl2-MalA, MalA and CB

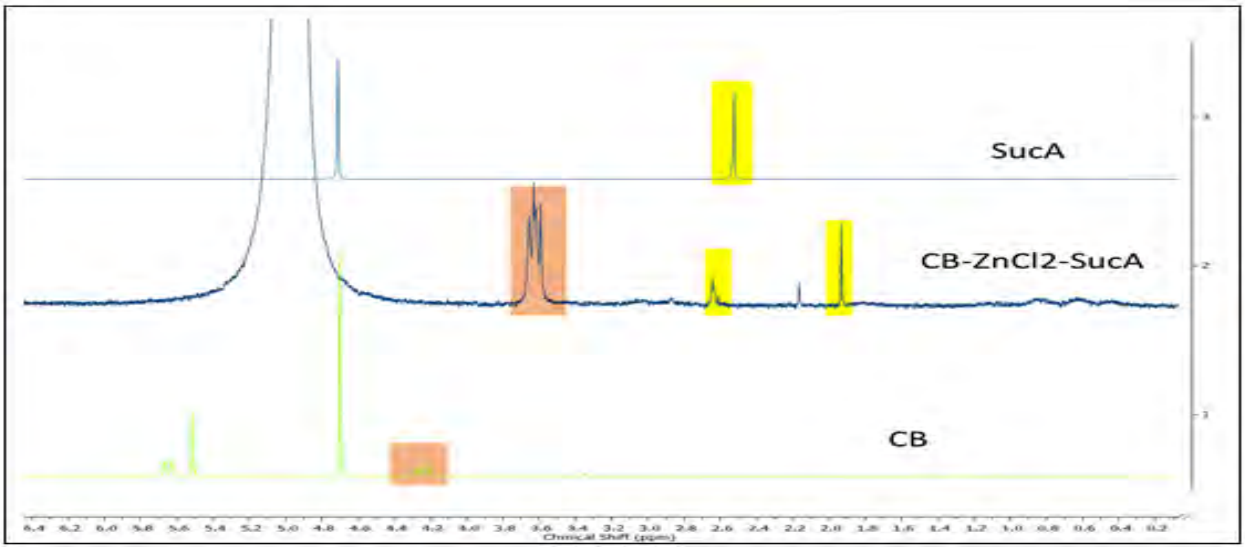

Figure 4.10: HNMR of CB-ZnCl2-SucA, SucA and CB

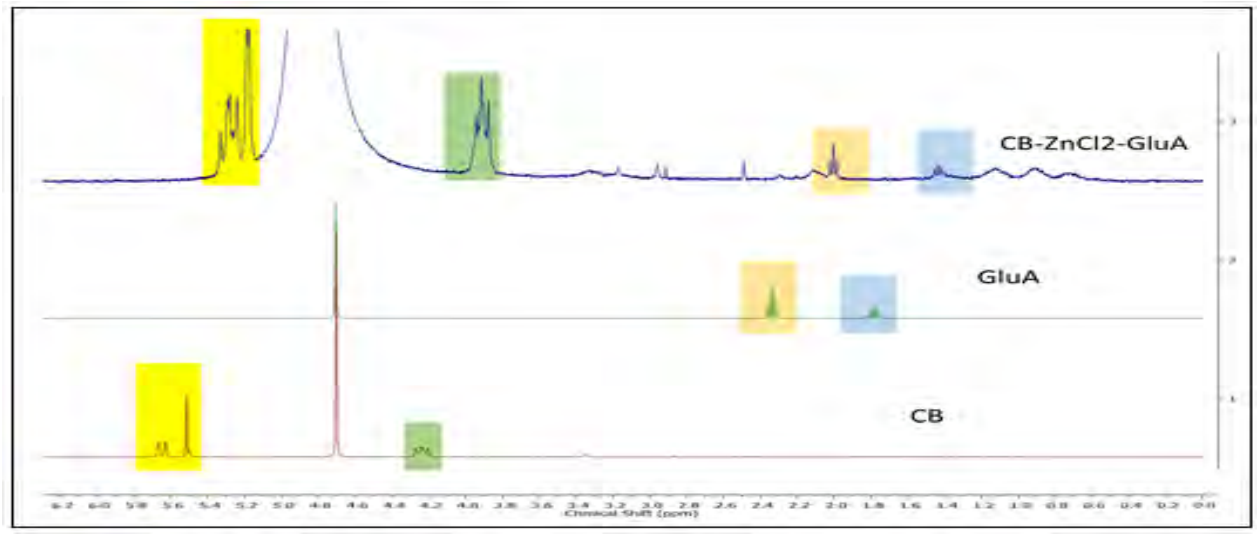

Figure 4.11: H-NMR of CB-ZnCl2-GluA, GluA and CB

Thermal analysis of the compounds also proved helpful in understanding the coordination within the complexes. The representative TGA thermograms of the obtained complexes is shown in ***Figure 4.12-Figure 4.15*** (*page* ***106-107***) and the others have been included in the appendix. The complexes generally undergo a multistep decomposition which begins with the evolution of unbound water molecules near 100 ºC followed by the evolution of coordinated water molecules in the region between 120-180 ºC. The evolution of the carboxylic acid occurs between 200-400 ºC, which is closely followed by a series of decomposition steps involving the cucurbituril. It can be observed from ***Table 4:3*** that increasing the carbon chain length of the carboxylic acid bridge results in a general decrease in thermal stability. This trend, however, does not appear evident in the case of iron complexes suggesting the mode of coordination within the complexes of iron is different from that of the other complexes.

The decomposition profile of iron complexes indicates that after the evolution of the carboxylic acid, the oxalic and malonic bridged complexes show a similar profile with the cucurbituril unit breaking down in a single step. However, when the bridging acid is either succinic or glutaric acid, the iron complexes show a decomposition profile akin to the complexes of the copper, zinc and manganese where the decomposition of the cucurbituril unit occurs in a series of steps. This observation suggests that the coordination mode in the CB-Fe-CA complexes (where CA is either succinic or glutaric acid) is different from cases where CA is either oxalic or malonic.

Table 4:3: Evolution temperature of carboxylic acid bridging linkers

	OxA	MalA	SucA	GluA
Mn^{2+}	328	--	325	324
Fe^{2+}	262	298	--	286
Cu^{2+}	298	273	270	264
Zn^{2+}	339	229	--	322

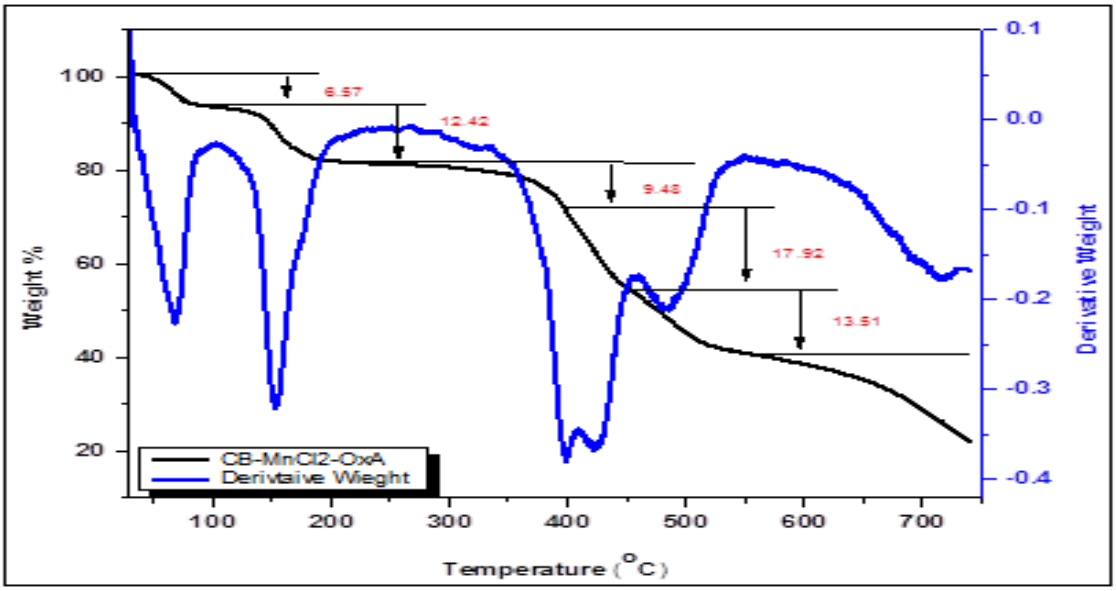

Figure 4.12: TGA thermogram (black) and derivative (Blue) of CB-$MnCl_2$-OxA

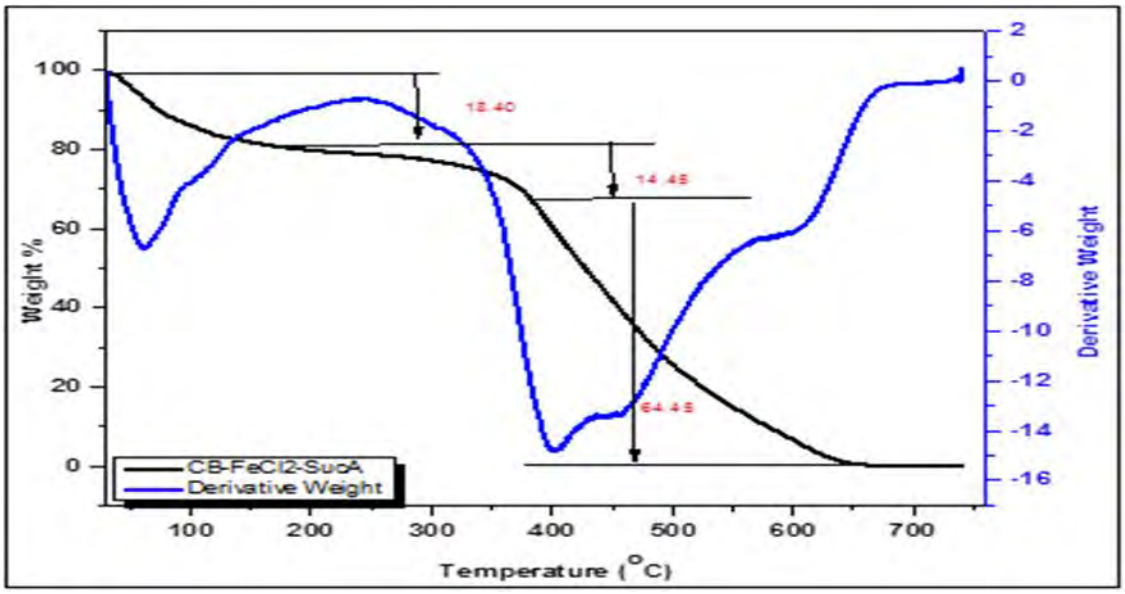

Figure 4.13: TGA thermogram (black) and derivative (blue) of CB-$FeCl_2$-SucA

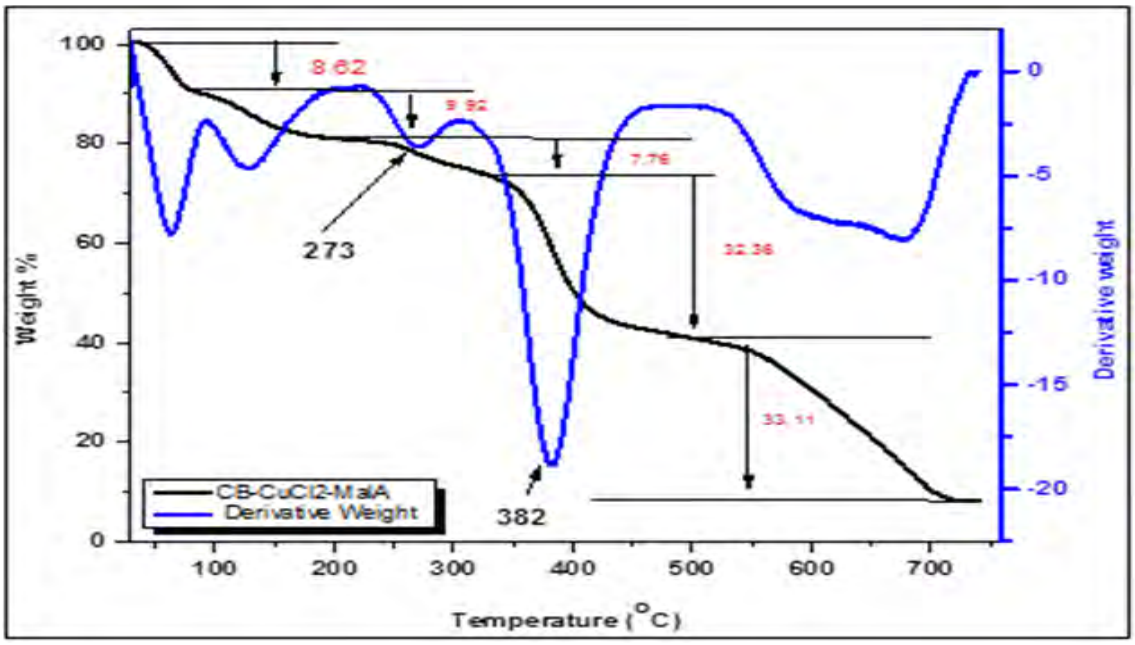

Figure 4.14: TGA thermogram (black) and derivative (blue) of CB-$FeCl_2$-GluA

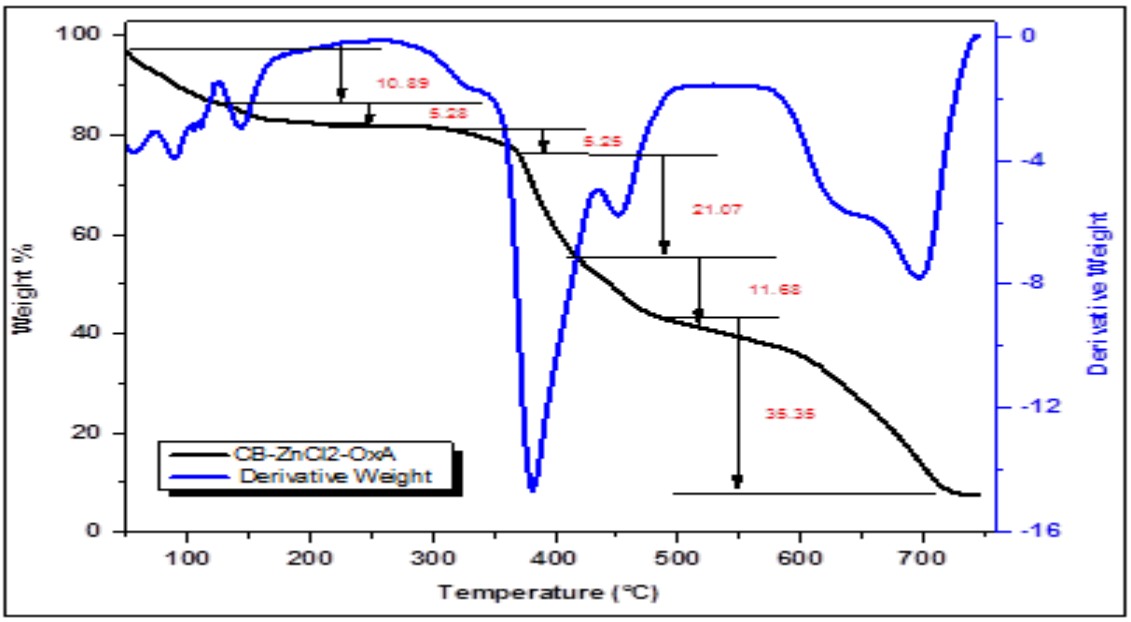

Figure 4.15: TGA thermogram (back) and derivative (blue) of CB-$ZnCl_2$-OxA

4.8 Structure of the complexes

Metal complexes of cucurbiturils are usually polymeric with alternating cucurbituril and metal ions. The FTIR analysis of complexes obtained in this work indicates that the metal ions coordinate to the cucurbituril through the portal carbonyl oxygen as in most reported cases. The bridging dicarboxylate ligands also coordinate with the metal ions. With the metal ions lidded on the portal of the cucurbituril, the dicarboxylate ligands could either bridge longitudinally or crosslinked or

both as shown in ***Figure 4.16A, B*** and ***C***. If the carboxylic bridges like shown in ***Figure 4.16A***, external pockets such as depicted ***Figure 4.16C*** are generated. With such external pockets, the complexes can form both inclusion and exclusion complex ensembles. It however, appears that while malonic, succinic, and glutaric acid can form complexes of the type represented in frame **A**, oxalic acid is precluded since its approximate length [169] is smaller than 5.5 Å, [170] the diameter of cucurbit[6]uril. The inability of this oxalic acid to form crosslinked bridges possibly explains the differences observed in the TGA decomposition profiles of oxalic acid-based complexes compared to the other acids.

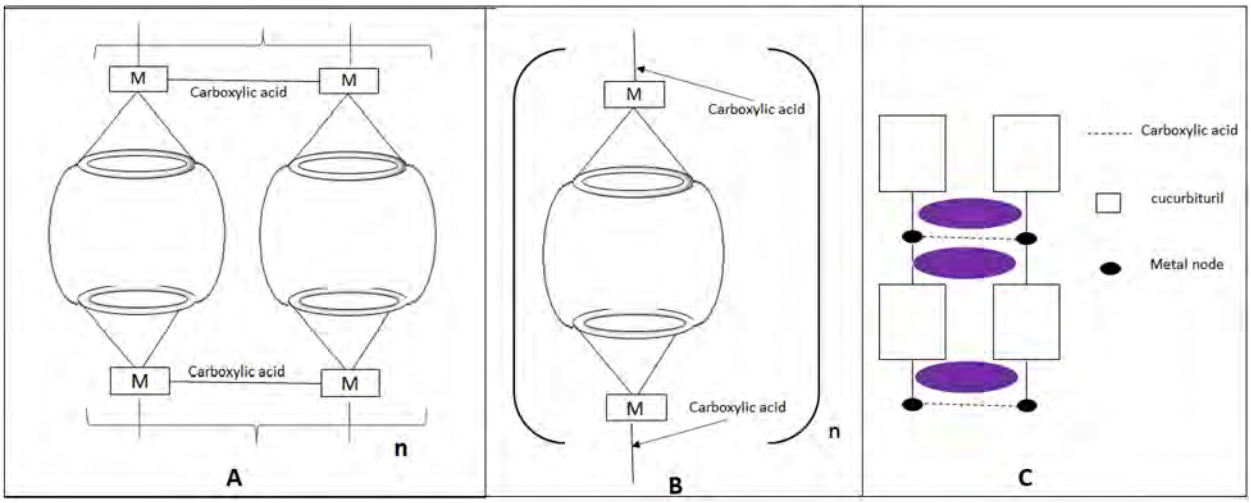

Figure 4.16: Bridging mode of the dicarboxylate ions.

4.9 Possible porosity in the obtained complexes

As earlier indicated, cucurbiturils form complexes in which the metal ions coordinate to the portal carbonyl oxygen atoms, thereby blocking the internal cavity of the cucurbituril unit [171]. Notwithstanding, these compounds form metal complexes that often display pores other than those linked to the cavity. An indirect approach of exposing the compounds to volatile solvent vapors and evaluating any adsorption was used to assess the presence of extrinsic pores. In this regard, airdried samples were exposed to methanol vapor and then characterized by FTIR and TGA analysis to determine if any adsorption had occurred.

After incubation of the sample for twelve hours, the FTIR spectrum showed a new band at 986 cm^{-1} which is indicative of the presence of methanol (***Figure 4.17***). The carbonyl band shifted slightly from 1700 cm^{-1} in the air-dried sample to 1706 cm^{-1} after incubation, also suggesting an

interaction between the methanol and the metal complex. Similar results were obtained with the other complexes suggesting that other than the cavity of the cucurbituril units, the complexes have other pores which are accessible. Feng et al. observed that external porosity is possible in cucurbituril metal complexes [171].

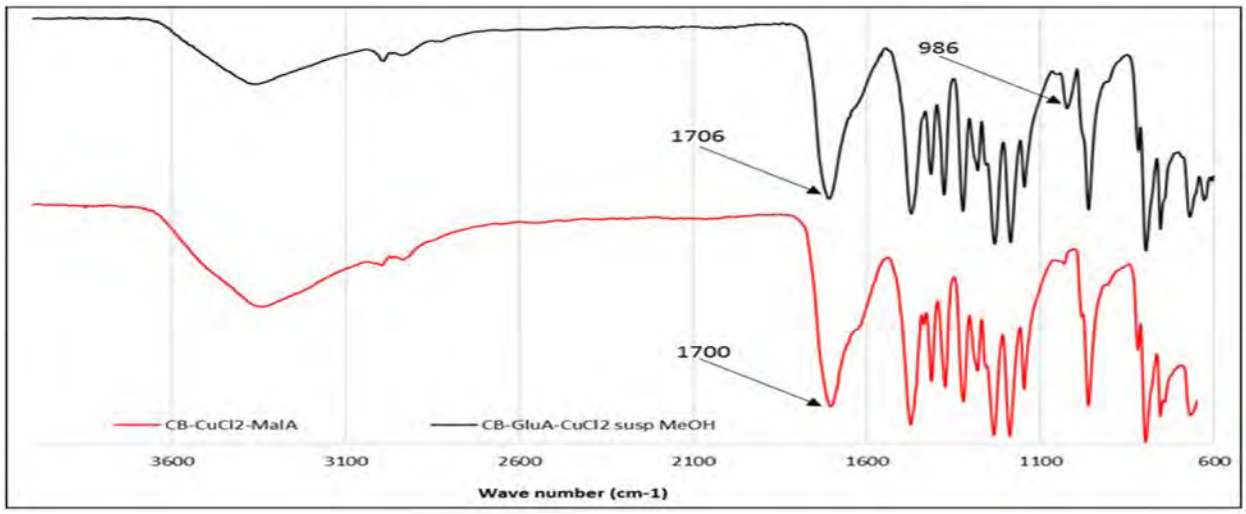

Figure 4.17: FTIR of CB-GluA-$CuCl_2$ before and after suspension over methanol vapors

The TGA data for the complexes (***Figure 4.18***) revealed that the release of adsorbed methanol peaks at 135 ^{o}C. After the methanol release, the complex undergoes a similar decomposition compared to the parent compound between 200-450 ^{o}C. The evolution of methanol at temperatures higher than its boiling point indicates that the methanol is inside the pores and not just surface-bound. Significant intermolecular interaction between the methanol justifies the higher temperatures required for its evolution. Feng et al. [171] observed that water molecules in the cucurbituril metal complex could be displaced by methanol molecules when the airdried compound is exposed to methanol vapor. TGA analysis of the sample further indicates that, unlike the parent compound, which shows a distinct thermal event in the region of 650 ^{o}C, upon methanol adsorption, the compound shows a gradual decomposition from 450 ^{o}C until 750 ^{o}C. As opposed to the parent compound, the gradual decomposition indicates that the adsorption of methanol into the pores leads to a change in structure.

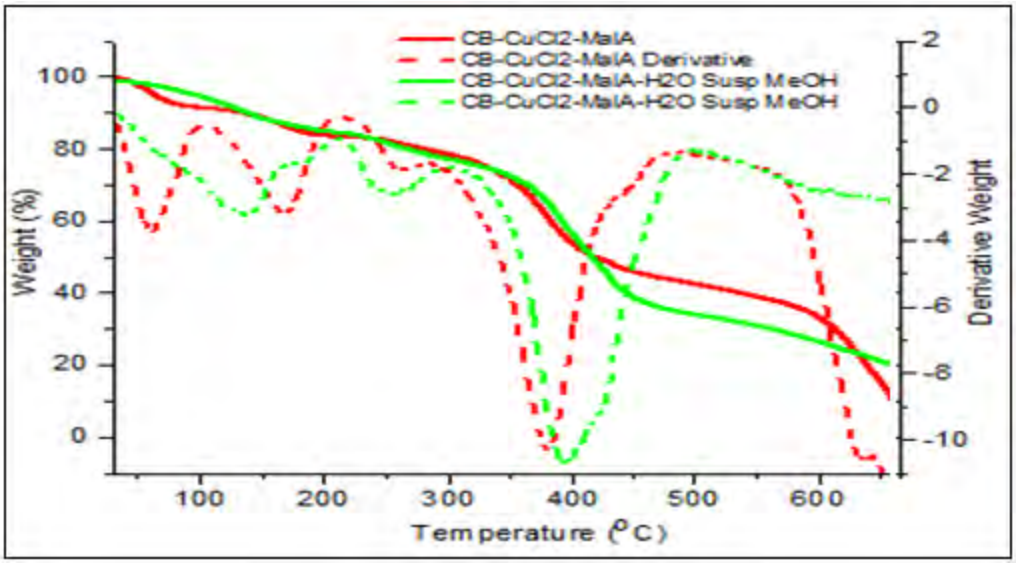

Figure 4.18: TGA profile for CB-$CuCl_2$-MalA before (red) and after (green) suspension over methanol (The derivative curves are indicated in dotted lines)

With the cucurbituril cavity lidded, and the compounds are yet able to adsorb methanol vapor upon exposure to methanol, it is evident that external channels are present in the material. It is postulated that the introduction of dicarboxylic acid bridging ligands acts as interlayer pillars creating channels which are external to the cucurbituril cavity. These results are parallel to report by Feng et al. [171] who observed that the presence of iodide ions in a cucurbituril supramolecular complex acts as interlayer pillars creating channels in the cucurbituril metal complex, accessible to the methanol vapors, a phenomenon not observed in the absence of the iodide ions. The results obtained here with carboxylate bridging ligands suggest that these compounds contained pores enabled by the introduction of the dicarboxylic acid. Further pore characterization using traditional BET is envisaged in future work.

4.10 One-pot synthesis of metal complex-drug supramolecular assembly

The metal complex-drug supramolecular assemblies were obtained in water mostly as crystals. Slow evaporation of water from the mother liquor afforded quantitative yields of the products characterized through FTIR, NMR, and TGA.

Table 4:4: Characteristic C=O band in the supramolecular assemblies of INHCl and Cu and Zn complexes

	C=O band in free INHCl	Oxalic acid		Malonic acid		Succinic acid		Glutaric acid	
	1637	C=O (*)		C=O (*)		C=O (*)		C=O (*)	
		CB	INHCl	CB	INHCl	CB	INHCl	CB	INHCl
Cu^{2+}		1704 (1692)*	1645	1727 (1697)*	1647	1729 (1707)*	1651	1725 (1692)*	1648
Zn^{2+}		1720 (1715)*	1612	1719 (1715)*	1612	1727 (1716)*	1611	1725 (1717)*	1612

Values in (*) are those of the C=O of CB in the metal complex without INHCl. These values are present in table 4.1 and stated here to indicate that a shift occurs once INHCl is introduced. The carbonyl band of INHCl in the supramolecular assembly is compared with the free same band in the free INHCl at 1637. Attention here is not paid to the C=O of the bridging acid but rather just the C=O band of the guest and the CB.

The FTIR of the supramolecular ensembles depicted in ***Figure 4.19*** and ***Figure 4****.20* reveal that the bands due to the cucurbituril are very intense thereby masking bands due to both the bridging ligand and the guest. Notwithstanding, the bands due to the carbonyl stretching of the INHCl guest are visible and have been indicated in ***Table 4:4***. Significant shifts in the stretching frequency of the INHCl C=O band suggest the most likely intermolecular interaction involving the $CONHNH_3^+$ end of the drug molecule. However, the masking of the NH bands by broad OH bands implies that it could not be determined from FTIR spectra (if the $NHNH_3^+$ was involved in intermolecular interaction). Still, since the cucurbituril moiety within which the drug molecule is enclosed has a hydrophobic cavity, it is reasonable to assume that there is at least a cation-π interaction between the drug molecule and the cucurbituril cavity.

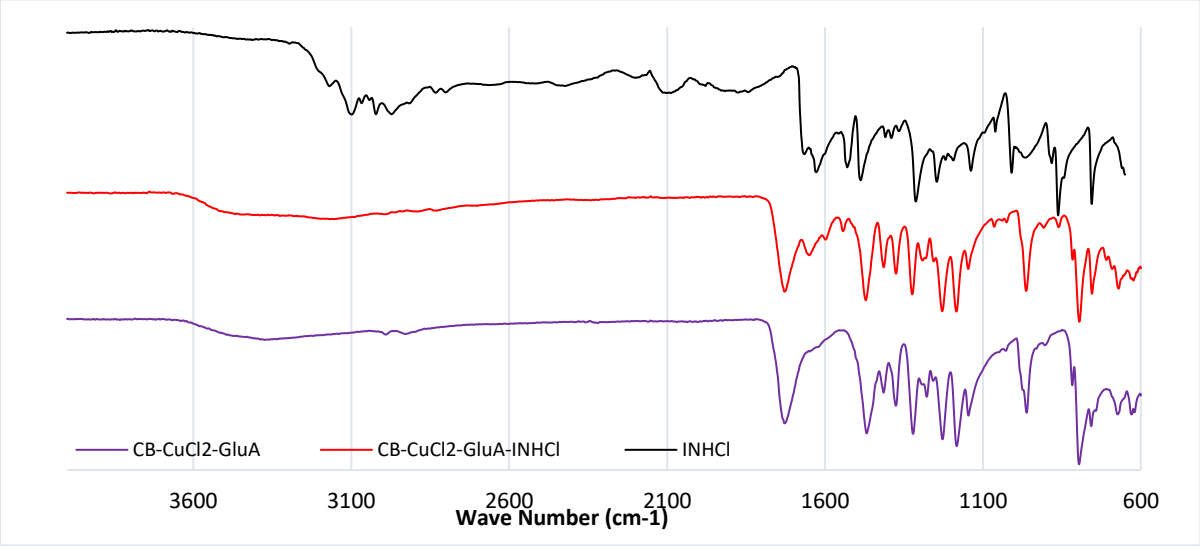

Figure 4.19: FTIR of INHCl (black), CB-$CuCl_2$-GluA-INHCl (red) and CB-CuCl2-GluA (purple)

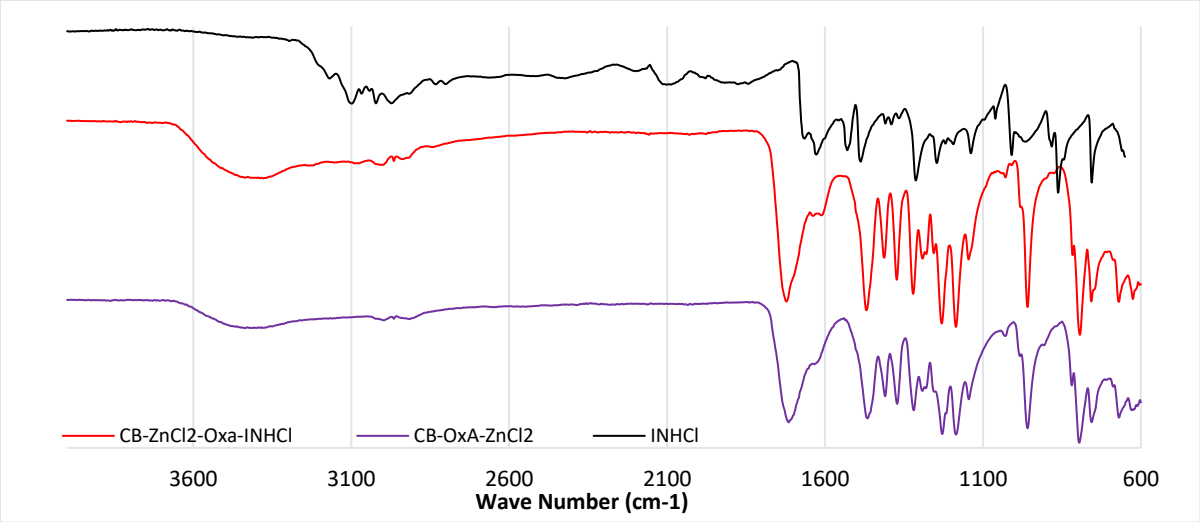

Figure 4.20: FTIR of INHCl (black) CB-ZnCl$_2$-OxA-INHCl (red) and CB-ZnCl$_2$-OxA

The zinc supramolecular assemblies were also investigated using H-NMR spectroscopy. The H-NMR data shown in ***Figure 4.21*** reveals the presence of two doublets assigned to the INHCl. Comparing the position of these signals with those in pure INHCl reveals a shift indicating that not only is the INHCl present, but it is also in a different chemical environment compared to the free molecule. The signals due to cucurbituril moiety and carboxylic acid were also found to shift when compared to the compound without the guest, suggesting an additional interaction is formed when the guest is introduced. These observations all suggest that the obtained product is not just a physical entity but a supramolecular ensemble of the host and guest.

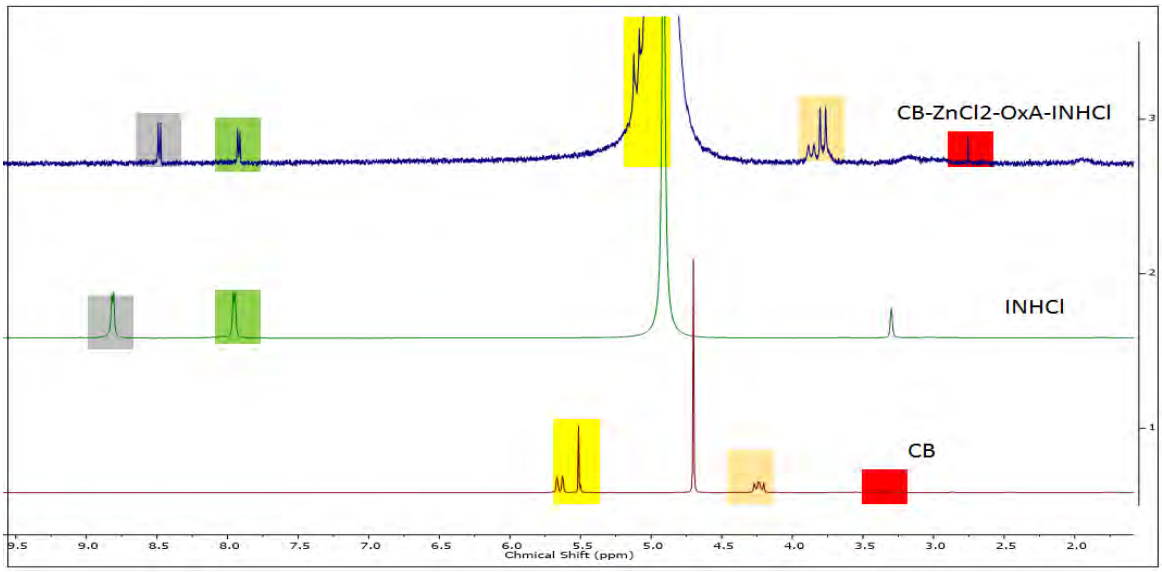

Figure 4.21: HNMR of CB-ZnCl2-OxA-INHCl supramolecular ensemble (blue), CB-ZnCl2-OxA (green) and INHCl (red)

Thermal analysis of the compounds was helpful in determining the stability and giving information as to whether an inclusion or an exclusion complex had been formed. In the case of an inclusion complex, it is expected that the guest will be released only once the complex begins to break since the metal ion lids the cucurbituril.

The thermal data indicates that the supramolecular ensemble containing the isoniazid guest is generally more thermally stable compared to the complex without the guest. The presence of two thermal events before 200 ^{o}C suggests that, as in the case of the complexes without the INHCl guest, water molecules occur both as guest and ligand. The mass loss occurring between 50 and 120 ^{o}C is ascribed to the loss of guest water molecules, while the mass loss between 130 to 200 ^{o}C is ascribed to the loss of coordinated water molecules. Again, as in the case of the metal complexes, the evolution of the bridging ligand from the supramolecular ensemble generally occurs between 200 to 400 ^{o}C, although at a slightly higher temperature compared to the corresponding metal complexes without the INHCl guest. Beyond 400 ^{o}C, the cucurbituril moiety breaks down in two or three steps across the ensembles.

In the case of copper complexes, the derivative of the TGA thermogram reveals a thermal event occurring just after the initial breakdown of the cucurbituril moiety, which is absent in the metal complexes. This event is ascribed to the decomposition of the isoniazid guest. For the supramolecular ensemble CB-$CuCl_2$-MalA-INHCl, for example, this event troughs at 441 ^{o}C. The isoniazid guest only breaks down after the cucurbituril macrocycle's initial collapse, suggesting that it is found inside the lidded cucurbituril cavity. The release of the guest, therefore, only occurs once the macrocycle collapses. Based on this data, the following (***Figure 4.22***) has been suggested as the structure of the formed supramolecular ensemble.

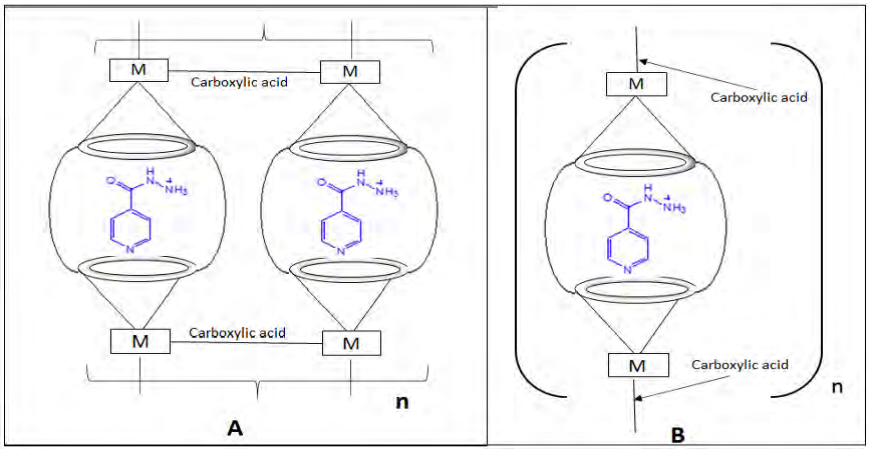

Figure 4.22: Proposed structure of the supramolecular ensemble

Although the presence of the INHCl in zinc-based ensembles was confirmed from H-NMR spectroscopy, the TGA did not reveal a distinct thermal event relating to the evolution of the INHCl like in the case of copper-based ensembles. The thermal data reveal that the cucurbituril moiety in the ensembles breaks down at a lower temperature than the non-guest metal complex. The absence of a specific guest evolution event suggests that the breakdown of the cucurbituril unit and the guest occurs simultaneously. The TGA data of CB-M-Mala-INHCl (M = Cu^{2+} or Zn^{2+}) reveal that the INHCl guest makes up between 5-10 % by weight of the supramolecular ensemble. Mass percent calculations from the TGA indicate that a single ensemble unit will enclose a single INHCl molecule. This observation is plausible since a single unit contains just one unit of the cucurbituril in whose cavity the guest becomes enclosed.

4.11 Mechanochemistry

Aware that cucurbiturils form metal complexes with both intrinsic and extrinsic pores, especially when such complexes employ bridging ligands and having confirmed that the obtained complexes contain both types of pores, we decided to investigate if the same supramolecular ensembles obtained from one-pot synthesis is possible via mechanochemistry. To this end, solvent assisted mechanochemistry was carried using acetone. The use of acetone was premised by its volatile nature. After grinding for ten minutes, the sample was air-dried then analyzed. ***Table 1:1*** displays the observed color changes. Drastic color changes observed with ciprofloxacin as opposed to less drastic color changes observed in the case of isoniazid. These color changes are likely to arise from π-π stacking interactions.

Table 4:5: Color changes obtained when complexes are mechanically ground with INHCl and ciprofloxacin

Color			
Cucurbituril Metal Complex		Cucurbituril metal Complex with	
		INHCl	Ciprofloxacin
CB-CuCl2-OxA	Green (A)	Apple Green (1)	Mustard (2)
CB-ZnCl2-OxA	White (B)	White (3)	Cream (4)

Compared to the initial reactants, the FTIR spectra of the mechanochemistry product (***Figure 4.23***) reveal shifts to higher frequencies, indicating a decrease in the double bond character. The spectra of the mechanochemistry complexes also reveal a shift to a lower frequency of the OH bands, suggesting an increase in hydrogen bonding strength within the system. A comparison with the one-pot synthesis products suggest that the two products are not identical. For instance, in the one-pot synthesis of the CB-$CuCl_2$-OxA-INHCl supramolecular ensemble, the C=O band of the cucurbituril unit is found at 1704 cm^{-1} (***Figure 4.4*** *page* ***99***). In contrast, in the mechanochemical synthesis, the same band is found at 1726 cm^{-1}. Similar observations are made when the CB-$CuCl_2$-OxA-INHCl one-pot supramolecular ensemble is compared with the mechanochemistry derived product. The obvious and drastic changes in the color of the complexes of ciprofloxacin from the original color of the complex may be due to the interaction of the ciprofloxacin with the metal center or pi-pi interactions.

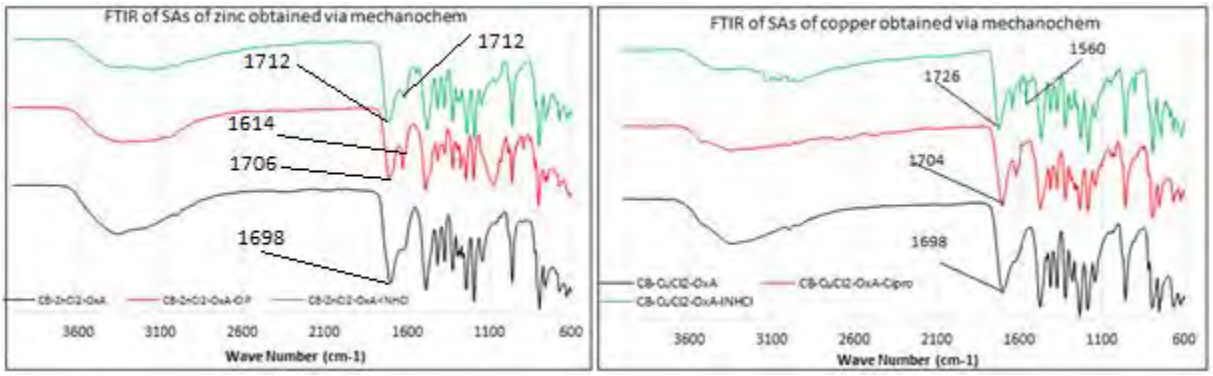

Figure 4.23: FTIR of mechanochemistry product

Like in the case of one-pot synthesis, where TGA analysis was critical in determining the complex ensemble's stability and the guest's position, a similar approach was employed here. TGA analysis

of the complex ensembles confirmed that these complexes are chemical entities different from the initial starting materials. While the TGA thermogram of copper complex ensembles look like the TGA of the starting complex, those of zinc differ distinctly from the starting material. In the TGA thermogram of zinc complex ensembles, the decomposition of the cucurbituril unit occurs beyond 550 ^{o}C, whereas in the starting complex, this decomposition occurs at about 380 ^{o}C. This significant thermal stabilization of the complex following mechanochemistry should result from some chemical interaction and not just some weak intermolecular interaction.

The cucurbituril unit of the CB-$ZnCl_2$-OxA-INHCl complex ensemble, like the starting complex, shows a two-step gradual mass loss between 370-430 ^{o}C ascribed to the loss of the INHCl guest. The evolution of the guest at this temperature indicates significant intermolecular interaction between the host and the guest. Once the INHCl guest has been lost, the complex then undergoes a slow decomposition losing about 6-10 percent mass (probably the bridging ligand) before the final two-step break down ascribed to the collapse of the cucurbituril moiety. The decomposition of CB-$ZnCl_2$-OxA-CIP seems to follow a similar profile with the slow decomposition of the guest occurring between 230-330 ^{o}C. The evolution of the bridging oxalic ligand follows around 430 ^{o}C before the final collapse of the cucurbituril units in a single step between 590-620 ^{o}C.

Copper supramolecular complexes, on the other hand, do not present such drastic thermal stabilization following mechanochemistry. The evolution of the INHCl guest from CB-$CuCl_2$-OxA-INHCl occurs just before 200 ^{o}C. After the guest has been removed, the complex undergoes a slow decomposition, losing about 7-10 percent of its mass ascribed to the loss of the bridging oxalic acid ligand. The breakdown of the cucurbituril unit then follows from 480-560 ^{o}C in a single step. The thermal decomposition profile of CB-$CuCl_2$-OxA-CIP is somewhat similar with the loss of the ciprofloxacin guest evolved at between 200-210 ^{o}C and oxalic acid at between 310-320 ^{o}C. The cucurbituril unit then breaks down in a single step from 340-420 ^{o}C.

These TGA results (***Figure 4.24, page 114***) suggest that unlike in the case of the one-pot synthesis where the guest is in the cavity of the cucurbituril unit, mechanochemistry gives complexes where the guest is in the pores. Extrinsic guest inclusion could be due to the metal ion blocking the portal of the cucurbituril upon coordination or the guest being too big (in the case of ciprofloxacin) to fit into the cavity of the cucurbituril unit.

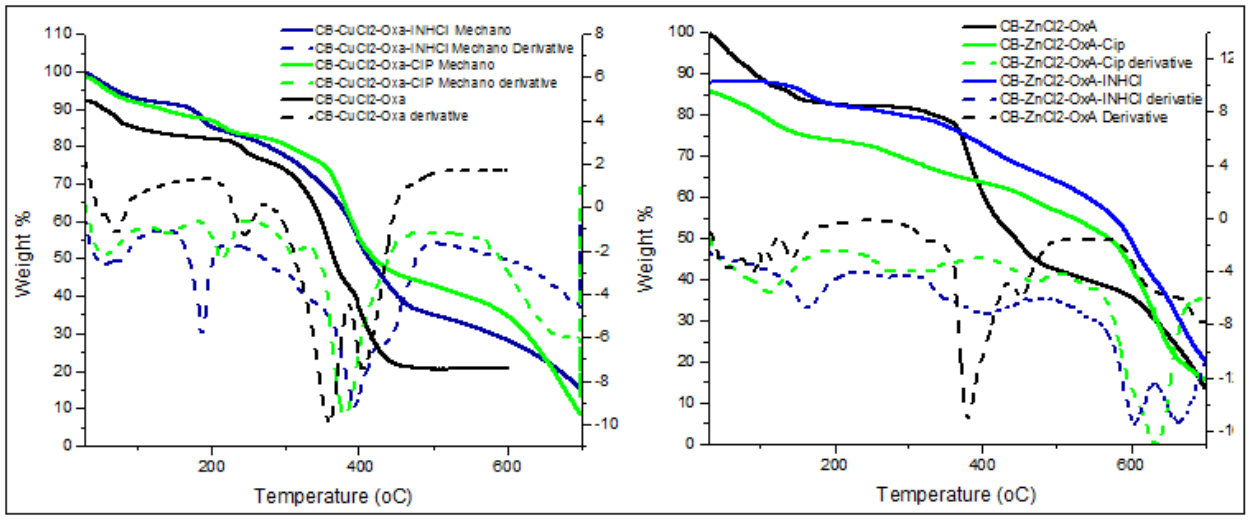

Figure 4.24: TGA spectra of mechanochemistry supramolecular ensembles

4.12 Conclusion

Glycoluril has been successfully synthesized and used as a precursor in the synthesis cucurbituril. Metal complexes of the obtained cucurbituril product have been prepared using different bridging dicarboxylic acid ligands. The porosity of the complexes was confirmed by exposing the complexes to volatile vapors and assessing any sorption. Supramolecular ensembles involving the complexes and isoniazid chloride (INHCl) and ciprofloxacin have been successfully synthesized by one-pot synthesis and mechanochemistry. Successful characterization of the one-pot and mechanochemistry synthesis products revealed that one-pot synthesis favors the inclusion of INHCl in the cavity of the cucurbituril unit while mechanochemistry favors the inclusion of the guests in extrinsic pores.

5 CHAPTER FIVE

This chapter deals with two calixarenes viz: *tetra*-(3,4-dihydroxybenzyl)resorcin[4]arene and *tetra*-(3,4-dihydroxybenzyl)pyrogallol[4]arene. Their synthesis, characterization and subsequent complexation with metal salts is discussed. Host-guest complexes of both the ligands and the metal complexes are discussed.

5.1 Synthesis, characterization and host-guest complexes of *tetra*-(3,4-dihydroxyphenyl) resorcin[4]arene and *tetra*-(3,4-dihydroxyphenyl)pyrogallol[4]arene and their metal complexes

The two compounds described here were synthesized following reports from literature [152] with some modifications and characterized using NMR, FTIR, DSC, and XRD. These compounds were then used as ligands for the synthesis of metal complexes. The Complexes and ligands were subsequently used as hosts for ciprofloxacin. The stoichiometry of the obtained complexes was determined using H-NMR titration.

5.1.1 Synthesis of *tetra*-(3,4-dihydroxyphenyl)resorcin[4]arene (BN15)

A mixture of resorcinol (0.45 g, 4.1 mmol), 3,4-dihydroxy benzaldehyde (0.50 g, 4.1 mmol) and about 5 mL of 50% HCl was refluxed at 70 – 80 ^{o}C in 50 mL of methanol for 36 hours, and the resulting precipitate filtered out and washed three times with ethanol and the filtrate left for eventual crystal growth. After drying in an oven at 50 ^{o}C for another 36 hours, the obtained cream powder weighed 0.74 g, 79% yield with respect to 3,4-dihydroxybenzaldehyde. Upon exposure to air for about a week, the *tetra*-(3,4-dihydroxyphenzl)resorcin[4]arene turned brown-purple. The compound is hereafter referred to as BN15.

5.1.2 Synthesis of *tetra*-(3,4-dihydroxyphenyl)pyrogallol[4]arene (3,4-dHBP)

A mixture of pyrogallol (0.52 g, 7.9 mmol), 3,4-dihydroxy benzaldehyde (0.50 g, 4.1 mmol) and about 5 mL of HCl was refluxed at 70 – 80 ^{o}C in 50 mL of ethanol for 36 hours, and the resulting precipitate filtered out and washed several times with ethanol and the filtrate left for eventual crystal growth. After drying in an oven at 50 ^{o}C for another 36 hours, the obtained brown-purple powder weighed 0.75g, 75 % yield with respect to 3,4-dihydroxybenzaldehyde. Reddish-brown rod-like crystals were obtained by slow evaporation from a solution of DMSO and water. The compound is hereafter referred to as 3,4-dHBP.

5.2 Synthesis of metal complexes

The metal complexes were synthesized (in a 1:4 ligand metal ratio) at room temperature using methanol, DMF and water. In a typical synthesis, 0.10 g of the ligand was dissolved in 0.25 mL DMF with heating (**Scheme 5.1**). The solution was made up to 50 mL using a methanol-water 1:1 mixture. 10 mL (0.02 mg) of the solution was then mixed with the corresponding amount of a metal salt dissolved in water. The addition of the metal salt solution to the ligand resulted in an

immediate color change of the solution; the color changes were metal-dependent. The clear solution was allowed to stand for 24 hours, after which the precipitate formed was filtered, washed with methanol, and dried in an oven. In the case of 3,4-dHBP, precipitates were obtained immediately with metal acetates but not with metal chlorides except in the case of zinc chloride. Products were generally obtained in yields ranging from 39 – 63 %.

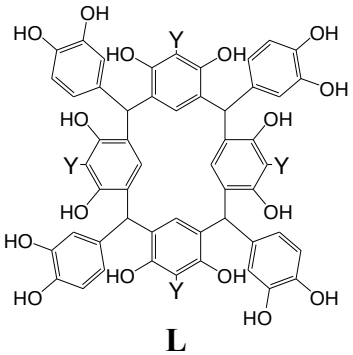

L

\+ **MX** $\xrightarrow[\text{RT, 24H}]{\text{DMF,H}_2\text{O, MeOH}}$ **ML$_n$**

M = Mn^{2+}, Fe^{2+}, Fe^{3+}, Co^{2+}, Ni^{2+}, Cu^{2+}, Zn^{2+}
X = Cl^-, $CHCOO^-$

Y= H; BN15
Y =OH; 3,4-HBP

Scheme 5.1: Synthesis of metal complexes

5.3 Mechanochemical synthesis of host-guest complexes

Non-covalent host-guest complexes of the ligands (BN15 and 3,4-dHBP) and ciprofloxacin were prepared by mechanochemistry using 1-2 drops of HCl. In a typical synthesis, ciprofloxacin (guest), hereafter referred to as CIP, was added to a mortar, and one drop of 36 % HCl was added and ground for two minutes. The desolvated host was then added, while grinding was continued for ten minutes and thereafter transferred to an oven maintained at 30 ^oC for 24 hours. After 24 hours, the mixture was ground again for 5 minutes and analyzed.

5.4 Results and discussions

Both BN15 and 3,4-dHBP were obtained in good yields and high purity. BN15 and 3,4-dHBP each possess two sets of unique C-O-H infrared ring patterns. The presence of C-O-H in BN15 and 3,4-dHBP give rise to three types of stretching and bending (O-H and C-OH stretch and δC-O-H bending) vibrations. The υO-H vibration usually occur above 2900 cm^{-1} while the υC-OH stretch and δC-O-H bending vibrations will occur variously coupled between 1400-950 cm^{-1} [157,172]. The substitution pattern of the aromatic rings determines the vibrational coupling within the two different ring systems [172] which is reflected in the C-OH stretches. Furthermore, the vibrational

coupling between the υC-OH stretch and in plane bending (δC-O-H) may also occur. The FTIR spectra of the two compounds are practically identical although, few differences arise due to the extra OH group and subsequent interactions on the pyrogallol (***Figure 5.1***). Both spectra are characterized by a very broad OH band between 2900 and 3600 cm^{-1}. The appearance of these υO-H bands at lower wavenumbers compared to the non-hydrogen bonded case, usually between 3550 -3700 cm^{-1} [173], is indicative of hydrogen bonding. The C-C aromatic stretching bands appear at 1603 cm^{-1} for both compounds. The corresponding OH in-plane vibrations are observed at 1185 cm^{-1} and 1182 cm^{-1} for BN15 and 3,4-dHBP [157]. The coupled C-OH stretching and bending vibrations occur at 1425/1072 cm^{-1} and 1456/1073 cm^{-1} for BN15 and 3,4-dHBP, respectively [173–175]. Due to the broad nature of the OH band stretch at 2900 cm^{-1}, the CH alkyl stretching band becomes masked. With the exception of an extra CH bending band at 967 and 771 cm^{-1} [157]arising from the extra CH in BN15, the FTIR spectra of both compounds show minor differences.

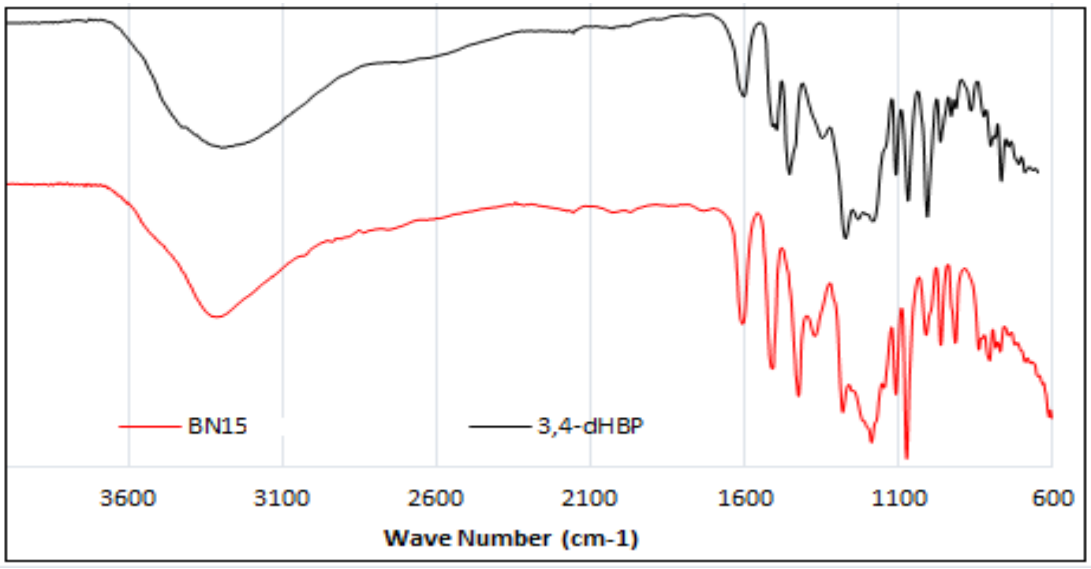

Figure 5.1: FTIR spectra of BN15 and 3,4-dHBP

The carbon and proton NMR spectrum of BN15 is displayed in ***Figure 5.2***. The H-NMR spectra of BN15 showed signals at 5.47 ppm (s, 4H), 6.10 ppm (s, 4H), 6.15 ppm (d, 4H), 6.28 ppm (s, 4H), 6.50 ppm (d, 4H) and 6.55 ppm (s, 4H). The signal at 5.47 ppm is assigned to the methine proton resonance. The corresponding methine carbon resonance appears at 41.18 ppm. The presence of these methine signals and the absence of an aldehyde proton or carbon signal confirms the formation of a new compound.

The signal at 6.10 ppm is assigned to the protons labelled “e” while the signal at 6.55 ppm is assigned to the resorcinolic proton sandwiched between the OH groups and is labelled “f”. The appearance of a single signal for the protons “e” and another for the protons “f” suggest that all the four protons giving rise to “e” are in the same chemical environment as is the case for the protons giving rise to the signal “f”. With all corresponding protons on the 3,4-didhydroxyphenyl rings appearing in the same chemical environment, it is evident that the resorcinolic rings are in the same plane and form a u,u,u,u conformation. A computational optimization revealed that the compound adopts an irregular hour-glass shaped (see insert in ***Figure 5.2***) where one end is wider than the other. The 3,4-dihydroxyphenyl rings form the wider end of the hour-glass shaped, and the resorcinol rings form the narrow end of the structure. The methine carbon lies around the narrow constriction of the structure. The assignment of the other carbon signals was unambiguous.

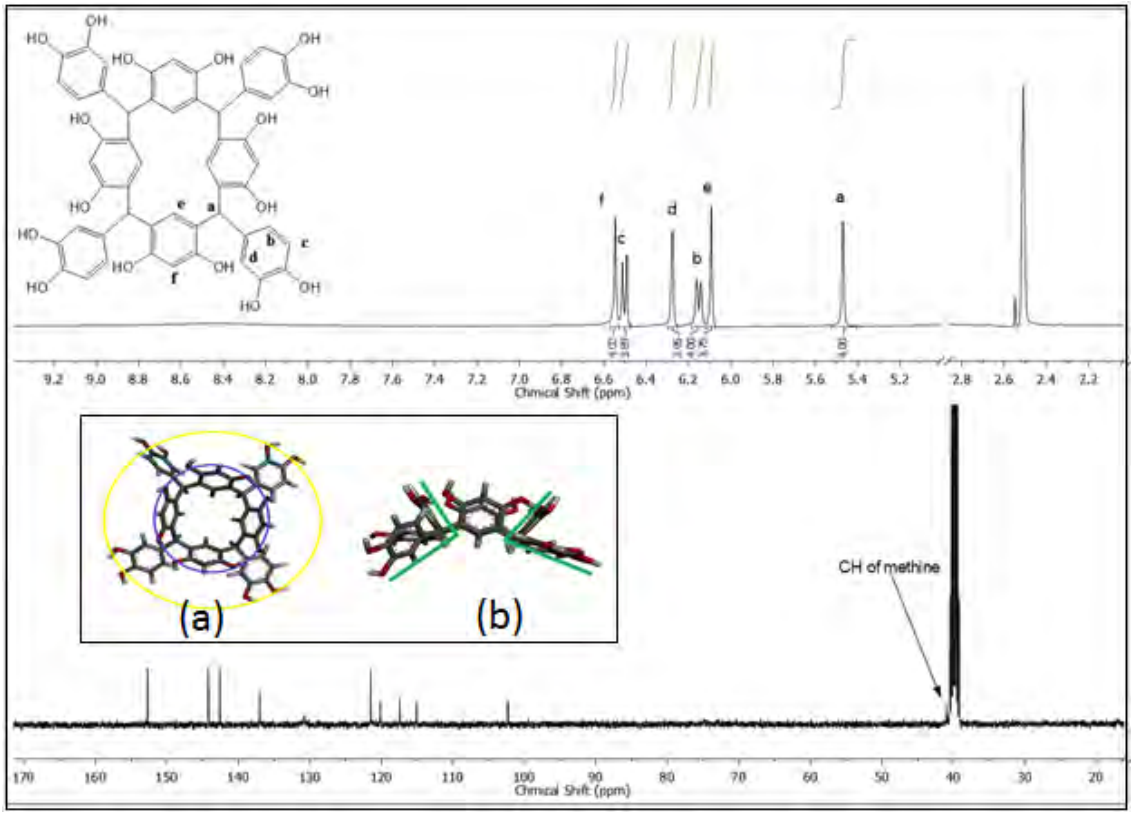

Figure 5.2: NMR spectra of BN15 and the energy minimized structure [insert (a) shows the wider (yellow circle) and narrower (blue circle) ends of the molecule when viewed from above (b) shows the hour-glass-shape of the molecule]

Mass spectrometry proved useful in not only confirming the formation of the compound but also in determining the ring size of the resorcinarene. It is known that the synthesis of calixarenes under the conditions used in this work usually gives rise to the cyclic compounds, in which the tetramer is the main product in appreciable yields and purity. The hexamer or octamer are also usually formed [16]. While analytical techniques were instrumental in deciding if the reaction had formed the product, mass spectrometry was critical in determining the size of the ring of the major product. The use of electrospray ionization (ESI) mass spectrometry, a soft ionization desorption technique that makes use of polar solvents such as acetonitrile, water, methanol, or sodium formate, was employed for direct measurement of cations in solution. The choice of such a soft technique was to avoid the complete fragmentation of the molecular ion before they get to the detector. This technique has been routinely used to analyze calixarene and calixarene derivatives with adduct formation, a common phenomenon [176]. The mass spectrum of BN15 reveals that the obtained sample is predominantly the cyclic tetramer. It is observed from the mass spectrum in ***Figure 5.3*** that adducts of the BN15 with sodium, hydrogen, and potassium are formed.

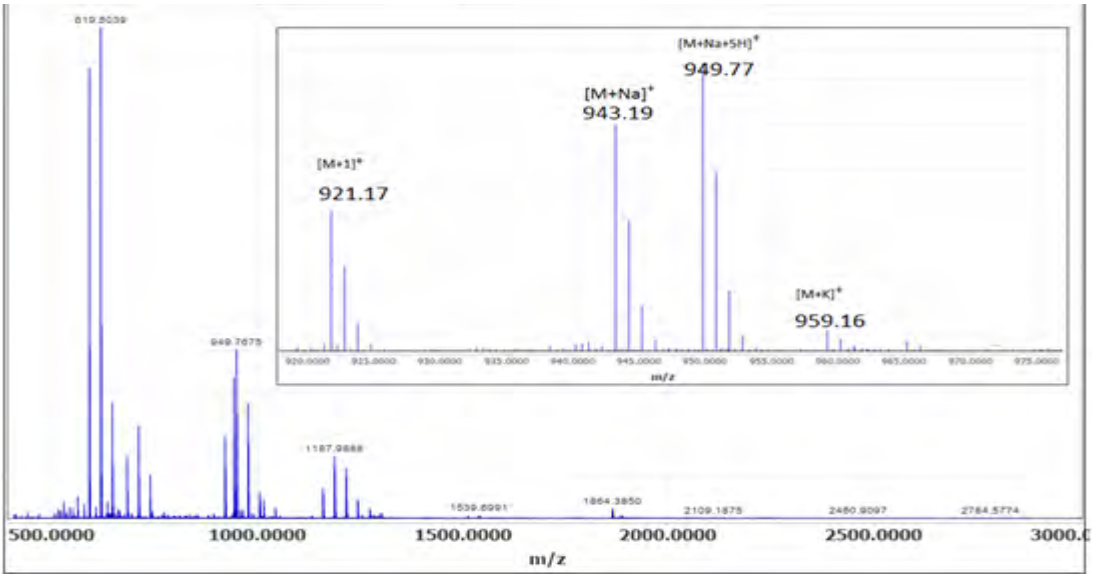

Figure 5.3: ESI-MS of BN15

Thermal analysis of the compound was carried using a Perkin Elmer TGA 4000 and Perkin Elmer DSC 6000 at a heating rate of 25 ºC/min under a nitrogen atmosphere. The compound losses solvent molecules in two steps between 40-120 ºC as shown in ***Figure 5.4***.

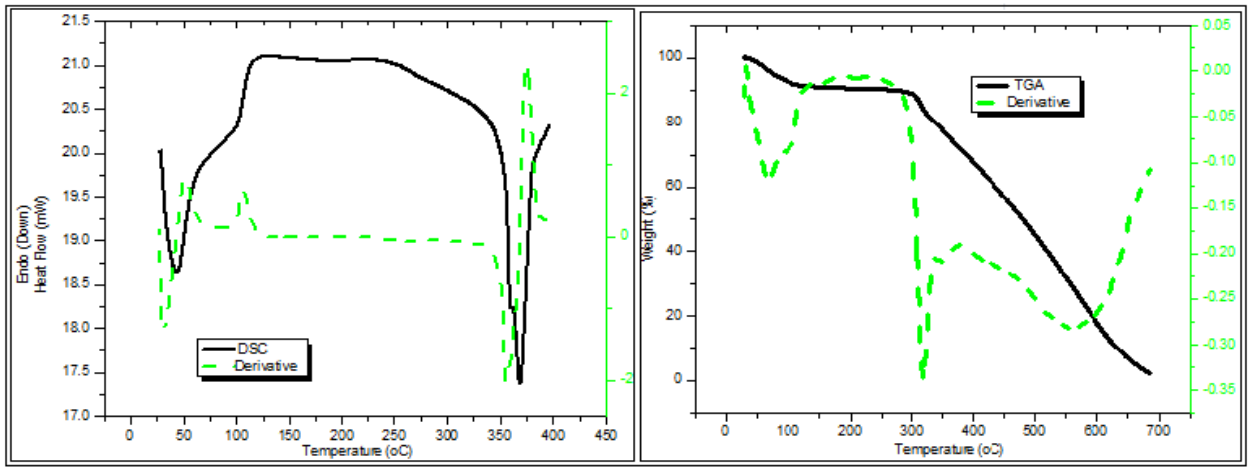

Figure 5.4: DSC and (left) and TGA (right) of BN15 [the corresponding derivatives are indicated in dashed green lines]

The first loss of solvent is probably molecules found on the surface of the molecule, while the second step occurring between 90-120 ºC is the loss of adsorbed molecules. After that, the compound remains stable until beyond 300 ºC, where the onset of melting begins at around 320 ºC and peaks at 368 ºC. This onset also coincides with decomposition, during which the compounds lose about 8 % of its mass before gradually decomposing. TGA analysis further indicates that this approximately 8 % loss corresponds to the evolution of four water molecules. This probably arises from the formation of an intermediate epoxide ring on the 3,4-dihydroxybenzaldehyde ring due to thermolysis (**Scheme 5.2**). The TGA evolved gas analysis indicates the evolution of water, confirming that there is indeed the loss of water molecules.

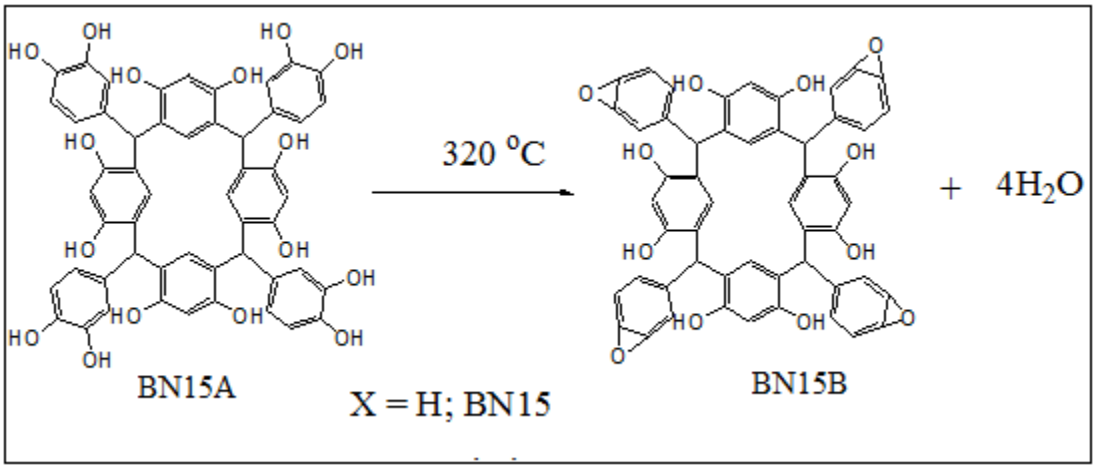

Scheme 5.2: Elimination of water from BN15 and 3,4-dHBP at 320 ºC

To further investigate this evolution, powder of BN15A was heated to 320 ºC to obtain BN15B, cooled and then analyzed using FTIR spectroscopy. Other characterization techniques are envisaged in future work to gain more insight into the epoxidation.

The FTIR spectra of BN15B after heating to 320 ºC shown in ***Figure 5.5*** reveals that the structure remains largely intact as most of the bands are still visible although shifted. The OH stretch in BN15B occurred at a higher wavenumber. The presence of the band indicates that complete dehydration has not occurred as postulated, while shifts to higher frequency indicate the destruction of intramolecular hydrogen bonding, which occurs during the dehydration. The aromatic bending and stretching band due to C-OH on the 3,4-dihydroxybenzoyl ring in BN15A appear at 1073 cm^{-1}. Upon epoxidation, this band disappears in the FTIR spectrum of the dehydrated product. Epoxides have a weak infrared ring stretch (υC-O-H) between 1280-1230 cm^{-1}), a strong asymmetric ring distortion (δa C-O-C) between 950-815 $cm^{-1}$and and a symmetric ring deformation between 880-750 cm^{-1} [157,177]. With respect to BN15B, the ring breathing can be observed at 1260 cm^{-1} while the bands at 890 cm^{-1} and 795 cm^{-1} are respectively assigned to the asymmetric and symmetric ring deformations of the formed epoxide ring. he strong band at 1425 cm^{-1}, also arising from the stretching and bending of the C-OH, splits into two bands (1432 and 1422 cm^{-1}) upon dehydration. It is suggested that this splitting is due to the change in symmetry following the epoxidation. Furthermore, it is also suggested that loss of the band at 1072 cm-1 is due to the loss of proton and change in symmetry during epoxidation. When the two spectra are compared significant vibration, bending and stretching band activity is observed between 1280-1145 cm^{-1}.

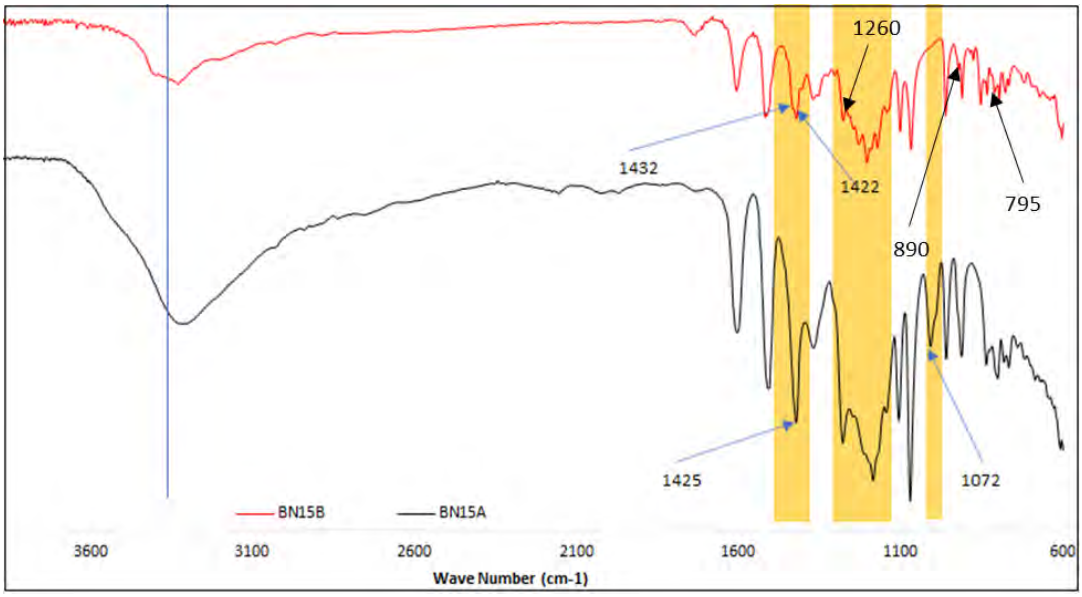

Figure 5.5: FTIR spectra of BN15 and the dehydrated product [BN15A is the as-synthesized sample while BN15B is the sample heated up to 320 ºC]

In the proton NMR spectra of 3,4-dHBP displayed in ***Figure 5.6***, signals are observed at 5.54 ppm (s, 4H), 5.60 ppm (s, 2H), 5.70 ppm (s, 2H), 5.89 ppm (s, 2H), 5.91 ppm (s,4H), 6.11 ppm (s, 4H), 6.18 ppm (d, 2H), 6.25 ppm (s, 2H), 6.31 ppm (s, 2H), 6.34 ppm (d, 4H) and 6.49 ppm (d, 2H). The carbon NMR spectra, on the other hand, showed twenty peaks, with only one peak appearing below 100 ppm.

The signal at 5.54 ppm in the H-NMR spectra is assigned to the methine proton, and the corresponding carbon signal was found at 42.30 ppm. The OH proton signals appear as a broad peak between 7.2 and 8.5 ppm. The doublets at 6.18, 6.34 and 6.49 ppm appear in the ratio 1:2:1. The doublet signals 6.18 and 6.49 are assigned to the proton alpha to the para OH group on the 3,4-dihydroxyphenyl rings, while the doublet at 6.34 ppm is assigned to the proton beta to the para OH group on the same ring. The split in the signal of the proton alpha to the para OH group suggests that corresponding protons on the four rings in the molecule are not in the same chemical environment. In the ^{13}C-NMR, the signals at between 142-145 ppm were assigned to the hydroxyl carbon atoms. The assignment of the other atoms was, however, not straightforward.

Integration of the signals reveal that the total hydrogen count exceeds the actual count by ten. This prompted the suggestion that the compound may exist as an equilibrium mixture of two conformers, which should perhaps accounts for why there are several carbon signals.

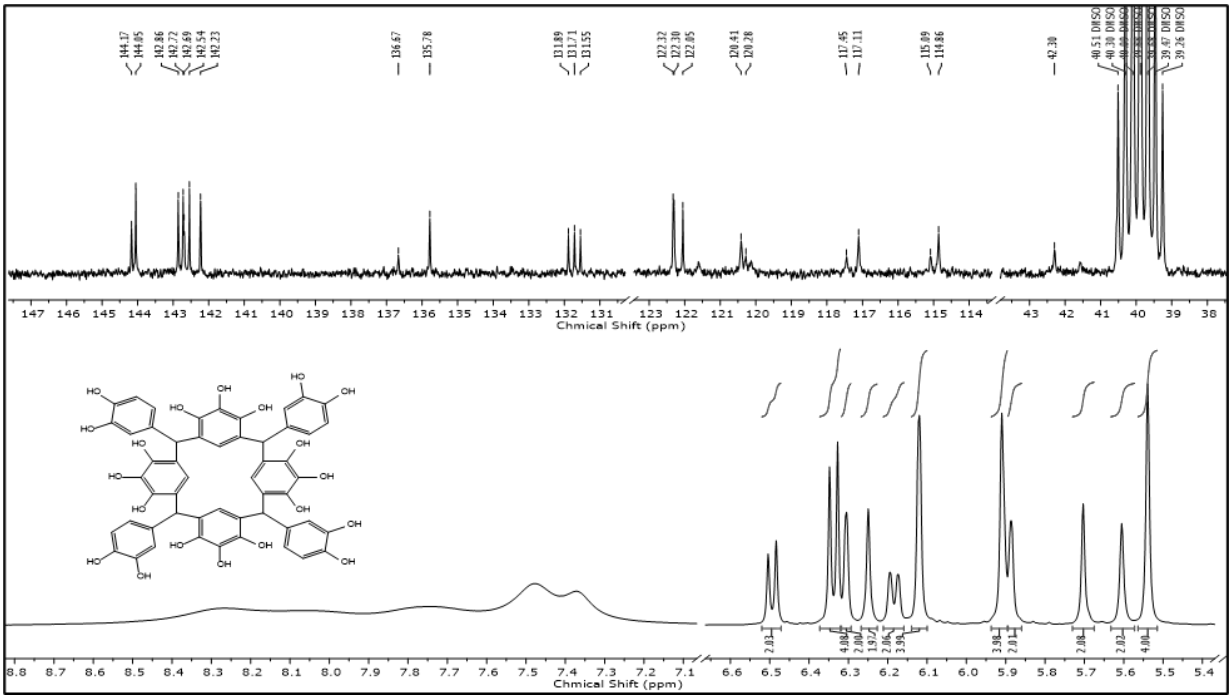

Figure 5.6: NMR spectra of 3,4-dHBP (top CNMR and bottom HNMR).

The thermal decomposition of 3,4-dHBP (***Figure 5.7***) is akin to that of BN15. The first step involves the loss of solvent molecules. The compound remains stable up to 340 ^{o}C after which it undergoes a further two-step decomposition characterized by loss of about 11.2 % ascribed to water evolution followed by gradual decomposition. The evolution of water molecules in the second step is analogous to what happens in BN15 and equally results in the formation of epoxide rings on possibly both the 3,4-dihydroxybenzyl and pyrogallol rings. The percent weight loss here, however, suggests that there are six molecules of water evolved implying there is also epoxidation on the pyrogallol rings. This assertion is plausible since pyrogallol contains adjacent OH groups.

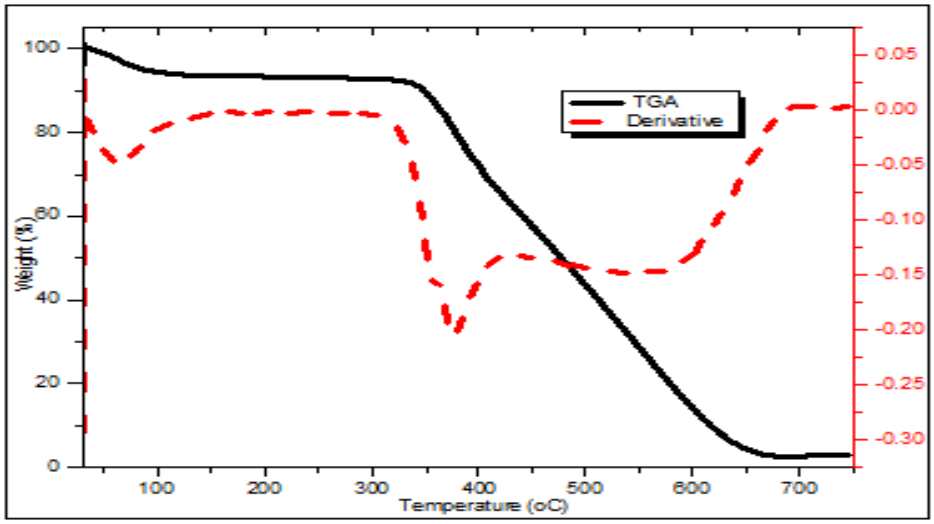

Figure 5.7: TGA thermogram of 3,4-dHBP

The compound was heated to 340 °C to afford dehydration, and then FTIR elemental analysis was carried out and compared with that of the original sample. The results are displayed below in ***Figure 5.8***.

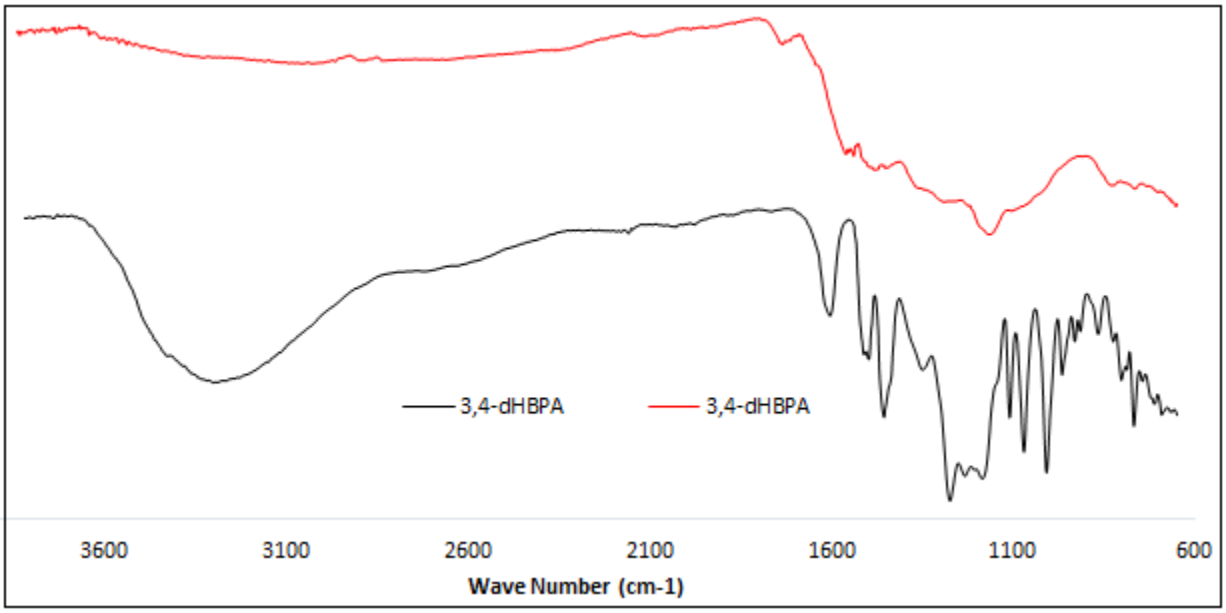

Figure 5.8: FTIR spectra of the 3,4-dHBP and the dehydrated product [3,4-dHBPA is the spectra of the 3,4-dHBP as-synthesized and 3,4-dHBPB is the spectra of 3,4-dHBP after heating to 320 °C)]

As in the case of BN15, the FTIR spectra of 3,4-dHBP (***Figure 5.8***) indicates that the compound is still intact. However, the flattening of the OH band seems to suggest a greater extent of dehydration compared to BN15. The poor resolution of the spectra between 1700 and 600 cm^{-1}, suggests the that the material is non-homogeneous. With the pyrogallol rings containing three

adjacent OH groups, epoxidation is also possible in this ring in addition to that occurring in the 3,4-dhydroxybenzyl rings. The epoxidation in the pyrogallol ring can however occur in one of two ways. This results to the loss in symmetry and consequently the non-homogeneous character displayed by the material. Considerable shifts in the bands due to C-O and aromatic stretching is observed. It is likely that thermolysis and epoxidation, as that which occurs in BN15, happens in the pyrogallol rings between adjacent OH groups (**Scheme 5.3**).

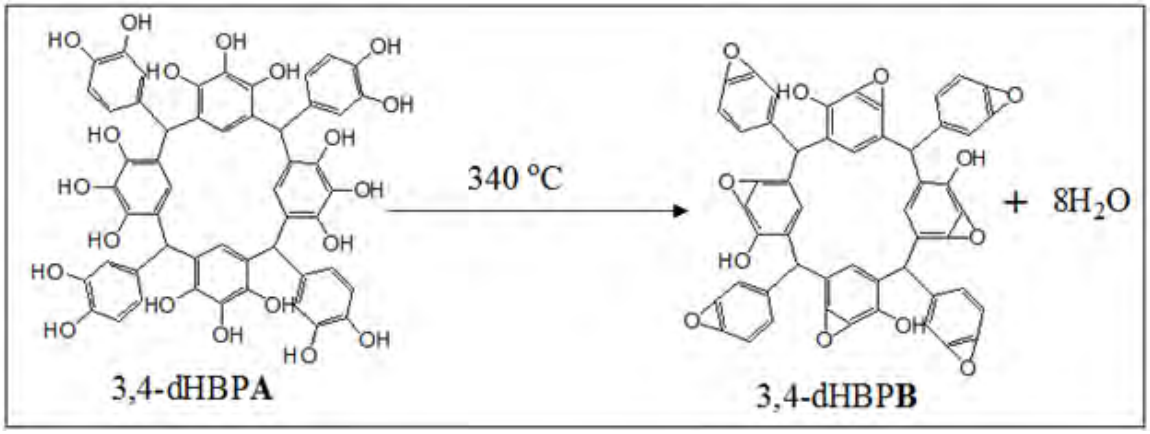

Scheme 5.3: Epoxide intermediate formation during the thermal decomposition of 3,4-dHBP

Single crystals of 3,4-dHBP suitable for diffraction were obtained by slow evaporation from water. The compound crystallizes in the space group *P-1* with five water molecules and a single 3,4-dHBP per unite cell. TGA analysis revealed the presence of four water molecules. The overall supramolecular assembly presents a layered structure where the bridging channels are occupied by water molecules that form hydrogen bonds with the host. The pyrogallol backbone form a 1,3-alternate-like conformation with one pair of opposite pyrogallol rings lying in the equatorial position with their lone hydrogen oriented to the cavity of the macrocycle (***Figure 5.9a***). Two of the 3,4-dihydroxybenzyl rings are directed to one end while the other face the opposite direction. The computer optimized structure of the compound is however different from the single crystal structure. The pyrogallol backbone rings form a 1,3-alternate conformation where opposite rings are planar. The 3,4-dihydroxylbenzyl rings lie in the equatorial position.

The single crystal structure lends more explanation to the NMR, as such an arrangement will give rise to four doublets and seven singlet signals. The doublet signal at 6.35 ppm is double those at 6.19 ppm and 6.50 ppm suggesting two of the four doublet signals have the same chemical shift.

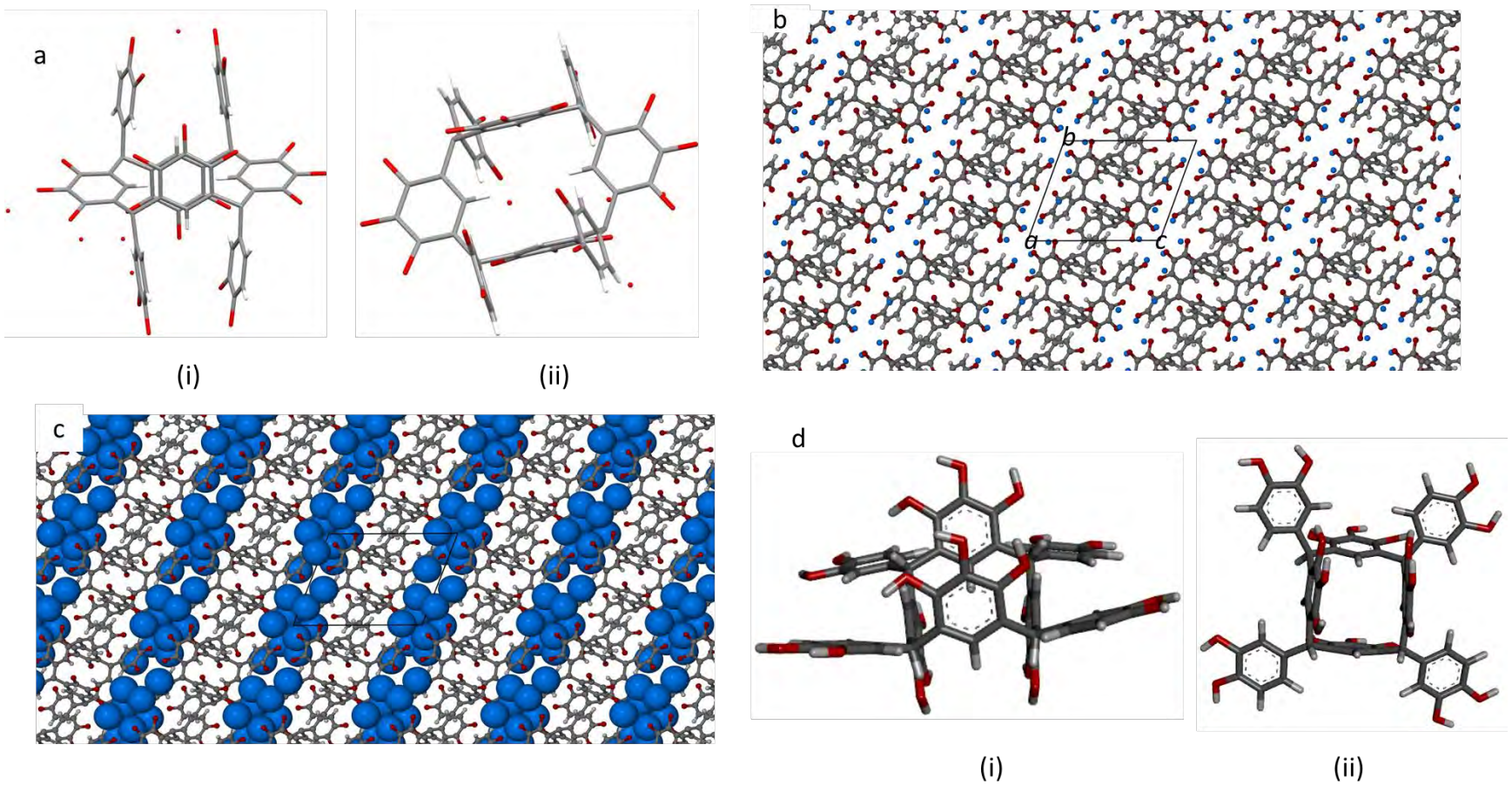

Figure 5.9: (a) Single crystal structure of 3,4-dHBP viewed from (i) the side and (ii) above (b) parking diagram for 3,4-dHBP (c) parking of 3,4-dHBP showing water molecules (in blue) along the channels (d) computer optimized structure of 3,4-dHBP viewed from (i) side and (ii) above

5.5 Metal complexes

5.5.1 BN15 metal complexes

Metal complexes of BN15 were obtained based on chlorides of manganese, iron, cobalt, nickel, copper, and zinc. These were characterized using FTIR, TGA and atomic absorption spectroscopy.

The FTIR spectra of the complexes (***Figure 5.10***), when compared to the ligand, showed very subtle differences. The OH stretch shifts from 3200 cm^{-1} in the free ligand to higher frequencies in all complexes. The introduction of metal ions leads to interaction with the OH groups which disrupts the hydrogen bonds resulting to the observed shift in the OH band. The persistence of the OH band in the complexes also suggests that not all the OH groups coordinate under these conditions. Additionally, the appearance of two new bands in all complexes between 1210 and 1250 cm^{-1} suggests that there is coordination between the metal ions and the ligands.

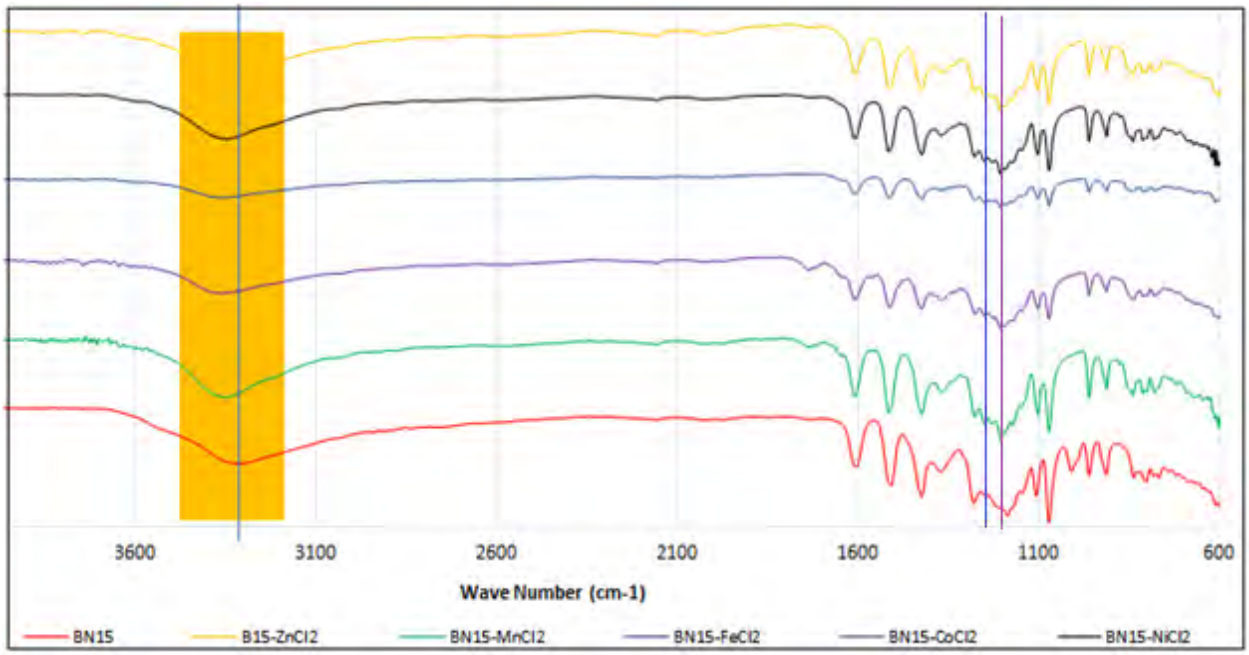

Figure 5.10: FTIR spectra of BN15 and its metal complexes.

Thermal analysis data also proved helpful in elucidating coordination within the complexes as well as thermal decomposition profiles. All metal complexes except that of $FeCl_2$ are generally more stable compared to the ligand as shown in ***Figure 5.11***. This suggest that the complexes involving manganese, cobalt and zinc are isostructural. The disparity shown by the iron complex is most likely due to the oxidation of iron(ii) to iron(iii) by residual oxygen in the nitrogen atmosphere. The iron-BN15 undergoes complete thermolysis to give the FeO. Like the ligand, the complexes

generally show a three-step decomposition profile characterized by loss of uncoordinated water, dehydration, and subsequent decomposition to give carbon dioxide, water, and metal oxides. The dehydration step in the complexes occurs at slightly higher temperatures compared to the ligand which is due to the thermal stabilization effect of complexation. With the complexes generally showing decomposition profiles akin to that of the ligand, it is evident that the ligand under these synthetic conditions coordinates through the oxygen atoms of the resorcinol rings. However, this second step of decomposition in the metal complexes results in a much higher percent mass loss, suggesting more than just the epoxidation of the complex occurring at this point. It is postulated that the mass loss here results from epoxidation, evolution of coordination water molecules and partial breakdown of the ligand within the complex.

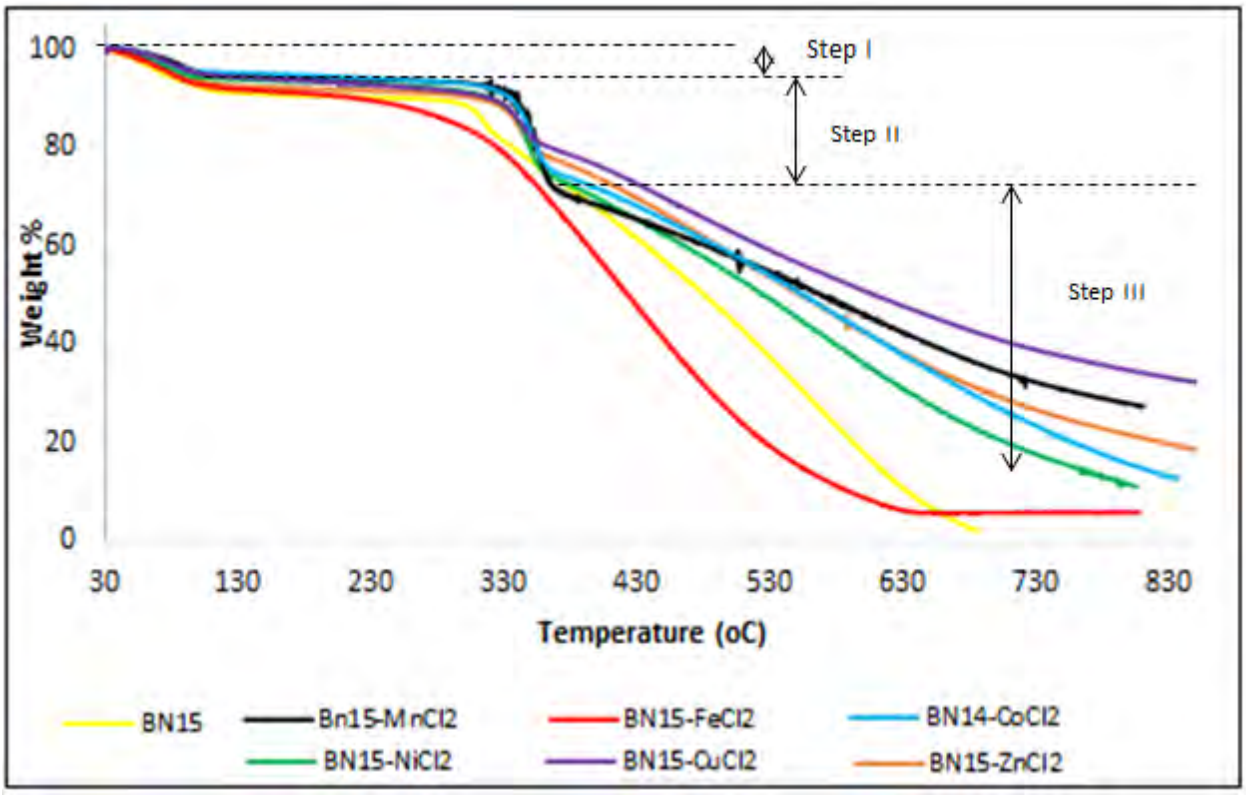

Figure 5.11: TGA thermograms of the ligand (BN15) and metal complexes showing the decomposition steps

Carbon and hydrogen microanalysis was done via combustion while metal analysis was carried out by means of atomic absorption spectroscopy. Water content was determined by means of TGA analysis. The TGA data reveals that the complexes contain varying amounts of coordinating and lattice water molecules. which are given off simultaneously with the dehydration of the ligand.

While the evolution of lattice water is evident and occurs between ambient temperature and 130 ^{o}C, the evolution of coordinated water molecules occurs in the second and third step.

Based on the elemental analysis shown in ***Table 5:1*** a 1:1 metal to ligand ratio has been proposed wherein the ligand coordinates through the resorcinol oxygen atoms. It is suggested that the metal ion coordinate the to one oxygen atom on each resorcinol ring for the isostructural complexes (those of Mn, Co, Ni, Cu, and Zn). However, in the case of the iron complex, two chlorine atoms coordinate to the metal ion; this accounts for the significant decrease in the carbon content of the complex. In the isostructural complexes, the coordination mode of the ligand (to all four resorcinol rings) restricts ring movement which results to more thermally stable structure compared to the iron complex where the two uncoordinated resorcinol rings can flip to induce thermal instability.

Table 5:1: Elemental analysis of ligand and metal complexes [L = BN15]

Compound	Percent Composition			Formula
	Carbon Found (calc'd)	Hydrogen Found (calc'd)	Metal Found (calc'd)	
BN15	67.83	4.35	-------	$C_{52}H_{40}O_{16}$
BN15-MnCl2	55.16 (55.96)	5.21 (4.70)	4.89 (4.92)	$[MnL^{4-}(H_2O)_2]$ $6H_2O$
BN15-FeCl2	52.29 (52.49)	4.84 (4.57)	4.71 (4.69)	$[FeL^{2-}(Cl)_2(H_2O)_2]$ $6H_2O$
BN15-CoCl2	59.65 (59.10)	4.72 (4.29)	5.64 (5.58)	$[CoL^{4-}(H_2O)_2]$ $2.5H_2O$
BN15-NiCl2	58.38 (58.60)	4.40 (4.35)	5.55 (5.51)	$[Ni\ L^{4-}(H_2O)_{2.5}]$ $2.5H_2O$
BN15-CuCl2	59.47 (58.84)	3.70 (4.27)	6.08 (5.99)	$[Cu\ L^{4-}(H_2O)_2]$ $2.5H_2O$
BN15-ZnCl2	59.33 (59.85)	4.00 (4.27)	6.32 (5.97)	$[Zn\ L^{4-}(H_2O)_{2.5}]$ $2.5H_2O$

In the uncoordinated ligand, the second step involves the loss of 9.81 % weigh which corresponds to the loss of four water molecules. Upon coordination, the amount of material lost in the second step is greater than 9.81 % (although the mass loss at this step is expected to be lower). This suggest that the mass loss here is not just the due to dehydration but possibly loss of some of the coordinated water. The uncoordinated OH groups of the 3,4-dihydroxy rings and lattice water molecules are responsible for the OH stretch observed on the FTIR spectra. When metal ions and the ligand are allowed to self-assemble, they form complexes wherein the resorcinolic oxygen atoms coordinate. This results in stabilized symmetrical six-membered rings as opposed to an unsymmetrical relatively unstable five-membered rings on the 3,4-dihydroxy rings. An hour-glass

shape depicted in **Figure 5.12** has been proposed for these complexes where the 3,4-dihydroxy end of the molecule is broader than the resorcinol end, which is capped by the metal ion.

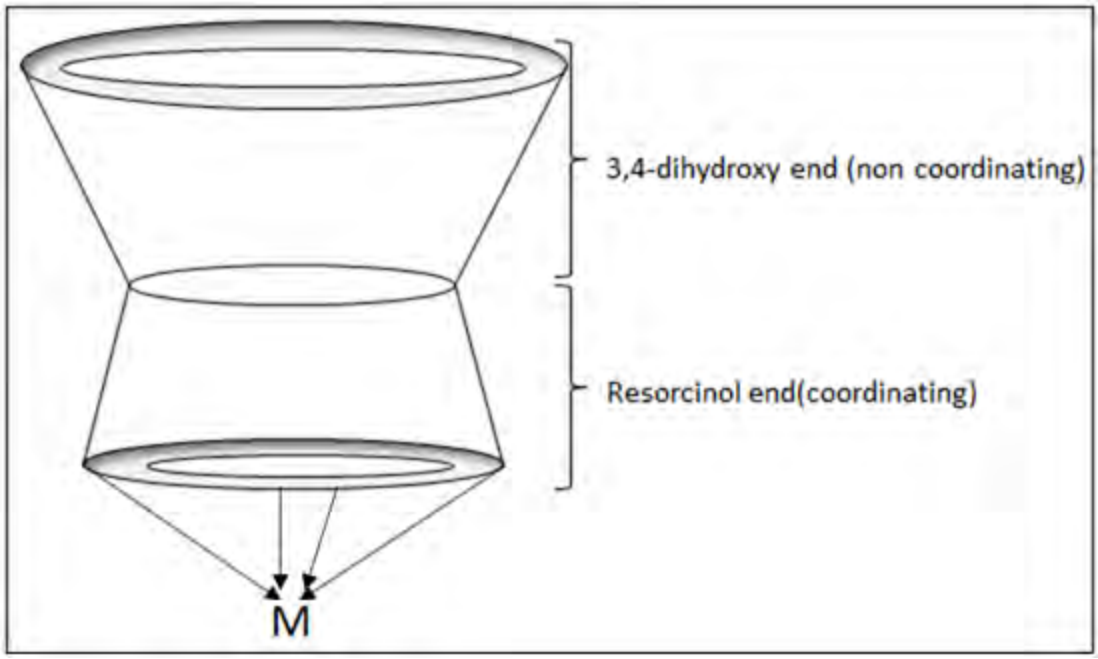

Figure 5.12: Proposed coordination model for the complexes of Mn, Co, Ni, Cu, and Zn in 1:1 metal-ligand ratio [in the case of Fe-BN15 only two oxygen atoms are coordinating]

3,4-dHBP Complexes

The complexes of 3,4-dHBP were prepared based on metal acetates. The FTIR spectra of metal acetate complexes of 3,4-dHBP shown in ***Figure 1.1*** show a broad, less intense shape in the OH stretching region, suggesting that unlike in the case of BN15, all the oxygen atoms are coordinating with little or no localized hydrogen bonding. Though resembling the spectra of the ligand, the FTIR spectra of the complexes appear more broadened between 1700-600 cm^{-1} is indicative of polymeric structure. Visible shifts in bands, particularly the C-O band, indicate that there is coordination through the oxygen atom of the ligand. The absence of a carbonyl band in the FTIR suggests that there is no coordinating or free acetate ion in the complexes.

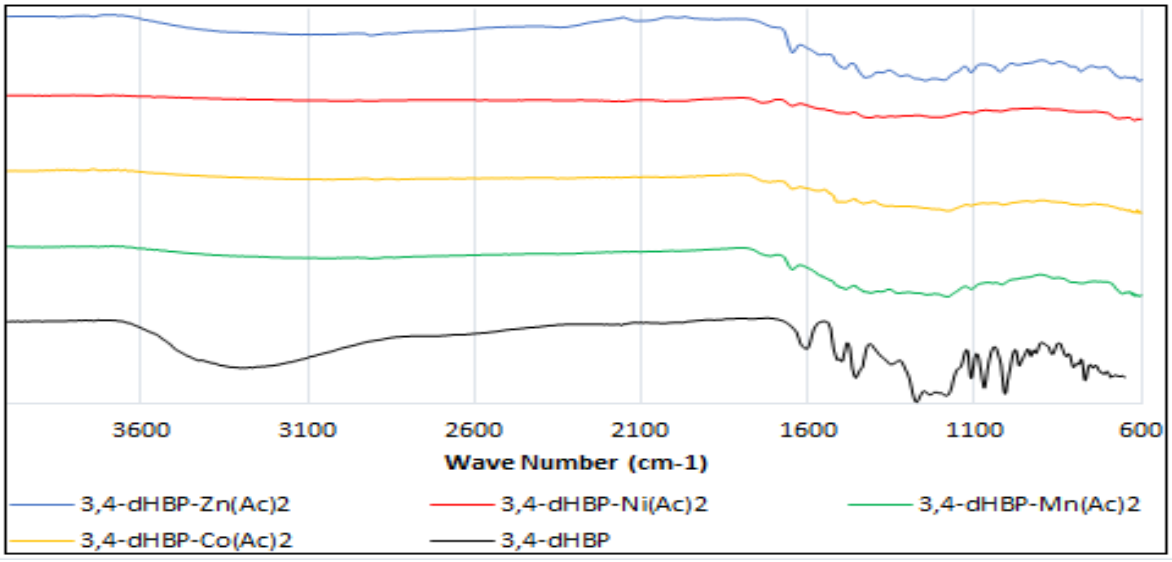

Figure 5.13: FTIR Spectra of 3,4-dHBP and its metal acetate complexes

From the microanalysis data, coordination of the ligand to metal ions is more extensive unlike the mono-complex case of BN15, where the percentage carbon drops by 8-11 percent upon complexation. Complexation of 3,4-dHBP with metal salts results in a decrease of 30-33 percent in carbon content (***Table 5:2***). This significant decrease in carbon content in the metal complexes indicates a high concentration of metal ions in the complexes as opposed to the complexes of BN15, where metal content is relatively low. Since the metal complexes were prepared using metal acetates, it is likely that due to the basic nature of the acetate anion in solution, the ligand is extensively deprotonated such that all twenty terminal oxygen atoms of the ligand coordinate to metal ions. As such, $M_7L.nH_2O$ complexes are formed in the case of Mn, Co, Ni, and Zn and $M_8L.6H_2O$ in the case of Cu.

Table 5:2: Microanalysis data for 3,4-dHBP and complexes prepared from metal acetates.

Compound	% C Found (cal'd)	% H Found (cal'd)	Molecular formula
3,4-dHBP			$C_{52}H_{40}O_{20}$
3,4-dHBP-Mn	39.17 (39.74)	2.23 (2.82)	$Mn_7C_{52}H_{20}O_{20}$ $12H_2O$
3,4-dHBP-Co	40.48 (40.10)	2.25 (2.59)	$Co_7C_{52}H_{20}O_{20}$ $10H_2O$
3,4-dHBP-Ni	39.84 (40.17)	2.33 (2.59)	$Ni_7C_{52}H_{20}O_{20}$ $10H_2O$
3,4-dHBP-Cu	39.56 (39.39)	2.07 (2.02)	$Cu_8C_{52}H_{20}O_{20}.6H_2O$
3,4-dHBP-Zn	38.20 (38.48)	2.30 (2.73)	$Zn_7C_{52}H_{20}O_{20}$ $12H_2O$

TGA analysis of the 3,4-dHBP (***Figure 5.14***) shows a similar profile to BN15 with a dehydration step around 330 ^oC followed by a decomposition. The TGA of the complexes depicted in ***Figure 5.14***, fails to show distinct thermolysis steps observed in the complexes of BN15, suggesting that

coordination here is very different from that of the complexes of BN15. The complexes are generally less stable than the ligand and show a slow decomposition up to around 330 ^{o}C after which they decompose to the metal oxides. All the metal complexes undergo complete decomposition to give either the pure metal or metal oxides. Complexes of Mn, Co, Ni and Zn show similar decomposition profile suggesting that they are isostructural. All four complexes decompose completely and leave the pure metal residue.

The copper complex undergoes complete thermolysis but leaves a higher percentage of residue compared to the other metal complexes. It is observed form the TGA curve that between 490 and 520 ^{o}C the copper sample increase in weight. Lamprecht et al [178] observed similar increase in mass ascribed to the oxidation (by residual air in the TG by the disproportionation of carbon dioxide to molecular oxygen) of copper residue in the sample. The increase in weight observed in the thermogram of the complex between 490 and 520 ^{o}C, is ascribed to the oxidation of copper to copper(I) oxide by residual oxygen from the nitrogen atmosphere with. The deviation in thermal behavior of the copper complex from the others could be due to Jahn-Teller distortions which are common in copper. The TGA data further reveals that the metal oxide formed in the case of the copper complex is about 42 % of the weight of the complex, indicative of the high copper content of the complex. This result was confirmed by microanalysis results which show that carbon constitutes only 29.56 % of the complex, down from 63.41 % in the ligand.

This implies that the loss in mass between 50 to 330 ^{o}C constitute the evolution of both coordinated and uncoordinated water molecules. The steps that follow the loss of these water molecules represent the breakdown of the complex, which results in the formation of metal oxide, carbon dioxide and water.

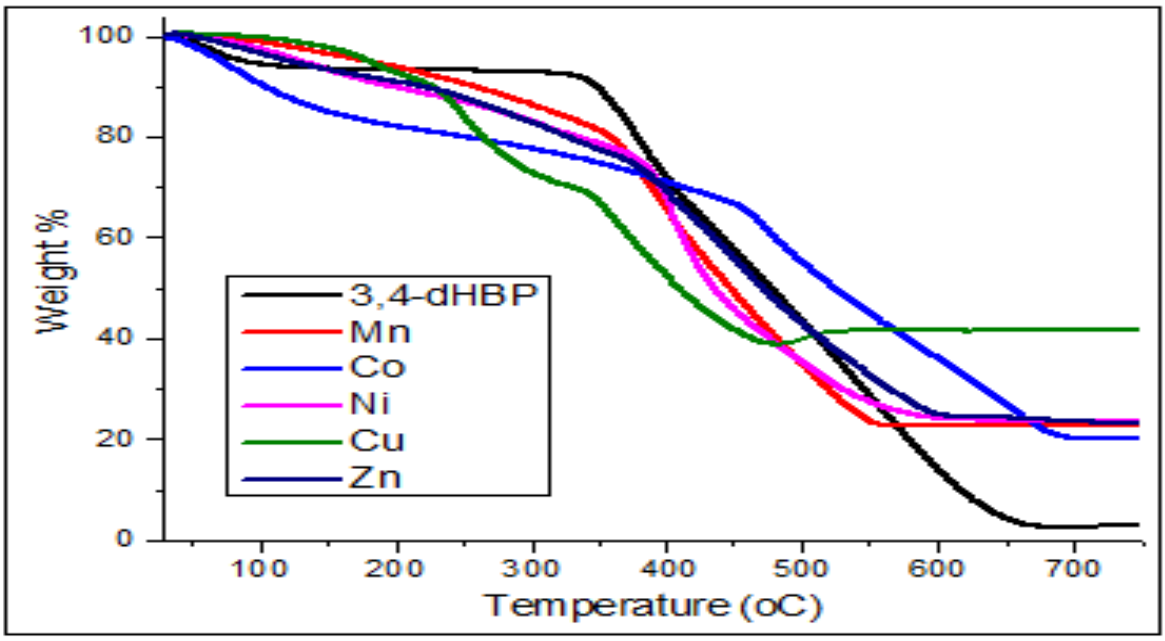

Figure 5.14: TGA thermograms for the metal complexes with 3,4-dHBP

5.6 Host-guest complexes of ligands and some complexes

The powders obtained from the mechanical grinding of the host and guest were analyzed employing FTIR, TGA, NMR and DSC where available. Generally, one drop of 32 % HCl was added [to (1) solubilize the drug, (2) formation of a cation (**Scheme 5.4**)] to the drug and ground for about a minute then the dried powder of the host added and grinding continued for the next 5 minutes. Solubilizing the drug facilitates diffusion of the drug molecules into the calixarene pores while the cationic nature renders attractive cation-π interaction with the calixarene cavity.

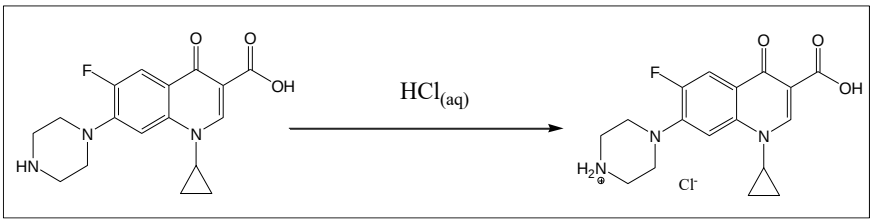

Scheme 5.4: Dissolution of ciprofloxacin in HCl to form a cation

Since calixarenes have a hydrophobic cavity, cation formation is critical to driving cation-π interactions, which stabilizes the complex and directs insertion by dictating which part of the ciprofloxacin enters the cavity. The carboxylate end of the molecule is then likely to be responsible for H-bonding interactions.

5.6.1 BN15-ciprofloxacin host-guest Complexes

The formation of host-guest complexes was ascertained using FTIR, NMR, PXRD and thermal analysis.

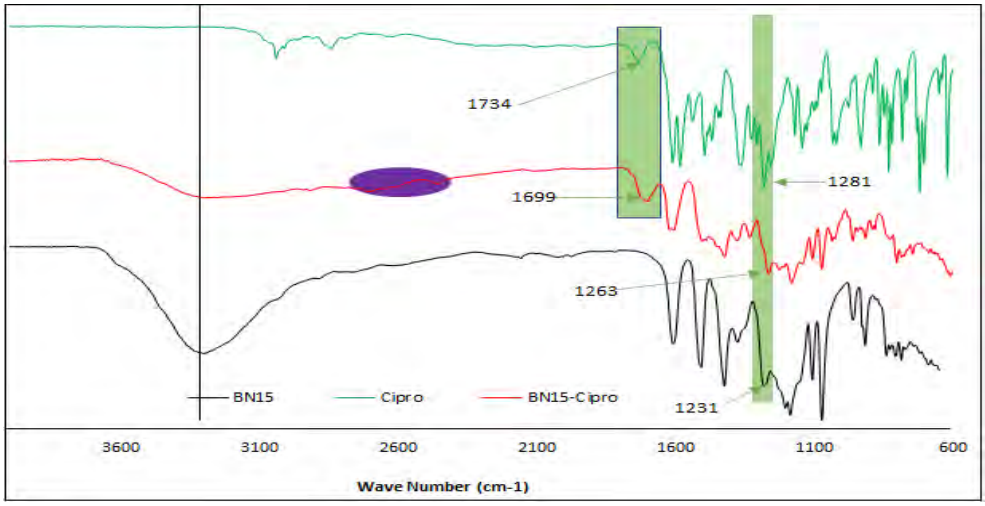

Figure 5.15: FTIR spectra of BN15(black), Cipro (green) and their host-guest complex (red)

The FTIR spectra of the complex (***Figure 5.15***) compared to the host and guest reveals broadening and a shift to higher frequency of the υOH band from 3302 cm^{-1} in the host to 3274 cm^{-1} in the complex. This shift suggests a weakening in intramolecular hydrogen bonding interactions in the host due to the presence of the guest. The formation of new hydrogen bonds is indicated by the weak bands appearing in the region shown in purple. Another observation made in the spectra of the complex is the shift in the band due to the stretching vibration of the carboxylate C=O of the ciprofloxacin from 1734 cm^{-1} in the free drug to 1699 cm^{-1} in the complex [179]. This shift indicates the interaction of the carboxylic acid end of the ciprofloxacin with the host through hydrogen bonds. The shift in the υC-O band of the ciprofloxacin from 1281 cm^{-1} in the free ciprofloxacin to 1263 cm^{-1} in the complex also confirms the assertion that the drug interacts with the host through its carboxylic end [179,180]. Similar shift in the C-O band of the host from 1263cm^{-1} to 1231 cm^{-1} also indicate that the host interacts through the OH groups.

The H-NMR spectra of the host, guest, and complex were also critical in determining interactions between the host and guest and if the host-guest complex was stable in solution. Comparing the H-NMR of the ciprofloxacin and the complex shown in ***Figure 5.16*** reveals significant up-field chemical shifts of almost all proton signals. This up-field shift is caused by the host-guest

interactions. The protonation of the ciprofloxacin with HCl results in the new NH signal appearing at 9.31 ppm in the complex. The broad and less intense peak at 7.51 ppm is assigned to the OH of the carboxylic end, which upon complexation shifts to 8.37 ppm and becomes even broader due to hydrogen bonding interactions [181].

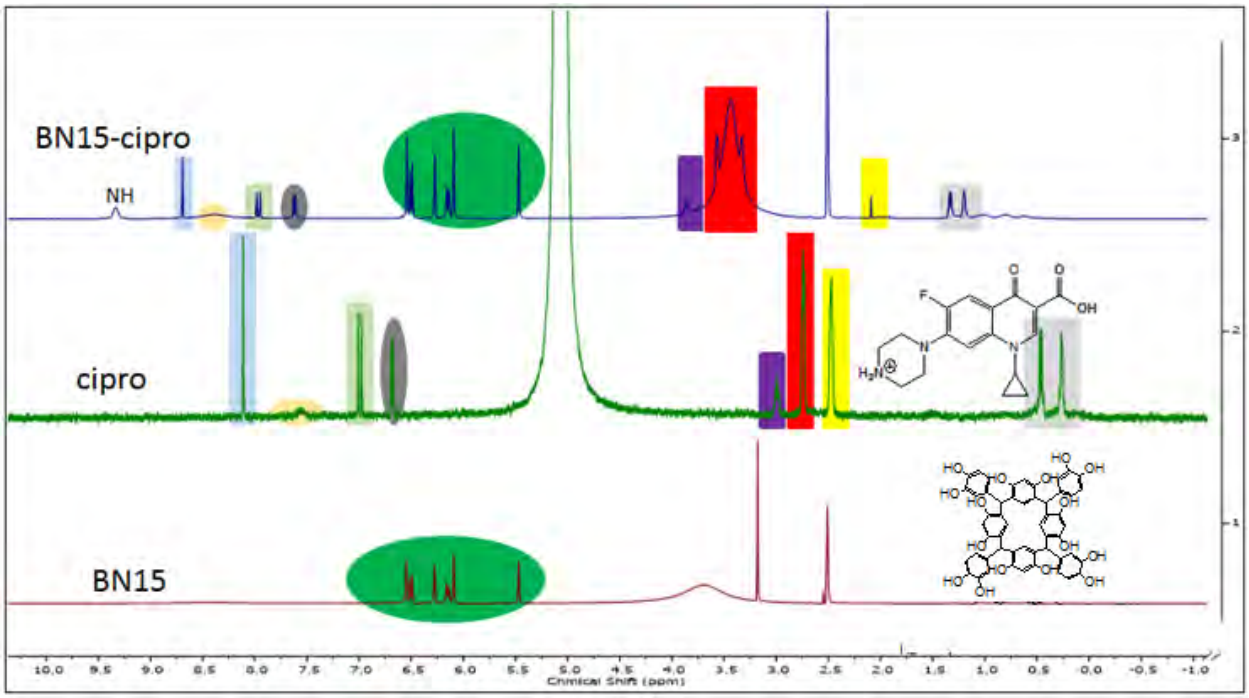

Figure 5.16: HNMR spectra of BN15 (red), Cipro (green) and BN15-cipro (blue) in DMSO-d6

At first sight, it appears the signals of the host does not shift significantly. However, careful observation (and zooming in as shown in ***Figure 5.16***) revealed that some peaks were split in addition to the minimal chemical shift changes (typically in the range of 0.1 to 0.3 ppm). Weak interactions reflecting long range coupling as proton exchange such as has been observed with through space coupling of hydrogen atoms with fluorine [182,183] may indicate exchange between two distinguishable chemical environments. The splitting of the proton signals on the 3,4-dihydroxy rings (***Figure 5.17***) was critical in determining which part of the host and guest were interacting. Given that the proton signals that undergo splitting are located on the 3,4-dihydroxy ring, it is evident that the piperazine end of the ciprofloxacin molecule with fluorine on the adjacent ring is interacting with the rim of the host containing the 3,4-dihydroxy ring. The carboxylic end of the ciprofloxacin then interacts with the OH protons of the resorcinol rings through hydrogen bonding. The resulting structure is a head-to-tail tubular arrangement of the host wherein the

piperazine end of the guest interacts with the head of the host and the carboxylic end with the tail (**Scheme 5.5**).

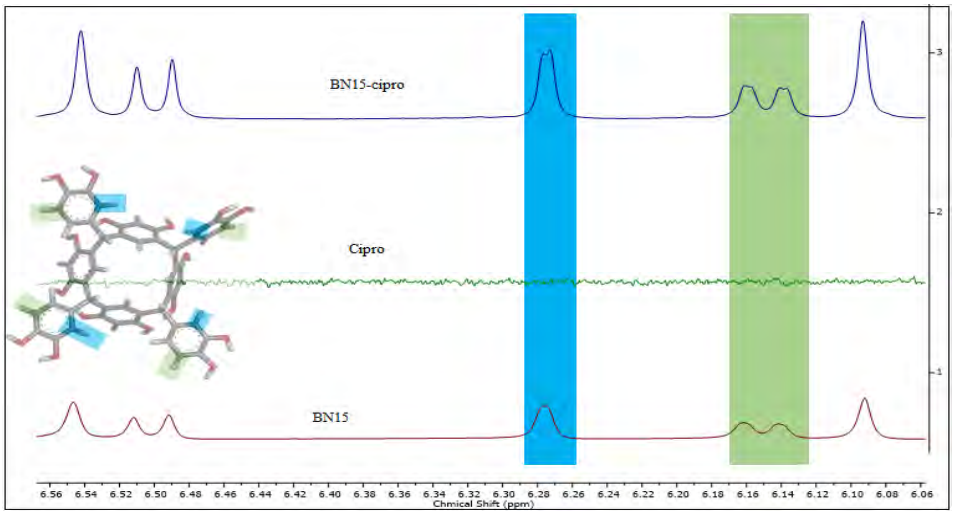

Figure 5.17: Overlayed HNMR spectra of BN15, ciprofloxacin and BN15-Cipro complex in DMSO-d6.

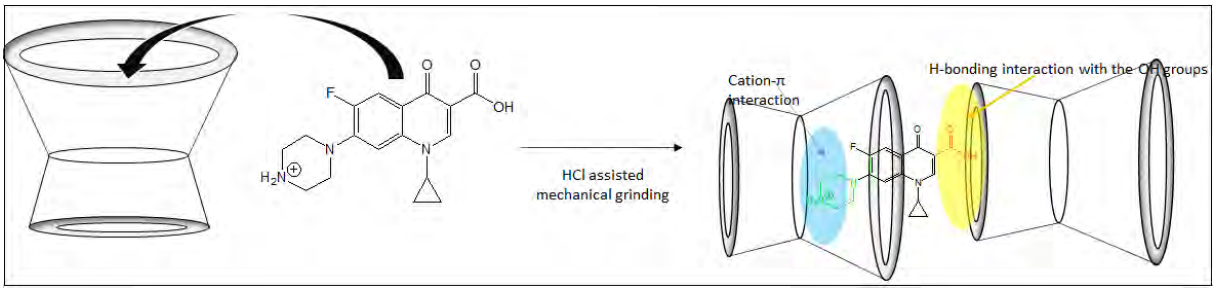

Scheme 5.5: Schematic representation of possible interaction of BN15 with a single ciprofloxacin molecule

The host, guest, and complex TGA was performed to evaluate the thermal stability of the supramolecular complex. Obtained data indicates that all three compounds, the host, guest, and complex decompose in three steps.

The first decomposition step of ciprofloxacin begins at about 100 ºC and lasts until 155 ºC, during which acetylene (C_2H_2) [180] gas is released from the breakdown of the cyclopropane ring attached to the quinoline nitrogen. The second step in the decomposition onsets at 300 ºC and ends at 400 ºC, while the third step continues from 400 ºC slowly to 700 ºC leaving a residue of about 20% due to incomplete thermolysis.

The decomposition of BN15 has already been discussed above. The TGA decomposition profile of the complex (***Figure 5.18***) reveals a weight loss that starts from ambient temperatures until 100

ºC. This loss is ascribed to the evolution of water molecules trapped within the host- guest complex. After that, a second decomposition step resulting in the loss of about 20% of the mass follows from 280 ºC to 310 ºC. The third step then follows from 310 ºC up to 700 ºC leaving a residue of about 37%. An observation worth noting is the fact that unlike in the free guest, where acetylene is released between 80-150 ºC due to the breakdown of the cyclopropane ring, this does not occur in the complex. This is because the guest molecule is enclosed in the center of the host and the intermolecular interaction of this side ring with the host protects it from breaking at temperatures near 100 ºC.

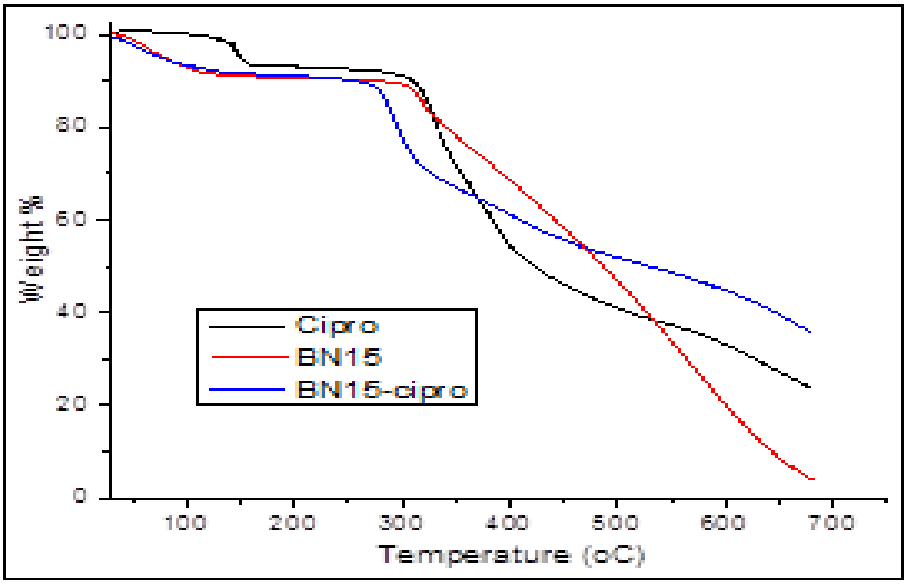

Figure 5.18: TGA thermogram for Cipro (black), BN15 (red) and BN15-Cipro (blue)

5.6.2 Determination of Stoichiometry

The stoichiometry of the complexes between the host and guest was determined using the continuous variation (Job's plot) method. To this end, ten mixtures of the host and guest were prepared with different host-guest mole fractions ($0<r<1$), in which the total volume of the solution was maintained constant. 0.02 g of ciprofloxacin was measured into ten NMR sample tube and the corresponding amount of host (BN15) added. A reference peak on the ciprofloxacin (encircled in red in ***Figure 5.19***) was chosen and its position monitored by H-NMR as BN15 was added to a solution of the guest. A jobs' plot of $\Delta\delta$ of the host versus the mole fraction was made and used to determine the stoichiometry.

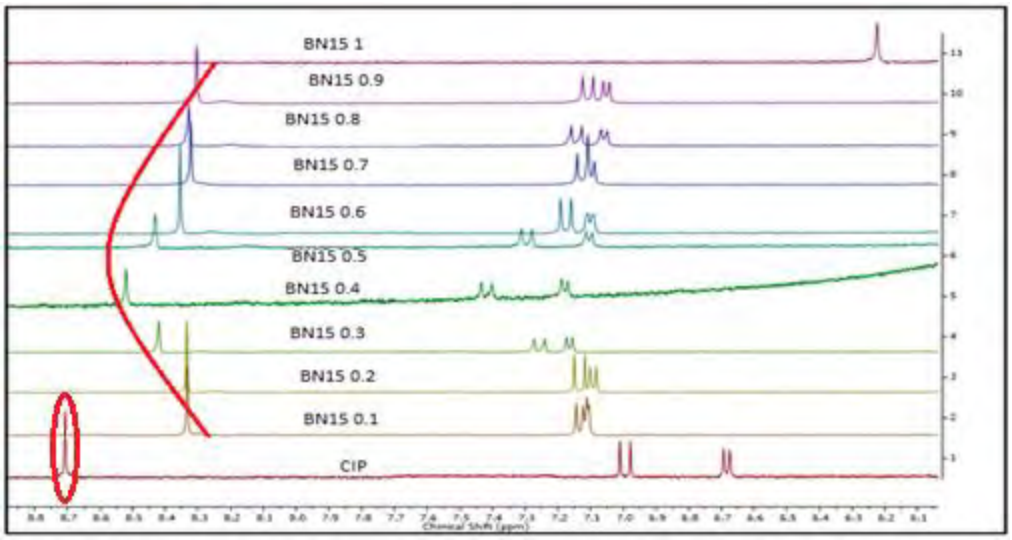

Figure 5.19: H-NMR spectra of titration of BN15 against ciprofloxacin

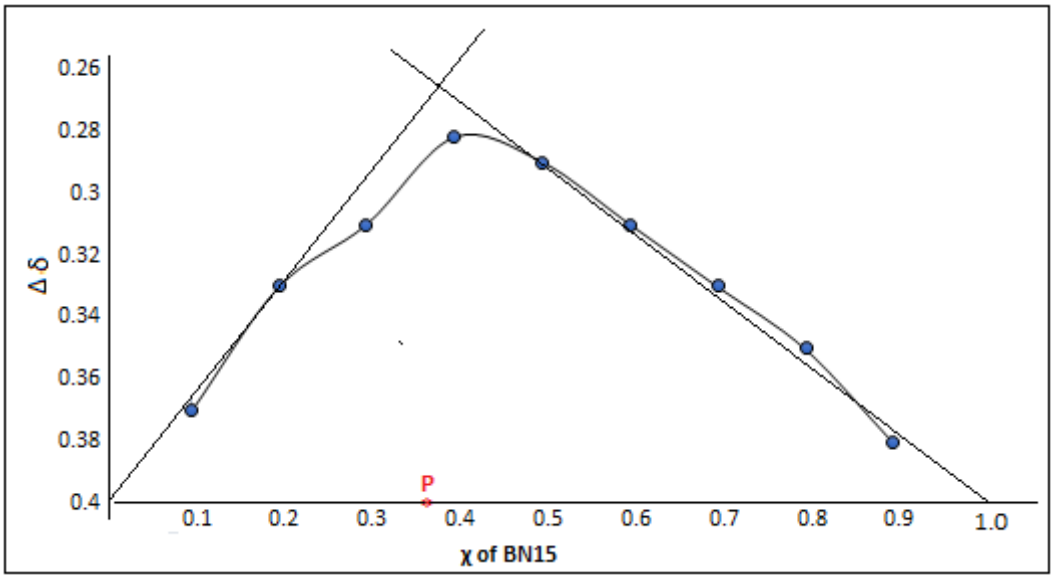

Figure 5.20: Job's plot for the titration of BN15 against Ciprofloxacin

The singlet around 8.7 ppm was chosen as the reference. As soon as a solution of BN15 is added into the ciprofloxacin, the chemical shift of this signal reduces. Incrementally adding host solution result to increase in chemical shift until at a critical point where further addition result to a decrease in chemical shift as shown in ***Figure 5.19.*** The red curve shows a parabolic shape with a maxima near 0.4 mole fraction of the host. A plot of the change in chemical shift versus mole ratio of the host is shown in ***Figure 5.20.*** The maxima of this curve suggest a 1:2 host-guest ratio. It is however unclear at this stage where the second guest is in the complex. It is anticipated that future work on single crystal diffraction will shed light.

For the determination of binding constant,

$[C] \alpha \Delta\delta^{\chi}_{h}$ (5.1)

where [C] is the concentration of the complex, $\Delta\delta$ is the change in chemical shift and $^{\chi}_{h}$ is the mole fraction of the host.

The expression 5.1 can be transformed as

$[C] = k\Delta\delta^{\chi}_{h}$ (5.2)

where k is the binding constant. By substituting the values of point 'P' in ***Figure 5.20***, in equation 5.2, the value of K is obtained as 111.76 µmol/(mL.ppm). This value is three times greater than that reported for testosterone-4-sulphonic calix[4]arenes host-guest complex [1].

The obtained host-guest complex between 3,4-dHBP and ciprofloxacin was characterized using FTIR, NMR, PXRD and thermal analysis.

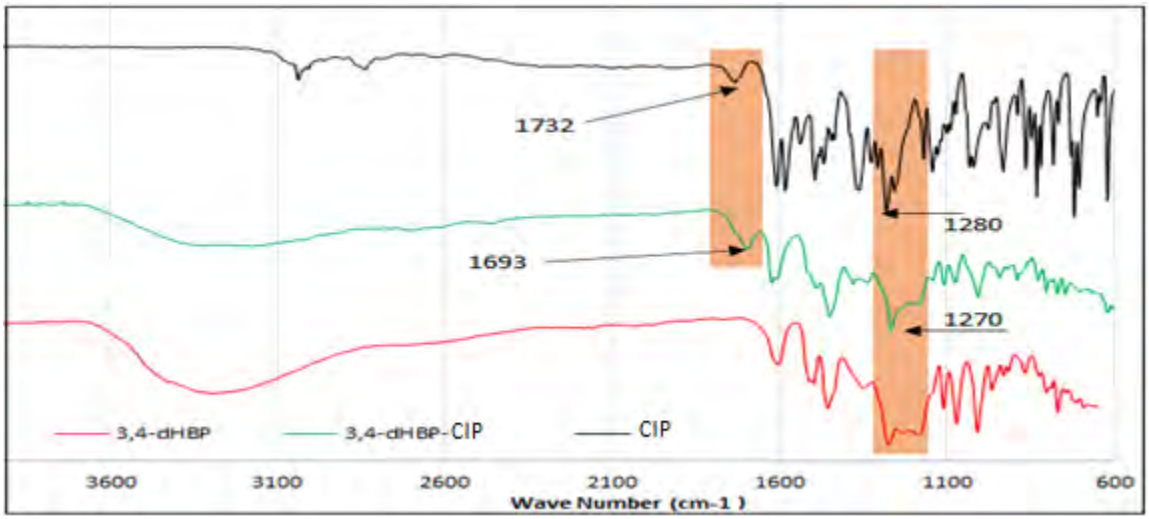

Figure 5.21: FTIR of 3,4-dHBP (red), Ciprofloxacin (black) and 3,4-dHBP (green)

Comparing the FTIR spectra (***Figure 5.21***) of the complex, with the host and guest reveals peak broadening and a shift to lower frequencies of the OH stretching band from 3280 cm^{-1} in the host to 3240 cm^{-1} in the complex. This suggests a weakening of the hydrogen bonding interactions in the host due to the presence of the guest. The formation of new hydrogen bonds is indicated by the weak bands appearing near 2600 cm^{-1}. The carboxylic υC=O vibrational band shifted from 1732 cm^{-1} in the ligand to 1639 cm^{-1} in the complex, suggesting there is an interaction of the carboxylic

functional group on the guest with the host. Because the host contains OH groups, interactions with the COOH group of the guest are most likely hydrogen bonds [179]. The shift in the υC-O stretching band and O-H deformation of the carboxylic function on ciprofloxacin from 1281 cm^{-1} stretching band in the free ciprofloxacin to 1263 cm^{-1} also confirms the assertion that the ciprofloxacin interacts with the host through the carboxylic end [179,180].

The H-NMR of the complex, as in the case of BN15-CIP (***Figure 5.22***) shows a significant shift for the resonance signals of the drug and very little shift for the host. The most notable observation in the supramolecular complex is the disappearance of the signals due to the host OH protons. This disappearance suggests that these OH groups are extensively involved in interaction with the guest. The appearance of the NH resonance signal in the H-NMR of the complex is a confirmation of protonation. The resonance of the methylene protons alpha to the protonated nitrogen atom broadens upon complexation. This broadening is due to the π-π interaction of these methylene groups with the aromatic π electrons [181]. This observation suggests that the protonated end of the guest molecule is located inside the hydrophobic π cavity of the host where a mix of cation-π and π-π interaction exist to stabilize the host-guest complex. The carboxylic end of the guest then interacts with OH groups of the pyrogallol rings on the following host molecule.

Again, as the case of the BN15-CIP complex discussed above, the splitting of some of the proton resonances on the host molecule was observed. This further supports the assertion that the protonated end of the guest molecule is located inside the hydrophobic cavity of the host, where the fluorine atom is in proximity with the split signals (***Figure 5.23***). The through-space interaction of the fluorine atom on the adjacent aromatic ring with the protons in its vicinity then results in the observed splitting.

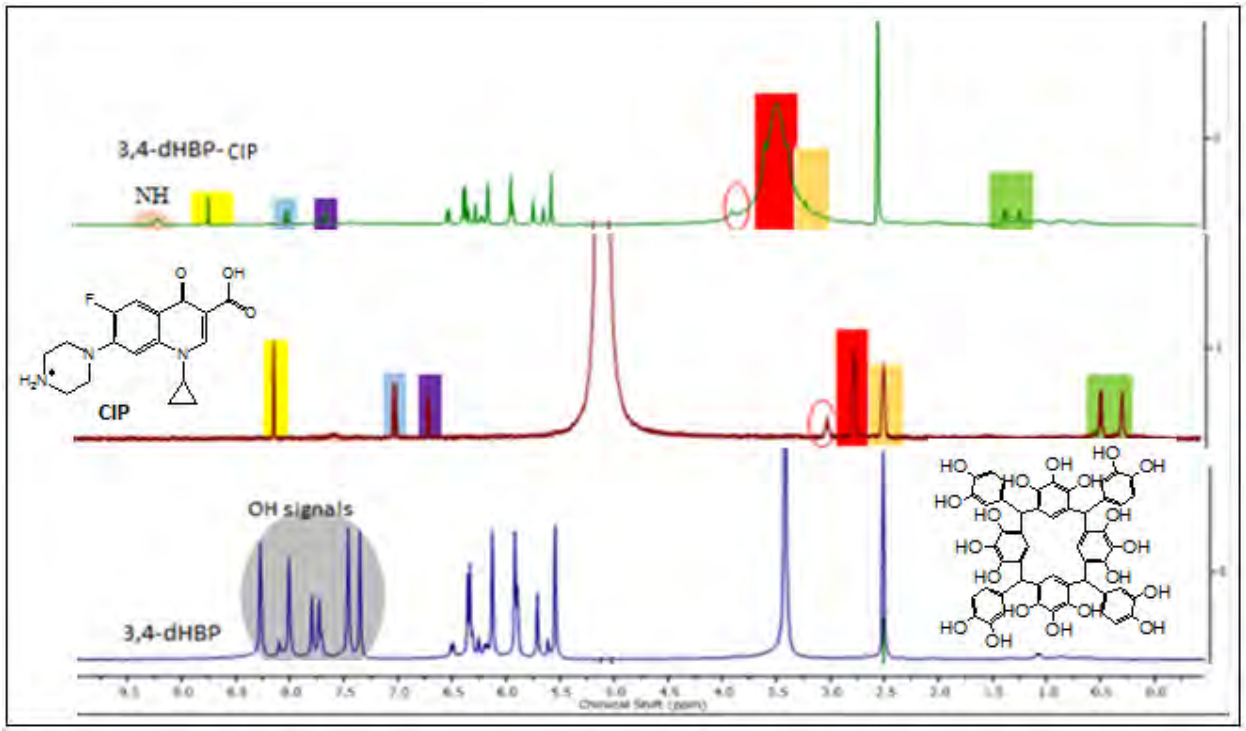

Figure 5.22: HNMR spectra of 3,4-dHBP (blue), ciprofloxacin (oxblood) and 3,4-dHBP-Cipro (green) indicating regions with observed changes in DMSO-d6

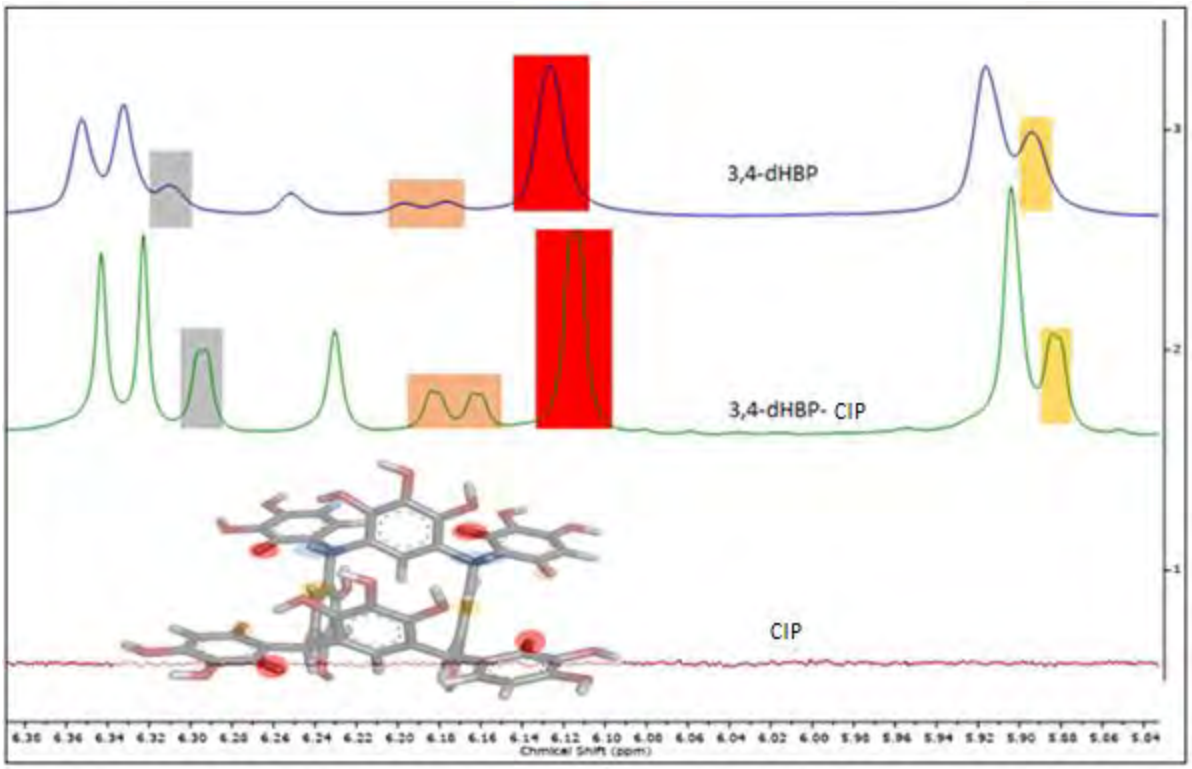

Figure 5.23: Section of HNMR spectra of the host, guest and host-guest complex showing splitting in the host

The thermogravimetric analysis of the host, the guest and the host-guest complex were compared to further understand the nature of the interactions between the species. The TGA of the host and guest have already been discussed above. The decomposition profile of the complex (***Figure 5.24***) shows remarkable similarity to the complex formed between the guest and BN15. The evolution of acetylene observed in the free guest is absent in the complex, suggesting that the guest is protected inside the host. The synergistic interplay of intermolecular interactions, including π-π and cation-π, are likely to be responsible for stabilizing the supramolecular complex. Unlike the free guest, where a second decomposition step involves the loss of approximately 60 % of the total mass, the complex thereof loses about 30 % of the initial mass in the second step. The complex decomposes slowly from about 330 ^{o}C to 700 ^{o}C leaving a 30 % residue due to incomplete thermolysis.

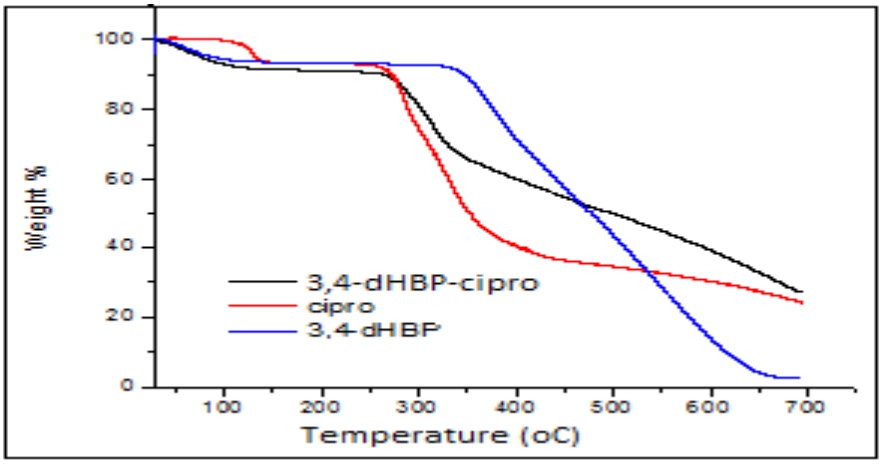

Figure 5.24: TGA thermogram of host 3,4-dHBP(blue), guest ciprofloxacin (red) and complex (black)

Determination of stoichiometry and stability constant

The stoichiometry of the complex formed between 3,4-dHBP and ciprofloxacin was investigated following procedure used the preparation of BN15-CIP complex. Mixtures of the host and guest were prepared with different host-guest mole fractions (0<r<1), in which the total volume of the solution was maintained constant. A reference peak on the ciprofloxacin (encircled in red in ***Figure 5.25***) was chosen and its position monitored by H-NMR as the 3,4-dHBP was added. A plot of Δδ of the host versus the mole fraction was made and used to determine the stoichiometry.

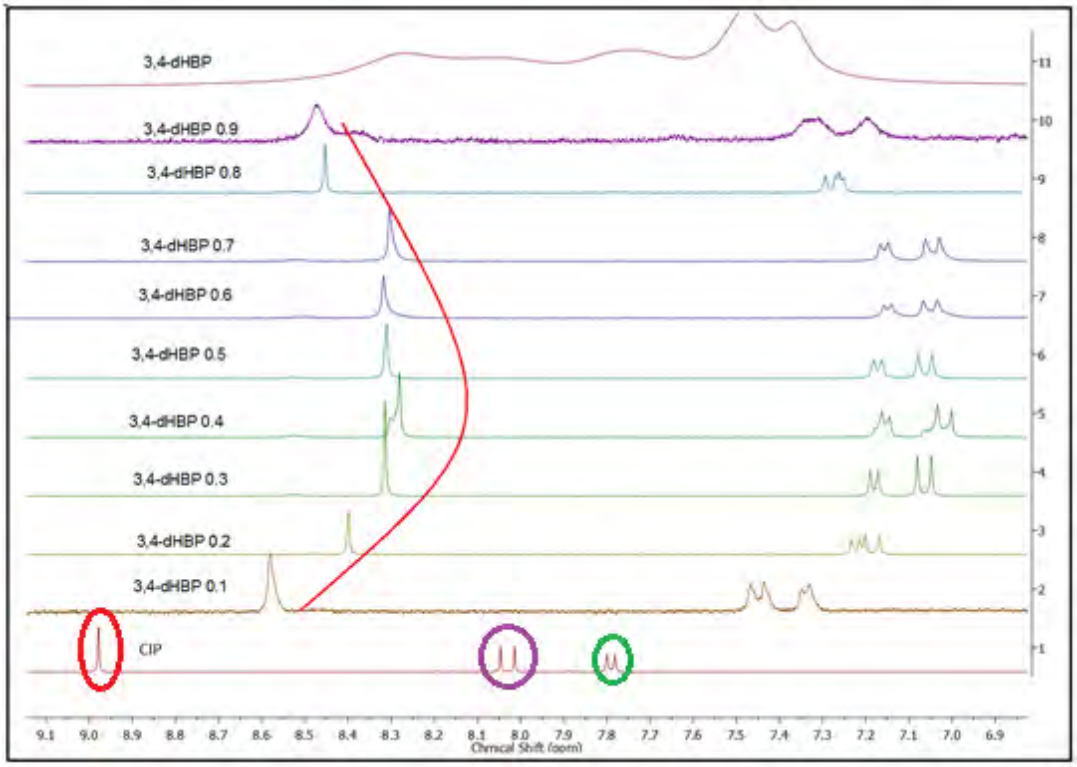

Figure 5.25: Section of the H-NMR titration between 3,4-dHBP and ciprofloxacin.

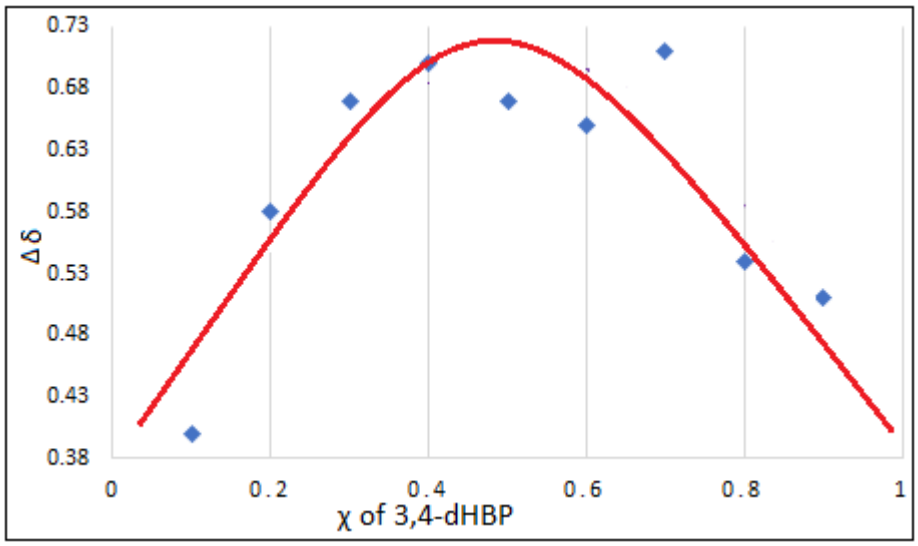

Figure 5.26: Job's plot for the titration of 3,4-dHBP against ciprofloxacin

The H-NMR data indicate that as the amount of 3,4-dHBP is added to the ciprofloxacin, the chemical shift of the signal at 8.9 ppm decreases due to the interaction between the host and the guest. Once the stoichiometric amount has been formed, further addition of 3,4-dHBP result to an increase. This trend is very similar to the complex formed between ciprofloxacin and BN15 suggesting that the stoichiometry is similar as well. A Jobs' plot for the data shown in ***Figure 5.26***

confirm a 1:1 guest-host complexation. Similar Job's plots for the reference signals indicated in purple and green in ***Figure 5.25*** are indicated in the appendix.

The association constant was determined using same approach as with BN15, and the value found to be 92.60 μmol/(mL.ppm). The binding interaction between BN15 and ciprofloxacin is therefore stronger than between 3,4-dHBP and ciprofloxacin.

5.7 BN15-$ZnCl_2$ rt-ciprofloxacin complexes

With both BN15 and 3,4-dHBP forming hollow structures in which the guest molecules are located inside the tube, BN15-$ZnCl_2$ was investigated as a host for ciprofloxacin to verify similarities between the supramolecular structures.

The FTIR spectra of the metal complex, the host-guest complex depicted in and the host ***Figure 5.27*** were compared. The OH stretching band becomes less intense and broader when the metal complex is combined with ciprofloxacin through mechanical grinding. Another salient observation is the appearance of a band at 3528 cm^{-1} in the spectra of BN5-$ZnCl_2$-CIP. This band is assigned to the NH stretching; interestingly, however, this band is absent in the supramolecular complexes of BN15-Cipro and 3,4-dHBP-CIP. The appearance of this band suggests that the interaction and location of guest, in this case, is different from the two previously discussed cases. At this stage, is however not possible to say the exact location of the guest; ongoing work to obtain single crystals of the complex suitable for diffraction will elucidate the exact nature of the interaction. The shifting of the C=O vibrational band of the COOH group from 1737 cm^{-1} in the free ciprofloxacin to 1703 cm^{-1} in the complex indicates guest interaction through the carboxyl group with the host [164]. This is further confirmed by shifts in the C-O stretching and O-H deformations bands in the 1280 cm^{-1} region of the spectra [180]. It is also observed that weak bands are formed in the region around 2600 cm^{-1} which are ascribed to the formation of hydrogen bonds [162,164].

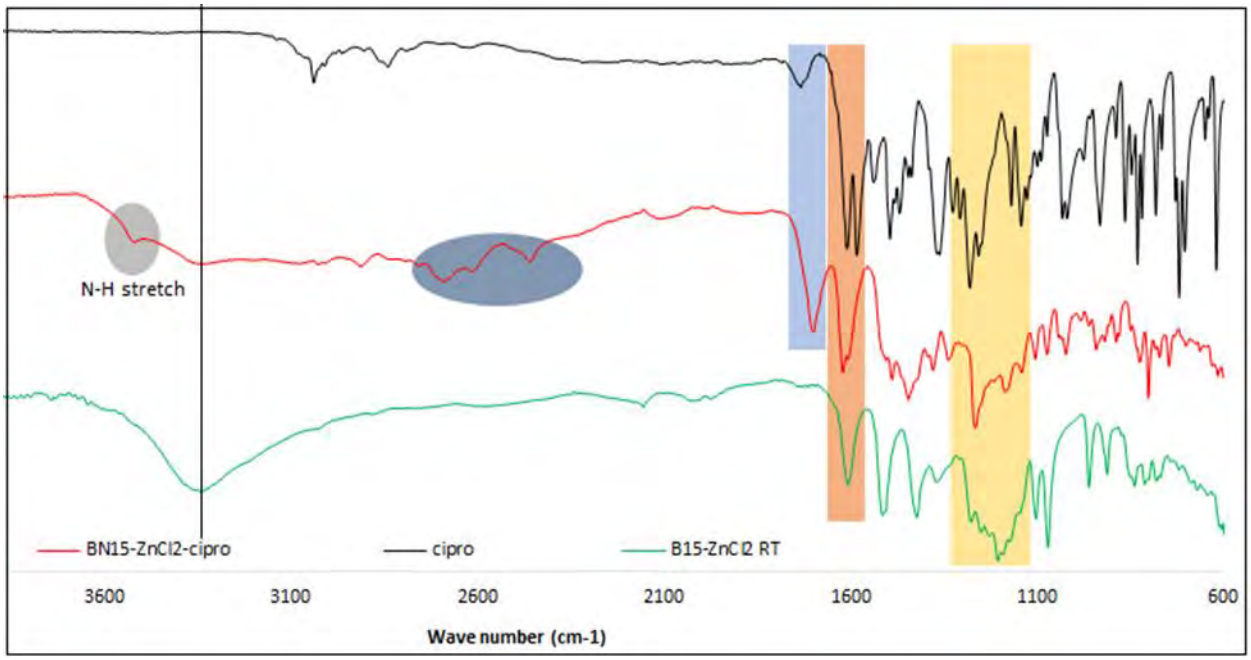

Figure 5.27: FTIR spectra of BN15-$ZnCl_2$-cipro (red), ciprofloxacin (black), and BN15-$ZnCl_2$ RT (green)

The TGA comparison of the supramolecular complex (***Figure 5.28***) with the host and guest revealed that the complex formed is thermally less stable compared to the guest. It is observed that the decomposition of the complex begins with the evolution of water and is closely followed by another mass loss which is ascribed to the loss of the acetylene [180], which takes place slowly and lasts until 200 ºC. The complex then remains stable until temperatures exceed 300 ºC from where it breaks down in three steps, leaving a residue. The decomposition profile of the complex reveals that unlike in the case wherein the host was purely organic, the guest is less tightly bound and more exposed.

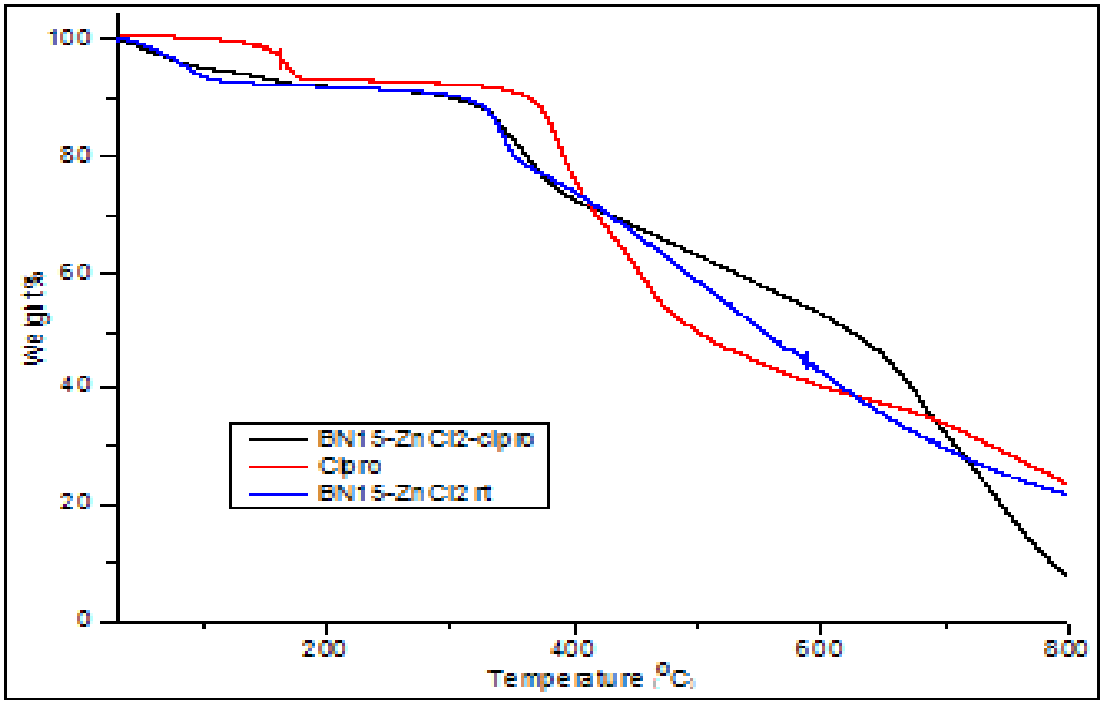

Figure 5.28: TGA thermograms of BN15-ZnCl2 rt (blue), ciprofloxacin (red) and BN15-ZnCl2-Cipro (black)

5.8 Conclusion

Two tetracyclic compounds have been successfully synthesized by reacting 3,4-dihydroxybenadehyde with resorcinol and pyrogallol (BN15 and 3,4dHBP, respectively). The resorcinol obtained compound (BN15) forms an hour-glass shaped structure with a u, u, u, u configuration with respect to resorcinol backbone rings. The overall structure of BN15 presents an undulating tube where individual molecules are linked via hydrogen bonding to the next. 3,4-dHBP, on the other hand, forms a 1,2-alternate configuration with respect to the pyrogallol rings. Metal complexes of the compounds were prepared based on metal chlorides (for BN15) and metal acetates (for 3,4-dHBP). In the presence of metal chlorides, the compound coordinates at the 3,4-dihydroxybenzaldehyde rings, while in the presence of metal acetates, 3,4-dHBP undergoes complete deprotonation so that all the oxygen atoms coordinate to the metal ion.

BN15; 3,4-dHBP and their metal complexes have been demonstrated to form supramolecular host-guest complexes with ciprofloxacin which are stabilized by various intermolecular forces. The orientation of the ciprofloxacin in the cavity of BN15 has been determined using H-NMR while the stoichiometry has been determined by means of titration.

6 CHAPTER SIX

This chapter is rather a proof of concept than a detailed investigation. The detail investigation is an ongoing project. The chapter reports on the biological studies on some of the compounds reported in this work. The bioassays of some of the compounds and supramolecular assemblies and the release of ciprofloxacin from BN15-ciprofloxacin supramolecular complex has been reported.

6.1 Cell toxicity assay

To investigate the cytotoxicity of the compounds, they were incubated at a concentration of 50 ug/ml in 96-well plates containing HeLa cells for 24 hours. The numbers of cells surviving after exposure to the compounds were determined by using the resazurin based reagent and reading resorufin fluorescence in a multiwell plate reader.

6.2 Drug release in simulated body fluid

The drug release was carried out in a phosphate buffer pH 5.8. Typically, a dry powder of the complex (in the case of the supramolecular ensembles) was placed in a dialysis tubing cellulose membrane and 1 mL of Millipore water added. The tube was sealed and placed in a vial containing 20 mL of the buffer maintained at 37.4 ºC. In the case of BN15-CIP, 1.97 mg of the complex was dissolved in 0.1 mL of DMSO and diluted to 1mL using water. The solution was transferred into the dialysis tubing cellulose membrane, sealed, and placed in a vial containing the phosphate buffer maintained at 37 (±0.4) ºC. The solution was constantly stirred throughout the experiment. At given times, aliquots were drawn from the buffer for analysis and replaced with fresh buffer. The UV-vis data of these aliquots was used to determine the release profile. The aliquots were also subject to biological evaluation to confirm that the drug was indeed present.

6.3 Antimicrobial assay

To assess the effect of the aliquots drawn from the buffer on the growth of *E. coli* cells and *S.aureus* cells. The compounds were dissolved in either DMSO or 11% HCl and diluted to 50 μg/mL and incubated for in 96-well plates containing the target cells for 24 hours. The numbers of cells remaining viable after exposure to the compound were then determined by using the resazurin based reagent and reading resorufin fluorescence in a multiwall plate reader.

6.4 Results and discussions

6.4.1 Cytotoxicity

The results indicate that the cucurbituril metal complexes and 3,4-dHBP generally do not show any significant cytotoxicity against HeLa cells as represented in ***Figure 6.1***. However, BN15 shows a significant cytotoxicity. The standard antibiotic drugs used as guest in the work isoniazid hydrochloride and ciprofloxacin also do not show any significant cytotoxicity. The supramolecular complexes obtained with these drugs as guest however show significant cytotoxicity.

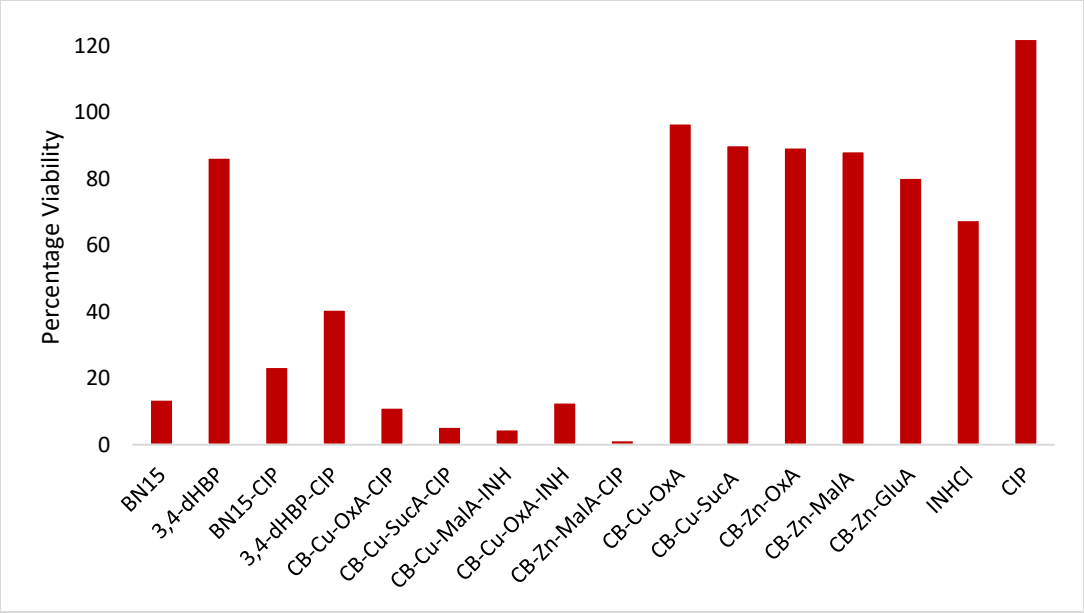

Figure 6.1: Cytotoxicity of representative compounds

6.4.2 Antibacterial assay

Figure 6.2a shows the activity of selected compounds against *S. aureus* and ***Figure 6.2b*** shows the activity of selected compounds against *E. coli*. As depicted in ***Figure 6.2a&b***, BN15 show significant activity against *S. aureus* and *E. Coli* killing more than 90% of cells in each case. The pyrogallol counter 3,4-dHBP also shows significant activity against both cell lines although lower than BN15 killing approximately 75% of cells in each case. The introduction of isoniazid (INH) or ciprofloxacin into both BN15 and 3,4-dHBP result to increased activity against both cell lines with lee than 5% of cells surviving in each case. The activity of these host-guest complexes is therefore a synergic effect of the activity of the host compound and the drug guest.

Across the cell lines is it observed that the activity of the supramolecular ensembles CB-Cu-MalA-INH and CB-Cu-OxA-CIP is not very high with the later killing less than 50% of the cells and the former just over 50%. The other supramolecular ensembles showed significant activity against the cell lines.

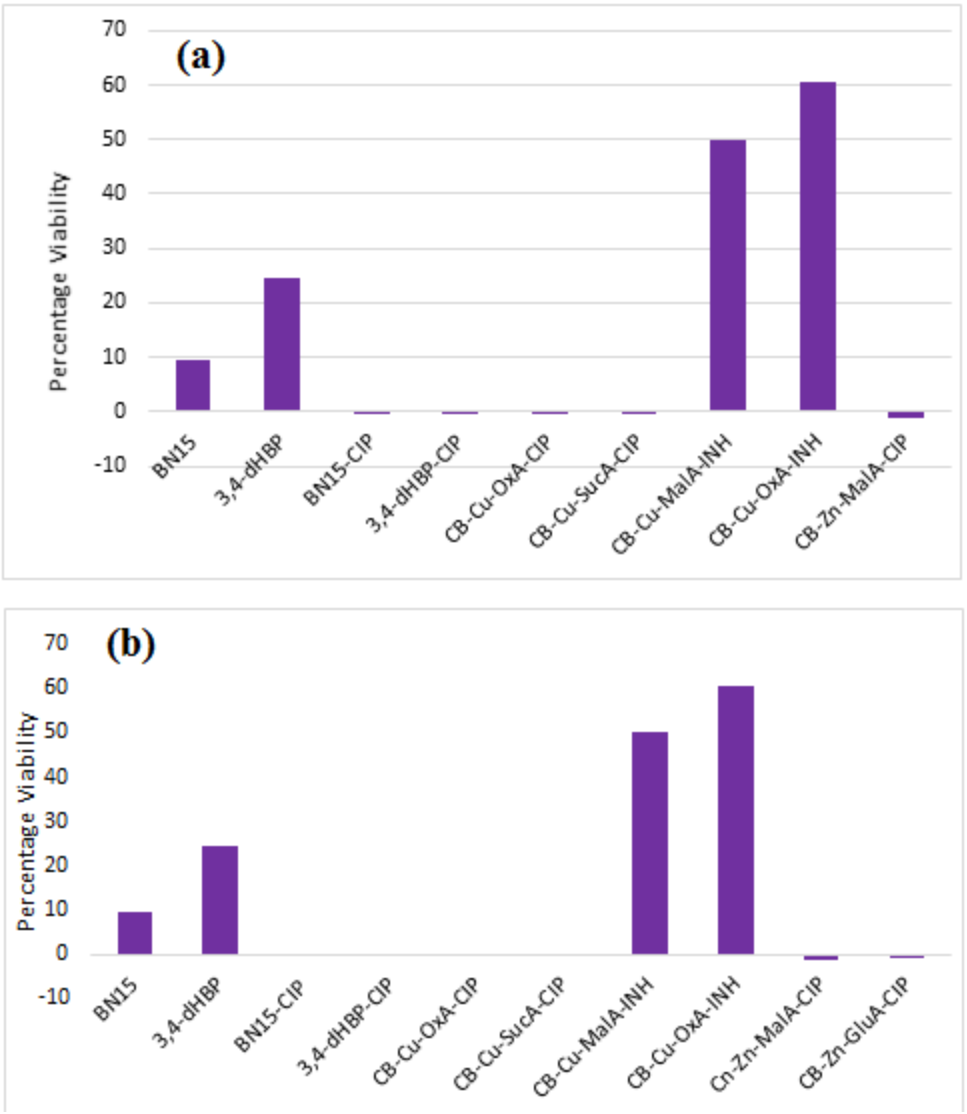

Figure 6.2: Activity of selected compound against (a) *S. aureus* (b) *E. coli*.

6.4.3 Drug release

We observed an increasing reddish coloration in the buffer solution which peaked after twenty-four hours of release. The UV spectra of the collected aliquots revealed that the color was a result of the carrier BN15 molecules diffusing through the membrane. The peaks due to BN15 can be observed near 480 nm in ***Figure 6.3***. The release of the drug from the carrier is gradual and takes approximately 96 hours for 90 percent of the drug to be released as shown in ***Figure 6.3***. Notwithstanding, about 80 percent of the drug is released during the first 36 hours of release. After one week of release, and allowing the vial to stand for 24 hours, fine powder of BN15 was visible in the buffer. FTIR of this powder reveals that very little change had occurred on the powder.

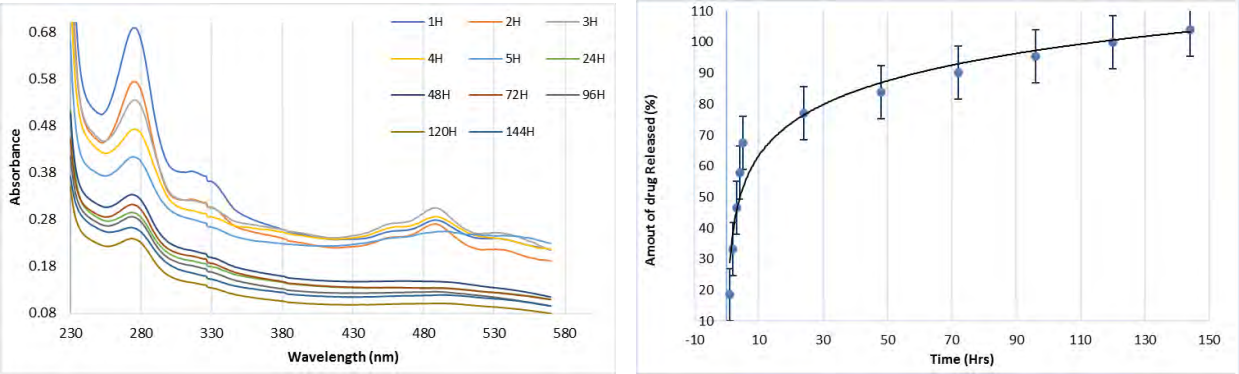

Figure 6.3: UV spectra of representative aliquots from release media and the release profile and pH 5.8

6.5 Conclusion

The compounds synthesized and the resulting supramolecular ensembles have been evaluated for cytotoxicity and antibacterial properties. BN15 shows significant cytotoxicity and antibacterial effect against *S. aureus* and *E. coli*. 3,4-dHBP on the other hand does not show any significant cytotoxic effect but is active against the investigated cell lines where it kills approximately 75% of the cells after 24 hours of incubation. The host-guest complexes of these two compounds show activity against the evaluated cell lines which is ascribed to the combined effect of the host and the drug guest. The release studies of BN15-CIP reveal that the drug guest and the host pass through the dialysis membrane. Into the buffer. The release of ciprofloxacin last until almost 50 hours for 90% of the guest to have been released.

The cucurbituril metal complexes are generally non-cytotoxic. The antibacterial effect of these complexes when the drug guest is introduced is ascribed to the drug since the metal complexes are not toxic to the cell lines under investigation.

7 CHAPTER SEVEN
CONCLUSION

The initial intention of this work was to synthesize a series of calixarenes based on aromatic aldehydes and cucurbiturils. Thereafter prepare complexes of these macrocycles and investigate their ability to form host guest complexes.

7.1 Synthesis of calixarenes and cucurbiturils and metal complexes

The envisioned aromatic aldehyde based calixarenes BN15, BN22, *p*-ClBP, 3,4-dHBP and cucurbiturils were successfully synthesized in appreciable yields and purity following reported literature.

These macrocycles have been used to obtain porous metal complexes with or without bridging ligands chiefly by solvothermal methods. Metal complexes involving cucurbiturils have been obtained and characterized using various techniques.

7.2 Application of the obtained compounds

The macrocycles and their metal complexes were investigated for various host-guest interactions.

BN22 and *p*-ClBP were investigated for selective sorption of DMSO whereas the others were investigated for hosting either isoniazid or ciprofloxacin hydrochloride. Host-guest complexes of isoniazid and ciprofloxacin have been achieved through both solution chemistry and mechanochemistry.

The biological activities of selected compounds and guest release from host in simulated body fluid were investigated.

7.3 Characterization and identification

The physicochemical characterization of the obtained compounds and the host guest complexes was achieved through NMR, DSC, TGA, FTIR, UV spectroscopy, single crystal X-ray diffraction powder X-ray diffraction, elemental analysis, and atomic absorption spectroscopy. NMR was used to ascertain the successful synthesis of the macrocycles, host-guest complexes. By analyzing the chemical shift variation of given protons in the guest, it was possible to determine the stoichiometry of the supramolecular host-guest complexes. FTIR and powder XRD provided further evidence of the supramolecular complexes while the single crystal XRD was used to

determine the structure of the obtained crystals. Data from elemental analysis and atomic absorption spectroscopy was essential in determining the stoichiometry of metal complexes. The UV spectroscopy data reveal that the release of ciprofloxacin from BN15 lasts until 48 hours for 90% of the drug to be released from the host. Furthermore, the host material was also found to cross the dialysis membrane.

Thermal analysis was useful in determining the thermal stability of the obtained complexes and the structural changes undergone by the compounds upon exposure with guest samples.

7.4 Significance of the obtained results

Separation of mixtures and solvent recovery remains an active research area. Newer and effective candidates for separation are therefore welcome as they offer alternatives for the existing ones. In this regard, we have therefore been able to obtain a compounds BN22 and p-ClBP that is capable of selectively adsorbing DMSO form a solvent mixture. Compound BN22 has also been found to show interesting structural dexterity in the presence of different solvents.

The formation of host-guest supramolecular complexes involving active pharmaceutical ingredients is also an important area of research as this form the basis of sustained release of these active ingredients. With the synthesis of porous materials essential to this development, we have obtained porous materials capable of forming supramolecular host complexes with ciprofloxacin and isoniazid. Our work has demonstrated that these supramolecular ensembles with isoniazid and ciprofloxacin can be obtained both by one pot synthesis and mechanochemistry. One pot supramolecular ensemble involving cucurbiturils reveals that the isoniazid is enclosed in the cavity of the cucurbituril despite the complex having pores extrinsic to the cavity. This offers the possibility of loading guest in the intrinsic and extrinsic pores of the complex although this has not been explored yet and is an area of future research.

7.5 Future work

Future work includes carrying complete investigation of drug release from the supramolecular complexes that have been reported, utilizing different pH and different guests. We also are looking forward to investigating if the guest content of the supramolecular ensembles obtained through one-pot synthesis can be further increased by carrying out mechanochemistry to increase bioavailability. An important future stud will be to load two active pharmaceutical moieties unto

a single metal complex; with one enclosed in the intrinsic pores and the other in the extrinsic pores. This presents as an interesting approach to combination therapy.

With respect to the aromatic aldehyde synthesized calixarenes, we observed that unlike those traditionally reported in literature, these do not easily form crystalline complexes with metal ions using similar approaches to those reported in literature. This implies that obtaining calixarenes from aromatic aldehydes yields compounds whose behavior with respect to complexation is quite different from those obtained with aliphatic aldehydes. We therefore intend to further explore on the complexation of such materials with different metal ions to obtain crystalline complexes. This is important since their elucidation will be easy through single crystal x-ray diffraction techniques.

7.6 Final comments

The author believes that the intended aims indicated in **Section 1.10** and **1.11** of this work have been achieved. We have sufficiently proven by various techniques that the intended compounds have been synthesized. We have furthermore established through the available techniques that the obtained compounds make good candidates for supramolecular chemistry as they form host-guest complexes with various guests. The formation of host-guest complexes with active pharmaceuticals implies these compounds make good candidate for application in drug delivery systems.

REFERENCES

[1] Español E S and Villamil M M 2019 Calixarenes: generalities and their role in improving the solubility, biocompatibility, stability, bioavailability, detection, and transport of biomolecules *Biomolecules* **9** 1–15

[2] Xiao X, Tao Z, Xue S F, Zhang Y Q, Zhu Q J, Liu J X and Wei G 2011 Coordination polymers constructed from alkali metal ions and (Ho)10cucurbit[5]uril *CrystEngComm* **13** 3794–800

[3] Scorsin L, Roehrs J A, Campedelli R R, Caramori G F, Osmar A, Ortolan A O, Parreira R L T, Fiedler H D, Acuna A, García-Río L and Nome F 2018 Cucurbituril-mediated catalytic hydrolysis: A kinetic and computational study with neutral and cationic dioxolanes in CB7 *ACS Catal.* **8** 12067–79

[4] Klock C, Dsouza R N and Nau W M 2009 Cucurbituril-mediated supramolecular acid catalysis *Org. Lett.* **11** 2595–8

[5] Da Silva D L, Fernandes S A, Sabino A A and De Fátima Â 2011 p-Sulfonic acid calixarenes as efficient and reusable organocatalysts for the synthesis of 3,4-dihydropyrimidin-2(1H)-ones /-thiones *Tetrahedron Lett.* **52** 6328–30

[6] Semedo M C, Karmali A, Barata P D and Prata J V. 2010 Extraction of hemoglobin with calixarenes and biocatalysis in organic media of the complex with pseudoactivity of peroxidase *J. Mol. Catal. B Enzym.* **62** 96–103

[7] Aziz A, Ruiz-Salvador A R, Hernández N C, Calero S, Hamad S and Grau-Crespo R 2017 Porphyrin-based metal-organic frameworks for solar fuel synthesis photocatalysis: Band gap tuning: Via iron substitutions *J. Mater. Chem. A* **5** 11894–904

[8] Huh S, Kim S J and Kim Y 2016 Porphyrinic metal-organic frameworks from custom-designed porphyrins *CrystEngComm* **18** 345–68

[9] Chen L X, Liu M, Zhang Y Q, Zhu Q J, Liu J X, Zhu B X and Tao Z 2019 Outer surface interactions to drive cucurbit[8]uril-based supramolecular frameworks: possible application in gold recovery *Chem. Commun.* **55** 14271–4

[10] Ke D, Feng J F, Wu D, Hou J B, Zhang X Q, Li B J and Zhang S 2019 Facile stabilization of a cyclodextrin metal-organic framework under humid environment via hydrogen sulfide treatment *RSC Adv.* **9** 18271–6

[11] Abuçafy M P, Caetano B L, Chiari-Andréo B G, Fonseca-Santos B, do Santos A M, Chorilli M and Chiavacci L A 2018 Supramolecular cyclodextrin-based metal-organic frameworks as efficient carrier for anti-inflammatory drugs *Eur. J. Pharm. Biopharm.* **127** 112–9

[12] Petrella A J and Raston C L 2004 Calixarenes as platforms for the construction of multimetallic complexes *J. Organomet. Chem.* **689** 4125–36

[13] Schulz M, Gehl A, Schlenkrich J, Schulze H A, Zimmermann S and Schaate A 2018 Molecular recognition a calixarene-based metal-organic framework for fighly selective NO2 detection *Angew. Chemie - Int. Ed.* **57** 12961–5

[14] Redshaw C, Rowe O, Elsegood M R J, Horsburgh L and Teat S J 2014 Pillared two-dimensional metal-organic frameworks based on a lower-rim acid appended calix[4]arene *Cryst. Growth Des.* **14** 270−277

[15] Bew S P, Burrows A D, Duren T, Mahon M F, Moghadam P Z, Sebastyen V M and Thurston S 2012 Calix[4]arene-based metal-organic frameworks: towards hierarchically porous materials *Chem. Commun.* **48** 4824–4826

[16] Gutsche D 1989 *Calixarenes* (Royal Society of Chemistry Cambridge ISBN: 0851869165)

[17] Gutsche D 1998 *Calixarenes Revisted* (Royal Society of Chemistry Cambridge ISBN: 0854045023)

[18] Kielhmann E, Laithioor C E and Lai W K 2008 Condensation of formaldehyde with phloroglucinol and its monoethyl ether *Org. Prep. Proced. Int. New J. Org. Synth.* **33** 1–66

[19] Bowley N 2008 *Synthetic and structural studies of calix[4]pyrogallolarenes towards biological applications* (PhD thesis, Nottingham Trent University)

[20] Carey S 2006 *The synthesis and medicinal applications of pyrogallol[4] arenes* (PhD thesis, Dublin City University)

[21] Sun J, Blaskovich M A, Jain R K, Delarue F, Paris D, Brem S, Wotoczek-obadia M, Lin Q, Coppola D, Choi K, Mullan M, Hamilton A D and Sebti M 2004 Blocking angiogenesis and tumorigenesis with GFA-116, a synthetic molecule that inhibits binding of vascular endothelial growth factor to its receptor *Cancer Res.* **64** 3586–92

[22] Dings R P M, Miller M C, Nesmelova I, Astorgues-Xerri L, Kumar N, Serova M, Chen X, Raymond E, Hoye T R and Mayo K H 2012 Antitumor agent calixarene 0118 targets human galectin-1 as an allosteric inhibitor of carbohydrate binding *J. Med. Chem.* **55** 5121–9

[23] Gale P A and Steed J W 2012 *Supramolecular Chemistry: From molecules to nanomaterials Vol3* (Wiley, Chechester West Sussex)

[24] Yang W and Villiers M M de 2005 Effect of 4-Sulphonato-Calix[n]Arenes and Cyclodextrins on the Solubilization of Niclosamide, a Poorly Water Soluble Anthelmintic *AAPS J.* **7** 241–8

[25] Dawn A, Chandra H, Ade-browne C, Yadav J and Kumari H 2017 Multifaceted supramolecular interactions from C-methylresorcin[4]arene lead to an enhancement in in vitro antibacterial activity of gatifloxacin *Chem. Eur. J.* **23** 18171–9

[26] Guo D and Liu Y 2014 Supramolecular Chemistry of p-Sulfonatocalix[n]arenes and Its Biological Applications *Acc. Chem. Res.* **47** 1925–34

[27] Silva E D A, Ficheux D and Coleman A W 2005 Anti-thrombotic activity of water-soluble calix[n]arenes *J. Incl. Phenom. Macrocycl. Chem.* **52** 201–6

[28] Coleman A W, Perret F, Moussa A, Dupin M, Guo Y and Perron H 2007 Calix[n] arenes as Protein Sensors *Creative Chemical Sensor Systems* (Springer: Berlin/Heidelberg, Germany,) pp 31–88

[29] Grare M, Mourer M, Fontanay S, Regnouf-de-Vains J-B, Finance C and Duval R E 2007 In vitro activity of para-uanidinoethylcalix[4]arene against susceptible and antibiotic-resistant Gram-negative and Gram-positive bacteria *J. Antimicrob. Chemetherapy* **60** 575–81

[30] Pasquale S, Sattin S, Escudero-adán E C, Martínez-belmonte M and Mendoza J De 2012 Giant regular polyhedra from calixarene carboxylates and uranyl *Nat. Commun.* **3** 1–7

[31] Guo T, Cheng D, Yang J, Xu X and Ma J 2019 Calix[4]resorcinarene-based [Co16] coordination cages mediated by isomorphous auxiliary ligands for enhanced proton conduction *Chem. Commun.* **55** 6277–80

[32] Zhang C, Baker G A, Sikligar K, Patil R S, Barnes C L and Atwood J L 2018 A M18L6 metal-organic nanocapsule with open windows using mixed macrocycles *Chem. Commun.* **54** 635–7

[33] Zhang C, Patil R S, Liu C, Barnes C L and Atwood J L 2017 Controlled 2D assembly of nickel-seamed hexameric pyrogallol[4]arene nanocapsules *J. Am. Chem. Soc.* **139** 2920–3

[34] Rathnayake A S, Feaster K A, White J, Barnes C L, Teat S J and Atwood J L 2016 Investigating reaction conditions to control the Self-assembly of cobalt-seamed nanocapsules *Cryst. Growth Des.* **16** 3562–3562

[35] Zhang C, Patil R S, Barnes C L and Atwood J L 2017 Preparation of anionic metal-seamed pyrogallol[4]arene nanocapsules via surface functionalization *Cryst. Growth Des.* **17** 4541–3

[36] Kumari H, Dennis C L, Mossine A V, Deakyne C A and Atwood J L 2012 Exploring the magnetic behavior of nickel-coordinated pyrogallol[4]arene nanocapsules *ACS Nano* **6** 272–5

[37] Mckinlay R M, Cave G W V, Atwood J L and Stang P J 2005 Supramolecular blueprint approach to metal-coordinated capsules *Proc. Natl. Acad. Sci. USA* **102** 5944–8

[38] Mckinlay R M, Thallapally P K, Cave G W V and Atwood J L 2005 Hydrogen-bonded supramolecular assemblies as robust templates in the synthesis of large metal-coordinated capsules *Angew. Chemie - Int. Ed.* **44** 5733–6

[39] Atwood J L, Brechin E K, Dalgarno S J, Inglis R, Jones L F, Mossine A, Paterson M J,

Power P and Teat S J 2010 Magnetism in metal-organic capsules *Chem. Commun.* **46** 3484–6

[40] Su K, Wu M, Tan Y, Wang W, Yuan D and Hong M 2017 A monomeric bowl-like pyrogallol[4]arene Ti12 coordination complex *Chem. Commun.* **53** 9598–601

[41] Thuery P, Asfari Z, Vicens J, Lamare V and Dozol J-F 2002 Synthesis and crystal structure of sodium and caesium ion complexes of unsubstituted calix[4]arene. New polymeric chain arrangements *Polyhedron* **21** 2497–503

[42] Kim K, Selvapalam N and Oh D H 2004 Cucurbiturils-A New Family of Host Molecules *J. Incl. Phenom.* **50** 31–6

[43] Freeman W A, Mock W L and Shih N Y 1981 Cucurbituril *J. Am. Chem. Soc.* **103** 7367–8

[44] Assaf K I and Nau W M 2015 Cucurbiturils: From synthesis to high-affinity binding and catalysis *Chem. Soc. Rev.* **44** 394–418

[45] Steed J W and Atwood J L 2009 *Supramolecular Chemistry 2nd Edition* (John Wiley and Sons Ltd, ISBN: 978-0-470-51234-0)

[46] Oliver C L, Báthori N B, Jackson G E, Kuter D and Cruickshank D L 2016 Solid-state isolation of a unique, small-molecule, supra-heterodimer of large hexameric assemblies of C-methylcalix[4]resorcinarene *CrystEngComm* **18** 3015–8

[47] Gerkensmeier T, Iwanek W, Agena C, Fröhlich R, Kotila S, Näther C and Mattay J 1999 Self-assembly of 2, 8, 14, 20-tetraisobutyl-5, 11, 17, 23-tetrahydroxyresorc[4]arene *European J. Org. Chem.* **2257**–**2262** 2257–62

[48] Cave G W V, Antesberger J, Barbour L J, McKinlay R M and Atwood J L 2004 Inner core structure responds to communication between nanocapsule walls *Angew. Chemie - Int. Ed.* **43** 5263–6

[49] Zafrani Y and Cohen Y 2017 Calix[4, 5]tetrolarenes: A new family of macrocycles *Org. Lett.* **19** 3719–22

[50] Nau W M, Florea M and Assaf K I 2011 Deep inside cucurbiturils: Physical properties and volumes of their inner cavity determine the hydrophobic driving force for host-guest complexation *Isr. J. Chem.* **51** 559–77

[51] Cong H, Li C R, Xue S F, Tao Z, Zhu Q J and Wei G 2011 Cucurbituril-resisted acylation of the anti-tuberculosis drug isoniazid via a supramolecular strategy *Org. Biomol. Chem.* **9** 1041–6

[52] Lim S, Kim H, Selvapalam N, Kim K-J, Cho S J, Seo G and Kim K 2008 Cucurbit[6]uril: Organic Molecular Porous Material with Permanent Porosity, Exceptional Stability, and Acetylene Sorption Properties *Angew. Chemie* **120** 3400–3

[53] Shen F F, Zhao J L, Chen K, Hua Z Y, Chen M D, Zhang Y Q, Zhu Q J and Tao Z 2017 Supramolecular coordination assemblies of a symmetrical octamethyl-substituted cucurbituril with alkali metal ions based on the outer-surface interactions of cucurbit[n] urils *CrystEngComm* **19** 2464–74

[54] Kim K 2019 *Cucurbiturils and related macrocycles* ed K Kim (Royal Society of Chemistry, London, ISSN: 2041-7144)

[55] Ni X L, Xiao X, Cong H, Zhu Q J, Xue S F and Tao Z 2014 Self-assemblies based on the "outer-surface interactions" of cucurbit[n]urils: New opportunities for supramolecular architectures and materials *Acc. Chem. Res.* **47** 1386–95

[56] Bardelang D, Udachin K A, Leek D M and Ripmeester J A 2007 Highly symmetric columnar channels in metal-free cucurbit[n]uril hydrate crystals (n = 6, 8) *CrystEngComm* **9** 973–5

[57] Hermann J, Alfè D and Tkatchenko A 2017 Nanoscale π-π Stacked molecules are bound by collective charge fluctuations *Nat. Commun.* **8** 1–8

[58] Zheng G, Li Y, Deng R, Song S and Zhang H 2008 Self-assembly of guest-induced calix[4]arene nanocapsules into three-dimensional molecular architecture *Cryst. Eng. Commun.* **10** 658–60

[59] Park J, Lee J H, Jaworski J, Shinkai S and Jung J H 2014 Luminescent calix[4]arene-based metallogel formed at different solvent composition *Inorg. Chem.* **53** 7181−7187

[60] Chen K, Kang Y S, Zhao Y, Yang J M, Lu Y and Sun W Y 2014 Cucurbit[6]uril-based supramolecular assemblies: Possible application in radioactive cesium cation capture *J. Am. Chem. Soc.* **136** 16744–7

[61] Dalgarno S J, Power N P and Atwood J L 2007 Ionic dimeric pyrogallol[4]arene capsules *Chem. Commun.* 3447–9

[62] Kumari H, Deakyne C A and Atwood J L 2014 Solution structures of nanoassemblies based on pyrogallol[4]arenes *Acc. Chem. Res.* **47** 3080–8

[63] Hanna T A, Liu L, Zakharov L N, Rheingold A L, Watson H and Gutsche C D 2002 Synthesis and crystal structures of mono-potassium salts of calix[4]arene and p - tert - butylcalix[4]arene *Tetrahedron* **58** 9751–7

[64] Orda-zgadzaj M, Wendel V, Fehlinger M, Ziemer B and Abraham W 2001 Inclusion of organic oations by calix[4]arenes bearing cyclohepta-2, 4, 6-trienyl substituents *European J. Org. Chem.* 1549–61

[65] Imonigie J A and Macartney D H 2006 Effects of inclusion of (ferrocenylmethyl) trimethylammonium complexes in para-sulfonated calixarenes on the kinetics of their electron transfer reactions *Inorg. React. Mech.* **6** 161–8

[66] Fairchild R M and Holman K T 2005 Selective anion encapsulation by a metalated

cryptophane with a π-acidic interior *J. Am. Chem. Soc.* **127** 16364–5

[67] Rosokha Y S, Lindeman S V, Rosokha S V and Kochi J K 2004 Charge-transfer complexes halide recognition through diagnostic "anion-π" interactions: molecular complexes of Cl-,Br-, and I- with olefinic and aromatic π receptors *Angew. Chemie - Int. Ed.* **43** 4650–2

[68] Wang D and Wang M 2012 Anion-π Interactions : Generality, binding strength and structure *J. Am. Chem. Soc.* **135** 892–7

[69] Holman K T, Halihan M M, Jurisson S S, Atwood J L, Burkhalter R S, Mitchell A R and Steed J W 1996 Inclusion of neutral and anionic guests within the cavity of π-metalated cyclotriveratrylenes *J. Am. Chem. Soc.* **118** 9567–76

[70] Staffilani M, Hancock K S B, Steed J W, Holman K T, Atwood J L, Juneja R K and Burkhalter R S 1997 Anion binding within the cavity of π-metalated calixarenes *J. Am. Chem. Soc.* **119** 6324–35

[71] Fochi F, Jacopozzi P, Wegelius E, Rissanen K, Cozzini P, Marastoni E, Fisicaro E, Manini P, Fokkens R and Dalcanale E 2001 Self-assembly and anion encapsulation properties of cavitand-based coordination cages *J. Am. Chem. Soc.* **123** 7539–52

[72] Ananchenko G S, Udachin K A, Pojarova M, Dubes A, Ripmeester J A, Jebors S and Coleman A W 2006 Van der Waals nanocapsular complexes of amphiphilic calixarenes *Cryst. Growth Des.* **6** 2141–8

[73] Thompson B, Cope S, Swift D and Notestein J M 2011 Recovery of n-butanol from dilute aqueous solution with grafted calixarenes *Langmuir* **27** 11990–8

[74] Huang Y, Xue S F, Tao Z, Zhu Q J, Zhang H, Lin J X and Yu D H 2008 Solubility enhancement of kinetin through host-guest interactions with cucurbiturils *J. Incl. Phenom. Macrocycl. Chem.* **61** 171–7

[75] Zhang H, Huang Y, Xue S F, Tao Z and Zhu Q J 2011 Host-guest interactions of 6-benzyladenine with normal and modified cucurbituril: 1H NMR, UV absorption spectroscopy and phase solubility methods *Supramol. Chem.* **23** 527–32

[76] Fileti E, Colherinhas G and Malaspina T 2014 Predicting the properties of a new class of host-guest complexes: C60 fullerene and CB[9] cucurbituril *Phys. Chem. Chem. Phys.* **16** 22823–9

[77] Heo J, Kim S Y, Whang D and Kim K 1999 Shape-induced, hexagonal, open frameworks: Rubidium ion complexed cucurbituril *Angew. Chemie - Int. Ed.* **38** 641–3

[78] Neri P, Sessler J L and Wang M X 2016 *Calixarenes and beyond* (Springer Nature DOI 10.1007/978-3-319-31867-7)

[79] Sato S, Iijima H, Haga N, Osono K, Mizugchi H, Kajima T and Onodera J-I 2006 First synthesis and properties of calix[4]arene with two alternately arranged phloroglucinols

and two p-tert-butylphenols *Supramol. Chem.* **18** 39–46

[80] Skala L P, Yang A, Klemes M J, Xiao L and Dichtel W R 2019 Resorcinarene cavitand polymers for the remediation of halomethanes and 1,4-dioxane *J. Am. Chem. Soc.* **141** 13315–9

[81] Avram L and Cohen Y 2002 The role of water molecules in a resorcinarene capsule as probed by NMR diffusion measurements *Org. Lett.* **4** 4365–8

[82] Liu Y, Li Z, Zhang H, Wang H and Li C 2008 Colorimetric sensor and inverse fluorescent behavior of anions by calix[4]arene possessing imidazo[4, 5- f]-1, 10-phenanthroline groups and its Ru (II) complex *Supramol. Chem.* **20** 419–26

[83] Kumar S, Kurur N D, Chawla H M and Varadarajan R 2001 A convenient one pot one step synthesis of p-nitrocalixarenes via ipsonitration *Synth. Commun.* **31** 775–9

[84] Shinkai S, Araki K, Tsubaki T, Arimura T and Manabe O 1987 New syntheses of calixarene-p-sulphonates and p-nitrocalixarenes *J. Chem. Soc. Dalt. Trans.* **1** 2297–9

[85] Miller-Shakesby D M, Burke B P, Nigam S, Stasiuk G J, Prior T J, Archibald S J and Redshaw C 2016 Synthesis, structures and cytotoxicity studies of: p-sulfonatocalix[4]arene lanthanide complexes *CrystEngComm* **18** 4977–87

[86] Tashakkorian H, Lakouraj M M and Rouhi M 2015 p-Sulfonic acid calix[4]arene as an efficient catalyst for one-pot synthesis of pharmaceutically significant coumarin derivatives under solvent-free condition *Int. J. Med. Chem.* 1–8

[87] Zhang W and Zheng Y 1997 New synthetic method of p- nitrocalixarenes *Synth. Commun.* **27** 3763–7

[88] Xiong D, Chen M and Li H 2008 Synthesis of para-sulfonatocalix[4]arene-modified silver nanoparticles as colorimetric histidine probes *Chem. Commun.* 880–2

[89] Basilio N, Francisco V and Garcia-Rio L 2013 Aggregation of p-sulfonatocalixarene-based amphiphiles and supra-amphiphiles *Int. J. Mol. Sci.* **14** 3140–57

[90] Wang P S, Lin R Sen and Zong H X 1999 Direct synthesis p-nitrocalix[4]arene from p-tert-butylcalix[4]arene *Synth. Commun.* **29** 2225–7

[91] Redon S, Li Y and Reinaud O 2003 Unprecedented selective ipso-nitration of calixarenes monitored by the O-substituents *J. Org. Chem.* **68** 7004–8

[92] Dalgarno S J, Szabo T, Siavosh-haghighi A, Deakyne C A, Adams J E and Atwood J L 2009 Exploring the limits of encapsulation within hexameric pyrogallol[4]arene nano-capsules *Chem. Commun.* 1339–41

[93] Dalgarno S J, Tucker S A, Bassil D B and Atwood J L 2005 Fluorescent guest molecules report ordered inner phase of host capsules in solution *Science (80-.).* **309** 2037–40

[94] Dalgarno S J, Bassil D B, Tucker S A and Atwood J L 2006 Cocrystallization and encapsulation of a fluorophore with hexameric pyrogallol[4]arene nanocapsules: structural and fluorescence studies *Angew. Chemie - Int. Ed.* **45** 7019–22

[95] Yaghi O M and Li H 1995 Hydrothermal synthesis of a metal-organic framework containing large rectangular channels *J. Am. Chem. Soc.* **117** 10401–2

[96] Li H, Eddaoudi M, O'Keeffe M and Yaghi O M 1999 Design and synthesis of an exceptionally stable and highly porous mettal-organic framework *Nature* **402** 276–9

[97] Kitagawa S, Kawata S, Nozaka Y and Munakata M 1993 Synthesis and crystal structures of novel copper(I) co-ordination polymers and a hexacopper(I) cluster of quinoline-2-thione *J. Chem. Soc. Dalt. Trans.* 1399–404

[98] Riou D and Fe G 1998 Hybrid open frameworks (MIL-n). Part 3† crystal structures of the HT and LT forms of MIL-7: a new vanadium propylenediphosphonate with an open-framework. Influence of the synthesis temperature on the oxidation state of vanadium within the same structural *J. Mater. Chem* **8** 2733–5

[99] Baa E, Watkins G M, Krause R W and Tantoh D N 2019 Current trend in synthesis, post-synthetic modifications and biological applications of nanometal-organic frameworks (NMOFs) *Chinese J. Chem.* **37** 378－404

[100] Fowler D A, Mossine A V., Beavers C M, Teat S J, Dalgarno S J and Atwood J L 2011 Coordination polymer chains of dimeric pyrogallol[4]arene capsules *J. Am. Chem. Soc.* **133** 11069–71

[101] Hu X, Chai J, Zhang C, Lang J, Kelley S P, Feng S, Liu B, Atwood D A and Atwood J L 2019 Biomimetic self-assembly of CoII-seamed hexameric metal-organic nanocapsules *J. Am. Chem. Soc.* **141** 9151–4

[102] Mohanty J 2015 Cucurbiturils, Synthesis and Applications *Encycl. Polym. Sci. Technol.* 1–31

[103] Zhu Q, Xue S and Tao Z 2013 Construction of cucurbit[7]uril based tubular nanochannels incorporating associated [CdCl4]2- and lanthanide ions *Inorg. Chem.* **52** 1909–15

[104] Zhao Y, Zhang T, Xiao X, Zhang Y, Tao Z, Xue F and Zhu Q 2013 Inorganic anion-aided coordination of lanthanide metal ions to cucurbituril and supramolecular self-assembly: Potential applications in the separation of light lanthanides *Cryst. Eng. Commun.* **15** 7987–98

[105] Jeon Y M, Kim J, Whang D and Kim K 1996 Molecular container assembly capable of conrolling binding and release of its guest molecules: Reversible encapsulation of organic molecules in sodium ion complexed cucurbituril *J. Am. Chem. Soc.* **118** 9790–1

[106] Whang D, Heo J, Park J H and Kim K 1998 A molecular bowl with metal ion as bottom: Reversible inclusion of organic molecules in cesium ion complexed cucurbituril *Angew.*

Chemie - Int. Ed. **37** 78–80

[107] Heo J, Kim J, Whang D and Kim K 2000 Columnar one-dimensional coordination polymer formed with a metal ion and a host-guest complex as building blocks: Potassium ion complexed cucurbituril *Inorganica Chim. Acta* **297** 307–12

[108] Koner A L, Márquez C, Dickman M H and Nau W M 2011 Transition-metal-promoted chemoselective photoreactions at the cucurbituril rim *Angew. Chemie - Int. Ed.* **50** 545–8

[109] Chen K, Cong H, Xiao X, Zhang Y Q, Xue S F, Tao Z, Zhu Q J and Wei G 2011 Hydroquinone-induced framework based on direct coordination of rubidium ions to cucurbit[7]uril *CrystEngComm* **13** 5105–10

[110] Ni X L, Xiao X, Cong H, Liang L L, Cheng K, Cheng X J, Ji N N, Zhu Q J, Xue S F and Tao Z 2013 Cucurbit[n]uril-based coordination chemistry: From simple coordination complexes to novel poly-dimensional coordination polymers *Chem. Soc. Rev.* **42** 9480–508

[111] Chen K, Liang L L, Cong H, Xiao X, Zhang Y Q, Xue S F, Zhu Q J and Tao Z 2012 P-hydroxybenzoic acid-induced formation of a novel framework based on direct coordination of caesium ions to cucurbit[8]uril *CrystEngComm* **14** 3862–4

[112] Wang B, Siahaan T and Soltero R 2005 *Drug Delivery: Principles and applications* (New Jersey: Wiley-Interscience New Jersey)

[113] Jain K K 2015 *Drug Delivery Systems* (Humana Press, ISBN: 978-1-58829-891-1)

[114] Juliano R L 1991 *Handbook of Experimental Pharmacology: Targeted Drug Delivery* vol 100 (Springer, ISBN-13: 978-3-642-75864-5)

[115] Swain S, Patra C N and Rao M E B 2016 *Pharmaceutical Drug Delivery Systems and Vehicles* (Woodhead Publishing India Pvt Ltd New Delhi)

[116] Thassu D, Deleers M and Pathak Y 2007 *Nanoparticulate Drug Delivery Systems* (Informa Healthcare USA, Inc.)

[117] Ahuja G and Pathak K 2009 Porous carriers for controlled/modulated drug delivery *Indian J. Pharm. Sci.* **71** 599–607

[118] Karavasili C, Amanatiadou E P, Kontogiannidou E, Eleftheriadis G K, Bouropoulos N, Pavlidou E, Kontopoulou I, Vizirianakis I S and Fatouros D G 2017 Comparison of different zeolite framework types as carriers for the oral delivery of the poorly soluble drug indomethacin *Int. J. Pharm.* **528** 76–87

[119] Tang L, Shi J, Wang X, Zhang S, Wu H, Sun H and Jiang Z 2017 Coordination polymer nanocapsules prepared using metal–organic framework templates for pH-responsive drug delivery *Nanotechnology* **28** 1–11

[120] Javanbakht S, Pooresmaeil M, Hashemi H and Namazi H 2018 Carboxymethylcellulose

capsulated Cu-based metal-organic framework-drug nanohybrid as a pH-sensitive nanocomposite for ibuprofen oral delivery *Int. J. Biol. Macromol.* **119** 588–96

[121] Matsuyama K, Hayashi N, Yokomizo M, Kato T, Ohara K and Okuyama T 2014 Supercritical carbon dioxide-assisted drug loading and release from biocompatible porous metal-organic frameworks *J. Mater. Chem. B* **2** 7551–8

[122] Wang C, Ye W, Zheng Y, Liu X and Tong Z 2007 Fabrication of drug-loaded biodegradable microcapsules for controlled release by combination of solvent evaporation and layer-by-layer self-assembly *Int. J. Pharm.* **338** 165–73

[123] Zhou Y, Li H and Yang Y W 2015 Controlled drug delivery systems based on calixarenes *Chinese Chem. Lett.* **26** 825–8

[124] Anand R, Borghi F, Manoli F, Manet I, Agostoni V, Reschiglian P, Gref R and Monti S 2014 Host-guest interactions in Fe(III)-trimesate MOF nanoparticles loaded with doxorubicin *J. Phys. Chem. B* **118** 8532–9

[125] Fahmy S A, Ponte F, El-rahman M K A, Russo N, Sicilia E and Shoeib T 2017 Investigation of the host-guest complexation between 4-sulfocalix[4]arene and nedaplatin for potential use in drug delivery *Spectrochim. Acta Part A Mol. Biomol. Spectrosc.* **193** 528–36

[126] Wheate N J, Abbott G M, Tate R J, Clements C J, Edrada-ebel R and Johnston B F 2009 Side-on binding of p-sulphonatocalix[4]arene to the dinuclear platinum complex trans-[{PtCl(NH3)2}2 μ-dpzm]2+ and its implications for anticancer drug delivery *J. Inorg. Biochem.* **103** 448–54

[127] Du S, Yu T, Liao W and Hu C 2015 Structure modeling, synthesis and X-ray diffraction determination of an extra-large calixarene-based coordination cage and its application in drug delivery *Dalt. Trans.* **44** 14394–402

[128] Bouchoucha M, Côté M F, C-Gaudreault R, Fortin M A and Kleitz F 2016 Size-controlled functionalized mesoporous silica nanoparticles for tunable drug release and enhanced anti-tumoral activity *Chem. Mater.* **28** 4243–58

[129] Zhang H, Jiang W, Liu R, Zhang J, Zhang D, Li Z and Luan Y 2017 Rational design of metal organic framework nanocarrier-based codelivery system of doxorubicin hydrochloride/verapamil hydrochloride for overcoming multidrug resistance with efficient targeted cancer therapy *ACS Appl. Mater. Interfaces* **9** 19687–97

[130] Yang Y, Hu Q, Zhang Q, Jiang K, Lin W, Yang Y, Cui Y and Qian G 2016 A large capacity cationic metal-organic framework nanocarrier for physiological pH responsive drug delivery *Mol. Pharm.* **13** 2782–6

[131] An L, Wang J W, Liu J D, Zhao Z M and Song Y J 2019 Design, preparation, and characterization of novel calix[4]arene bioactive carrier for antitumor drug delivery *Front. Chem.* **7** 1–14

[132] Mo J, Eggers P K, Yuan Z X, Raston C L and Lim L Y 2016 Paclitaxel-loaded phosphonated calixarene nanovesicles as a modular drug delivery platform *Sci. Rep.* **6** 1–12

[133] Sindelar V, Silvi S and Kaifer A E 2006 Switching a molecular shuttle on and off: Simple, pH-controlled pseudorotaxanes based on cucurbit[7]uril *Chem. Commun.* 2185–7

[134] Pennakalathil J, Jahja E, Özdemir E S, Konu Ö and Tuncel D 2014 Red emitting, cucurbituril-capped, pH-responsive conjugated oligomer-based nanoparticles for drug delivery and cellular imaging *Biomacromolecules* **15** 3366–74

[135] Song B H, Ding X, Zhang Z F and An G F 2019 Efficient drug delivery of 5-fluorouracil by a biocompatible Zn-metal–organic framework nanostructure and anti-liver cancer activity study *J. Iran. Chem. Soc.* **16** 333–40

[136] Cunha D, Yahia M Ben, Hall S, Miller S R, Chevreau H, Elka E, Maurin G, Horcajada P and Serre C 2013 Rationale of drug secapsulation and release from biocompatible porous metal−organic frameworks *Chem. Mater.* **25** 2767−2776

[137] Sun C Y, Qin C, Wang X L and Su Z M 2013 Metal-organic frameworks as potential drug delivery systems *Expert Opin. Drug Deliv.* **10** 89–101

[138] Horcajada P, Serre C, Vallet-Regí M, Sebban M, Taulelle F, Férey G, Maurin G, Ramsahye N A, Balas F, Vallet-Regí M, Sebban M, Taulelle F and Férey G 2006 Metal-organic frameworks as efficient materials for drug delivery *J. Am. Chem. Soc.* **130** 5974–8

[139] Bahojb Noruzi E, Kheirkhahi M, Shaabani B, Geremia S, Hickey N, Asaro F, Nitti P and Kafil H S 2019 Design of a thiosemicarbazide-functionalized calix[4]arene ligand and related transition metal complexes: Synthesis, characterization, and biological studies *Front. Chem.* **7** 1–15

[140] Naseer M M, Ahmed M and Hameed S 2017 Functionalized calix[4]arenes as potential therapeutic agents *Chem. Biol. Drug Des.* **89** 243–56

[141] Wang J F, Huang L Y, Bu J H, Li S Y, Qin S, Xu Y W, Liu J M and Su C Y 2018 A fluorescent calixarene-based dimeric capsule constructed: Via a MII-terpyridine interaction: Cage structure, inclusion properties and drug release *RSC Adv.* **8** 22530–5

[142] Holder C F and Schaak R E 2019 Tutorial on Powder X-ray Diffraction for Characterizing Nanoscale Materials *ACS Nano* **13** 7359–65

[143] Bishnoi A, Kumar S and Joshi N 2017 Wide-angle X-ray diffraction (WXRD): Technique for characterization of Nnnomaterials and polymer nanocomposites *Microscopy Methods in Nanomaterials Characterization* (Elsevier Inc. ISBN 13: 9780323461474) pp 313–37

[144] Fadeeva V P, Tikhova V D and Nikulicheva O N 2008 Elemental analysis of organic compounds with the use of automated CHNS analyzers *J. Anal. Chem.* **63** 1094–106

[145] Bader N R 2011 Sample preparation for flame atomic absorption spectroscopy: An

overview *Rasayan J. Chem.* **4** 49–55

[146] Smith J C, Butrimovitz G P and Purdy W C 1979 Direct measurement of zinc in plasma by atomic absorption spectroscopy *Clin. Chem.* **25** 1487–91

[147] Brown M E 1998 *Handbook of thermal analysis and calorimetry* ed P GALLAGHER, K. (Elsevier Science Amsterdam)

[148] Gabbot P 2008 *Principles and applications of thermal analysis* (Blackwell Pubishing Ltd ISBN-13: 978-1-4051-3171-1)

[149] Mayo D W, Miller F A and Hannah R W 2003 *Course Notes on the interpretation of infrared and raman spectra* (John Wiley and Sons, Inc. New Jersey)

[150] Deleanu C and Jocelyn Paré J R 1997 Nuclear magnetic resonance spectroscopy (NMR): Principles and applications *Tech. Instrum. Anal. Chem.* **18** 179–237

[151] Simmler C, Napolitano J G, McAlpine J B, Chen S N and Pauli G F 2014 Universal quantitative NMR analysis of complex natural samples *Curr. Opin. Biotechnol.* **25** 51–9

[152] Nakajima L, Yusof N N M and Kobayashi T 2015 Calixarene-composited host-guest membranes applied for heavy metal ion adsorbents *Arab. J. Sci. Eng.* **40** 2881–8

[153] Gutsche C D 1989 Spectral properties of calixarenes *Calixarenes 1st Edtion* ed J F Stoddart pp 78–86

[154] Sverker Hógberg A G 1980 Stereoselective synthesis and DNMR study of two 1,8,15,22-tetraphenyl [I4]metacyclophan-3,5,10,12,17,19,24,26-octolss *J. Am. Chem. Soc.* **102** 6046–50

[155] Macrae C F, Sovago I, Cottrell S J, Galek P T A, McCabe P, Pidcock E, Platings M, Shields G P, Stevens J S, Towler M and Wood P A 2020 *Mercury 4.0* : from visualization to analysis, design and prediction *J. Appl. Crystallogr.* **53** 226–35

[156] Zadmard R, Hokmabadi F, Jalali M R and Akbarzadeh A 2020 Recent progress to construct calixarene-based polymers using covalent bonds: synthesis and applications *RSC Adv.* **10** 32690–722

[157] Alpert N and Kieser, William E. and Szymanski H A 1970 *IR: Theory and practice of infrared spectroscopy (1970)* (Plenum Press New York)

[158] Periasamy R, Nayaki S K, Sivakumar K and Ramasamy G 2020 Synthesis and characterization of host-guest inclusion complex of β-cyclodextrin with 4, 4′-methylenedianiline by diverse methodologies *J. Mol. Liq.* **316** 113843

[159] Periasamy R, Kothainayaki S, Rajamohan R and Sivakumar K 2014 Spectral investigation and characterization of host – guest inclusion **114** 558–66

[160] Noack K, Kiefer J and Leipertz A 2010 Concentration-dependent hydrogen-bonding

effects on the dimethyl sulfoxide vibrational structure in the presence of water, methanol, and ethanol *ChemPhysChem* **11** 630–7

[161] Santos F, Branco C and Duarte A R C 2020 Organic salts based on isoniazid drug : Synthesis , bioavailability and cytotoxicity studies *Pharmaceutics* **12** 952

[162] Sahoo S, Chakraborti C K, Naik S, Mishra S C and Nanda U N 2011 Structural analysis of ciprofloxacin-carbopol polymeric composites by X-ray diffraction and fourier transform infra-red spectroscopy *Trop. J. Pharm. Res.* **10** 273–80

[163] Yamada Y, Mikami N and Ebata T 2008 Relaxation dynamics of NH stretching vibrations of 2-aminopyridine and its dimer in a supersonic beam *Proc. Natl. Acad. Sci.* **105** 12690–12695

[164] Sahoo S, Chakraborti C and Mishra S 2011 Qualitative analysis of controlled release ciprofloxacin/carbopol 934 mucoadhesive suspension *J. Adv. Pharm. Technol. Res.* **2** 195

[165] Lee J W, Samal S, Selvapalam N, Kim H J and Kim K 2003 Cucurbituril homologues and derivatives: New opportunities in supramolecular chemistry *Acc. Chem. Res.* **36** 621–30

[166] Liu S, Zavalij P Y and Isaacs L 2005 Cucurbit[10]uril *J. Am. Chem. Soc.* **127** 16798–9

[167] Cheng X J, Liang L L, Chen K, Ji N N, Xiao X, Zhang J X, Zhang Y Q, Xue S F, Zhu Q J, Ni X L and Tao Z 2013 Twisted cucurbit[14]uril *Angew. Chemie - Int. Ed.* **52** 7252–5

[168] Thuéry P 2010 Second-sphere tethering of rare-earth ions to cucurbit[6]uril by iminodiacetic acid involving carboxylic group encapsulation *Inorg. Chem.* **49** 9078–85

[169] Jeffrey G . and Sparry G . 1952 The Structure of oxalate ion *Carcinog. Nitrogen Compd. . Part XIII* 4864–7

[170] Park K M, Whang D, Lee E, Heo J and Kim O 2002 Transition metal ion directed supramolecular assembly of one- and two-dimensional polyrotaxanes incorporating cucurbituril *Chem. - A Eur. J.* **8** 498–508

[171] Feng X, Chen K, Zhang Y Q, Xue S F, Zhu Q J, Tao Z and Day A I 2011 Stable cucurbit[5]uril MOF structures as “beaded” rings built on a p-hydroxybenzoic acid template - A small molecule absorption material *CrystEngComm* **13** 5049–51

[172] Varsanyi G and Zsoke S 1969 *Vibrational spectra of benzene derivatives (1969), Academic Press New York*

[173] Teimouri A, Chermahini A N, Taban K and Dabbagh H A 2009 Experimental and CIS, TD-DFT, ab initio calculations of visible spectra and the vibrational frequencies of sulfonyl azide-azoic dyes *Spectrochim. Acta - Part A Mol. Biomol. Spectrosc.* **72** 369–77

[174] Furer V L, Borisoglebskaya E I and Kovalenko V I 2005 Band intensity in the IR spectra and conformations of calix[4]arene and thiacalix[4]arene *Spectrochim. Acta - Part A Mol. Biomol. Spectrosc.* **61** 355–9

[175] Zvereva E E, Katsyuba S A, Vandyukov A E, Chernova A V., Kovalenko V I, Solovieva S E, Antipin I S and Konovalov A I 2010 IR and NMR spectra, intramolecular hydrogen bonding and conformations of para-tert-butyl-aminothiacalix[4]arene in solid state and chloroform solution *Spectrochim. Acta - Part A Mol. Biomol. Spectrosc.* **75** 872–9

[176] Goolsby B J, Brodbelt J S, Adou E and Blanda M 1999 Determination of alkali metal ion binding selectivities of calixarenes by matrix-assisted laser desorption ionization and electrospray ionization in a quadrupole ion trap *Int. J. Mass Spectrom.* **193** 197–204

[177] Nyquist R 2001 *Interpreting infrared, raman and nuclear magnetic resonance spectra. Vol 2, (2001), pg 1-26, Academic press New York.*

[178] Lamprecht E, Watkins G M and Brown M E 2006 The thermal decomposition of copper(II) oxalate revisited *Thermochim. Acta* **446** 91–100

[179] Turel I, Leban I and Bukovec N 1997 Crystal structure and characterization of the bismuth(III) compound with quinolone family member (ciprofloxacin). Antibacterial study *J. Inorg. Biochem.* **66** 241–5

[180] Sadeek S A, El-Shwiniy W H, Zordok W A and El-Didamony A M 2011 Spectroscopic, structure and antimicrobial activity of new Y(III) and Zr(IV) ciprofloxacin *Spectrochim. Acta - Part A Mol. Biomol. Spectrosc.* **78** 854–67

[181] Bichenkova E V., Raju A P A, Burusco K K, Kinloch I A, Novoselov K S and Clarke D J 2018 NMR detects molecular interactions of graphene with aromatic and aliphatic hydrocarbons in water *2D Mater.* **5** 1–13

[182] Mishra S K and Suryaprakash N 2017 Intramolecular hydrogen bonding involving organic fluorine: NMR investigations corroborated by DFT-based theoretical calculations *Molecules* **22** 1–44

[183] Lyga J W, Henrie R N, Meier G A, Creekmore R W and Patera R M 1993 'Through-space' hydrogen-fluorine, carbon-fluorine and fluorine-fluorine spin-spin coupling in 2-phenyl-3-alkyl-4,5,6,7-tetrahydroindazoles *Magn. Reson. Chem.* **31** 323–8

APPENDIX

Appendix A: FTIR Spectra

1) FTIR of i) CB-$CuCl_2$-MalA [purple], ii) CB-$CuCl_2$-MalA-INHCl [red] and iii) INHCl [black].

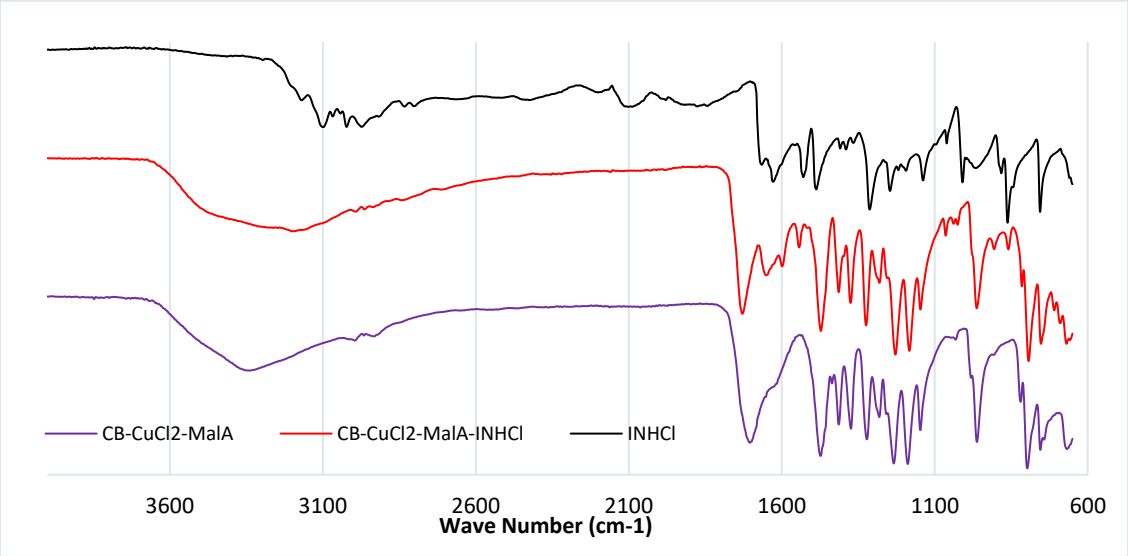

Appendix A 1: FTIR of i) CB-$CuCl_2$-SucA [purple], ii) CB-$CuCl_2$-SucA-INHCl [red] and iii) INHCl [black].

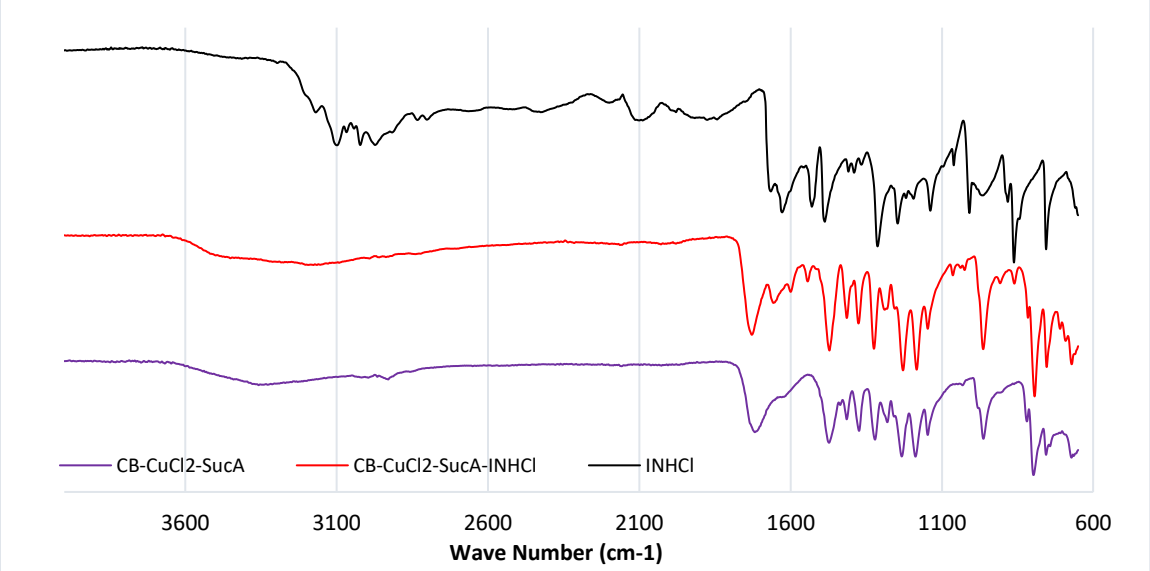

Appendix A 2: FTIR of i) CB-$ZnCl_2$-MalA [purple], ii) CB-$ZnCl_2$-MalA-INHCl [red] and iii) INHCl [black].

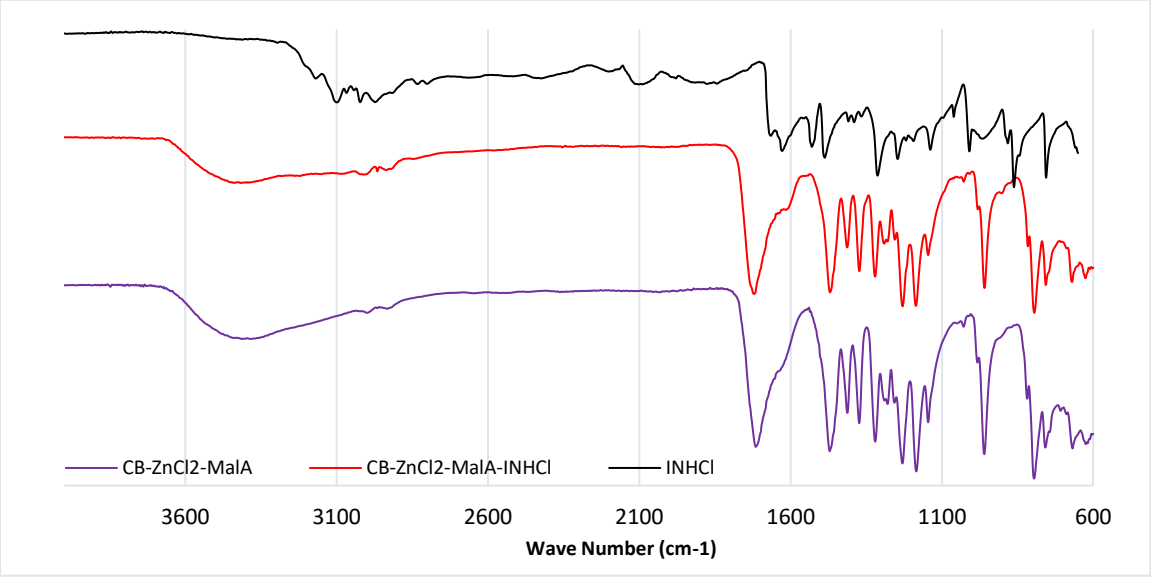

Appendix A 3: FTIR of i) CB-$ZnCl_2$-SucA [purple], ii) CB-$ZnCl_2$-SucA-INHCl [red] and iii) INHCl [black].

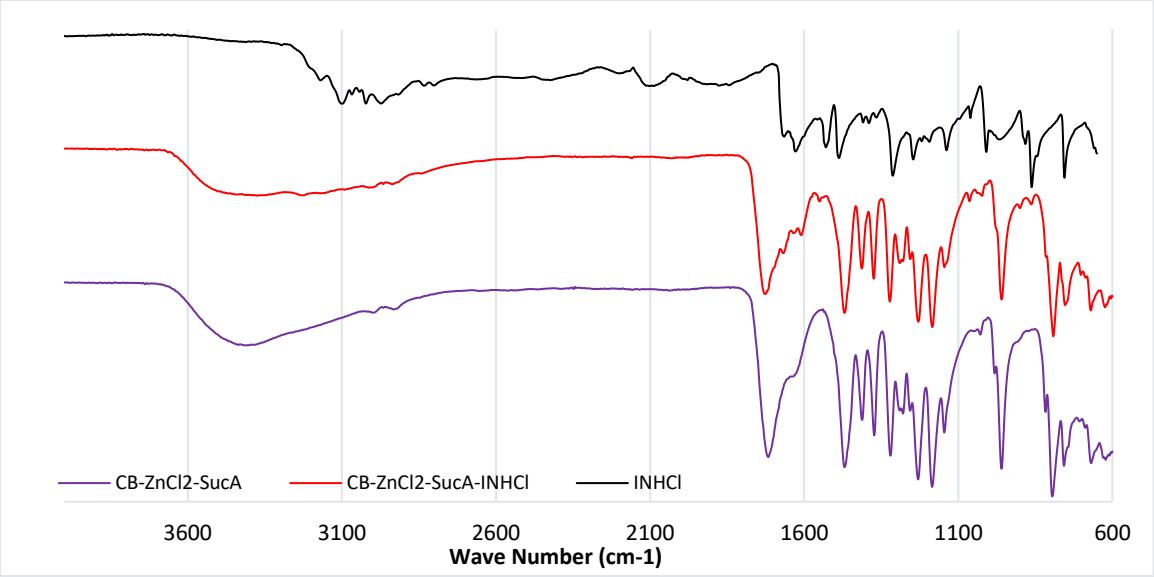

Appendix A 4: FTIR of i) CB-$ZnCl_2$-GluA [purple], ii) CB-$ZnCl_2$-GluA-INHCl [red] and iii) INHCl [black].

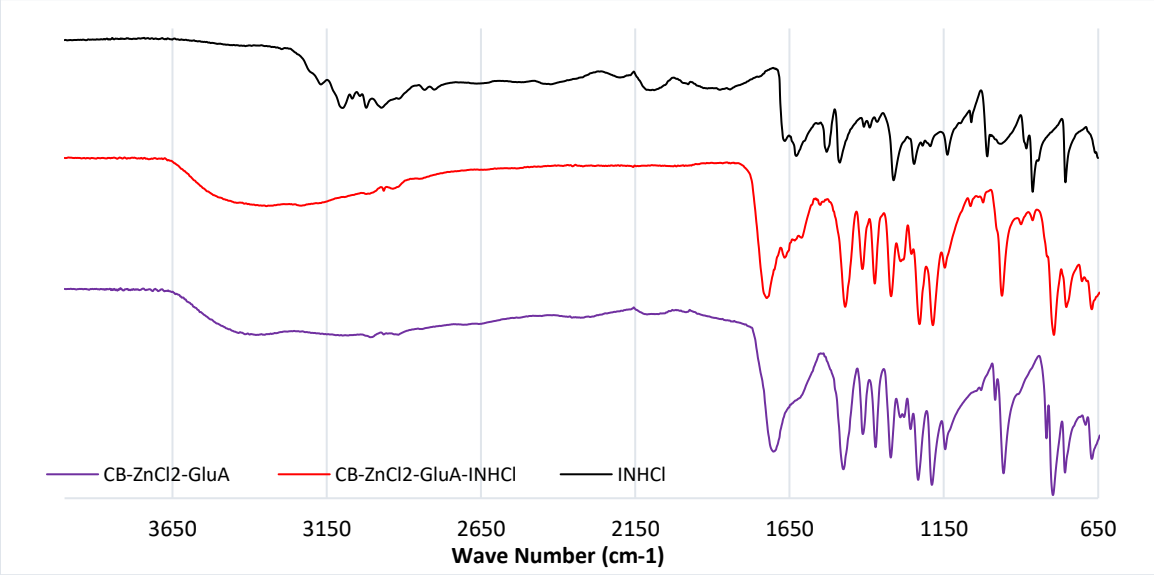

Appendix A 5: FTIR of i) CB-$CuCl_2$-MalA-INHCl at RT [green], ii) CB-$CuCl_2$-MalA-INHCl heated to 140 ºC and cooled [black].

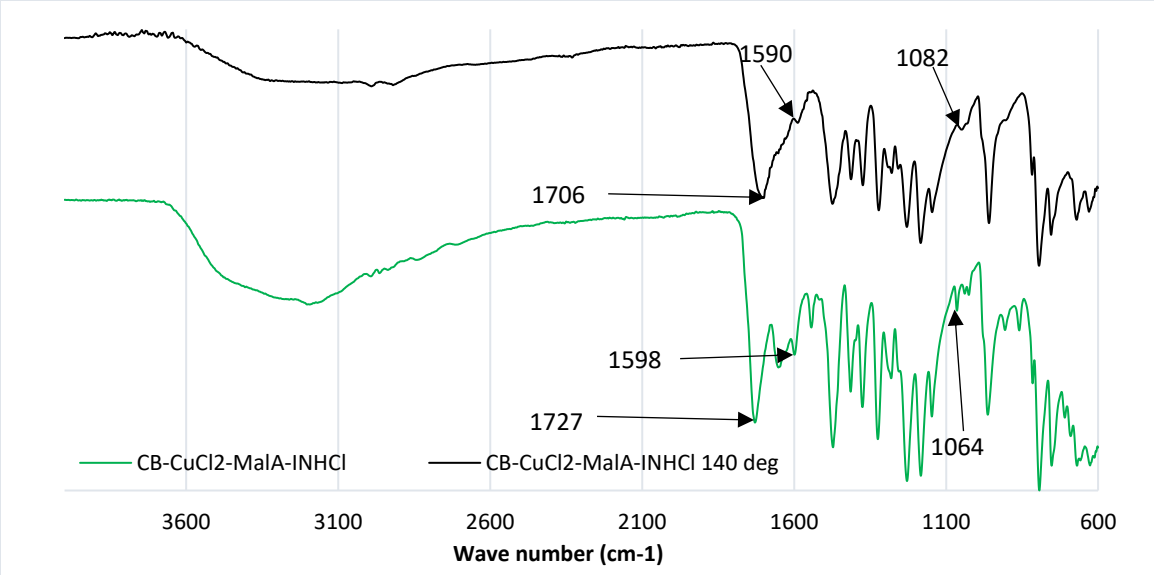

Appendix A 6: FTIR spectra of 3,4-dHBP and it metal complexes

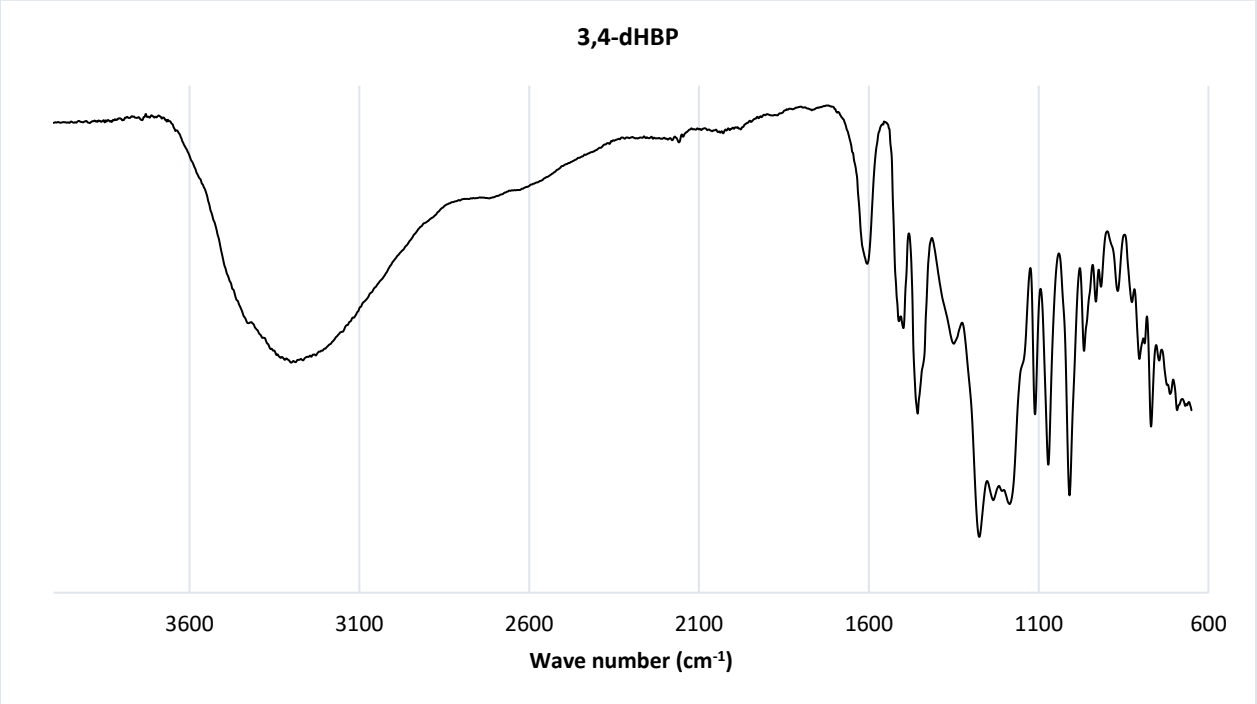

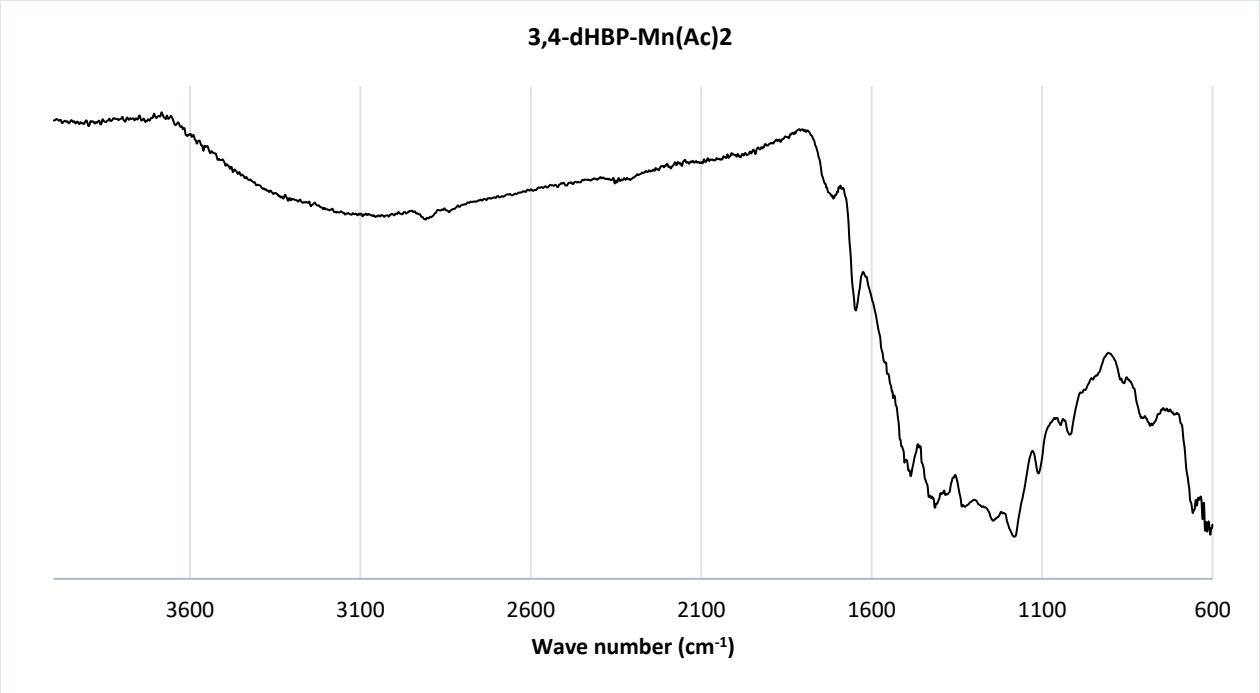
3,4-dHBP-Mn(Ac)2
3600
3100
2600
2100
1600
1100
600
Wave number (cm-1)

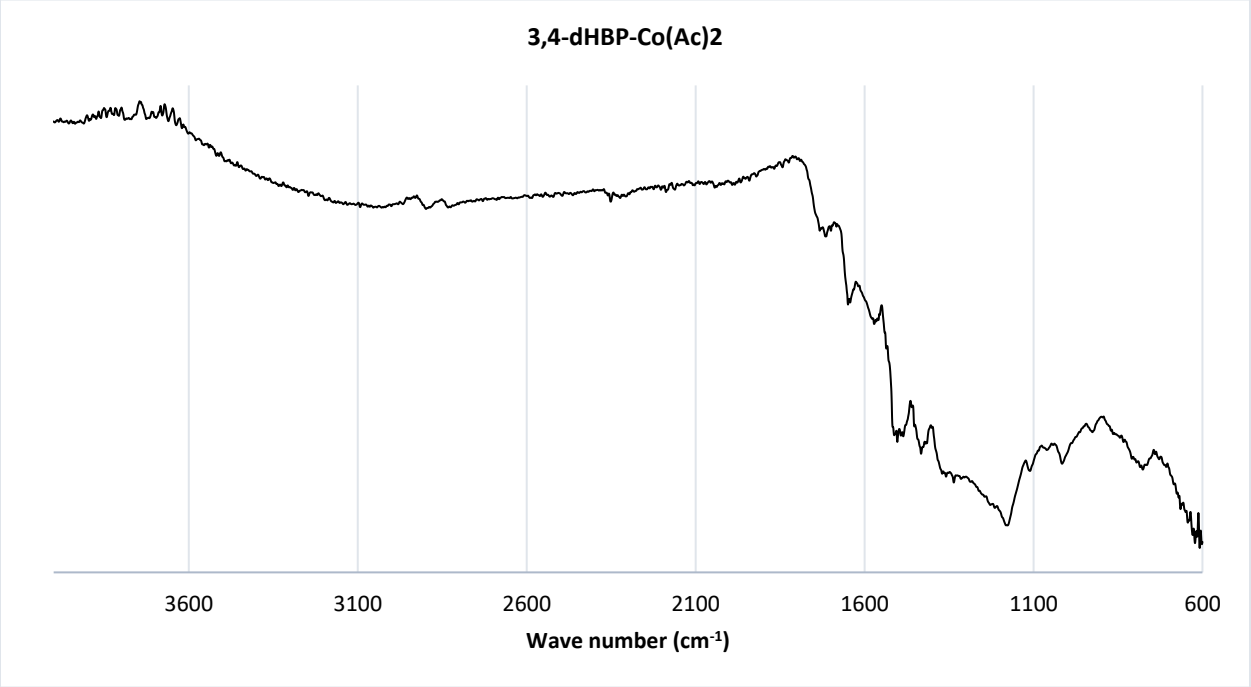
3,4-dHBP-Co(Ac)2
3600
3100
2600
2100
1600
1100
600
Wave number (cm-1)

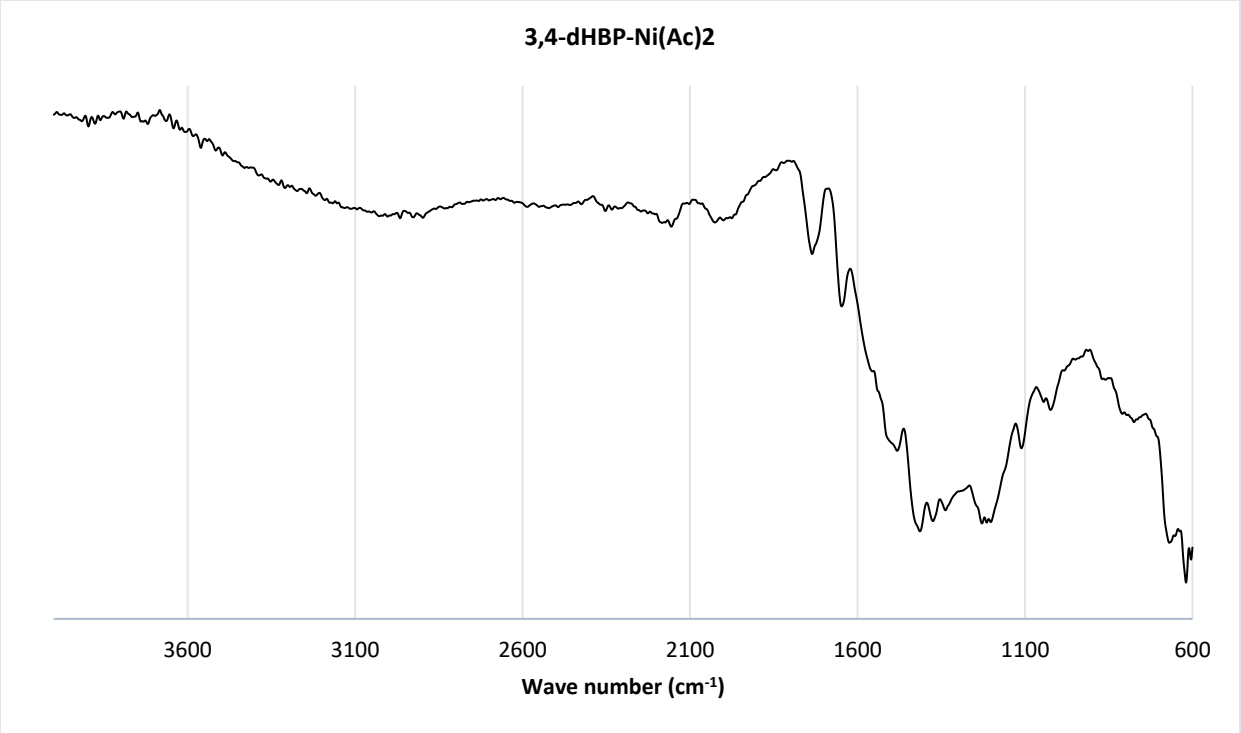
3,4-dHBP-Ni(Ac)2
3600
3100
2600
2100
1600
1100
600
Wave number (cm-1)

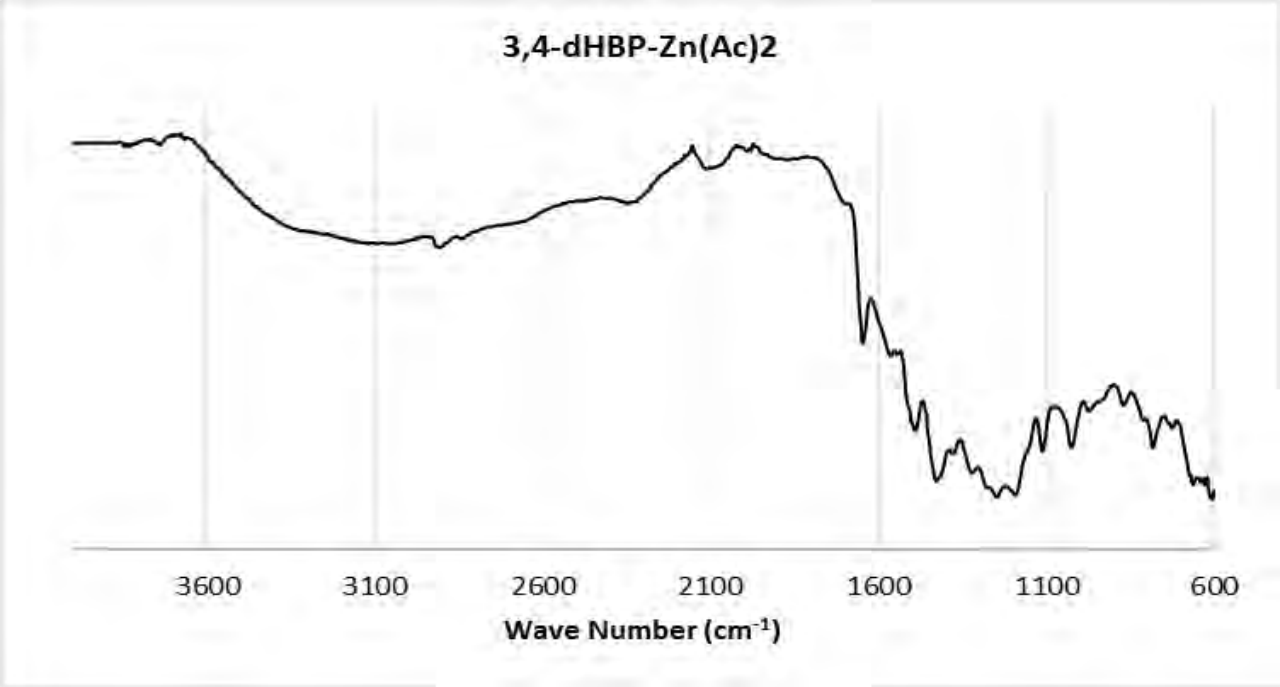
3,4-dHBP-Zn(Ac)2
3600
3100
2600
2100
1600
1100
600
Wave Number (cm-1)

Appendix B: TGA Thermograms

APPENDIX B 1:TGA thermogram for CB-$MnCl_2$-MalA (black) and Derivative (blue)

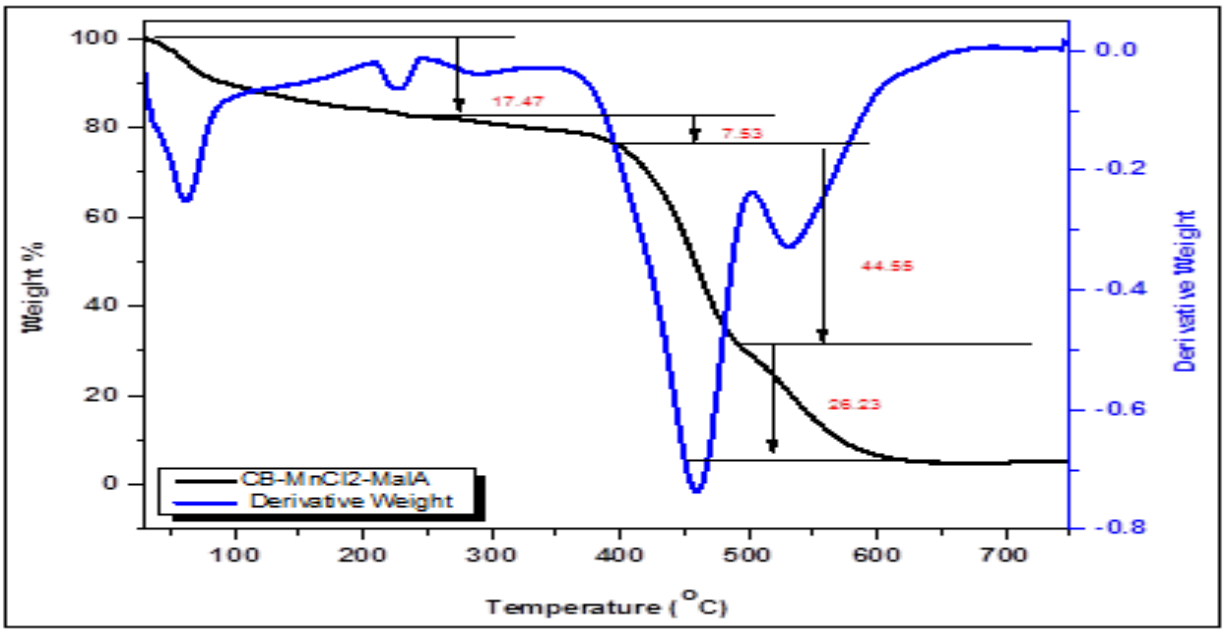

APPENDIX B 2: TGA thermogram of CB-$MnCl_2$-SucA (black) and derivative (blue)

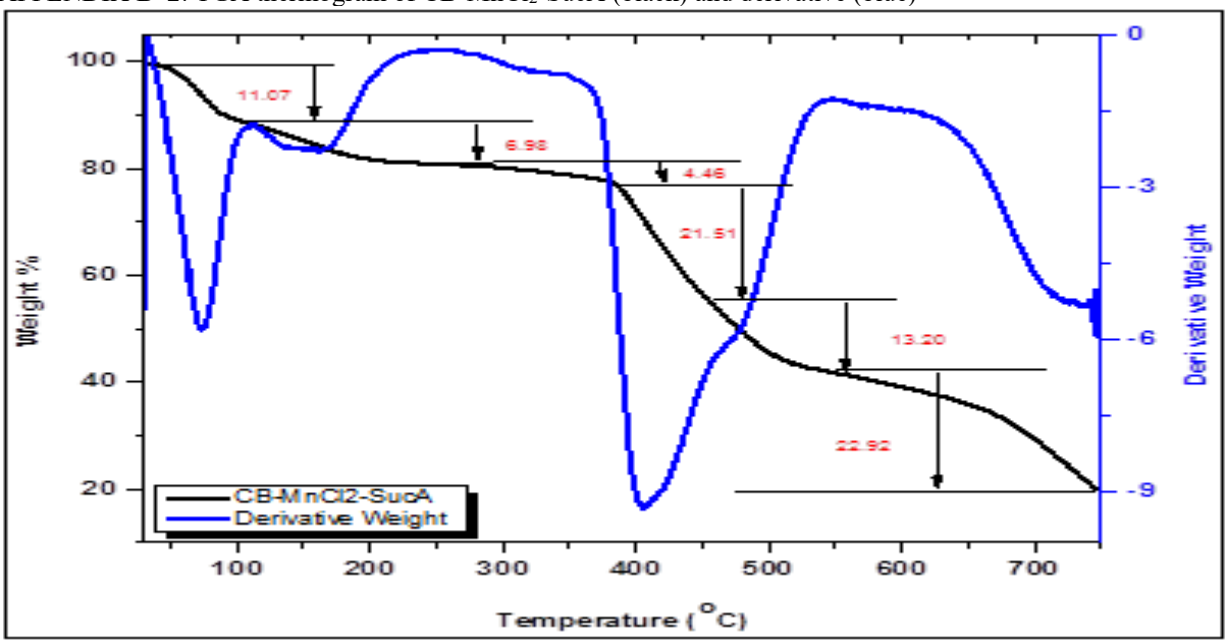

APPENDIX B 3: TGA thermogram for CB-$FeCl_2$-OxA (black) and derivative (blue)

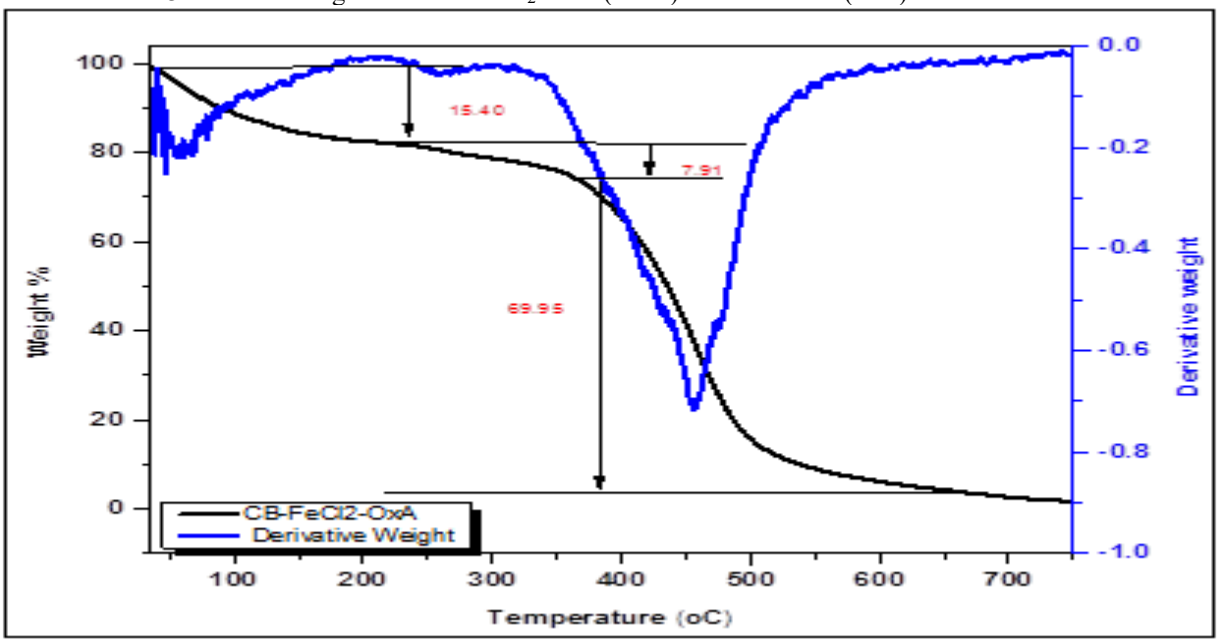

Appendix B 4: TGA thermogram for CB-$FeCl_2$-MalA (black) and derivative (blue)

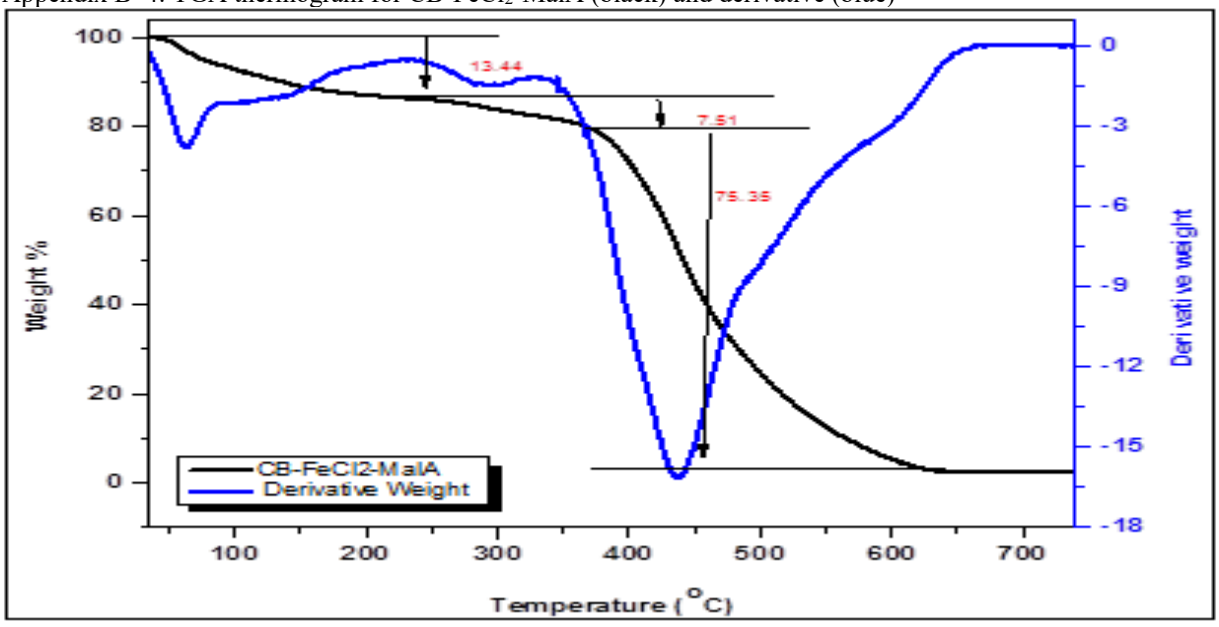

Appendix B 5: TGA thermogram CB-$FeCl_2$-GluA-HCl (black) and derivative (blue)

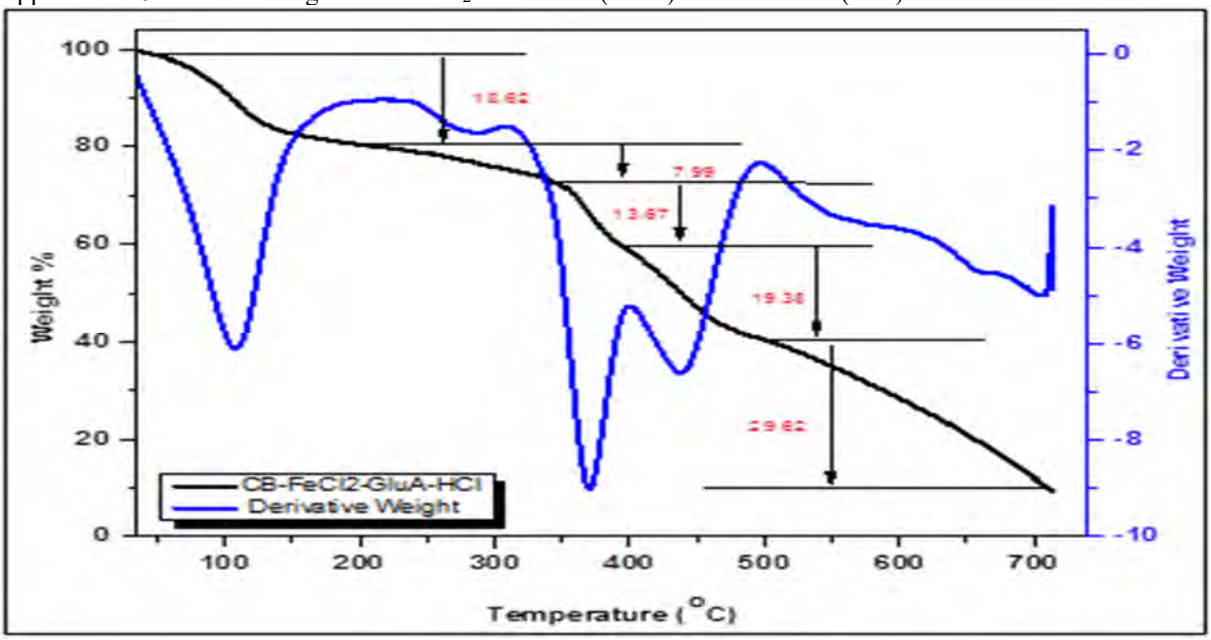

Appendix B 6: TGA thermogram for CB-CuCl2-OxA (black) and derivative (blue)

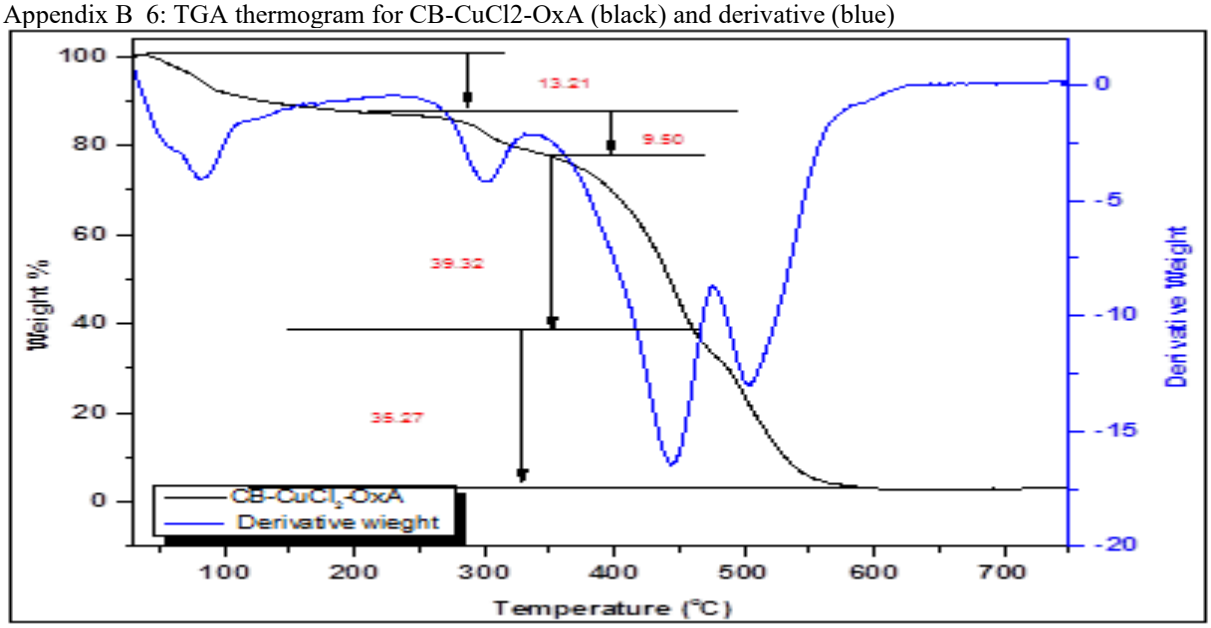

Appendix B 7: TGA thermogram for CB-$CuCl_2$-SucA (black) and derivative (blue)

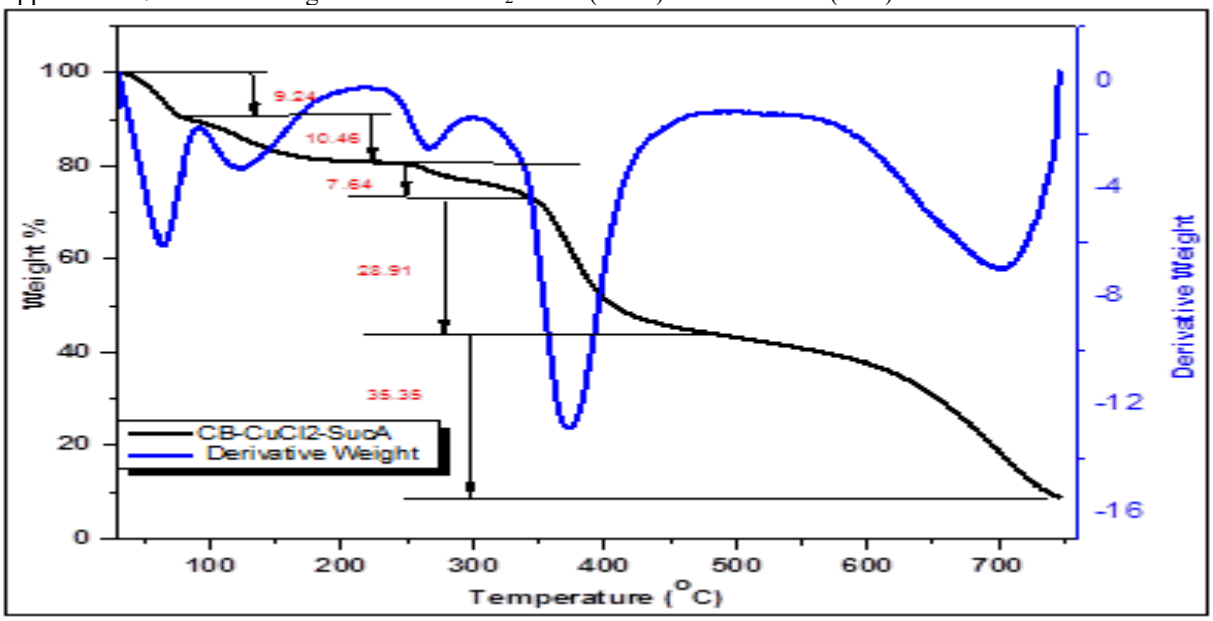

Appendix B 8: TGA thermogram of CB-$CuCl_2$-GluA (black) and derivative (blue)

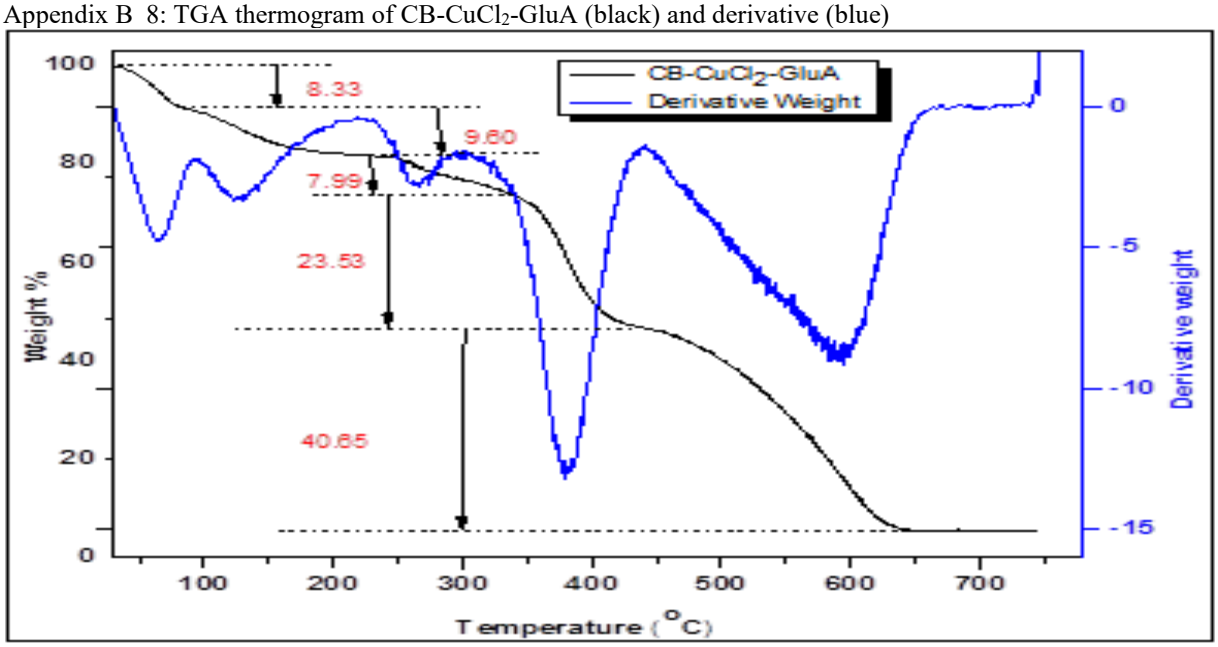

Appendix B 9: TGA thermogram of CB-$ZnCl_2$-MalA (black) and derivative (blue)

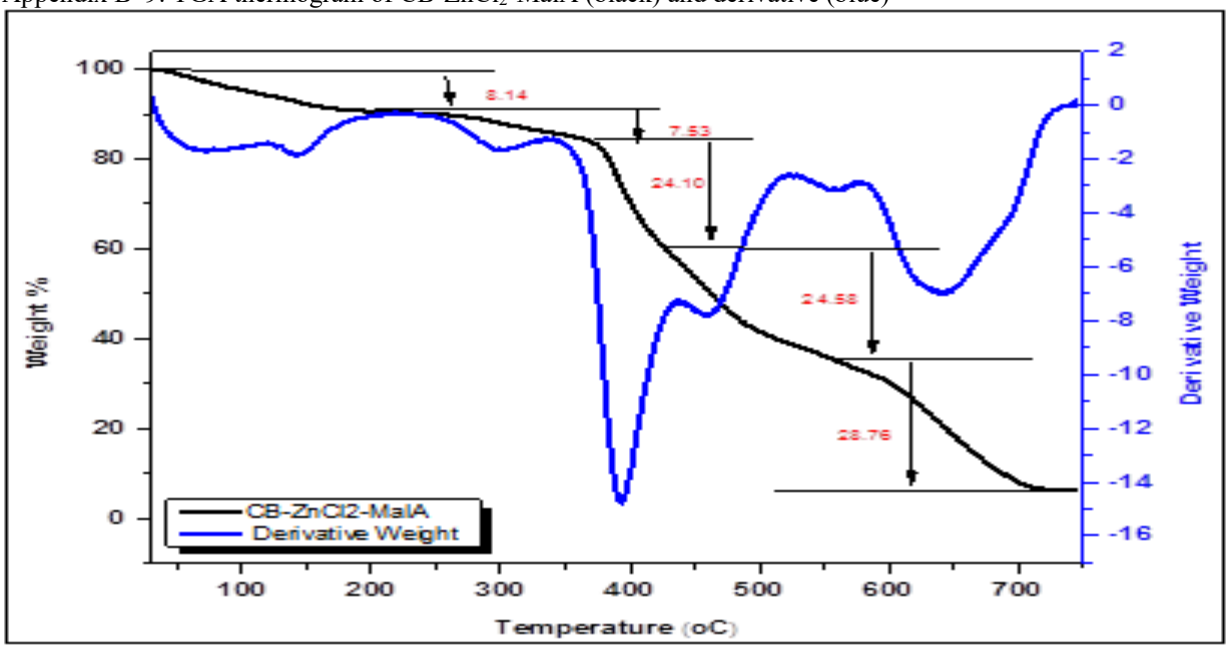

Appendix B 10: TGA thermogram of CB-$ZnCl_2$-SucA (black) and derivative (blue)

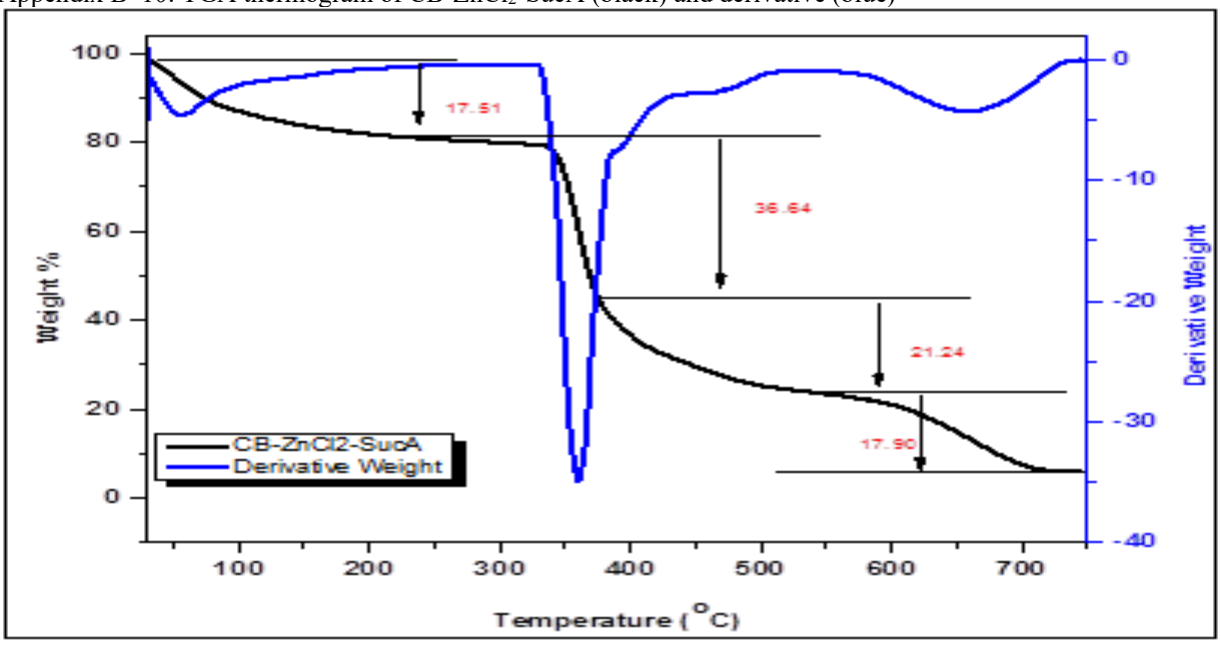

Appendix B 11:TGA thermogram of CB-$ZnCl_2$-GluA (black) and derivative (blue)

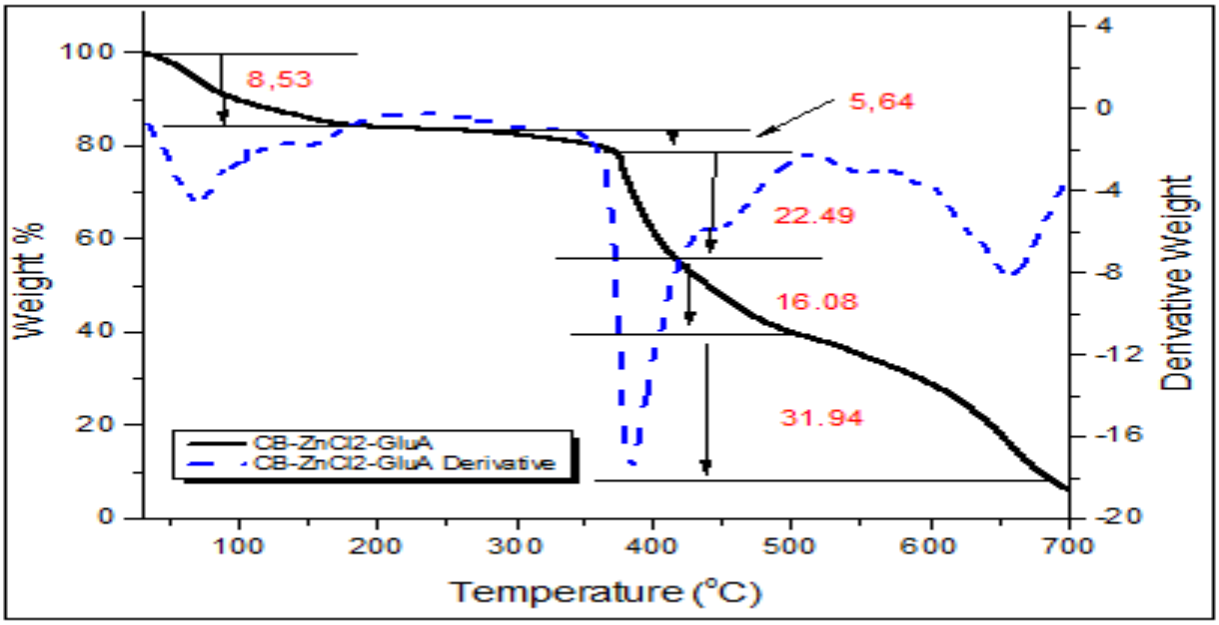

Appendix B 12: TGA thermogram of CB-$CuCl_2$-MalA (green) and CB-$CuCl_2$-MalA-INHCl (red). The respective derivatives are indicated in dotted lines

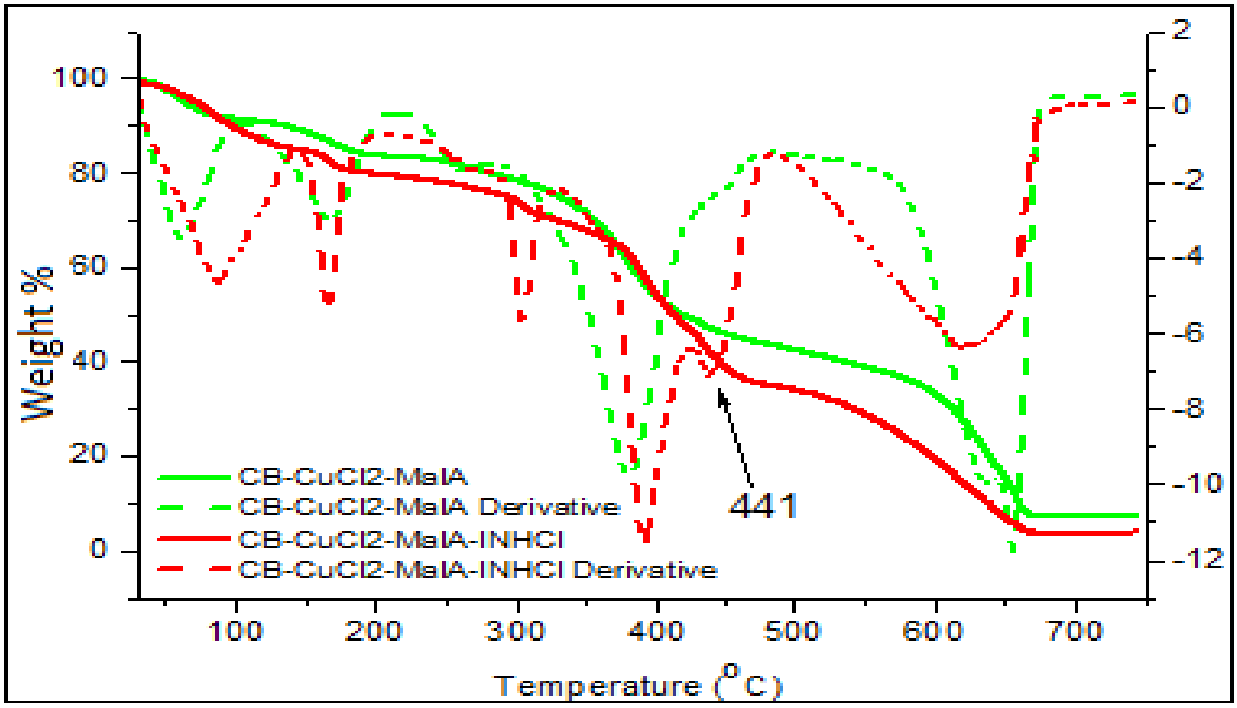

Appendix B 13: TGA thermogram of CB-$CuCl_2$-SucA (green) and CB-$CuCl_2$-SucA-INHCl (red). The respective derivatives are indicated in dotted lines

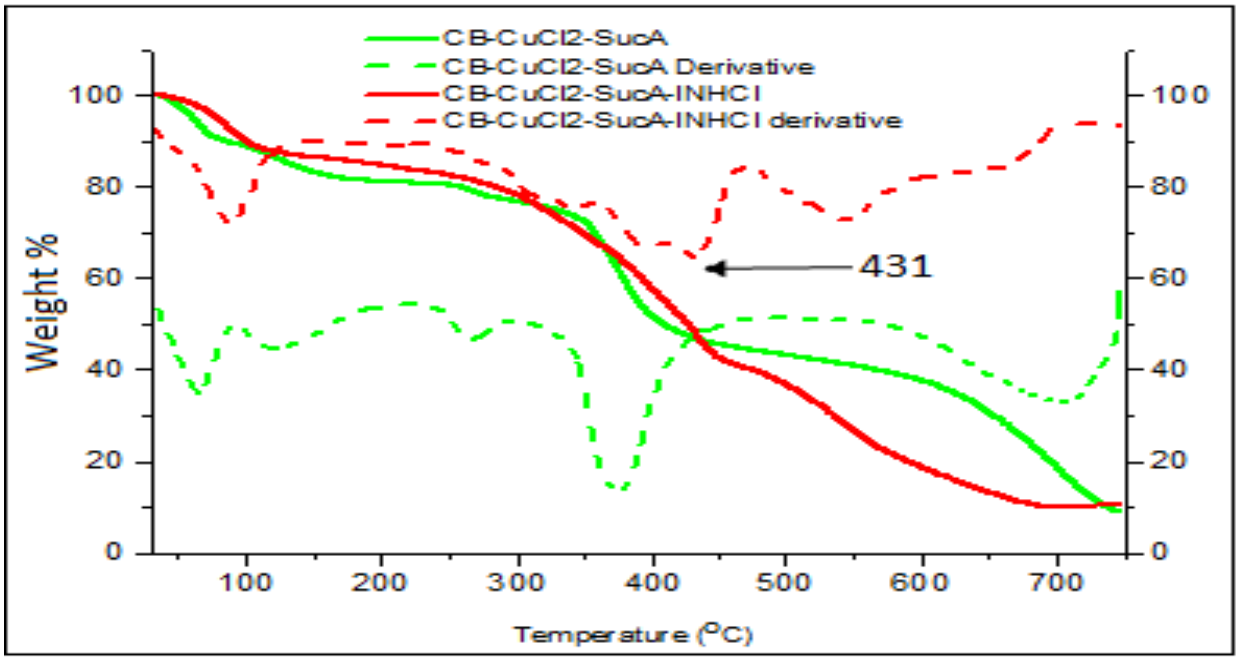

Appendix B 14: TGA thermogram of CB-$CuCl_2$-GluA (green) and CB-$CuCl_2$-GluA-INHCl (red). The respective derivatives are indicated in dotted lines

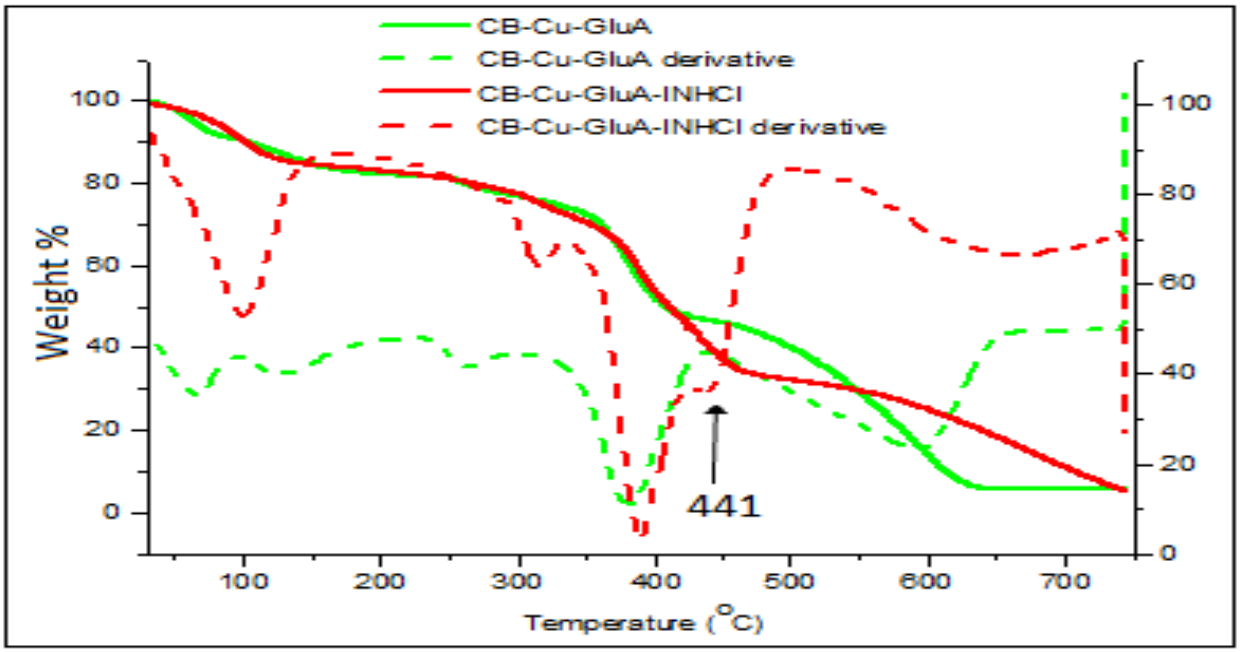

Appendix B 15: TGA thermogram of CB-$ZnCl_2$-OxA (green) and CB-$ZnCl_2$-OxA-INHCl (red). The respective derivatives are indicated in dotted lines

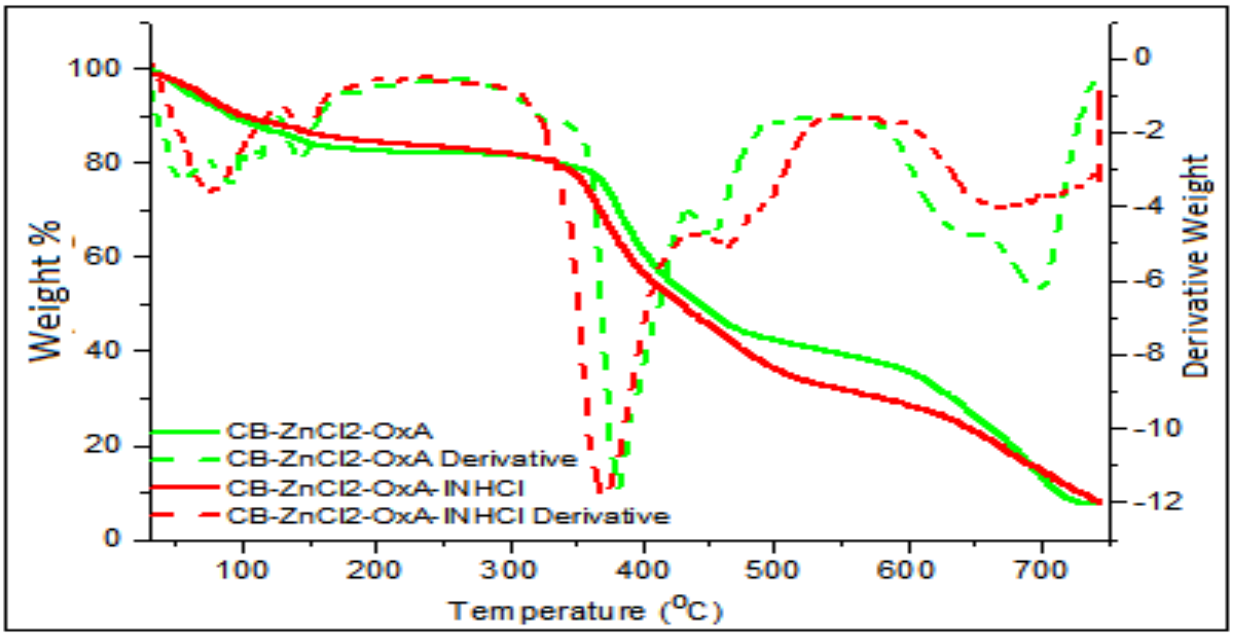

Appendix B 16: TGA thermogram of CB-$ZnCl_2$-MalA (green) and CB-$ZnCl_2$-MalA-INHCl (red). The respective derivatives are indicated in dotted lines

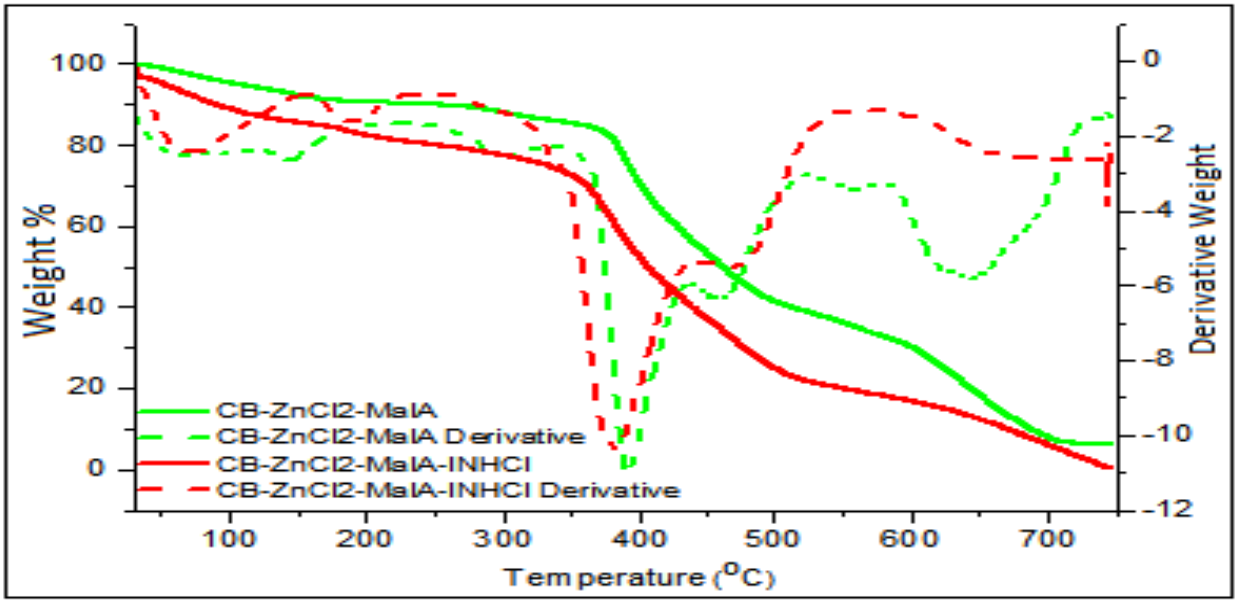

Appendix B 17: TGA thermogram of CB-$ZnCl_2$-GluA (green) and CB-$ZnCl_2$-GluA-INHCl (red). The respective derivatives are indicated in dotted lines

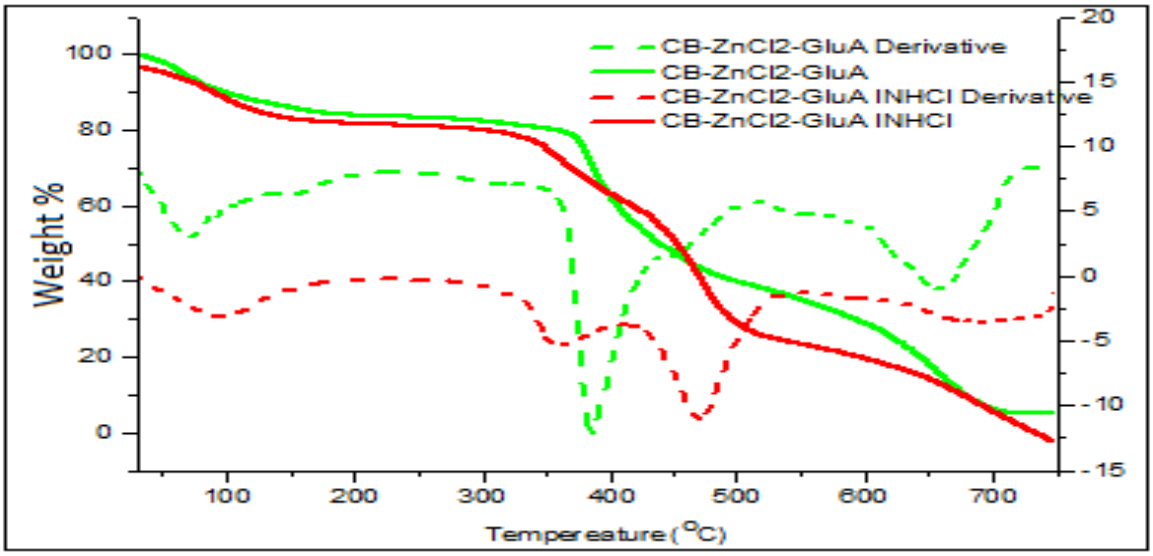

Appendix B 18: TGA thermograms of BN22E after exposure solutions of DMSO/H_2O

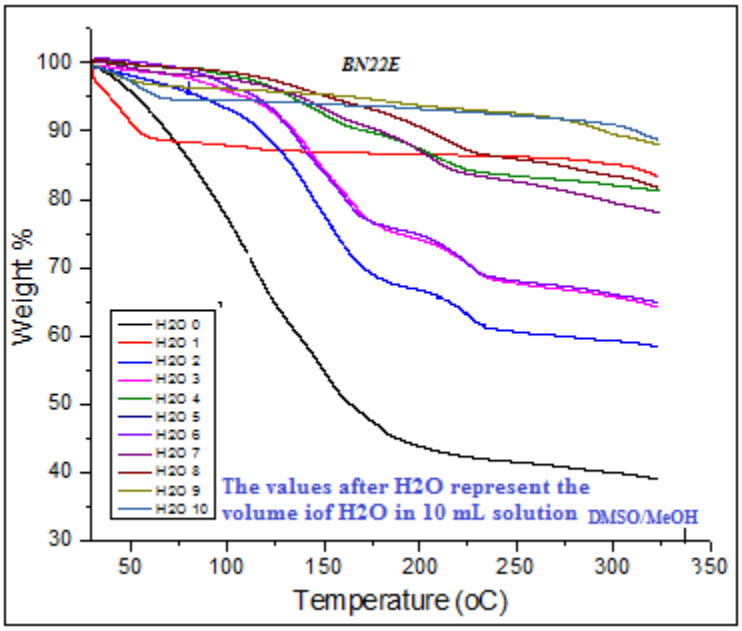

Appendix B 19: TGA thermograms of BN22E after exposure solutions of DMSO/MeOH

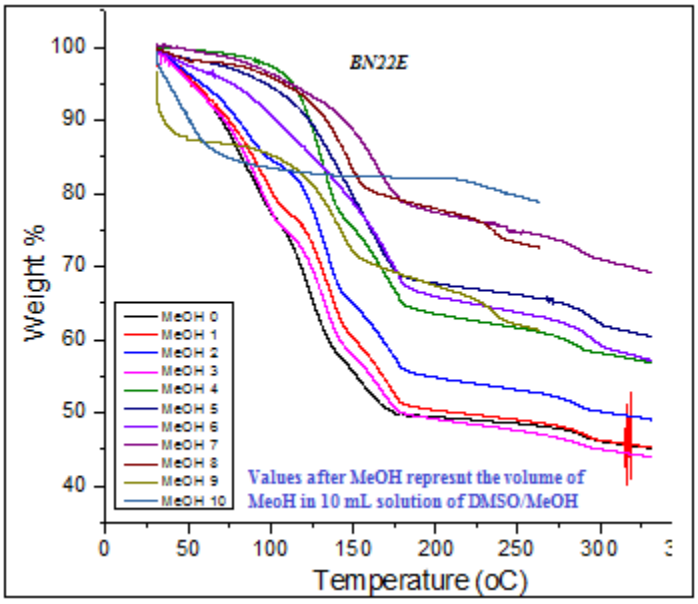

Appendix B 20: TGA thermograms of *p*-ClBP after exposure solutions of DMSO/MeOH

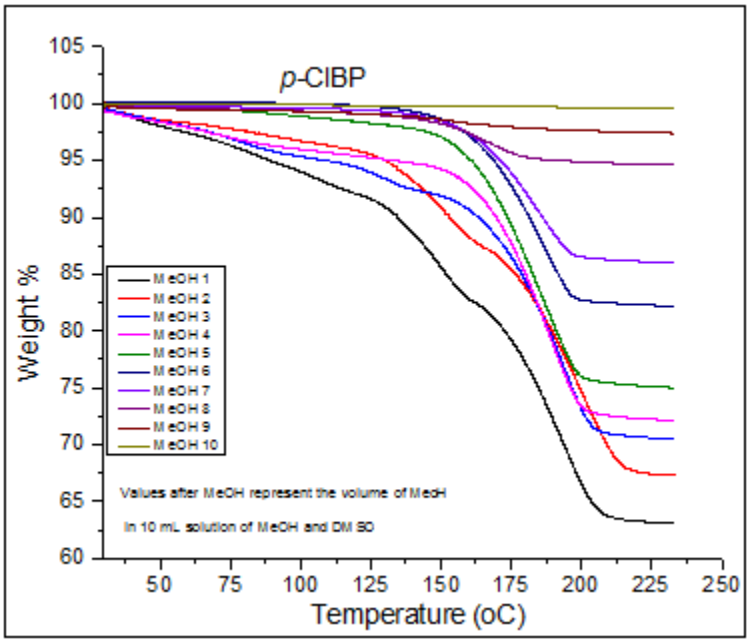

Appendix B 21: TGA thermograms of *p*-ClBP after exposure solutions of DMSO/MeOH

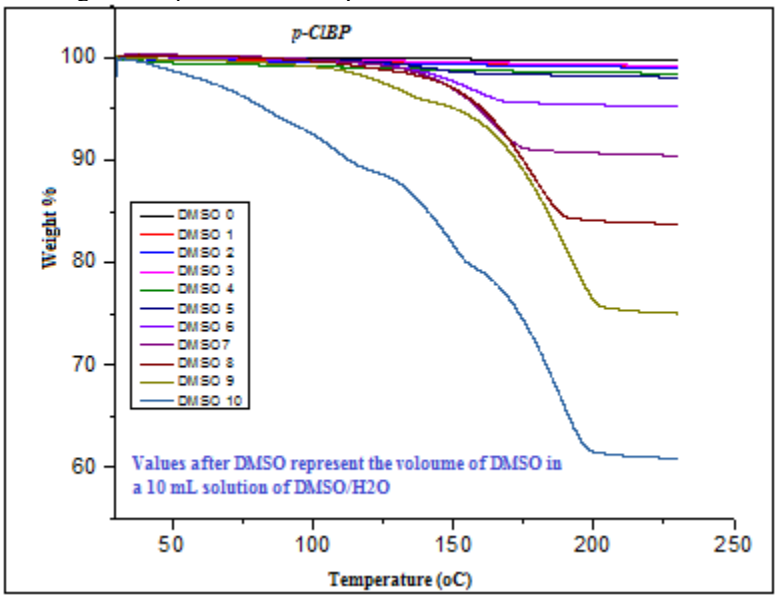

Appendix C: H-NMR spectra

Appendix C 1: HNMR spectra of CB (red), INHCl (green) and CB-$ZnCl_2$-OxA-INHCl (blue)

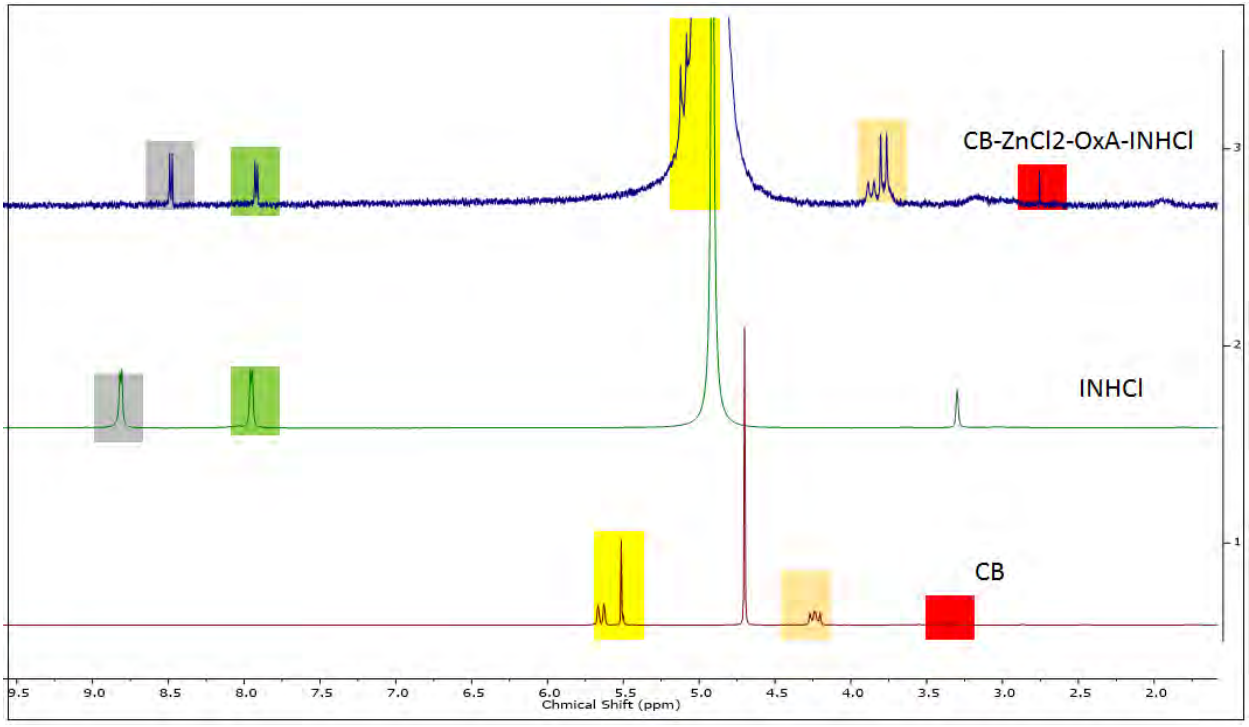

Appendix C 2: HNMR spectra of INHCl (blue), CB-ZnCl2-MalA-INHCl (green) and CB-$ZnCl_2$-MalA

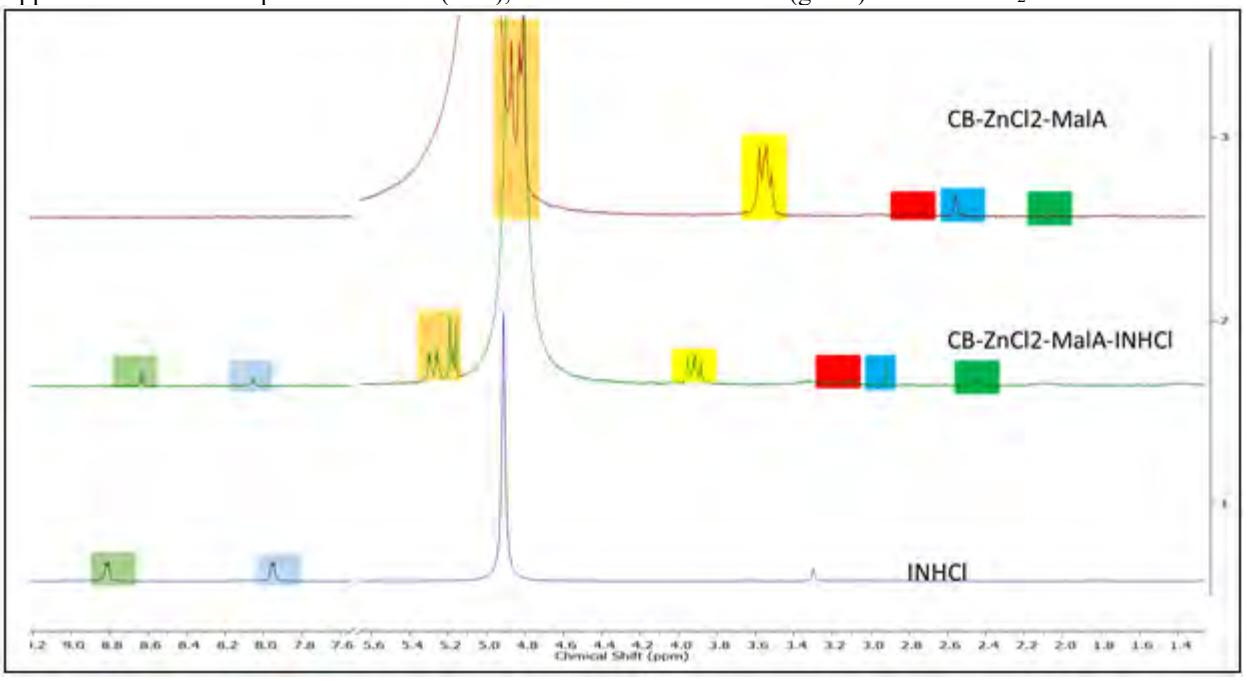

Appendix C 3: HNMR spectra of INHCl (green), CB-$ZnCl_2$-SucA (marron) and CB-$ZnCl_2$-SucA-INHCl (blue)

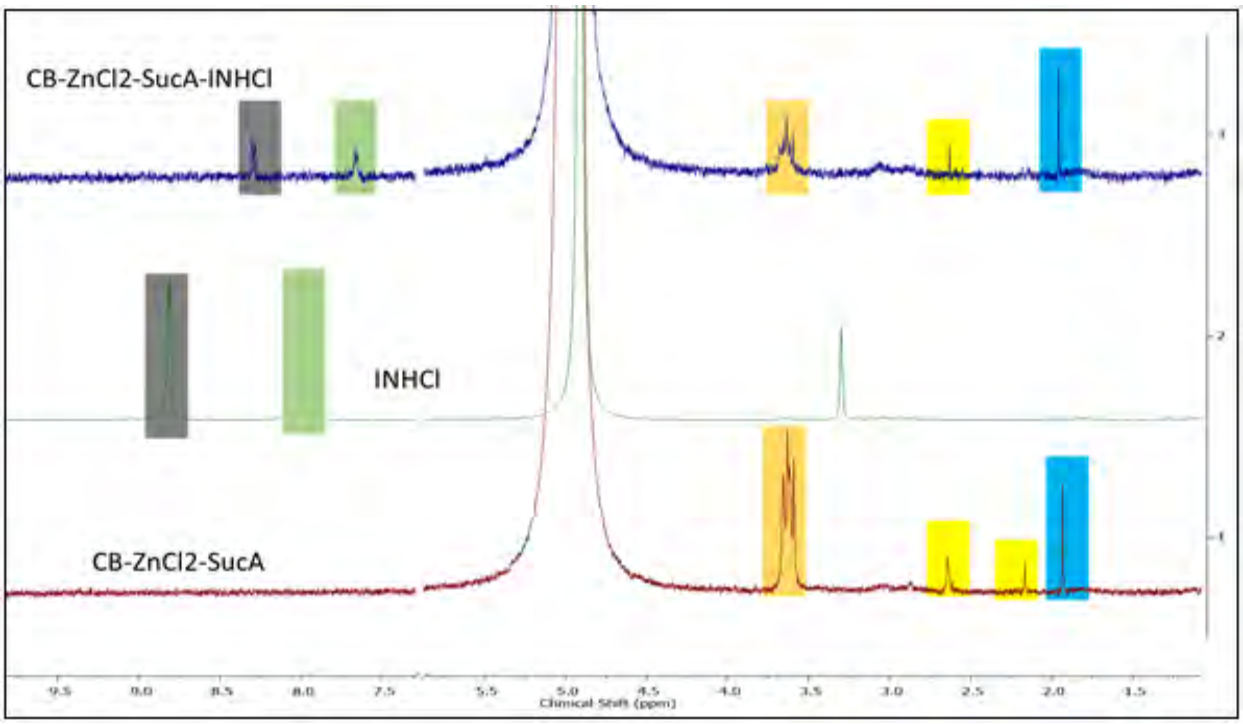

Appendix C 4: H-NMR spectra of crystals obtained from (top)BN22E and (bottom) BN22M

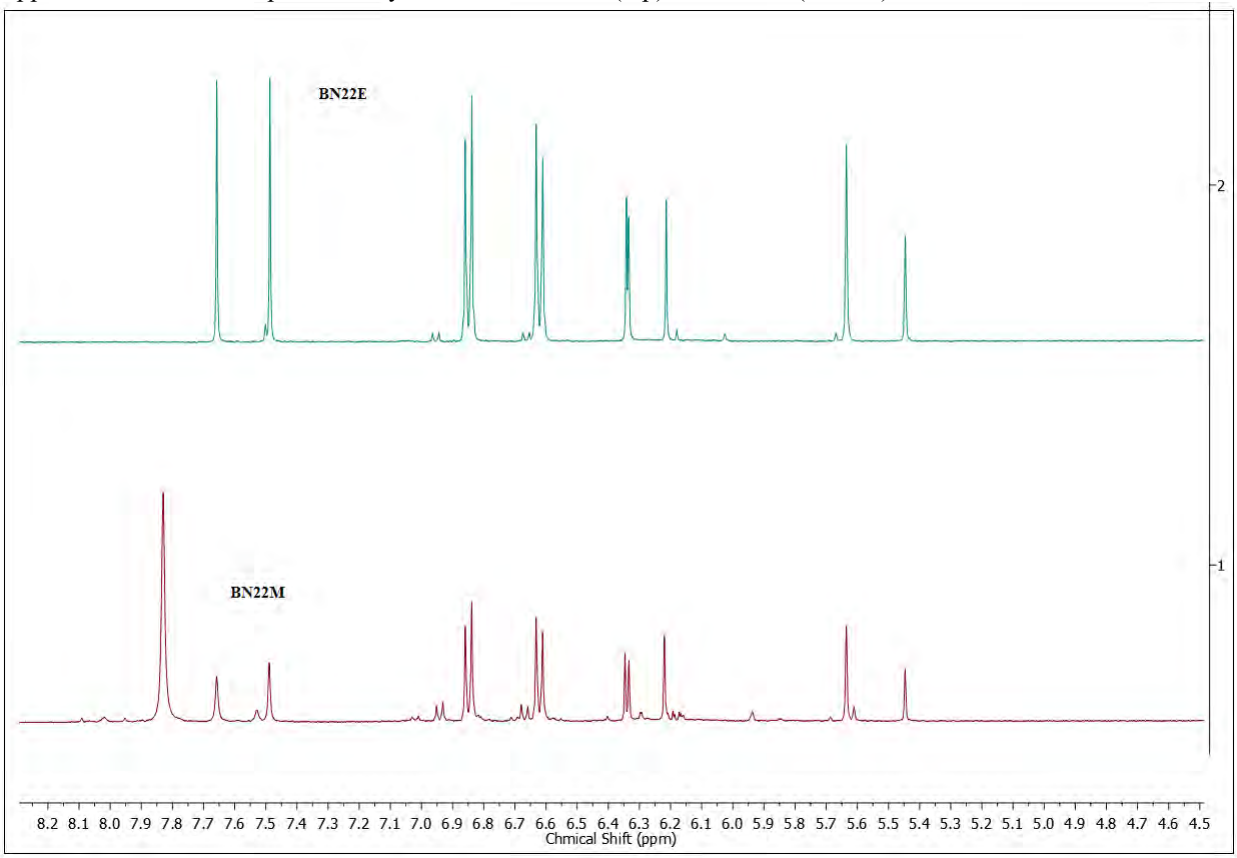

Appendix D: Evolve gas FTIR spectra

Appendix D1: Evolve gas analysis FTIR of BN22E for DMSO/H_2O and DMSO/MeOH systems

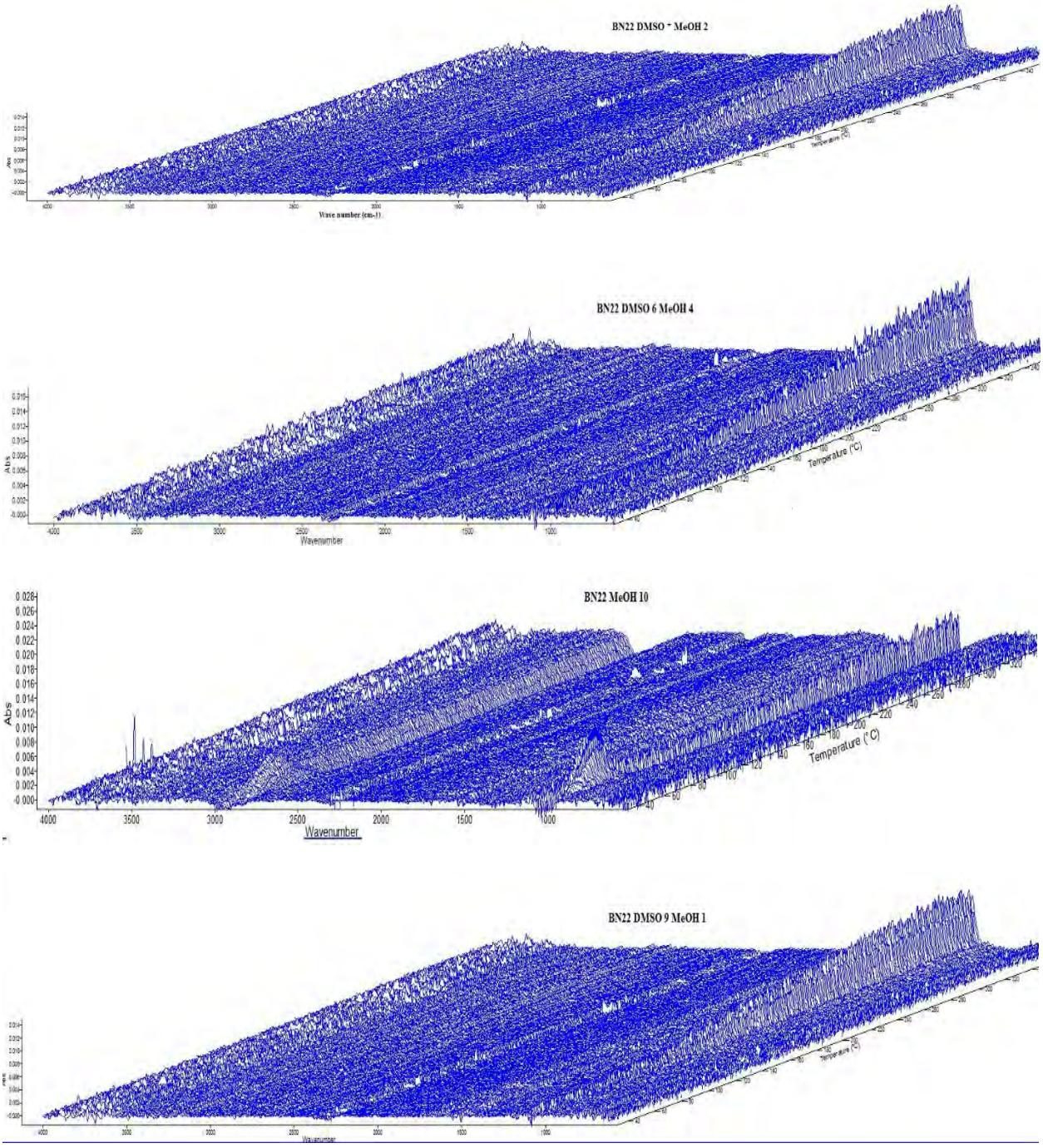

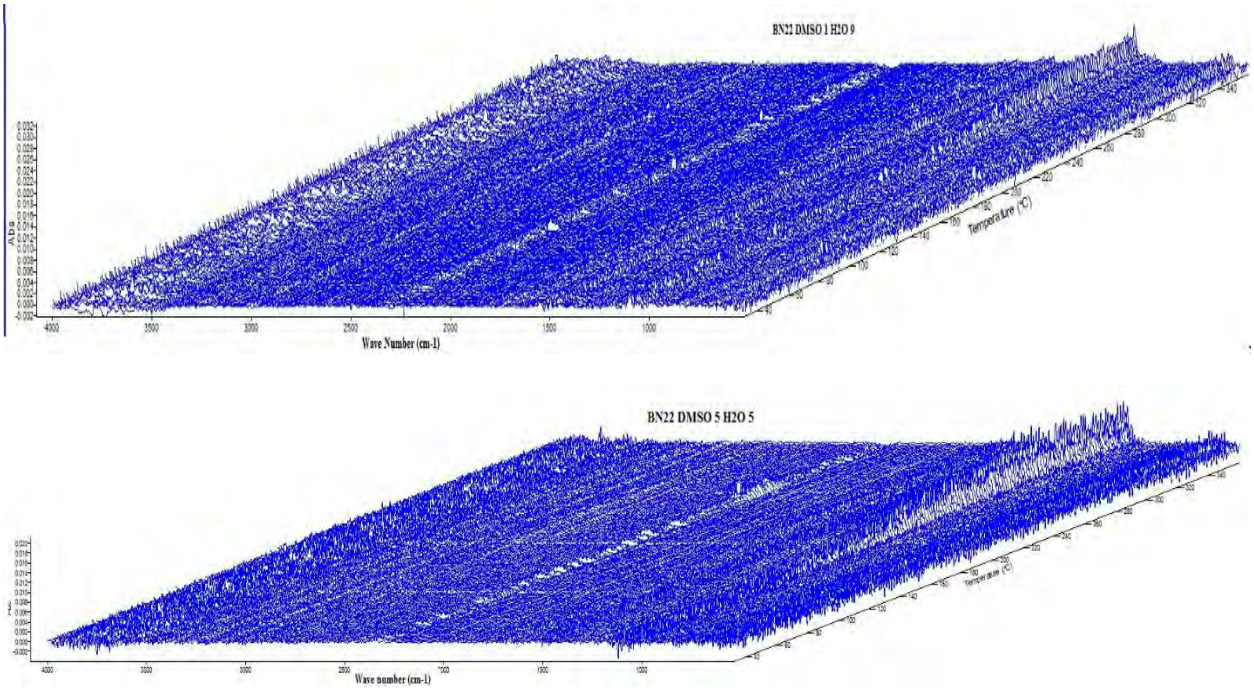

Appendix D2: Evolve gas FTIR Spectra of p-ClBP after exposure to DMSO/H2O and DMSO/MeOH spectra

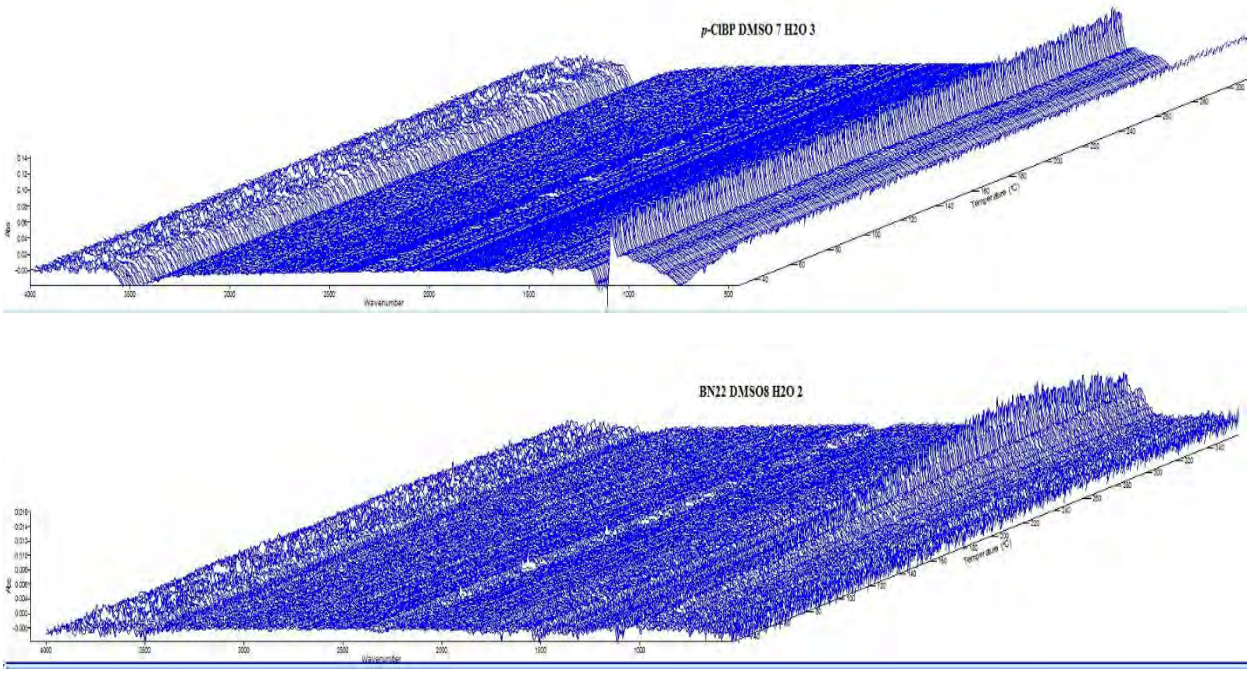

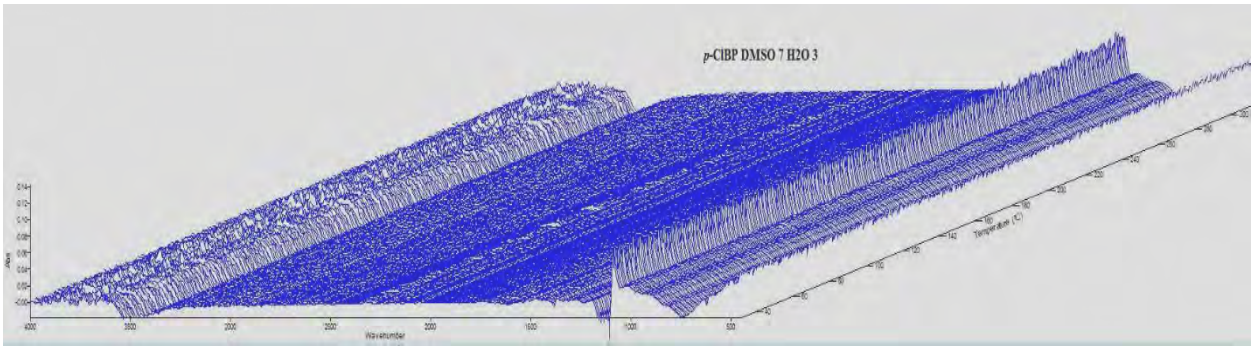

Appendix E: DSC thermograms

Appendix E1: DSC thermograms of BN22E after exposure to DMSO/H_2O system

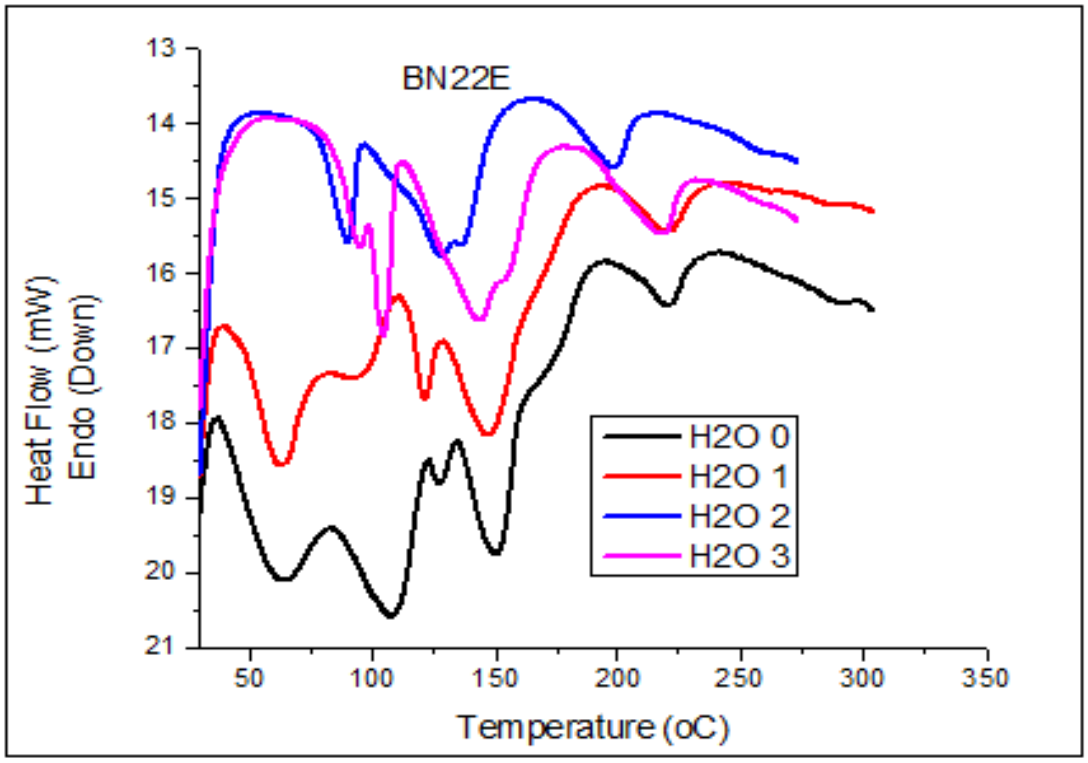

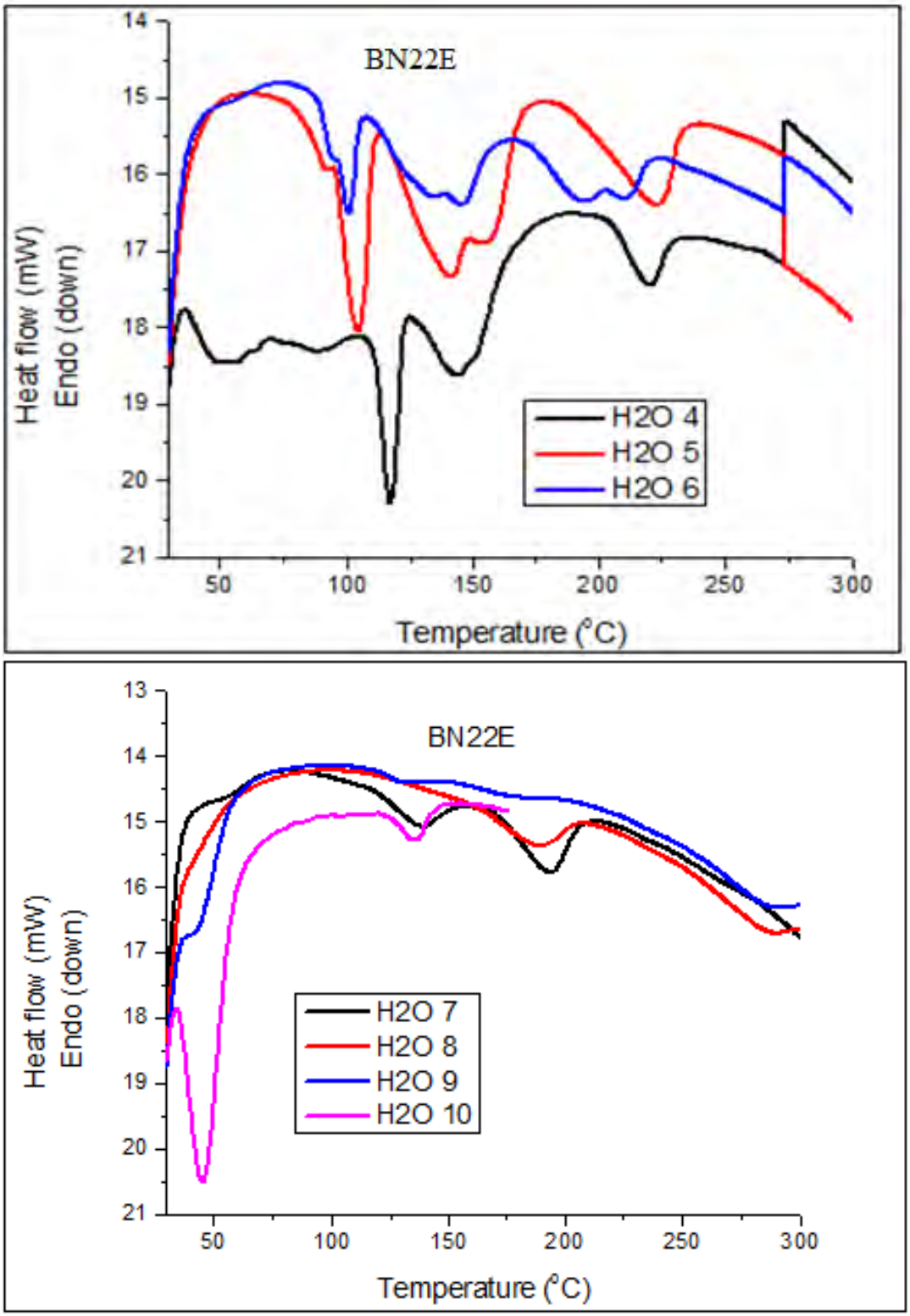

Appendix E2: DSC thermograms of BN22E after exposure to DMSO MeOH system

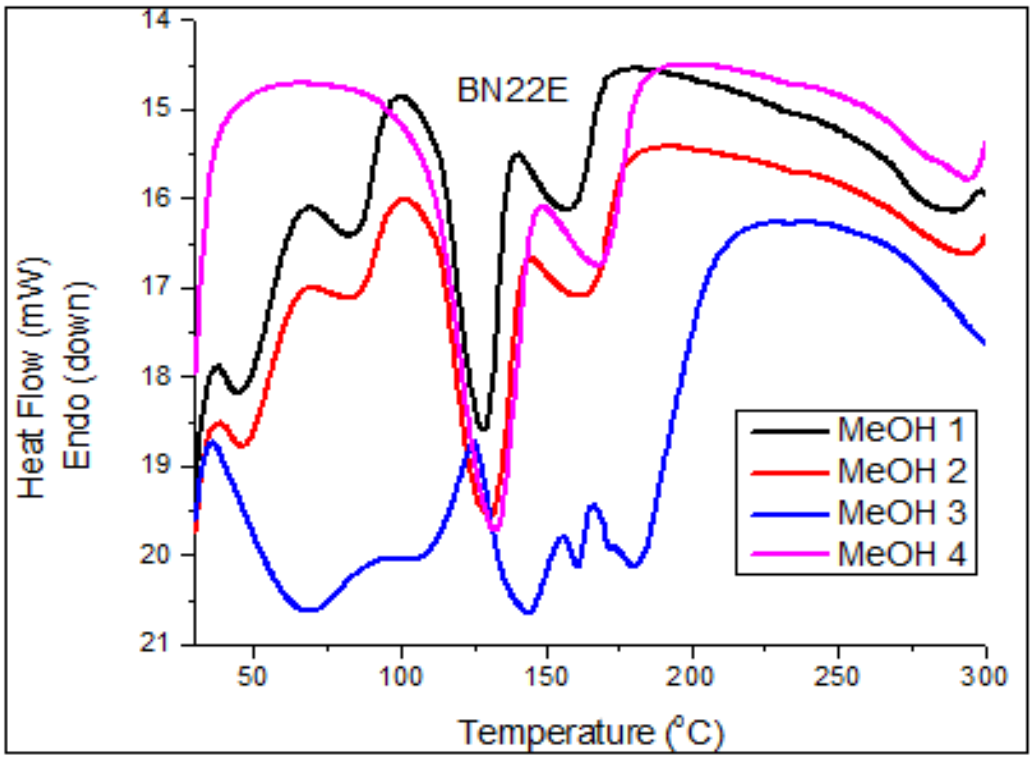
BN22E
Heat Flow (mW)
Endo (down)
Temperature (°C)
MeOH 1
MeOH 2
MeOH 3
MeOH 4
14
15
16
17
18
19
20
21
50
100
150
200
250
300

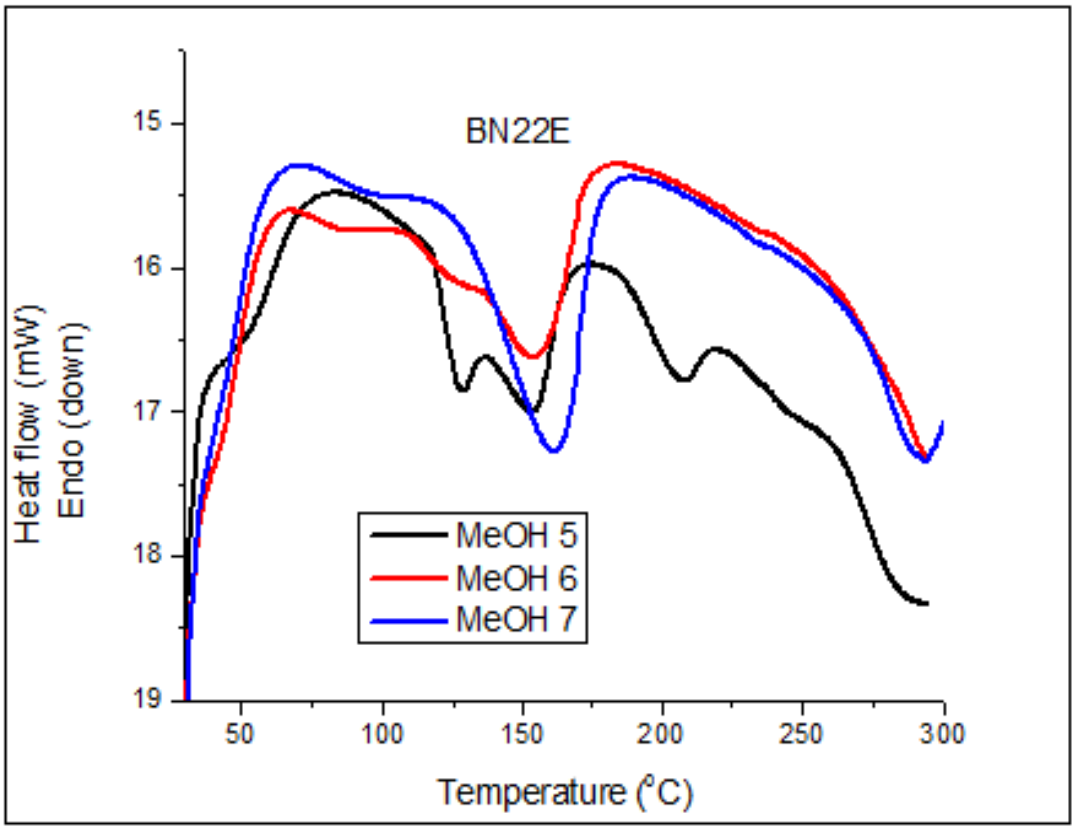
BN22E
Heat flow (mW)
Endo (down)
Temperature (°C)
MeOH 5
MeOH 6
MeOH 7
15
16
17
18
19
50
100
150
200
250
300

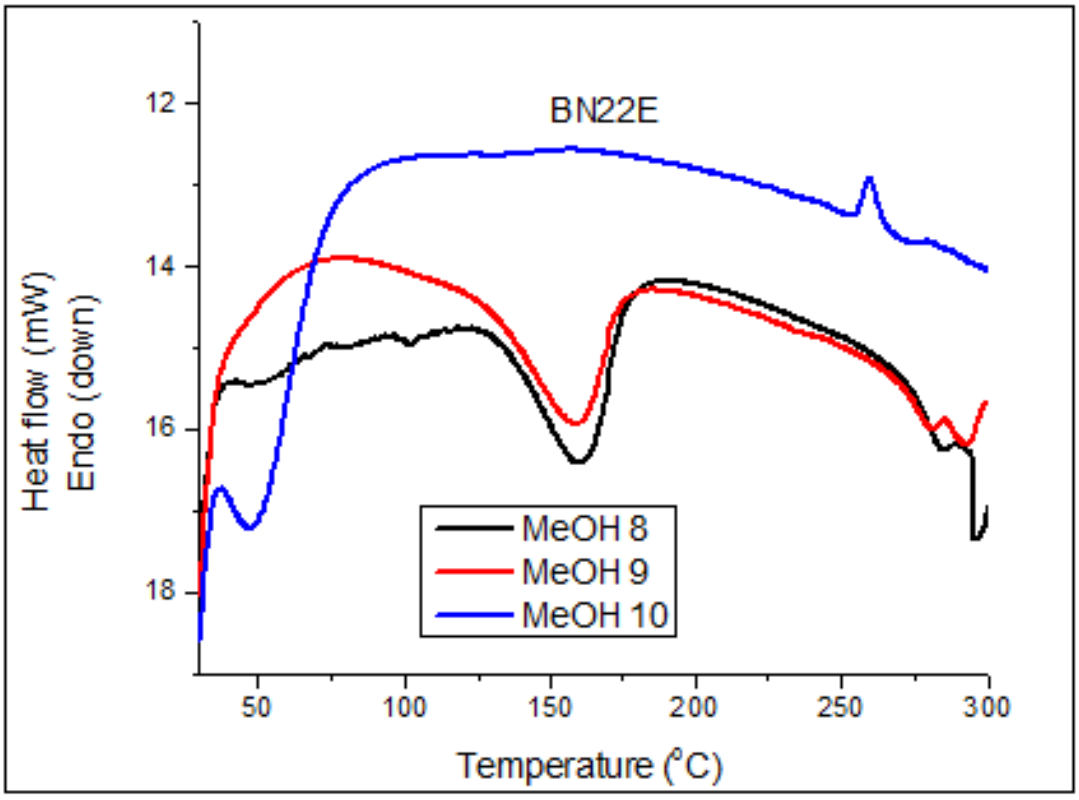

Appendix E3: DSC thermograms of *p*-ClBP after exposure to DMSO/H_2O system

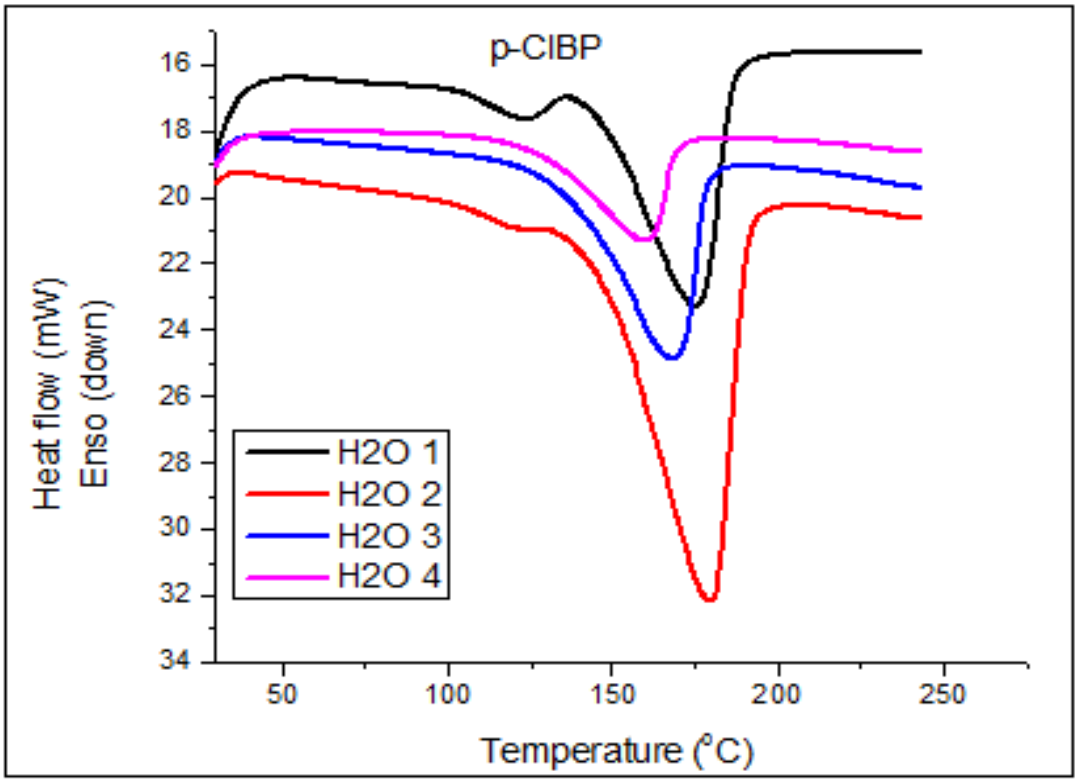
p-ClBP
Heat flow (mW)
Enso (down)
16
18
20
22
24
26
28
30
32
34
50
100
150
200
250
Temperature (°C)
H2O 1
H2O 2
H2O 3
H2O 4

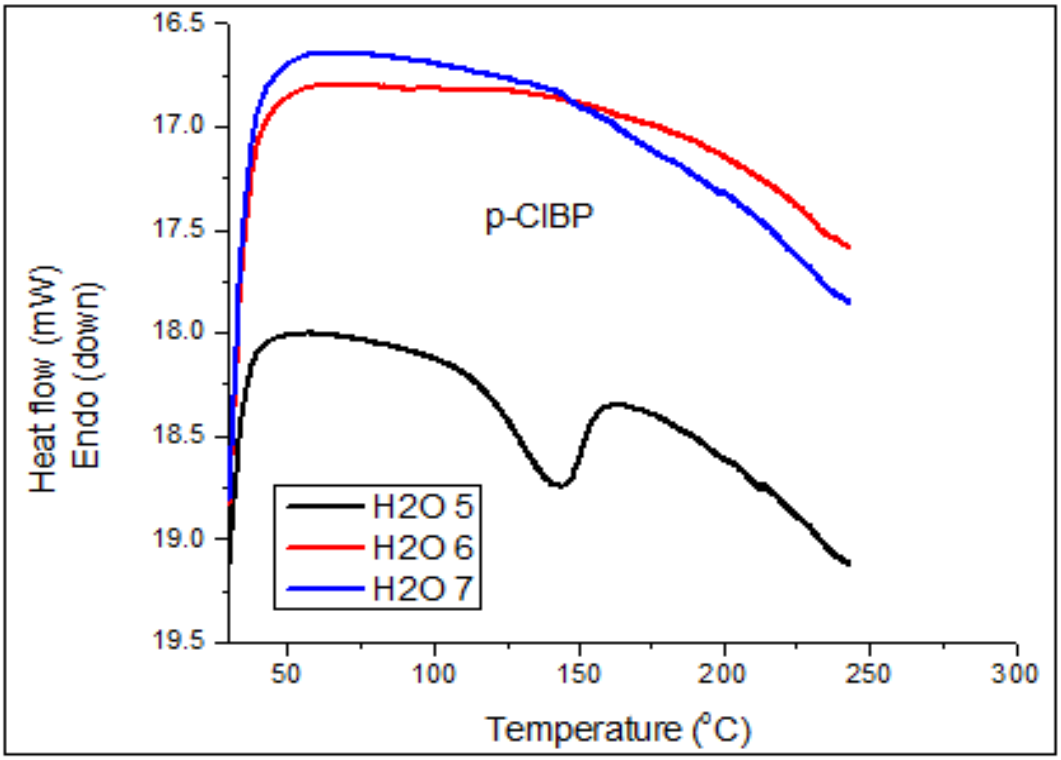
p-ClBP
Heat flow (mW)
Endo (down)
16.5
17.0
17.5
18.0
18.5
19.0
19.5
50
100
150
200
250
300
Temperature (°C)
H2O 5
H2O 6
H2O 7

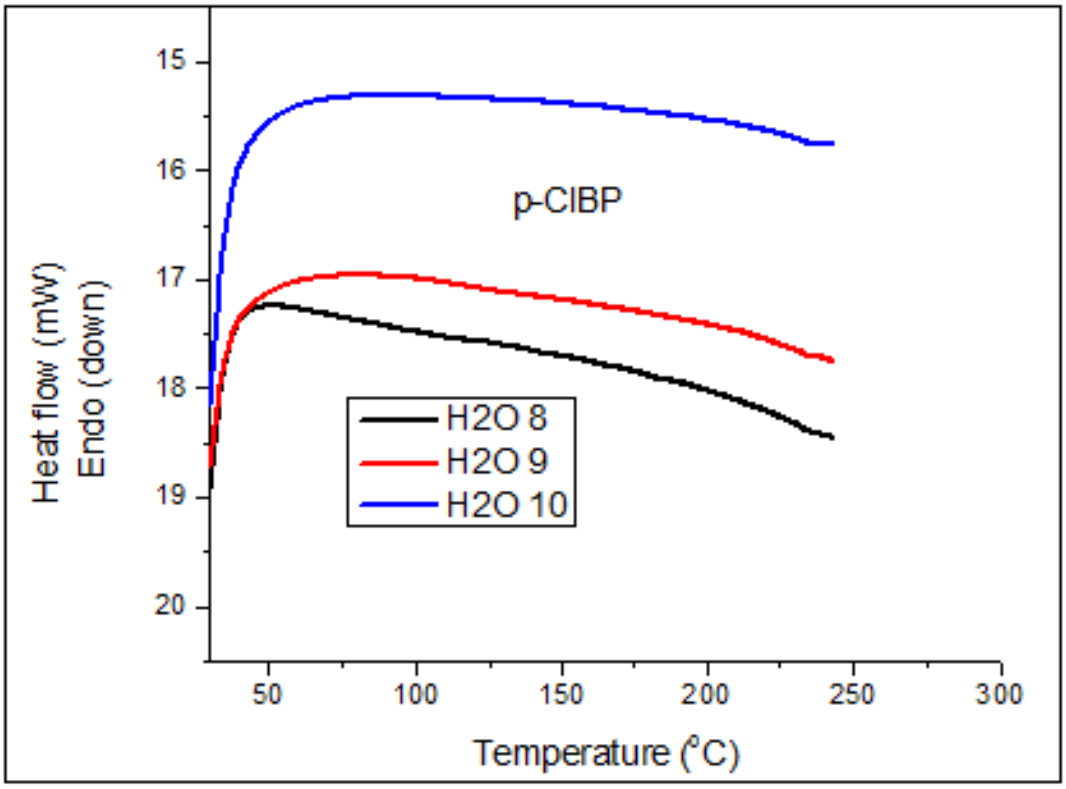

Appendix E4: DSC thermograms of *p*-ClBP after exposure to DMSO/MeOH system

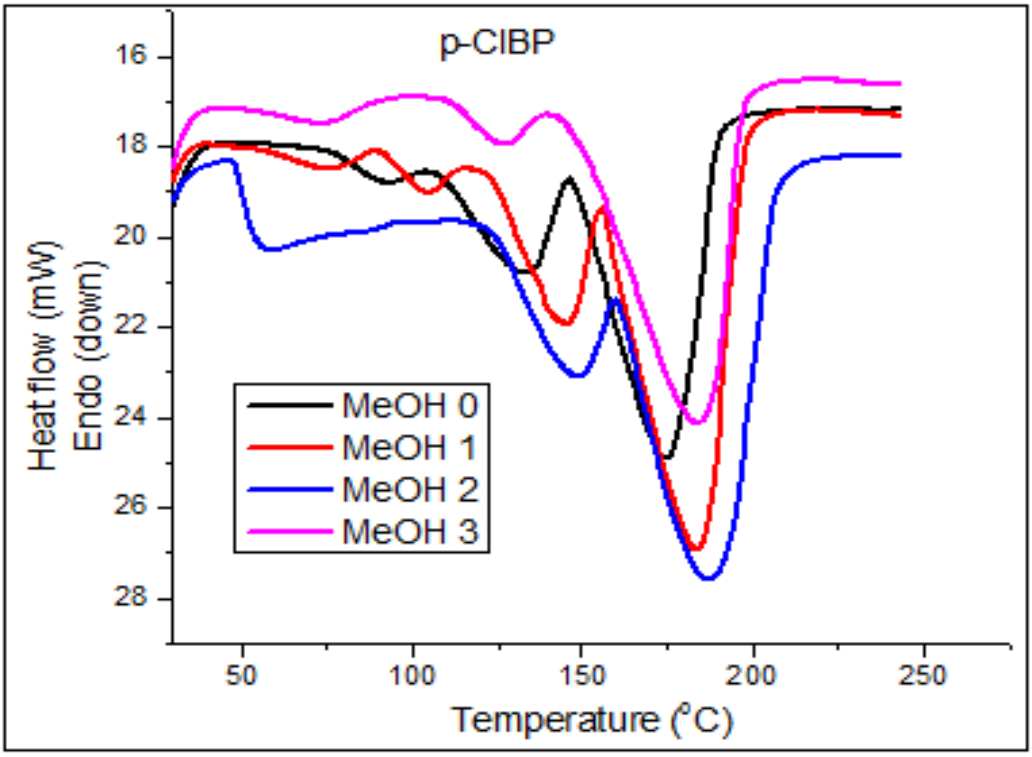

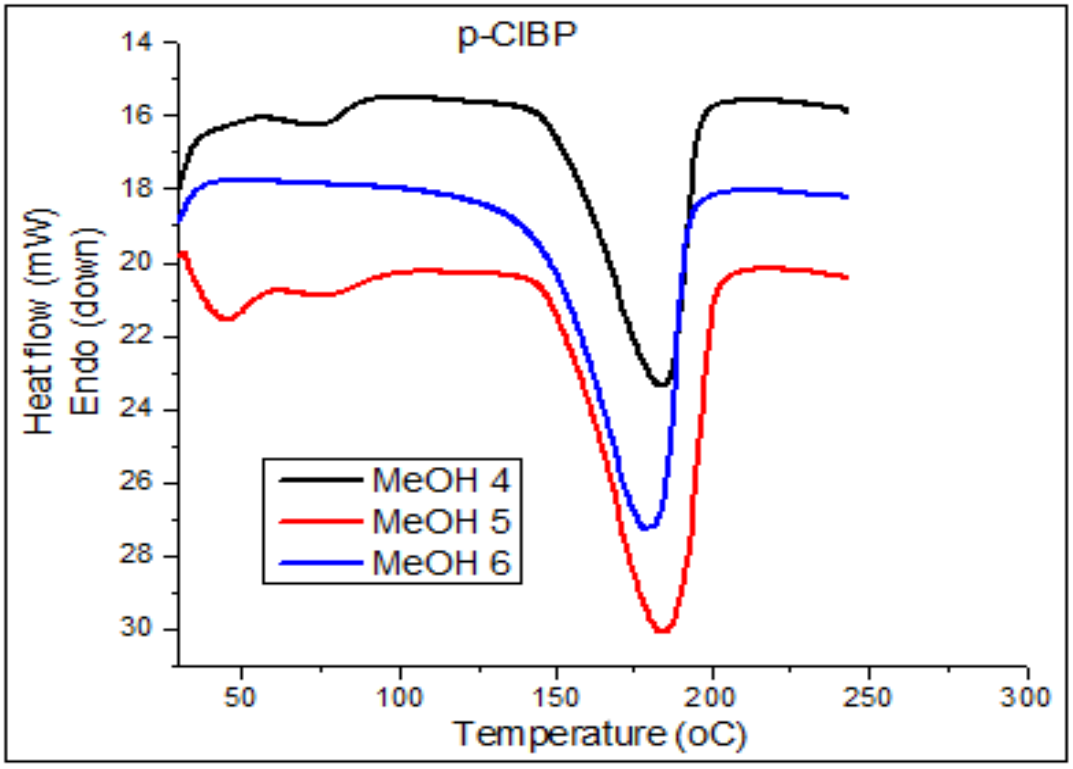
p-ClBP
Heat flow (mW)
Endo (down)
Temperature (oC)
MeOH 4
MeOH 5
MeOH 6
14
16
18
20
22
24
26
28
30
50
100
150
200
250
300

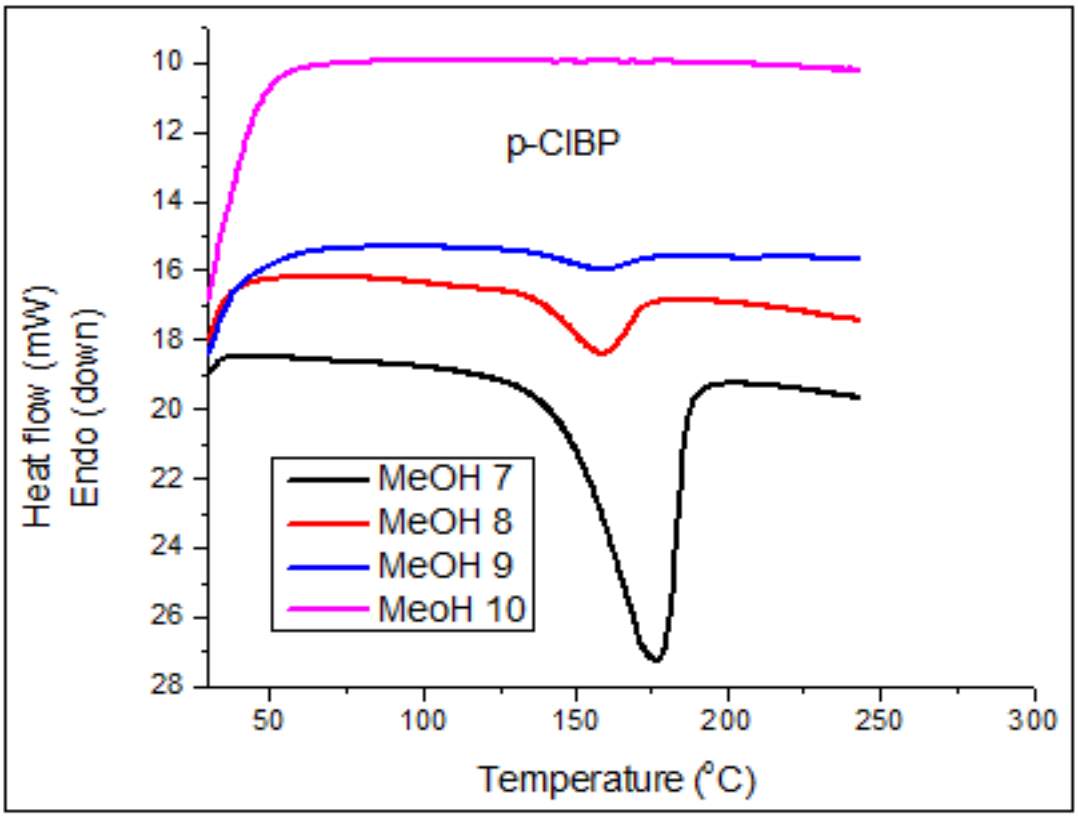
p-ClBP
Heat flow (mW)
Endo (down)
Temperature (°C)
MeOH 7
MeOH 8
MeOH 9
MeoH 10
10
12
14
16
18
20
22
24
26
28
50
100
150
200
250
300

Appendix F: PXRD diffractograms

Appendix F1: Powder XRD patterns for BN22E exposed to DMSO/H_2O system

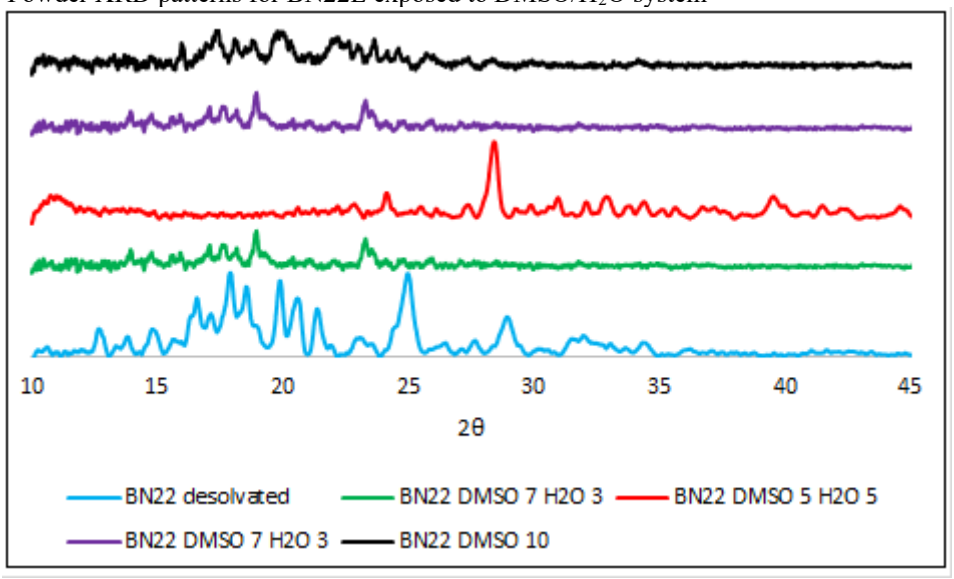

Appendix F2: Powder XRD pattern of BN22E exposed to DMSO/MeOH system

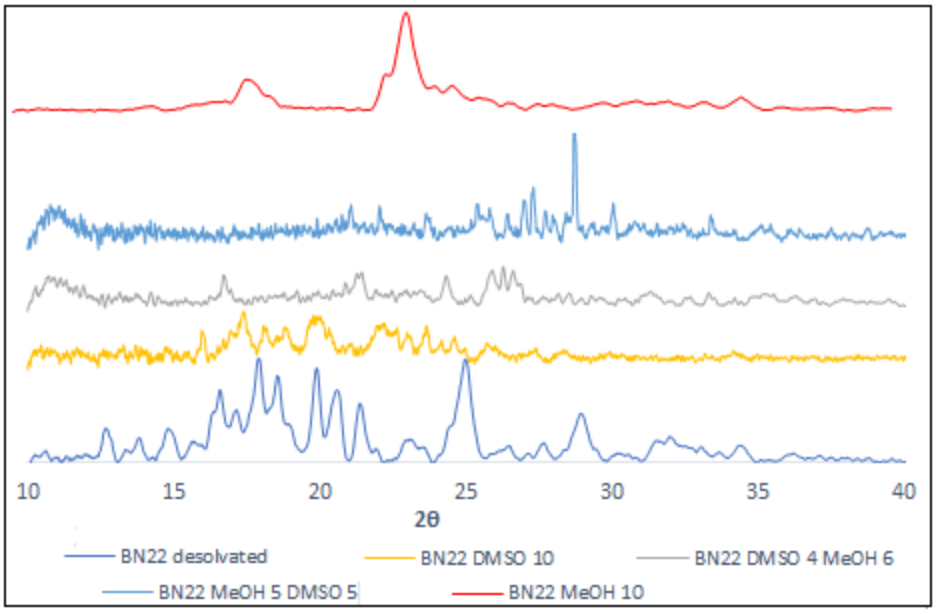

Appendix G: Job's plots for host-guest complexes [the Job's plot for the proton signal in red has been presented in chapter 5**]**

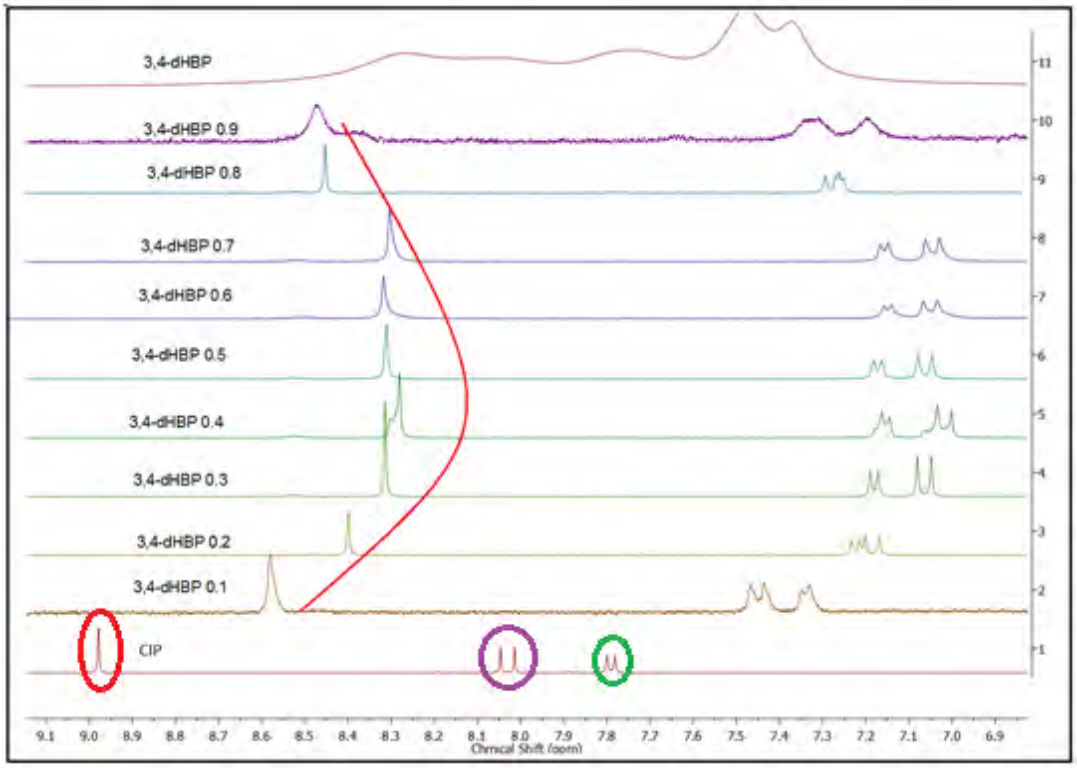

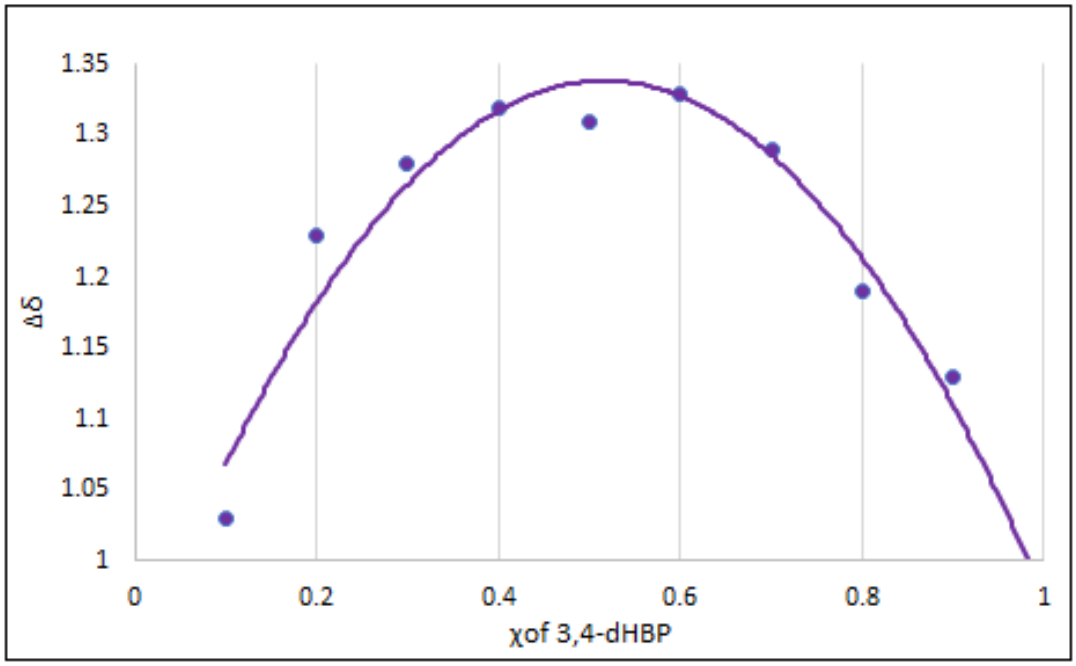

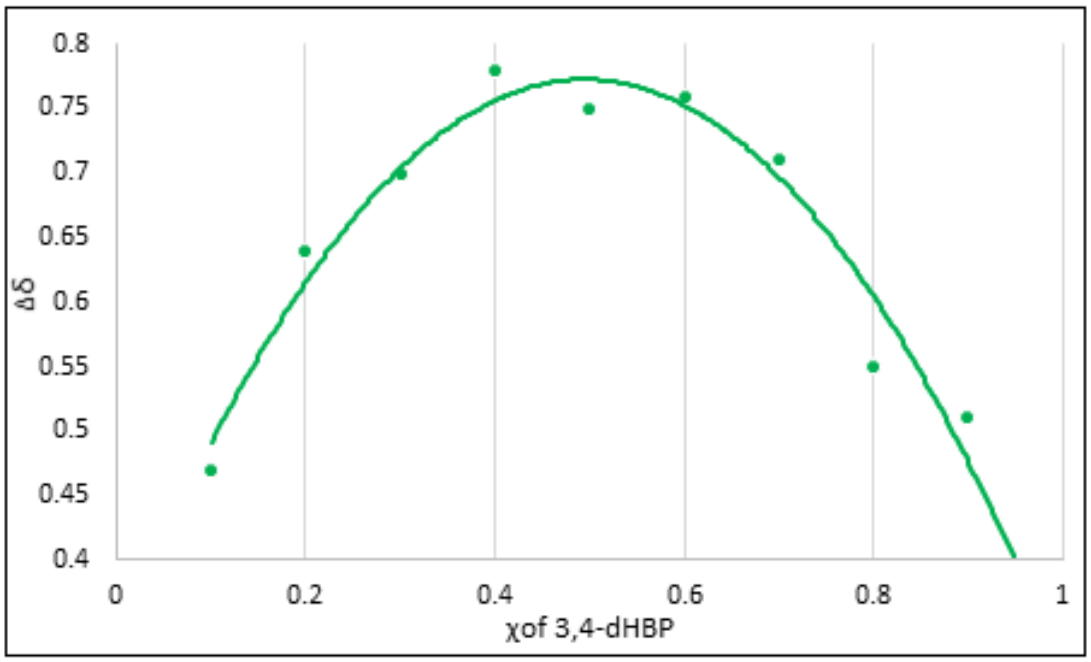
0.8
0.75
0.7
0.65
0.6
0.55
0.5
0.45
0.4
Δδ
0
0.2
0.4
0.6
0.8
1
χof 3,4-dHBP

Appendix H: Channel system of p-ClBP show along a b and c axes

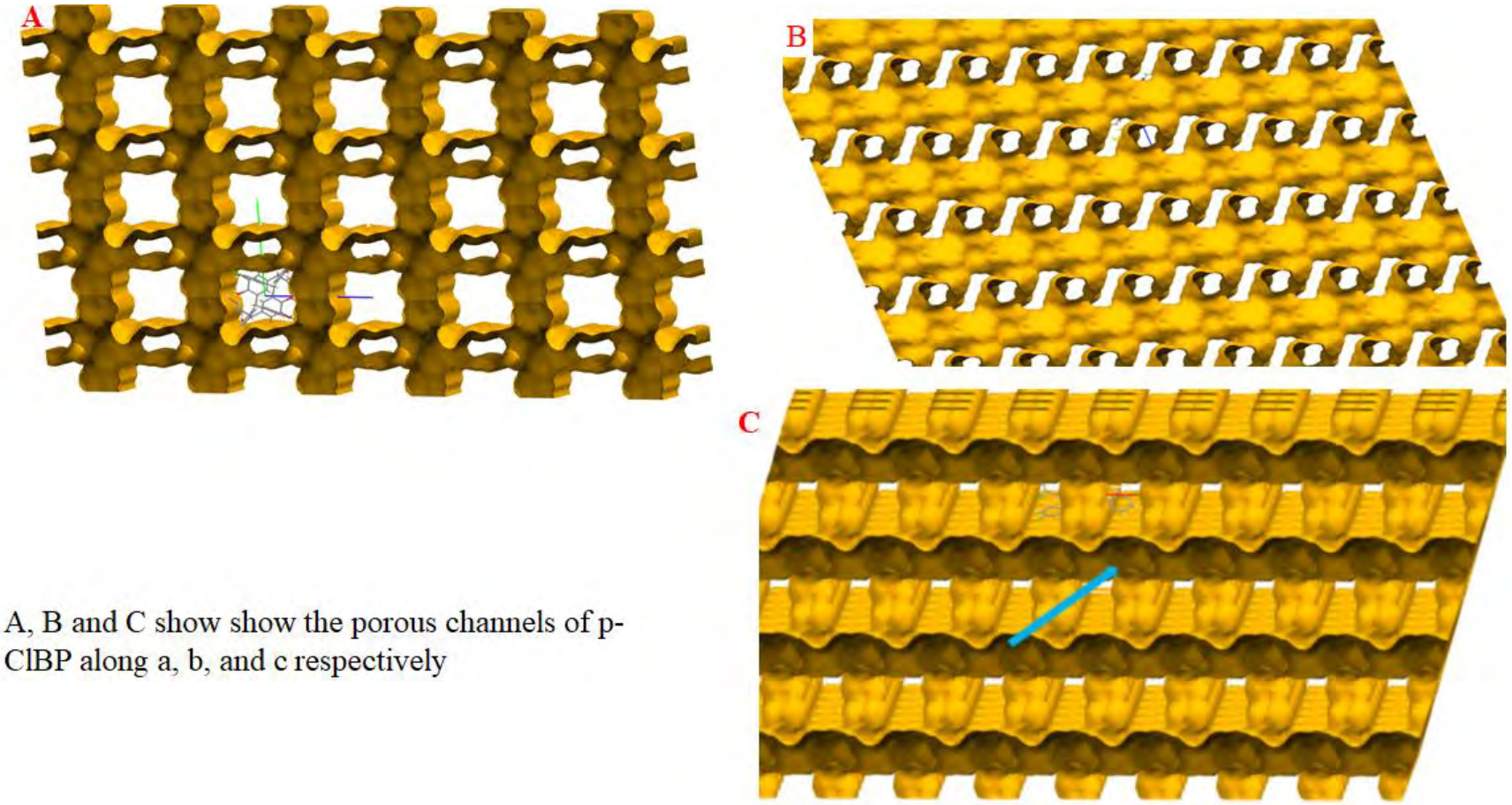

A, B and C show show the porous channels of p-ClBP along a, b, and c respectively